



UNIVERSITY OF THE BALEARIC ISLANDS
DEPARTMENT OF PHYSICS

Nonlinear Dynamics of Semiconductor Laser Systems with Feedback:

*Applications to Optical Chaos Cryptography,
Radar Frequency Generation, and Transverse Mode Control*

Thesis presented by

Yanne CHEMBO KOUOMOU

*at the Department of Physics of the University of the
Balearic Islands, for the obtention of the*

PHD DEGREE OF PHYSICS

Supervised by **Dr. Pere COLET RAFECAS**

Palma de Mallorca, October 2006

El director de tesi Dr. Pere COLET RAFECAS, Investigador Científic en el Departament de Física Interdisciplinar del Institut Mediterrani d'Estudis Avançats (IMEDEA, Consell Superior d'Investigacions Científiques - Universitat de les Illes Balears)

CERTIFICA

Que aquesta tesi doctoral ha estat realitzada pel Sr. Yanne Chembo Kouomou, i perquè quedi constància escrita firma

a Palma de Mallorca, 25 de Octubre de 2006.

Dr. Pere COLET RAFECAS

Vist-i-plau

Prof. Maximino SAN MIGUEL RUIBAL (Ponent)
Catedràtic de Física de la Materia Condensada, UIB.

“Ke sim bi sòm mō, bi sòm mō...”

Acknowledgments

WE use to say in Africa that it doesn't matter how tall a tree may be, it will never be worth a forest.

This PhD thesis has been realized between november 2002 and october 2006 at the Department of Cross-Disciplinary Physics of the **Mediterranean Institute for Advanced Studies** (IMEDEA), Palma de Mallorca, Spain, and it has been funded by a fellowship from the *Govern de les Illes Balears*. During the four years I have spent on this thesis, I have fortunately benefited from a very wide variety of constructive interferences. It is my pleasure to have here the opportunity to warmly acknowledge for this multidimensional support.

I would first like to express my gratitude to Dr. Pere Colet for the supervision of this thesis. It has been a great experience to profit from his enthusiastic interest for science, and I have also highly appreciated his entire disponibility and implication for the successful completion of this research work. I extend my gratitude to his family for the open doors.

I would have certainly never come to Mallorca without a bifurcation-like encounter with Prof. Maxi San Miguel at Trieste, four years ago. I sincerely hope he will appreciate this thesis as a valuable outcome.

I would also like to thank Dr. Claudio Mirasso for proposing me to join the IMEDEA group within the frame of a truely passionating research project.

I am grateful to Prof. Paul Woaf for the teachings and for the fruitful collaboration that has been sustained during so many years.

I have had the chance to visit some foreign research centers, and it has represented for me a very important opportunity of further learning and exchanges.

I am therefore extremely grateful to Prof. Laurent Larger for receiving me in his Laboratory of the FEMTO-ST Institute at Besançon, France. This six months visit has been an excellent opportunity for me to learn more about experimental opto-electronics and microwave physics, and I have appreciated the discussions and his insights on various topics related to laser physics. I am also very thankful

to his family for the welcome at Besançon.

It has been a great academical opportunity to visit Prof. Rajarshi Roy for three months at his Laboratory of IREAP, University of Maryland, USA. I would like to thank him for his warm hospitality, and for the skills I have acquired from his pluridisciplinary vision of laser science.

An important milestone on my way to this PhD has been my visit to Dr. Ingo Fischer at the Technical University of Darmstadt, Germany. I have truly enjoyed all our exchanges in Darmstadt and in so many other places, on an incredibly wide spectrum of topics, including, of course, semiconductor laser physics.

I would also like to thank all the PhD students and postdocs with whom I have been (very very hard) working during all these stays, namely Nikos “*the Jacky touch*” Gastaud, Shyam Mandre, Will Ray, Hervé Tavernier, and Ryad Bendoula.

I have a special thought for my *Muunganiko* brothers: Abogo, Mitoha, Osa, and Toasijé. Thanks to you for all what you have given me along the way, for the endless bursts of laughs, the endless Fela sessions, for the world recreated every night, fold and unfold again and again. “*Old men see visions young men dream dreams*”... Mallorca would have been empty without you.

Many thanks to the Cameroonian community of Palma, for sharing with me so many good moments; to Omar for the uncountable number of *mojitos* and *caipirinhas*, for the cinematographic deliria, for forging the new Big Bang; and thanks to you, Motea, for your pantagruelic, and ultimately tasteful kemitic banquets.

DFI-IMEDEA is a kind of United Nations microcosme, and my odyssey in Mallorca has also been a period of numerous interactions (strong, weak, ...) with dozens of persons coming from all over the world: Brasil, Italia, Argentina, Poland, France, etc. It has been a wonderful opportunity to actualize my cultural hard-disk day by day, and I would like to express my gratitude to all of them. But I will however keep particular recordings of enriching and delightful discussions with Raúl “*El Pichi*” Quinto, and of course, with the unsuspected Mayor of Palma, the energetic Pierre Scotto. I am also indebted to Pep Mulet for enlightning discussions on VCSELs.

To my worldwide Kmr-connection: Tins, Debah, Coach, Keintosh, etc. In memory of the past times, “*Back in the days, when things were cool*”...

At last, I would like to say to my parents, and especially to Na, San, Simo and Redig: I said it once, and I will say it twice, without you I am nothing.

Yanne Chembo Kouomou,
October 23rd 2006, Palma de Mallorca.

Contents

1	General Introduction	3
I	Optical Chaos Cryptography	23
2	Dynamics of Semiconductor Laser Systems with Electro-Optical Feedback	25
2.1	Introduction	25
2.2	Electro-optic modulators	26
2.2.1	The electro-optic effect	26
2.2.2	Electro-optic phase modulation	26
2.2.3	Electro-optic intensity modulation: the Mach-Zehnder interferometer	27
2.3	Modelization of semiconductor laser systems with electro-optical feedback	29
2.3.1	The system	29
2.3.2	The model	30
2.4	Dynamical behavior of the system	32
2.4.1	Steady-states and stability analysis	32
2.4.2	Periodic solutions	33
2.4.3	Breathers	34
2.5	Topological nature of the chaotic breathers	36
2.6	Experimental results	37
2.7	Influence of random noise: stochastic effects	39
2.8	Conclusion	41
3	Chaos Synchronization of Semiconductor Laser Systems with Electro-Optical Feedback: Influence of Parameter Mismatch	43
3.1	Introduction	43
3.2	Synchronization of electro-optical laser hyperchaos	44

3.2.1	Coupled system under study	44
3.2.2	Synchronization error and cross-correlation function	46
3.3	Single parameter-mismatches	48
3.3.1	Delay-time mismatch (T)	48
3.3.2	Nonlinear feedback-strength mismatch (β)	53
3.3.3	Off-set phase mismatch (ϕ)	53
3.3.4	Low cut-off response time mismatch (θ)	58
3.3.5	High cut-off frequency mismatch (τ)	60
3.4	Multiple parameter-mismatch	61
3.4.1	Global synchronization error and cross-correlation	61
3.4.2	One-parameter optimization	64
3.4.3	Multiple-parameter optimization	66
3.5	Experimental Results	67
3.6	Conclusion	70
4	Optical Chaos Cryptography Using Semiconductor Laser Systems with Electro-Optical Feedback	73
4.1	Introduction	73
4.2	Software cryptography	73
4.2.1	A secret-key cryptosystem: the Vernam cipher	74
4.2.2	A public-key cryptosystem: the RSA algorithm	75
4.3	Quantum cryptography	76
4.3.1	Fundamental principles of quantum cryptography	77
4.3.2	The BB84 protocol	78
4.4	Principles of optical chaos cryptography	79
4.4.1	Chaos cryptography	79
4.4.2	Cryptography in optical fiber networks	80
4.4.3	The problem of mismatch noise in chaos cryptosystems	80
4.4.4	The optical chaos cryptosystem under study	81
4.5	Performances of the electro-optical laser chaos cryptosystem	84
4.5.1	Determination of the Signal-to-Noise Ratio	84
4.5.2	Determination of the Bit Error-Rate	86
4.5.3	Influence of the non-Gaussianity of the chaotic mismatch noise	90
4.5.4	Numerical simulations	91
4.6	Experimental Results	92
4.7	Conclusion	94

II Nonlinear and Stochastic Dynamics of Ultra-Pure Microwave Generators	97
5 Single-Mode Microwave Dynamics of Opto-Electronic Oscillators	99
5.1 Introduction	99
5.2 Fundamental principles of radars	99
5.2.1 Microwaves and radar frequencies	99
5.2.2 Types of radars	101
5.2.3 Applications of radars	102
5.2.4 Other applications of ultra-pure microwave generators	103
5.3 The opto-electronic oscillator	103
5.3.1 The system	104
5.3.2 A deterministic model for the OEO	105
5.4 Stationary solutions of the OEO and their stability	108
5.4.1 Stationary solutions	108
5.4.2 Stability analysis: emergence and stability of the monochromatic solution	109
5.5 Experimental results	110
5.6 Conclusion	111
6 Stochastic and Multimode Microwave Dynamics of Opto-Electronic Oscillators	113
6.1 Introduction	113
6.2 Stochastic microwave dynamics of OEOs	114
6.2.1 Phase noise	114
6.2.2 The stochastic model	114
6.2.3 Numerical simulations	116
6.3 Temporal evolution of the radio-frequency spectrum	117
6.4 Experimental results	119
6.5 A modal expansion approach to OEO's dynamics	119
6.5.1 The multiple timescales method	120
6.5.2 Modal equations	121
6.6 Multimode dynamics of OEOs: a paradigm for globally coupled oscillators	127
6.7 Conclusion	127
III Transverse-Mode Control in Vertical-Cavity Surface-Emitting	

Lasers	129
7 Modelization of Multimode VCSELs with Polarization- and Frequency-Selective Feedback	131
7.1 Introduction	131
7.2 Principles of VCSELs	132
7.2.1 The active medium: quantum wells	134
7.2.2 The resonator: Bragg reflectors	135
7.2.3 Injection and confinement of carriers	136
7.2.4 Emission properties of VCSELs	137
7.3 Equations for the field and carrier dynamics	138
7.3.1 Field dynamics	139
7.3.2 Carrier dynamics	153
7.4 Conclusion	157
8 Transverse-Mode Control in VCSELs: Modal Gain and Stationary Modal Amplitudes	159
8.1 Introduction	159
8.2 The system	160
8.2.1 The experimental set-up	160
8.2.2 Effect of geometrical anisotropies	160
8.2.3 Effect of material anisotropies	162
8.2.4 The model	162
8.3 Effect of the PFSF on the dynamics of the VCSEL	166
8.3.1 Determination of the external cavity modes	166
8.3.2 Determination of the stationary modal amplitudes	170
8.4 Experimental results	173
8.5 Numerical simulations	174
8.6 Conclusion	176
9 General Conclusion	179
Bibliography	185
List of Figures	191
Curriculum Vitae	i

General Introduction

Chapter 1

General Introduction

“But the time.”

Sony Labou Tansi, *Life and a half*.

IN the ancient Egyptian civilization, the paradigm of chaos was a snake biting its own tail. Hence, to some extent, they had yet understood that self-feedback is potentially a source of complexity.

Typically, in systems subjected to feedback, the dynamical state at a given time depends on the state of the system at an anterior time, and the delay time generally coincides with the propagation time of the feedback signal. In fact, delayed variables should be taken into account in absolutely all dynamical systems, because the propagation velocity of the various interactions are always finite. But as long as they are small comparatively to the relevant timescales of the system's dynamics, these delays can be neglected and the dynamical equations degenerate into a flow of **Ordinary Differential Equations** (ODE), which inherently assume instantaneous interactions.

Sometimes however, the delay time has the same order of magnitude as the system's typical timescales. This may for example occur in ultrafast systems, or for particularly long delay times. In these cases, the delay can not be neglected anymore and the system should rather be modeled with a **Delay Differential Equation** (DDE). Even though it is not apparent at first view, DDEs are very complex equations: at the opposite of ODEs, they are **infinite-dimensional**, because their initial condition is a continuous and compact interval.

Therefore, the simple fact to introduce and account for a delay time in a dynamical system increases its dimensionality to infinity, and thereby opens the way to a wide variety of very complex behaviors.

Surprisingly, despite the huge advances of physics and mathematics in the twentieth century, it is only at the early sixties that delay differential equations gained sufficient attention from the scientific community. In the first years, though, the interest was purely mathematical and these equations were studied under the terminology of **Functional Differential Equations**, mainly by **Krasovskii** and **Hale** [1, 2]. Then, these new ideas rapidly started to spread in various areas of applied science, particularly in control theory. An archetypal example in this case emerged at the early seventies, at the golden age of space exploration: it is the problem of ground-based satellites and rockets control [3], where the propagation time of the command signal is far from being negligible.

In physics, in particular, delay differential equations have been found to be the idoneous tool to investigate the behavioral properties of dynamical systems where delays had to be taken into account. To take just an illustrative example in applied engineering, it had been observed that some high-speed milling and cutting processes did yield polygon-like instead of cylindrical metallic pieces; it was later understood that the stability -and thus the optimization- of this cutting process had to be studied within the frame of delayed systems, as the relative rotation motion of the cutter depends on the state of the metallic piece one round-trip earlier [4].

In fact, far beyond the scope of physics, delay differential systems have been successfully used to investigate a very large spectrum of problems, ranging from predator/prey ecosystems [5] to neurology [6]. If for example we consider the particular case of human physiology, a famous delay differential equation is the so-called **Mackey-Glass** model, which has been proposed to describe the dynamics of white blood cells production in the human body [7]. This dynamical systems approach even empowered the concept of **dynamical disease**, as it was suggested by Mackey and Glass that the model could explain the occurrence of some forms of leukemia.

It has resulted from thirty years of theoretical and experimental investigations that the delay may globally have two opposite effects: either a **destabilization effect**, through the excitation of many of the latent degrees of freedom; or either a **stabilization effect** by somehow acting as a selective energy sink. In both cases, there is a plethora of applications where one of these effects may be highly desired.

Within the frame of this thesis, we will lay emphasis upon those of these applications which are related to **semiconductor laser systems**.

Semiconductor lasers

The concept of **stimulated emission** was proposed for the first time in 1917 by **Albert Einstein**, in a seminal paper entitled “*On the quantum theory of radiation*” [8]. Typically, in the stimulated emission process, an incoming photon “stimu-

lates” an atom to emit another photon of identical characteristics - same direction, same frequency, same polarization, and same phase. On the base of thermodynamical principles, Einstein showed that exclusive consideration of spontaneous emission and absorption could not explain the thermodynamical equilibrium between matter and radiation, the missing contribution being precisely the stimulated emission. This stimulated emission is usually small comparatively to absorption at room temperature. In the simple case of two-level systems for example, there are more electrons in the lowest level of energy than in the highest when the system is in the thermodynamical equilibrium: that is why common materials absorb light, and are labeled as **passive** media.

However, if an *inversion of population* is induced in the material, that is, if the out-of-equilibrium situation where there are more electrons in the highest level than in the lowest is achieved, then the medium predominantly emits stimulated radiations, and thereby amplifies incoming light: it becomes an **active** medium.

It was yet known that the combination of an amplifier and a resonator does constitute an oscillator. Then, at the late 50s, it was understood that a system associating an active media and an appropriate optical resonator would oscillate. This optical oscillator was later given the name **LASER**, an acronym standing for **L**ight **A**mplification by **S**timulated **E**mission of **R**adiations. Today, there is a wide variety of lasers (principally solid state-, gas-, dye-, and fiber-lasers), but the most widespread lasers are by far the **semiconductor lasers**.

The idea of coherent emission from semiconductor media was proposed for the first time by **John Von Neumann** in 1953¹, and the first semiconductor lasers have been experimentally realized in 1962 by independent american research groups (see ref. [9]).

Typically, the semiconductor laser is a micrometric device: its longitudinal and transverse dimensions can be as low as 1 μm , that is, of the order of visible light wavelengths. Like all lasers, they are constituted of two basic ingredients: an **active medium** which amplifies light by stimulated emission of radiations, and a **resonator** which shapes the optical modes and couples out the coherent light. More concretely, in its simplest architecture, the active medium in a semiconductor laser consists in a thin *p-n* junction layer, whose cleaved facets act as reflectors. This basic architecture is extremely flexible, and today there exist several kinds of

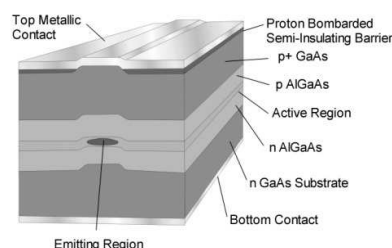


Figure 1.1. A typical edge-emitter semiconductor laser. After ref. [10].

¹**John Von Neumann**, ‘Notes on the photon-disequilibrium-amplification scheme’, private correspondence with E. Teller, 16 sept. 1953.

semiconductor lasers, which may by the way incidentally share some common features: double heterostructure lasers (DHLs), vertical-cavity surface-emitting lasers (VCSELs), vertical external-cavity surface-emitting lasers (VECSELs), distributed feedback lasers (DFB), multi-quantum well lasers (MQW) distributed Bragg reflector lasers (DBR), separate confinement heterostructures (SCH), etc.

Semiconductor lasers generally produce coherent radiations whose wavelength lies from the ultraviolet to the infrared frequency ranges. This large range of wavelengths, coupled to the wide variety of structures, have empowered an impressively large amount of applications for semiconductor lasers: optical fiber and free-space communications, laser printers, optical storage, bar-code readers, image scanning, combustion ignition, laser surgery, industrial sorting and machining, ranging, sensing, tracking, spectroscopy, illumination, holography, etc. They have also naturally crossed the barrier of the latest innovative applications, such as photobiology and photodynamic therapy, terahertz waves generation, or clock generation in optoelectronics. Semiconductor lasers can also be associated in array configurations, in order to produce high-power laser sources which are used for drilling and cutting, or even to pump other types of lasers.

It can therefore be easily understood that semiconductor lasers have an overwhelming weight in laser technology. This can be illustrated by a very simple data: more than 99% of all the lasers that are fabricated and sold today are semiconductor lasers, and this corresponds to more than a 60% share of the capital flow in the laser market.

Hence, according to all what has been written above, an open question is: what does occur when a semiconductor laser system is subjected to feedback? Is it possible to find out new applications, related to the association of semiconductor lasers and feedback? The aim of this thesis is to answer to these questions for three particular cases, leading to three different applications:

- **Optical chaos cryptography**, which consists in encrypting signals within the noise-like output of a chaotic laser system.

- **Radar-frequency generation**, where lightwave and microwave technologies are associated to produce ultra-pure radio-frequencies.

- **Transverse-mode control in vertical-cavity surface-emitting lasers**, whose principle relies on the spectral discrimination and tailoring of a broad-area laser's transverse modes.

The thesis will therefore be divided into three parts, each of them devoted to one of these applications.

Optical chaos cryptography

Chaos is a paradigmatic name used to describe deterministic dynamical systems whose behavior is complex, unpredictable and extremely sensitive to initial conditions [11–15]. Chaos was first explicitly evidenced by **Edward Lorenz** in a pioneering paper entitled “*Deterministic nonperiodic flow*” [16]. It is typically characterized by complex attractors in the state space, associated to apparently random oscillations in the time domain.

Chaos is likely to appear in *nonlinear* systems which are at least *three-dimensional*. However, chaos is the most of the time evidenced by the computation of **Lyapunov exponents**, which measure the divergence rate of initially nearby trajectories in the state space, that is, the sensitivity to initial condition. By definition, a dynamical system is said to be chaotic when at least one of its averaged Lyapunov exponents is positive. It is also a common terminology to consider that a system is chaotic when it has only one positive Lyapunov exponent, and hyperchaotic when it has more than one positive Lyapunov exponent.

Optical chaos

The possibility of chaotic behavior in lasers was first foreshadowed by **Haken** in 1975 [17], as he showed that the dynamics of some ring-laser devices could be described by a Lorenz-like set of ordinary differential equations. Since then, chaos has been theoretically and experimentally encountered in almost all types of lasers (solid-state, gas, semiconductor, etc...). Methods to lead lasers to chaos are numerous: as earlier emphasized, two necessary conditions are nonlinearity and threefold dimensionality. Hence, when the nonlinearity of the laser (system) is not strong enough, an external nonlinear element can be introduced. Along the same line, when the dimensionality of the laser system is not high enough, it can be increased by parameter modulation or by delayed feedback loops.

As far as semiconductor lasers are concerned, there are two delayed systems that are commonly used to obtain chaos. The first one was proposed by **Ikeda**, and it consists in a continuous-wave laser whose output light propagates in a nonlinear ring-cavity [18]. The second one, studied in detail by **Lang** and **Kobayashi**, corresponds to the situation where a fraction of the delayed output radiation of a semiconductor laser is fed back into the active region layer [19]. In both case, hyperchaos can be generated, that is, the delay plays here a destabilizing role as it drastically broadens the laser light linewidth. This loss of coherence was given the name **optical turbulence** in the Ikeda model [20], while it received the name **coherence collapse** in the Lang-Kobayashi model [21].

In Ikeda-like systems, though, only *pure* delay differential systems have been given proper attention. Within that frame for example, Ikeda-like equation with higher-order differential terms have yet been studied [22, 23]. However, only a very limited interest has been paid until now to the chaotic behavior of *integro-differential* delayed systems.

The first objective of the thesis will be to fill this gap for the particular case of an electro-optical hyperchaos generator, which will later be used for cryptography.

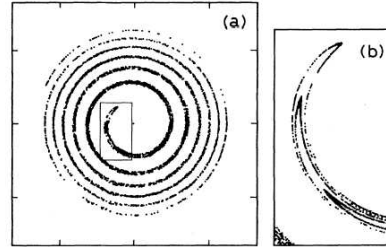


Figure 1.2. Numerical simulation of a phase space projection corresponding to the laser field in Ikeda optical turbulence (a), and enlargement showing the fractal structure of the spiral (b). After ref [20].

Optical chaos synchronization and parameter mismatch

The concept of synchronization in dynamical systems has first been introduced by **Christian Huygens**, back to 1665. He observed that two pendulum clocks which are suspended on the same support, display perfectly out of phase oscillations. He also observed that when perturbed, this synchronization (or anti-synchronization, according to nowadays nomenclature) behavior was recovered after a few minutes long transient time. Huygens proposed an explanation to this phenomenon, to which he referred to as “*an odd kind of sympathy*”: the clocks did influence each other through imperceptible movements of the common support. Today, it is established that synchronization is an ubiquitous phenomenon, which can be encountered in almost all the scientific disciplines where coupled oscillators do play a role [24].

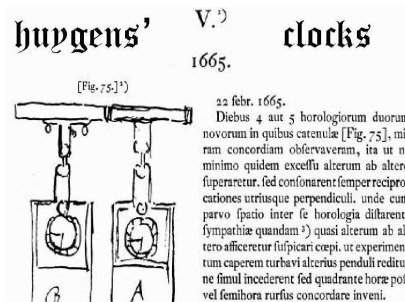


Figure 1.3. Original article of Huygens on clock synchronization, published in the *Journal des Sçavants* on February 22nd, 1665.

As far as chaotic systems are concerned, it can easily be understood that two distinct but identical chaotic systems starting from two different initial conditions can converge to the same chaotic attractor, which is an invariant. However, because of the sensitivity to initial conditions, it is quite counter-intuitive to imagine that they can synchronize, that is, display the same temporal behavior. Nevertheless, few years after a pioneering paper by **Fujisaka** and **Yamada** [25], it was

demonstrated by **Pecora** and **Carroll** that such a synchronized behavior is possible, provided that a convenient coupling is achieved between both systems [26,27]. When such a convenient coupling is set up, they can display timetraces which are perfectly identical.

In case of unidirectional coupling, the system which emits the synchronization signal is indistinctly referred to as the *emitter*, the *drive* or the *master* system; the system which receives this synchronization signal and thereby tries to track the dynamics of the emitter is referred to as the *receiver*, the *response* or the *slave* system. Since we study synchronization phenomena within the frame of communication systems, we will preferably adopt the “emitter/receiver” terminology.

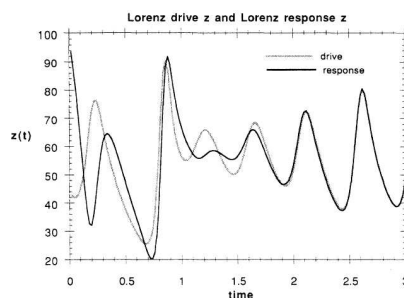


Figure 1.4. Numerical simulation of chaos synchronization in the Lorenz system. After a transient time, the drive and the response systems do perfectly synchronize. After ref. [27].

After the breakthrough of the chaos synchronization concept, an ever increasing amount of investigations did focus on the synchronization of chaotic lasers. Early and noteworthy examples are the numerical study by **Winful** and **Rahman** with semiconductor lasers [28], the experimental synchronization of Nd:YAG lasers by **Roy** and **Thornburg** [29], and the experimental synchronization of passive Q -switched CO_2 lasers by **Sugawara**, **Tachikawa**, **Tsukamoto**, and **Shimizu** [30].

Laser chaos synchronization was experimentally complicated by the difficulty to build almost identical lasers. In reality, it is impossible to build two systems which are perfectly identical. Therefore, if these systems are characterized with a set of intrinsic parameters, they will unavoidably display some **parameter mismatch**. In the time domain, this parameter mismatch induces a **synchronization error**, which is obviously equal to zero in case of perfect matching. This synchronization error is also sometimes referred to as **mismatch noise**.

Despite its importance for practical applications, studies on the effect of parameter mismatch in chaotic synchronization are quite scarce in the literature. In references [31,32], the effect of parameter mismatch was studied analytically for non-delayed and low-dimensional chaotic systems. In high-dimensional chaotic systems, such as semiconductor lasers with optical feedback, there are some numerical [33] and analytical [34] results. In delayed optoelectronic wavelength oscillators the root-mean-square synchronization error amplitude induced by two simultaneous mismatches has also been studied [35].

But beyond a purely theoretical interest, the issue of parameter mismatch is specially relevant in the context of **optical chaos cryptography**.

As we will further see, it is crucial to achieve a very stable and accurate synchronization between the emitter and receiver chaotic systems. Particularly important is the double role of the mismatch between the parameters of both systems, which is unavoidable in the fabrication process. On the one hand, mismatch can degrade the synchronization quality between the emitter and the receiver. Therefore, synchronization should be robust enough to allow for the use of slightly different devices. On the other hand, the lack of synchronization due to mismatch is a key element for security since it prevents the use by an eventual eavesdropper of a similar device to decode the message. This is particularly important because successful decryption is not possible when the amplitude of the encrypted message is smaller than the one of the residual oscillations resulting from the parameter mismatch, the so-called mismatch noise.

A key challenge in synchronization theory is therefore to characterize this mismatch noise as a function of the various mismatches. A chapter will be devoted to that issue.

Chaos cryptography

Security of information in public or opened transmission channels is a key-challenge in modern telecommunication networks. Nowadays, an ever growing proportion of data do require a very high level of confidentiality while they are transmitted. Ensuring such a confidentiality is the purpose of cryptography [36].

We are actually in the **software cryptography** era, or better said, the *algorithmic cryptography* era. Effectively, information is nowadays encrypted by performing logic and/or arithmetic operations between the binary message to be encrypted and a binary “key”. The security provided by this technique can be quite high, and even complete as it is the case for the so-called **Vernam cipher** proposed by **Gilbert Vernam**, which is by the way the *unique* cryptosystem up to date proven to be *absolutely* unbreakable. However, such an absolute unbreakability is not always necessary, first of all because various levels of security can be attached to an information: transferring personal data of students in a university network needs less “security” than transferring strategic military information from one country to another. The second reason is that information may by essence be sensitive for only a limited duration of time: for example, a credit card number should be kept secret during the validity term of the card, after which this number is of absolutely no value. A cryptosystem which could guarantee security in the meantime would therefore be perfectly convenient.

The most popular software encryption scheme fulfilling these flexibility crite-

ria is the **RSA algorithm** proposed by **Rivest, Shamir** and **Adelman** [37]. This cryptosystem relies on the factorization of very large integers in terms of prime numbers, and the algorithmic complexity associated to the best known factorizing algorithms grows exponentially with the size of the number to factorize. That is why this cryptosystem is considered as very safe, and nowadays plays the role of a standard in software cryptography. However, it was demonstrated twelve years ago that the use of a quantum computer would reduce the algorithmic complexity of the RSA cryptosystem from an exponential to a polynomial [38], thus drastically threatening the base above which almost all security systems are built. Moreover, research activities on cracking algorithms to be run in “classical” computers with polynomial complexity are quite intense, and nothing theoretically prevents them to be discovered - if it has not yet been done.

Consequently, there is a need to turn towards new alternatives able to *strengthen* software cryptography. The best candidates up to date are **hardware** cryptosystems, that is, cryptosystems relying on the *physical* properties of the emitters and of the receivers. As we will further see, the principal interest of hardware cryptosystems is that they are fully compatible with their software counterpart, in the sense that data can first be encrypted by software, and later encrypted again by hardware, thereby providing additional security.

A first hardware cryptosystem which is currently widely investigated is **quantum cryptography**, or better said, **Quantum Key Distribution (QKD)** [39]. Effectively, QKD does not aim to encrypt messages directly, but rather to send *safely* a key in order to use it later for message encryption, through the Vernam cipher for example. In an optical communication network, an eavesdropper trying to measure the photons in order to read the transmitted signal will unavoidably perturb them, and such a perturbation can be detected at the receiver. It is thereby possible to know if someone is tapping the line, and also to discard sequentially any portion of the key which is supposed to be unsafe. This technique has the great advantage to provide the highest security at the hardware level for now: on the one hand, the security of the key transfer is guaranteed by the fundamental laws of quantum mechanics, and on the other, the Vernam cipher encryption of a given message with that key is unbreakable according to the **Shannon** information theory. However, QKD has quite severe limitations: it can not encrypt information in real time, and until now, it has a quite limited span (few tens of km) and very low bit-rate (few tens of kbits/s).

Another interesting alternative is **chaos cryptography**, which aims to exploit the nonlinear properties of nonlinear emitter-receiver systems (see ref. [40] and references therein).

In a chaos cryptosystem, the information to be secured is somehow “mixed” or “hidden” into the noise-like output of a chaotic emitter. However, this idea may be

fruitful if and only if one can build a receiver able to separate the chaos from the message at the receiver, and if such a separation remains difficult for an eventual eavesdropper. An elegant solution fulfilling these two requirements relies on the phenomenon of **chaos synchronization**.

Since the synchronized state is deterministic, the receiver oscillator only couples to the deterministic -that is, chaotic- component of the incoming coupling signal: this is the **chaos-pass-filtering** phenomenon, which can precisely be used to extract the originally encrypted message by filtering out the chaotic oscillations used for encryption. Such a filtering results efficient if and only if the message is small enough relatively to the chaotic carrier, condition which also ensures that the message is satisfactory “camouflaged” within the deterministic randomness of chaos. With electronic circuits, **Cuomo** and **Oppenheim** experimentally demonstrated for the first time in 1993 that such cryptosystems can be built, and operate efficiently [41].

In optical systems, chaos cryptography was first theoretically proposed for solid-state lasers with modulated losses in 1994 by **Colet** and **Roy** [42]. However, the first experimental demonstrators have been built only in 1998, by **Van Wiggeren** and **Roy** using erbium-doped fiber ring-lasers [43, 44], and by **Larger et al.** using the wavelength chaos generated with a semiconductor laser [35, 45].

In optical-fiber telecommunication networks, emitters and receivers are semiconductor lasers, so that chaos cryptography in such networks requires to have **chaotic semiconductor lasers systems**. In fact, semiconductor laser systems with feedback are highly desirable for the purpose of chaos cryptography, because at the opposite of low-dimensional chaotic systems which possess only few positive Lyapunov exponents, they can display a highly hyperchaotic behavior, that is, a very complex temporal oscillations characterized by hundreds of positive Lyapunov exponents. In consequence, intensive research on semiconductor laser systems with feedback were developed in order to lead them to a synchronized hyperchaotic regime, and the feasibility of optical chaos cryptography with such lasers was independently proposed in 1996 by **Mirasso et al.** [46], and by **Annovazzi-Lodi et al.** [47]. However,

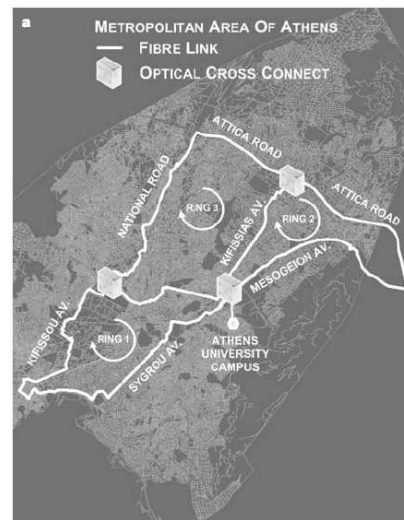


Figure 1.5. Optical chaos cryptography was successfully performed in a field experiment on the metropolitan area optical fiber network of Athens, with a BER equal to 10^{-7} at 1 Gb/s. After ref. [51].

robust experimental synchronization of all-optical chaotic semiconductor lasers and signal retrieval was only achieved in 2000 by **Fischer** *et al.* [48].

Beside all-optical delayed systems, investigations have been led to develop other alternatives such as electro-optic and opto-electronic delayed feedback systems, which may produce a wide variety of chaotic behaviors ranging from wavelength chaos (as noted earlier) [35, 45] to intensity [49] or phase chaos [50]. A milestone in chaos cryptography research is the successful field experiment reported in 2005, consisting in chaos encryption and transmission at 1 Gb/s over a network of 120 km of optical fiber in the metropolitan area of Athens, Greece [51].

An important aspect of optical chaos cryptosystems is the characterization of their performances under perturbations, and this task is made extremely difficult by the fact that the laser systems under study are operating in strongly nonlinear regimes.

The quality of a digital communication link is almost always evaluated in terms of **Bit Error-Rate** (BER). The issue of BER efficiency in optical chaos communication schemes is quite scarcely addressed in the literature [52–54]. A noteworthy exception is the work of **Liu** and co-workers, who did numerically explore the BER efficiency of different laser-chaos communication systems (optical injection, optical feedback, optoelectronic feedback) with various encryption schemes (chaos shift-keying, chaos masking, additive chaos modulation) [55]. In general, the BER depends on several elements such as the random noise in the emitter and receiver systems, dispersion and nonlinear effects in the fiber communication channel, and of course parameter mismatch between the emitter and receiver.

Chaos Shift-Keying (CSK) schemes for encryption of binary signals in a chaotic carrier [47, 56, 57] also critically depend on parameter mismatch. Effectively, CSK relies on a sequential switching of a given parameter between two values, the first one being matched with the receiver (thereby ensuring synchronization), the second being slightly detuned from the first one (so that the receiver desynchronizes). The synchronization/desynchronization sequence at the receiver enables the message decryption provided that intrinsic mismatch noise allows the distinction between both states. Within that frame, ref. [58] focused on the performance comparison of the CSK encryption scheme for various “switched” mismatched parameters.

One of the aim of this thesis will be to study the mismatch-induced BER for an optical communication scheme based on intensity chaos generated by a delayed nonlinear electro-optic oscillator. In particular, we will integrate some tools of conventional communication engineering like the **Signal-to-Noise Ratio** (SNR) in order to gain a insight into the influence of chaotic noise on the BER.

Radar-frequency generation

The possibility to use electromagnetic waves to detect distant objects was proposed for the first time by **Guglielmo Marconi** in 1922:

“In some of my tests, I have noticed the effects of reflection and deflection of [electromagnetic] waves by metallic objects miles away. It seems to me that it should be possible to design apparatus by means of which a ship could radiate or project a divergent beam of these rays in any desired direction, which rays, if coming across a metallic object, such as a ship, would be reflected back to a receiver and thereby immediately reveal the presence and bearing of ships.”

This idea became reality during World War II, and the “apparatus” was given the name **RADAR**, which is the acronym of **RA**dio **D**etection **A**nd **R**anging.

Radars are used to detect distant (groups of) objects and evaluate their distance, velocity or structure. The generic principle of radars is *a priori* quite simple. A directional antenna sends a microwave, and receives back the echo, that is, a reflected portion of the emitted microwave. The properties of this echo, by contrast with those of the originally emitted microwave, enable to have access to some physical or geometrical properties of the reflecting/scattering object.

Radars are therefore in constant need of ultra-pure microwaves, precisely because of this contrast-like principle of operation: the more pure and precise the reference microwave, the greater the precision and resolution of the radar.

Opto-electronic oscillators

A very efficient way to produce ultra-pure microwaves has been proposed in 1994 by **Yao** and **Maleki** [59], and it is known under the name of **opto-electronic oscillator** (OEO). The principle of operation of this oscillator relies on an innovative energy storage principle, based on very long delay lines instead of the classical concept of high-finesse resonators. Hence, at the opposite of chaos cryptosystems, it is here the *stabilizing effect of the delay time* that is used on purpose.

The architecture of the OEO consists in a Mach-Zehnder modulator which modulates nonlinearly a continuous-wave input from a semiconductor laser. The modulated output then circulates within an extremely long fiber delay-line, whose typical length is few kilometers. The optical signal is afterwards converted back into an electrical signal which is amplified, narrowly filtered around the microwave frequency to be generated, and connected to the electrode of the Mach-Zehnder. Typically, the central frequency of the filter is between 1 and 40 GHz, while the

bandwidth of the radio-frequency (RF) filter has few tens of MHz. This closed-loop architecture therefore plays the role of a cavity. However, its quality factor is very low, of the order of 200. In fact, the outstanding performances of this oscillator originate from the few-kilometers long delay line, which generates thousands of narrowly spaced cavity modes. Even though hundreds of this microwave cavity modes do fit within the bandwidth of the RF filter, only one mode is amplified under optimal conditions, and oscillates in a continuous, stable way.

Surprisingly, the phase noise performance of this oscillator has been found to be very superior to the previous state of the art resonator-based oscillators [59–62]. These performances can even be improved if ameliorations are brought to the initial single-loop architecture. For example, the neighboring cavity-modes can be overdamped by using the Vernier effect of a dual-loop architecture [63], or alternatively, by designing a suitable coupling between two OEOs [64]. It is also possible to build tuneable OEOs [65], or even to enhance the frequency selection using a photonic filter instead of a RF filter [66]. Therefore, owing to this multiplicity and flexibility of architectures, OEOs are serious candidates for time-frequency metrology and of course for radar applications, but they are also of great interest for many applications in spatial and lightwave technologies. Just to take an example in lightwave technology, OEOs have been pointed out as idoneous systems to produce ultra-low-jitter optical pulses at high rates (> 10 GHz) [67], or to produce multi-wavelength and synchronized optical pulses [68].

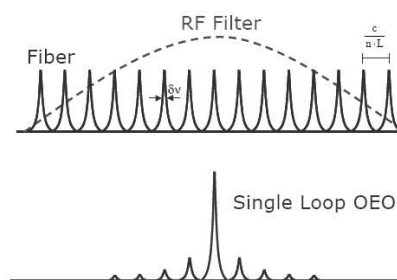


Figure 1.6. Principle of OEOs. An ultra-pure microwave is generated by frequency selection of ring cavity-modes through RF filtering. After ref. [62].

Despite the large amount of experimental investigations developed around the concept of OEOs, very few has been done to investigate theoretically its dynamical properties. In particular, there is no dynamical model able to describe the behavior of these oscillators. This lack analytical insight is due to the extreme features of this system: strong nonlinearity, very large delayed feedback, and widely spaced timescales. That is why most of OEO studies do implicitly assume no time-dependent amplitude dynamics, as they try to capture essentially stationary features.

However, the stationary hypothesis may not be always satisfied, and *a priori*, it can logically be considered that OEOs may as any delayed dynamical system display other dynamical behaviors. Absence of a dynamical framework does not enable a deep understanding of existing architecture’s performances, and of course

does not enable the prediction of eventual instabilities.

Therefore, one of the objectives of the thesis is the derivation of a delay differential equation which can describe accurately the deterministic dynamical behavior of OEOs. Such an equation should of course be easily extended to all OEO's architectures, as well as to the study of multimode and stochastic behaviors.

Stochastic and multimode behavior

The OEO is ideally in a single-mode oscillator. However, this is highly counter-intuitive, because as emphasized earlier, the delay line plays the role of a cavity and thereby gives birth to thousands of longitudinal cavity-modes, amongst which hundredths are within the RF filter bandwidth. Nothing theoretically prevents all these modes to oscillate simultaneously. Moreover, the system is also subjected to noise influences, so that an unavoidable phase noise dynamics which is tightly related to the purity of the generated ultra-pure microwave is sustained. In fact, multi-longitudinal mode dynamics has been thoroughly studied in other oscillators like lasers for example [69–72]. These modes are attached to the longitudinal resonance condition of the resonator, and they are generally coupled through the common reservoir of energy provided by the gain. When the multimode system is abruptly switched on, all the modes are initially amplified and then they compete for the available gain energy. In most cases, the so-called **maximum gain mode** finally wins the competition and oscillate solitarily after a transient time which may be as low as few nanoseconds in semiconductor lasers. In some other cases, the modal competition is sustained and the oscillator indefinitely displays a multimodal dynamics, with its habitual associated features: self- and cross-saturation/modulation, etc.

However, there is no study which has focused on the case of multimode OEOs. It even seems that multimode behavior has never been reported in the literature. Two interpretations can be given to this absence: either this phenomenon had never been observed experimentally, or either it has been observed but was not reported because it was misunderstood, considered as a marginal phenomenon, unworthy of deeper analysis.

The first case is not totally improbable because multimode behavior may occur only when the OEO is switched on abruptly, something that is scarcely practiced

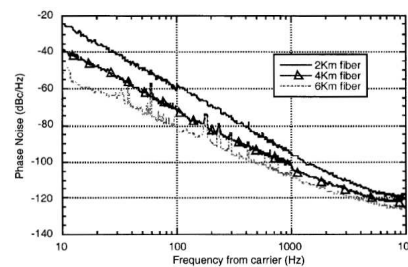


Figure 1.7. Some experimental phase noise spectra, with different fiber cavity lengths. The phase noise performance is here approximately equal to -120 dBc/Hz @ 10 kHz of the carrier. After ref. [61].

in experimental procedures in order to protect the optoelectronic devices from the high peak-power relaxation oscillations of the transient dynamics. The second hypothesis is more probable: since the multimode dynamics is of no immediate technological interest, it may have simply been ignored in application-oriented experiments.

The multimode behavior may however be interesting for several reasons. From a purely theoretical point of view, the OEO provides an excellent opportunity to investigate the dynamics of a huge quantity of globally coupled cavity-modes, at the opposite of the usual cases where only very few of them are considered. From a technological point of view, procedures like active mode-locking do address individual modes, and can not be studied properly if the system is not modeled through a modal dynamics approach.

Another aim of the thesis will therefore be to provide a convenient modal description for OEOs.

Transverse-mode control of VCSELs

At the early age of semiconductor laser technology, the lasers were structured such that the output beam was emitted *along* the direction of the active medium: they were referred to as **edge-emitter** semiconductor lasers.

The first prototype of a semiconductor laser emitting *perpendicularly* to the active region's surface was presented by **Soda, Iga, Kitahara** and **Suematsu** in 1979 [73]. These lasers were later given the name **Vertical-Cavity Surface-Emitting Lasers**, which has been contracted to the acronym **VCSELs**.

These vertical-cavity surface emitting lasers offer numerous advantages comparatively to their edge-emitter counterpart. To name just a few, VCSELs are intrinsically single-longitudinal mode lasers, and they have a significantly lower threshold current, as well as a lower power consumption. They are very cost effective because they can simultaneously be fabricated in a planar structure, and then tested "on wafer"; this planar structure also allows for easy integration in two-dimensional arrays. The circular cross-section of VCSELs produces low-divergence beams (thus limiting the need of corrective optics), and enables a highly efficient laser-fiber coupling. VCSELs are nowadays particularly spread in optical fiber data transmission (mostly in gigabit-ethernet networks), free-space optical communications, absorption spectroscopy, laser printers, sensors, pointers and trackers.

Polarization- and frequency-selective delayed feedback

The first study where a correct understanding of the effect of delayed feedback on semiconductor lasers was provided is an article of **Lang** and **Kobayashi** published in 1980 [19]. Since then, a large amount of contributions have focused on the topic of optical feedback in semiconductor lasers. As we may expect, there are cases where the delayed feedback can be used on purpose to *destabilize* the laser, for example to induce hyperchaos in view of optical cryptography (see [40] and references therein); in other cases, the effect can be exactly opposite and the feedback *stabilizes* the laser emission (stabilization of broad-area lasers [74]); at last, there are situations where feedback is at the same time unavoidable and undesirable, and should just be taken into account to fit with the experimental reality (*i. e.*, backwards reflection from fiber tips during laser-fiber coupling [75]).

Most of the studies which have been dedicated to optical feedback in semiconductor lasers have been done within the framework of the Lang-Kobayashi model, which deals with single-mode and single-polarization edge-emitter lasers [76–80], so that polarization and multimode effects were not taken into account. In fact, owing to their relatively high Fresnel number (~ 100), VCSELs have a natural tendency to multimode behavior, and they also have a **polarization** degree of freedom because of their circular cross-section: however, the multimode dynamics of the laser can be studied with a modal expansion in terms of cold-cavity modes [81,82], while the polarization dynamics can be studied within the framework of the **spin-flip model** proposed by **San Miguel, Feng** and **Moloney** [83].

As far as VCSELs with feedback are concerned, some investigations have been devoted to the case of single-mode and multiple polarizations [85,86], and on the case of multiple modes and single polarization [87–89]. A study has also been devoted to the case of a single-mode with multiple polarizations VCSEL subjected to polarization-selective feedback [90]. In all cases, it has been shown that optical feedback has a wide variety of different effects, depending on the strength and on the phase of the optical feedback.

Therefore, even though there is apparently no investigation that has been led for the case of multimode and multipolarization VCSELs subjected to optical feedback, there is a strong hint that the spectral emission properties may be drastically modified by feedback. An even more subtle way to control this emission dynam-

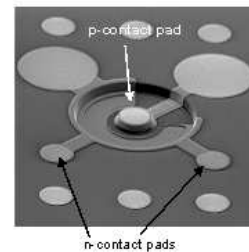


Figure 1.8. Electron microscope image of a VCSEL, with its electrical connections. The diameter of a VCSEL aperture is typically 10 to 100 times smaller than the diameter of human hair's cross section. After ref. [84].

ics may be the feedback of individually addressed modes in a given polarization. In fact, all the transverse modes have different eigenfrequencies, so that a resonant frequency-selective mirror can filter out all the modes but the one we want to feed back into the laser cavity. This frequency-selective mirror is generally a diffraction grating in the **Littman** or in the **Littrow** configuration. On the other hand, a polarizer inserted into the external cavity is sufficient to select the fed back polarization.

Our aim therefore to propose a theoretical framework for the study of VCSELs subjected to this polarization- and frequency-selective feedback. A chapter of the thesis will be devoted to the modelling of such external-cavity VCSELs.

Controlling the emission properties of VCSELs

A difficult challenge in most of VCSELs applications is the design high-power, single-mode, and single-polarization output beams. This is for example a critical issue in optical communication networks with ultra-dense wavelength-division-multiplexing (UD-WDM), where the spectral spacing between adjacent channels can be as low as 25 GHz. To some extent, if VCSELs are nowadays almost standard emitters in most of optical networks, it is precisely because they can emit in a single longitudinal mode.

Unfortunately, the circular aperture VCSELs supports two orthogonal polarizations which are spectrally splitted because of birefringence, even for the fundamental mode. Moreover, in broad-area VCSELs (diameter greater than $5 \mu\text{m}$), the transverse-modes of the laser cavity are rapidly excited when the pumping current is increased. Hence, monochromaticity in the output optical radiation these VCSELs is limited by the unavoidable emergence multiple transverse and polarization lasing modes, even for pumping currents relatively close to threshold [91]. Therefore, there is usually a trade-off between spectral purity and optical power for VCSELs. An end-user solution to circumvent this drawback is precisely to control this multi-transverse mode dynamics by feeding back the laser the mode to be enhanced (generally the fundamental mode), with the desired polarization. With this feedback scheme, it has yet been experimentally shown that a good stabilization of the fundamental mode in a fixed polarization is possible in the continuous-wave regime [92].

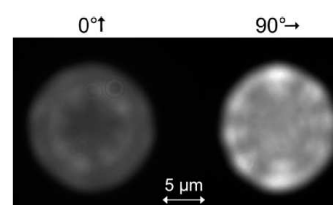


Figure 1.9. Experimental snapshots of the nearfield radiation from a multi-polarized and multi-transverse mode VCSEL. After ref. [91].

But beyond the fundamental-mode stabilization which is of technological in-

terest, the polarization- and frequency-selective feedback of VCSELs, can also represent an excellent benchmark to investigate the spatiotemporal dynamics of a spatially extended optical system. Effectively, the selective feedback of mode chosen amongst many others can provide an interesting insight into the coupling mechanisms amongst the potentially lasing modes.

These two aspects will be particularly investigated in the last chapter of the thesis.

Outline of the thesis

The thesis will be divided in three parts, corresponding to the three principal applications of semiconductor laser systems with feedback under study. Each of these parts will be divided in chapters.

The first part of the thesis will be devoted to **Optical Chaos Cryptography**, and will be divided into three chapters:

- In **Chapter 2**, we study the dynamics of a semiconductor laser system with feedback. We describe the system in detail, and investigate its dynamics as the feedback gain is increased. This study will evidence a new phenomenology, the so-called *chaotic breathers*.

- **Chapter 3** is devoted to the study of the synchronization of such laser systems. A particular emphasis will be given to the problem of parameter mismatch, as we will investigate the effect of each mismatch on the global synchronization error.

- The focus of **Chapter 4** is optical chaos cryptography *per se*. Encryption and decryption at multi-gigabits/s bit rates will be performed with satisfyingly low bit-error rates; we will moreover demonstrate that in our case, a meaningful signal-to-noise ratio can be defined, and directly related to the bit error-rate of the cryptosystem.

Radar-Frequency Generation will be the central topic of the second part, which will be divided in two chapters:

- **Chapter 5** is devoted to the single-mode microwave dynamics of optoelectronic oscillators. A deterministic model will be derived to investigate the amplitude dynamics of OEOs, and it will be evidenced that new bifurcation phenomena do emerge when the feedback gain is increased beyond a given critical value.

- In **Chapter 6** is studied the stochastic and multimode behavior of optoelectronic oscillators. It will be shown that phase noise can be accurately accounted for with a stochastic differential equation, and a multiple timescale anal-

ysis will be developed to track the modal dynamics of the system after abrupt switch-on.

The third part of the thesis addresses the issue of **Transverse Mode Control in VCSELs**, and it is also divided into two chapters:

- The aim of **Chapter 7** is the derivation of a modal expansion model in order to describe the dynamics of VCSELs subjected to polarization- and frequency-selective feedback. This mesoscopic model is intended to provide a polarization, spectral and spatial resolution of the modal dynamics of the laser.
- **Chapter 8** is devoted to the characterization and optimization of the transverse-mode control scheme. Modal gains, external-cavity modes and stationary amplitudes will be calculated, and a light will be shed on the lasing mode selection mechanism.

At last, the main results of the thesis will be resumed in a **General Conclusion** chapter, where we will also propose some perspectives of future investigations.

Part I

Optical Chaos Cryptography

Chapter 2

Dynamics of Semiconductor Laser Systems with Electro-Optical Feedback

“If, then, there is any error whatever in observing the present state - and in any real system such errors seem inevitable - an acceptable prediction of the instantaneous state in the distant future may well be impossible.”

Edward Lorenz, Deterministic nonperiodic flow.

2.1 Introduction

IN this first chapter, we study the nonlinear dynamics of a semiconductor laser system subjected to an electro-optical feedback loop. We first briefly describe the electro-optical effect and the principles of Mach-Zehnder modulators. Then, the experimental set-up is presented, as well as the model used to investigate its various dynamical regimes, which range from periodic solutions to full hyperchaos, passing through hyperchaotic breathers. At last, the issue of stochastic effects is addressed and a method to calibrate the background noise level in the system is proposed.

2.2 Electro-optic modulators

2.2.1 The electro-optic effect

The optical properties of certain materials can be significantly influenced by external electric fields. Effectively, an applied electric field can modify the geometrical properties of molecules (orientation, shape, etc...), thereby modifying the refraction index of the material: this is called the **the electro-optic effect**, and the material is referred to as an **electro-optic medium**.

In the simple case of a scalar electric field, this dependence of the refraction index can be Taylor-expanded as

$$n(E) = n_0 + \left[\frac{dn}{dE} \right]_{E=0} \cdot E + \frac{1}{2} \left[\frac{d^2n}{dE^2} \right]_{E=0} \cdot E^2 + \mathcal{O}(E^3), \quad (2.1)$$

where only the first odd and first even higher order terms have been considered. In some media, the first order correction is much stronger than the subsequent terms, so that the refraction index varies linearly with E : this is the **linear electro-optic effect** or **Pockels effect**, discovered by **Friedrich Pockels** in 1893. In other materials (generally isotropic), $n(E)$ can not depend on the sign of E , so that the first-order derivative vanishes and the refraction index varies quadratically with the electric field: this is the **quadratic electro-optic effect** or **Kerr effect**, first evidenced by **John Kerr** in 1875 [93].

The Pockels and Kerr corrections generally induce very small changes of the refraction index ($\sim 10^{-5}$), but if the incoming light travels on a distance which is thousands of times greater than its wavelength, the accumulated phase shift can be macroscopically significant. The electro-optic effect therefore enables to control the physical properties of light with electricity, in particular optical phase and intensity.

2.2.2 Electro-optic phase modulation

To modulate the optical phase of coherent light with the electro-optic effect, let us consider that a light beam of wavelength λ_0 passes through a Pockels medium of length L , while a constant voltage V is applied in the transverse direction of thickness d . An electric field $E = V/d$ is therefore applied on the electro-optic medium and the phase-shift accumulated at the output of the slab is

$$\Delta\varphi = \frac{2\pi}{\lambda_0} n(E)L. \quad (2.2)$$

Using Eq. (2.1), we can rewrite this phase-shift under the form

$$\Delta\varphi = \Delta\varphi_0 + \pi \frac{V}{V_\pi}, \quad (2.3)$$

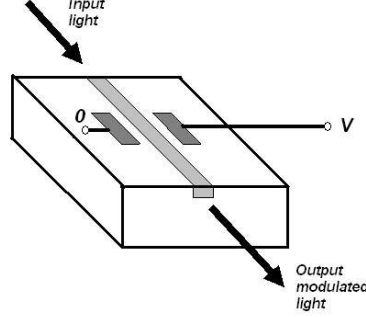


Figure 2.1: Integrated electro-optic phase modulation.

where

$$\begin{aligned}\Delta\varphi_0 &= \frac{2\pi}{\lambda_0} n_0 L, \\ V_\pi &= \frac{\lambda_0 d}{2L} \left\{ \left[\frac{dn}{dE} \right]_{E=0} \right\}^{-1}.\end{aligned}\quad (2.4)$$

According to Eq. (2.3), the optical phase of the input beam can hence be controlled with the electric voltage V . The parameter V_π is called **half-wave voltage** and it corresponds to the voltage to be applied to impose a π phase-shift. This characteristic parameter of the modulator depends on the wavelength of the incoming light, as well as on the geometrical and electro-optical properties of the Pockels cell. Figure 2.1 shows a representation of an electro-optic phase modulation scheme. Generally, the coherent light proceeds from a semiconductor laser and the electro-optic substrate is made of Lithium Niobate (LiNbO_3): the corresponding values of V_π can in this case be as low as 3 volts.

2.2.3 Electro-optic intensity modulation: the Mach-Zehnder interferometer

A coherent light beam can also be modulated in intensity using the electro-optic effect and the principle of interferometry. The incoming light beam of power (or intensity) P_{in} is ideally divided into two equal parts which are routed into two diverging optical paths (see Fig. 2.2). In the first path light undergoes phase modulation and $\frac{1}{2}\sqrt{P_{in}}$ is transformed into $\frac{1}{2}\sqrt{P_{in}}e^{i\Delta\varphi}$, while in the other path the amplitude of the second beam only suffers the material phase-shift and is transformed into $\frac{1}{2}\sqrt{P_{in}}e^{i\Delta\varphi_0}$. Then, the two optical paths are reconnected and the

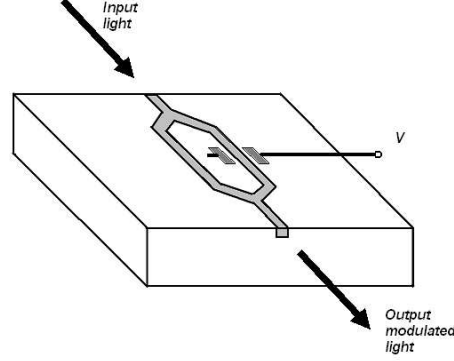


Figure 2.2: Intensity modulation using a Mach-Zehnder interferometer.

beams interfere, yielding in the ideal case a total output power

$$P_{out} = \left| \frac{1}{2} \sqrt{P_{in}} e^{i\Delta\varphi_0} + \frac{1}{2} \sqrt{P_{in}} e^{i\Delta\varphi} \right|^2 = P_{in} \cos^2 \left[\frac{\pi V}{2 V_{\pi}} \right]. \quad (2.5)$$

This intensity modulator is sometimes referred to as a **Mach-Zehnder interferometer** or **Mach-Zehnder modulator**. From Eq. (2.5), it therefore appears that the power of the input beam can be controlled and tuned to any value from 0 to P_{in} . However, at the opposite of the phase modulation which depends *linearly* on the applied voltage, the intensity modulation depends *nonlinearly* on V . This nonlinearity is generally undesirable in lightwave technology applications because it is a source of signal distortion. However, for our purpose, this potentially strong nonlinearity is a key element which enables to investigate a wide variety of complex behaviors, which may find interesting technological applications. On Fig. 2.2, a schematic representation of an integrated Mach-Zehnder modulator is shown, with the typical “double-Y” configuration of the waveguides.

The controlling voltage usually has two components: a **constant** or **DC** (direct current) component V_B which serves to select the operating point of the modulator; and a **variable** or **RF** (radio-frequency) component $V(t)$ which is the effective modulating signal. On the one hand, the bias voltage V_B can simply be applied across the electro-optic substrate with a simple electrode of half-wave voltage $V_{\pi_{DC}}$ as explained in the preceding sections. On the other hand, the RF modulation voltage $V(t)$ needs a special kind of electrode, because its value is not constant along the electro-optic path of length L : therefore, a *travelling-wave electrode* of half-wave voltage $V_{\pi_{RF}}$ is needed for the RF modulation signal $V(t)$. The output

intensity of the modulator therefore reads

$$P_{out} = P_{in} \cos^2 \left[\frac{\pi V(t)}{2V_{\pi_{RF}}} + \frac{\pi V_B}{2V_{\pi_{DC}}} \right], \quad (2.6)$$

and generally, the DC and RF half-wave voltages have different values, even though very close the most of the time.

2.3 Modelization of semiconductor laser systems with electro-optical feedback

2.3.1 The system

The system under study has been represented in Fig. 2.3, and the electro-optical feedback loop is composed with the following elements:

- An integrated electro-optic Mach-Zehnder modulator, built on a LiNbO_3 substrate. Its RF and DC half-wave voltages are respectively $V_{\pi_{RF}}$ and $V_{\pi_{DC}}$. A voltage V_B is applied to the DC electrode, and an amplitude voltage $V(t)$ is applied to the RF electrode to ensure a nonlinear dynamical operation of the electro-optic interferometer.
- A continuous-wave (CW) semiconductor laser of constant optical power P , serving as the light source to feed the Mach-Zehnder modulator.
- A few-meters long monomode optical fiber delay-line, yielding a delay time T .
- An amplified photodiode of sensitivity S to detect the fed back optical signal, and convert it into an electrical signal.
- A RF-amplifier with a gain G is finally used to close the chaotic oscillation loop, applying the previous electrical signal to the RF Mach-Zehnder electrode. Its -3 dB bandwidth spans from 30 kHz to 25 GHz.
- The overall attenuation of this feedback loop (delay line, connectors, etc.) is described in terms of the attenuation parameter $\kappa < 1$.

This electro-optical feedback loop is therefore constituted of an electrical path and an optical path. In the electrical path, the signal is amplified by the RF-amplifier, and band-pass filtered by various electronic components involved in the loop, whereas in the optical path, the signal only suffers attenuation and delay while propagating in the fiber. On the other hand, the photodiode transforms linearly light into electricity, while the Mach-Zehnder modulator establishes a nonlinear correspondance between the electric voltage and its optical output. Therefore, the modelization of this system requires to take into account five principal features: amplification (including attenuation), linear energy conversion, band-pass filtering, nonlinear modulation and time-delay.

Even though the feedback loop is closed onto the Mach-Zehnder modulator instead of the semiconductor laser, this system is sometimes simply referred to as

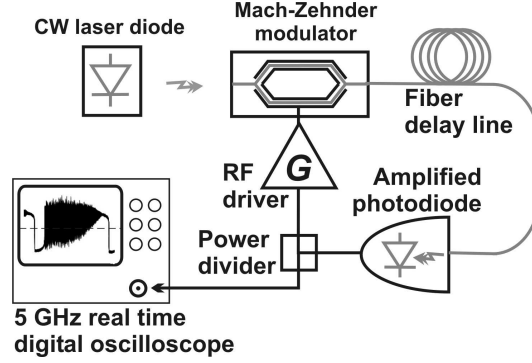


Figure 2.3: Experimental set-up.

a **semiconductor laser with electro-optical feedback**. This terminology can be indeed misleading, but it has been adopted in the scientific literature as a standard denomination for this type of electro-optical architecture.

2.3.2 The model

The dynamical properties of the system are ruled by the overall band-pass filtering induced by the superimposed bandwidths of the RF-amplifier, the photodiode and the Mach-Zehnder modulator. We can take advantage of the fact that the low and high cut-off frequencies f_L and f_H are very distant one from each other, and consider that this band-pass filter is constituted of two cascaded high-pass and low-pass first order linear filters. The variable describing this dynamical system would therefore be the radio-frequency voltage $V(t)$ at the RF electrode of the Mach-Zehnder modulator, and the steps to derive its governing equation have been explained in detail in ref. [49].

The output voltage $U(t)$ of the low-pass filter is related to the input $V_{in}(t)$ as

$$V_{in}(t) = \frac{1}{2\pi f_H} \frac{d}{dt} U(t) + U(t), \quad (2.7)$$

while the output voltage $V_{out}(t)$ of the high-pass filter is related to the input $U(t)$ as

$$U(t) = 2\pi f_L \int_{t_0}^t V_{out}(s) ds + V_{out}(t), \quad (2.8)$$

so that the input and output of the cascaded band-pass filter obey

$$V_{in}(t) = \left[1 + \frac{f_L}{f_H} \right] V_{out}(t) + \frac{1}{2\pi f_H} \frac{d}{dt} V_{out}(t) + 2\pi f_L \int_{t_0}^t V_{out}(s) ds. \quad (2.9)$$

On the other hand, $V_{in}(t)$ is also the output voltage of the photodetector; hence, it is proportional to the optical power of the semiconductor laser which had been electro-optically modulated by the amplified voltage $V = \kappa G V_{out}$ at the time $t-T$; consequently we have the relationship

$$V_{in}(t) = SP \cos^2 \left[\frac{\pi V(t-T)}{2V_{\pi_{RF}}} + \frac{\pi V_B}{2V_{\pi_{DC}}} \right]. \quad (2.10)$$

Therefore, the radio-frequency voltage $V(t)$ obeys the following equation

$$\begin{aligned} \left[1 + \frac{f_L}{f_H} \right] V(t) + \frac{1}{2\pi f_H} \frac{d}{dt} V(t) + 2\pi f_L \int_{t_0}^t V(s) ds \\ = \kappa G S P \cos^2 \left[\frac{\pi V(t-T)}{2V_{\pi_{RF}}} + \frac{\pi V_B}{2V_{\pi_{DC}}} \right], \end{aligned} \quad (2.11)$$

and if we take $f_L \ll f_H$ into account, this equation can be rewritten under this simplified and dimensionless form

$$x(t) + \tau \frac{d}{dt} x(t) + \frac{1}{\theta} \int_{t_0}^t x(s) ds = \beta \cos^2 [x(t-T) + \phi], \quad (2.12)$$

where

$$x(t) = \frac{\pi V(t)}{2V_{\pi_{RF}}} \quad (2.13)$$

and

$$\begin{aligned} \beta = \kappa G S P \frac{\pi}{2V_{\pi_{RF}}} \quad ; \quad \phi = \frac{\pi V_B}{2V_{\pi_{DC}}}; \\ \tau = \frac{1}{2\pi f_H} \quad ; \quad \theta = \frac{1}{2\pi f_L}. \end{aligned} \quad (2.14)$$

The new dimensionless radio-frequency variable is $x(t)$, and the new parameters are the normalized feedback gain β , the normalized bias offset ϕ , the high cut-off response time τ and the low cut-off response time θ .

It is noteworthy that Eq. (2.12) is an **integro-differential delay equation**, a kind of equation which does not appear frequently in dynamical systems' studies; one should also note that as a voltage, $x(t)$ does not a priori have any sign restriction. On the other hand, the instantaneous intensity $P_{mod}(t)$ of the output modulated laser light can be obtained through

$$P_{mod}(t) = P \cos^2 [x(t) + \phi], \quad (2.15)$$

and obviously it is a strictly positive variable. In the following sections, the various parameters of the system will be fixed to values compatible with the experimental set-up, that is, $\tau = 25$ ps, $\theta = 5$ μ s and $T = 30$ ns.

2.4 Dynamical behavior of the system

2.4.1 Steady-states and stability analysis

We can now analyze the dynamics of the system with respect to the feedback strength β (which is proportional to the feeder-laser power P) and the off-set phase ϕ (proportional to the bias voltage of the Mach-Zehnder V_B). If we introduce the intermediate variable

$$u(t) = \frac{1}{\tau} \int_{t_0}^t x(s) ds, \quad (2.16)$$

the evolution equation (2.12) may formally be rewritten as

$$\begin{aligned} \dot{u} &= x \\ \dot{x} &= -x - \epsilon u + \beta \cos^2(x_R + \phi), \end{aligned} \quad (2.17)$$

where the overdot denotes the derivative relatively to the dimensionless time t/τ , and $x_R \equiv x(t - R)$. The dynamics of the system is now ruled by two new dimensionless parameters. The first one is the ratio between the low and the high cut-off frequencies $\epsilon = \tau/\theta = 5 \times 10^{-6}$. The second one is the dimensionless delay $R = T/\tau = 1.2 \times 10^3$, which also roughly indicates the order of magnitude for the effective number of degrees of freedom attached to the system [49]. The flow of Eq. (2.17) has a single stationary point $(x_{st}, u_{st}) = (0, \frac{\beta}{\epsilon} \cos^2 \phi)$, and the stability of this unique fixed point can be investigated through the eigenvalue equation

$$\lambda^2 + \lambda + \epsilon + \beta \sin 2\phi \cdot \lambda e^{-\lambda R} = 0. \quad (2.18)$$

It is known that a Hopf bifurcation may occur in the system when λ becomes pure imaginary, that is, when $\lambda = i\omega$. According to equation (2.18), the frequency ω of the limit-cycle induced by the Hopf bifurcation should obey to the nonlinear algebraic system

$$-\omega^2 + \epsilon + \gamma \omega \sin \omega R = 0 \quad (2.19)$$

$$1 + \gamma \cos \omega R = 0, \quad (2.20)$$

where $\gamma \equiv \beta \sin 2\phi$ is the relevant control parameter for the bifurcation. The solutions (γ_H, ω_H) of the above algebraic system give the critical value γ_H of the control parameter for which the fixed point turns unstable and bifurcates to a limit-cycle of frequency ω_H . We can first uncouple Eqs. (2.19) and (2.20) to obtain

independent equations for γ and ω following

$$1 + \gamma \cos \left[R \frac{(\gamma^2 - 1) \pm \sqrt{(\gamma^2 - 1)^2 + 4\epsilon}}{2} \right] = 0 \quad (2.21)$$

$$-\omega^2 + \epsilon = \omega \tan \omega R, \quad (2.22)$$

whose solutions may be approximated with an excellent precision as

$$\gamma_0 = -1 - \epsilon R/2, \quad \omega_0 = \sqrt{\epsilon/R} \quad (2.23)$$

on the one hand, and as

$$\gamma_k = (-1)^{k+1} \left[1 + \frac{(\epsilon R^2 - k^2 \pi^2)^2}{2k^2 \pi^2 R^2} \right], \quad \omega_k = k \frac{\pi}{R} \quad (2.24)$$

on the other, k being a strictly positive integer.

From Eq. (2.20), it clearly appears that the fixed point $x = 0$ is stable independently of R when $|\gamma| = |\beta \sin 2\phi| < 1$. In particular, it is interesting to note that this trivial fixed point is stable independently of ϕ when $\beta < 1$.

2.4.2 Periodic solutions

Limit-cycles of frequency ω_k may emerge when crossing the critical bifurcation value of their related counterpart γ_k (which is always such that $|\gamma_k| > 1$).

For positive γ , the first bifurcation occurs at $\gamma_1 = 1 + 2.5 \times 10^{-7}$, leading to the emergence of a limit-cycle of frequency $\omega_1 = \pi/R$, corresponding to a period of $2T = 60$ ns. When γ is further increased, the fundamental frequency of that limit-cycle remains constant, even though the waveform changes from a sinusoid to a quasi-square-wave [94] as it can be seen in Fig. 2.4. Numerical simulations show that starting from an initial condition corresponding to the stationary fixed point, the system always evolves to limit-cycles of period $2T$ when γ is increased beyond 1 (see Fig. 2.6), and chaos is observed when γ is sufficiently high.

On the other hand, for $\gamma < 0$, the first limit-cycle to emerge appears at $\gamma_2 = -1 - 9.1 \times 10^{-6}$ with a frequency $\omega_2 = 2\pi/R$, corresponding to a period of $T = 30$ ns. But in this case, when γ is increased in absolute value and reaches the value $\gamma_0 = -1.003$, the limit-cycle of frequency $\omega_0 = \sqrt{\epsilon/R}$ emerges and becomes the attracting limit-cycle when the initial condition is taken nearby the unstable fixed point. Effectively, the frequency of the system's oscillations switches beyond γ_0 from ω_2 to ω_0 , which is approximately 100 times smaller. Figures 2.5 and 2.6 clearly indicate this drastic change of timescale: while we have oscillations of period $T = 30$ ns when $\beta \sin 2\phi = -1.001$, we rather have oscillations of period $\sim 3 \mu\text{s}$ when $\beta \sin 2\phi = -1.01$. The emergence of a stable

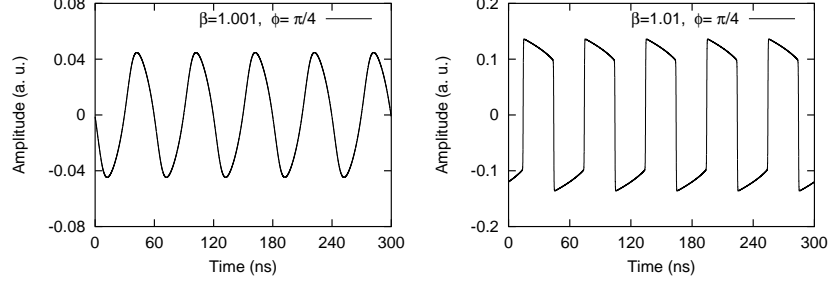


Figure 2.4. Numerical timetraces of $x(t)$ just after the bifurcation at $\gamma \approx 1$, when $\phi = \pi/4$ and $\beta \approx 1^+$. a) $\beta = 1.001$, limit-cycle of period $2T = 60$ ns b) $\beta = 1.01$, the period remains the same, but the waveform changes.

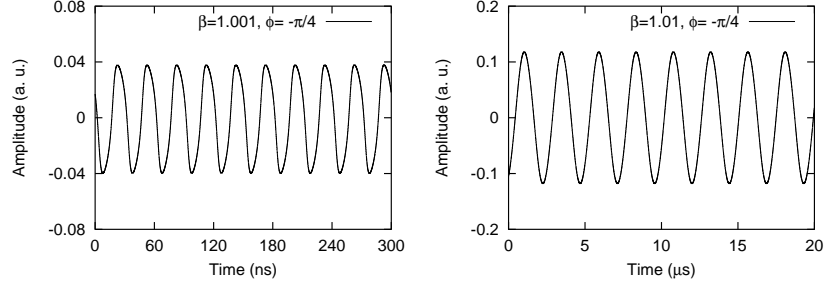


Figure 2.5. Numerical timetraces of $x(t)$ just after the bifurcation at $\gamma \approx -1$, when $\phi = -\pi/4$ and $\beta \approx 1^+$. a) $\beta = 1.001$, limit-cycle of period $T = 30$ ns b) $\beta = 1.01$, limit-cycle of period ~ 3 μ s.

limit-cycle whose period is significantly greater than τ and T opens the way to a very interesting phenomenology.

2.4.3 Breathers

When β is increased subsequently to the secondary bifurcation at $\gamma = \gamma_0$, we can witness the arising of an hybrid regime where a fast-scale dynamics is superimposed onto the slow-scale limit-cycle. For example, it can be seen in Fig. 2.7a that when β is increased to 1.5, the amplitude extrema begin to behave *locally* like pairs of fixed points, in the sense that the dynamics becomes significantly slow at their neighborhood. As β is further increased, quasi-square-wave oscillations of period $2T$ emerge at their vicinity, but as it can be seen in Fig. 2.7b they are rapidly damped just after their birth, that is, as soon as the system moves away from an extremum: we refer to them as **breathers**, and at this stage, these breathers are still periodic. The internal frequency and the exponential damping

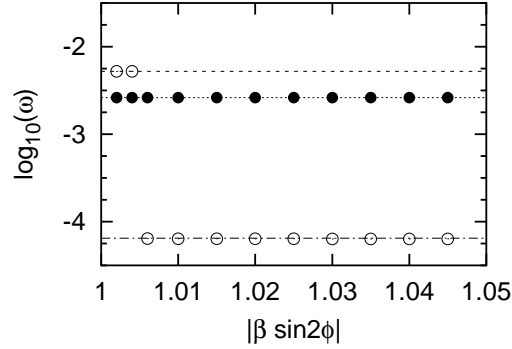


Figure 2.6. Numerical variation of the limit-cycles frequencies after the Hopf bifurcations (\circ for the bifurcation after $\gamma = -1$, \bullet for the bifurcation after $\gamma = 1$). The initial condition in the whole $[-T, 0]$ interval is the trivial fixed point. The three horizontal dashed lines respectively correspond to (from top to bottom) $\omega_2 = 2\pi/R$, $\omega_1 = \pi/R$ and $\omega_0 = \sqrt{\epsilon/R}$. Note that the frequencies found numerically always perfectly coincide with one of the three aforementioned analytical frequencies. Birth, evolution and destruction of the breathers as the nonlinear feedback strength parameter β is increased, when $\phi = -\pi/4$ (symmetric case).

of the emerging breathers can also be estimated analytically. In fact, at this early stage, the mean value contribution of the feedback term $\beta \cos^2(x_R + \phi)$ in Eq. (2.17) is cancelled by the mean value of filter term ϵu , whose fluctuating component is negligible. Therefore, the extrema \tilde{x}_{st} of the low-frequency oscillation coincide with a good approximation to the solutions of the transcendental algebraic equation $x = \frac{1}{2}\beta \cos 2(x + \phi)$. Then we can track the evolution of a perturbation $\delta\tilde{x} = \delta\tilde{x}_0 e^{(\tilde{\kappa} + i\tilde{\omega})t}$ around the extrema \tilde{x}_{st} , and it is found that the breathers emerge with a winding frequency $\tilde{\omega} = \pi/R$, and are damped at a rate $\tilde{\kappa} \simeq \ln(\tilde{\gamma})/R$, with $\tilde{\gamma} = \beta \sin 2(\tilde{x}_{st} + \phi)$. When β is increased, the fluctuating component of the term ϵu also increases, and it can be calculated from a multiple time scales analysis (using ϵ as the expansion parameter) that as a consequence, the damping drops to $\tilde{\kappa} \sim -\epsilon^{-1}$, *i.e.* the breathers begin to span over a timescale of the order of θ .

When β continues to increase, the breathers become chaotic as it can be seen in Fig. 2.7c. Here, we are in front of an hybrid regime where the hyperchaos is triggered at a ns-timescale and superimposed onto the low-frequency limit-cycle whose period is of the order of few μs . In Fig. 2.7d, it is shown that further increase of β leads to the destruction of the breathers, and to hyperchaotic oscillations without any trace of slow-scale dynamics. In Fig. 2.8, we can see the inner structure of the breathers of Fig. 2.7. The zoom-in of Fig. 2.8a shows the quasi-square-wave $2T$ -periodic structure of the breathers of Fig. 2.7b, in accordance to the winding frequency $\tilde{\omega} = \pi/R$ predicted by the theory, while Fig. 2.8b displays the fast-scale hyperchaotic nature of the breathers shown in Fig. 2.7c.

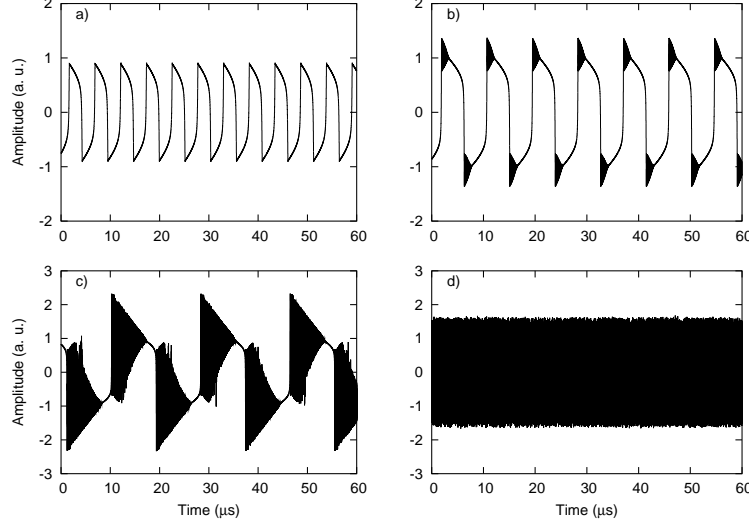


Figure 2.7. Birth, evolution and destruction of the breathers as the nonlinear feedback strength parameter β is increased, when $\phi = -\pi/4$ (symmetric case). *a)* $\beta = 1.5$ *b)* $\beta = 2.0$ *c)* $\beta = 3.0$ *d)* $\beta = 3.5$.

2.5 Topological nature of the chaotic breathers

From a topological point of view, the origin of this phenomenon lies in the structure of nonlinearity (folding) in the high-dimensional state space corresponding to the model. Effectively, if we discretize the delayed equation system (2.17) to map it into an set of coupled ordinary differential equations, it can schematically be rewritten in vectorial notation as

$$\frac{d\mathbf{z}}{dt} = [\mathbf{A}] \cdot \mathbf{z} + f(\mathbf{z}) \cdot \mathbf{b} \quad (2.25)$$

where $\mathbf{z} = (y, x_0, x_1, \dots, x_N)$ and $x_k(t) \equiv x(t - k\frac{T}{N})$ [note that $N \rightarrow +\infty$ in the ideal case]. The flow is characterized by a constant matrix \mathbf{A} , a constant vector \mathbf{b} , and a nonlinear scalar function $f(\mathbf{z})$. Here, the linear and nonlinear parts of the flow are clearly distinct, and moreover, *the nonlinearity is only active along the single direction \mathbf{b} of the high-dimensional state space.*

Rius and co-workers have intensively studied analytically, numerically and experimentally the dynamics of N -dimensional systems whose evolution equation can be expressed under the form of Eq. (2.25) [95]. Their work was motivated by the study of the so-called BOITAL systems, which consist of a Fabry-Pérot cavity in which the input mirror is partially absorbing and the spacer is a multi-layer of transparent materials with alternatively opposite thermo-optic effects [96].

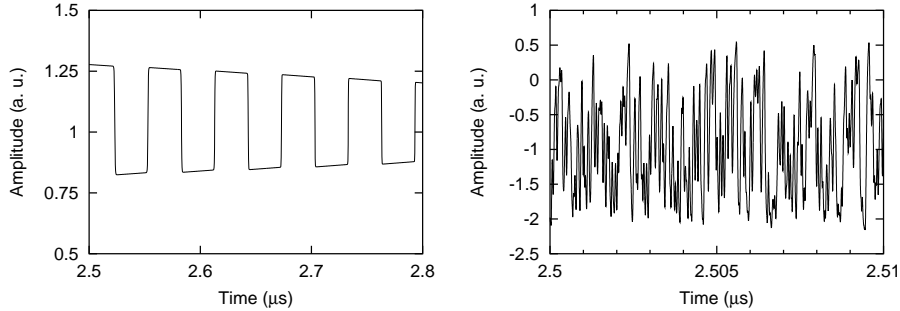


Figure 2.8. Inner structure of the breathers (fast-scale dynamics). *a)* Zoom of Fig. 2.7b ($\beta = 2$): the breathers are $2T$ -periodic. *b)* Zoom of Fig. 2.7c ($\beta = 3$): the breathers are chaotic.

They showed that in such systems, complexity can emerge through the nonlinear superposition of internal oscillatory modes according to the **Landau** scenario. They observed that as the explicit parameter controlling the nonlinearity strength is increased, a full-instability regime (nonlinear combination of $N - 1$ oscillation modes) can be reached. The mechanism of this behavior was found to be the occurrence of successive Hopf bifurcations in a saddle-node pair of fixed points, up to exhaust their instability capabilities in N dimensions. Their results were obtained in the low-dimensional case (maximum value of $N = 6$), and the resulting time-traces could be periodic, quasiperiodic, or sometimes weakly chaotic at fast-scale, while remaining periodic at slow-scale.

Low-dimensional chaotic breathers have also been met in nonlinear systems excited by a high-frequency forcing term modulated in amplitude by a slowly varying quasiperiodic envelope [97], but these breathers are somehow artificial in the sense that they appear because of a periodic external forcing, exerted on purpose. In our study, however, hyperchaotic breathers are for the first time identified in a delayed dynamical system where they appear as a new solution in autonomous and delayed dynamical systems, a robust intermediate state between periodicity and full hyperchaos.

2.6 Experimental results

This¹ dynamical behavior has also been recovered experimentally. In the experimental set-up, the electro-optical modulator is a 10 GHz commercial LiNbO₃ integrated Mach-Zehnder modulator with $V_{\pi_{DC}} = 4.0$ V and $V_{\pi_{RF}} = 4.2$ V. The coherent optical feeder of this modulator is a Distributed FeedBack (DFB) semi-

¹These experimental results have been obtained in collaboration with N. Gstaad and L. Larger at the Optoelectronics Laboratory of GeorgiaTech-Lorraine, Metz, France.

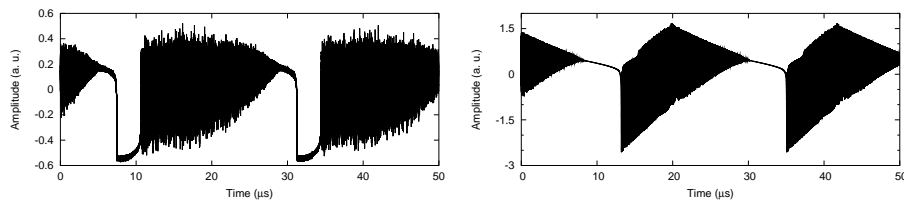


Figure 2.9. Large-scale timetraces of the hybrid regime of simultaneous slow-scale periodicity and fast-scale chaos. Adjacent asymmetrical breathers can also merge as they are growing. *a*) Experimental timetrace, with $P = 4.15$ mW and $V_B = 3.09$ V. *b*) Numerical timetrace, with $\beta = 2.8$ and $\phi = -\pi/10$.

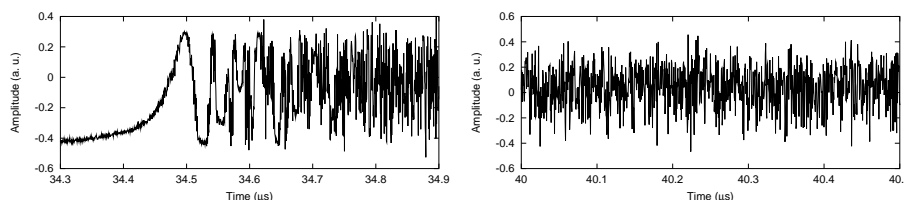


Figure 2.10. Small-scale experimental timetraces (zoom of Fig. 2.9a). *a*) Onset of chaos in the breathers. Transients associated to the time-delay T can clearly be identified. *b*) Fully developed chaos within the breathers.

conductor laser emitting at the standard infrared wavelength of 1550 nm. The delay-line is a 6 meters long single-mode optical fiber yielding an overall time delay of 30 ns. The wide-band amplified photodetector has a sensitivity of 2 V/mW and a 10 GHz bandwidth. The radio-frequency electronic driver SHF100CP has a bandwidth ranging from 30 kHz to 25 GHz, and it performs within the nonlinear feedback loop an amplification whose gain is 18 dB (26 dBm at 1 dB compression).

Figure 2.9a presents the experimental large-scale timetraces corresponding to the chaotic breathers, and Fig. 2.9b displays the related numerical simulation. These experimental breathers correspond to the most general case of *asymmetric* breathers (obtained when $\phi \neq -\pi/4$), by opposition to the breathers of Fig. 2.7c which were *symmetric* relatively to the horizontal axis ($\phi = -\pi/4$). In Fig. 2.10, a zoom of the experimental time traces is displayed and it enables to have a better insight into the underlying mechanism of the process. The onset of chaos at the beginning of each breather is shown in Fig. 2.10a. The transients related to the time delay T can clearly be recognized. Enough time is provided for these transients to evolve towards fully developed chaos as it can be seen in Fig. 2.10b, and therefore the occurrence of this phenomenon is not only related to the integro-differential dynamical property of the feedback loop, but also to the ratio between the different timescales of the system.

In Fig. 2.11, the experimental evolution of these breathers as the feedback

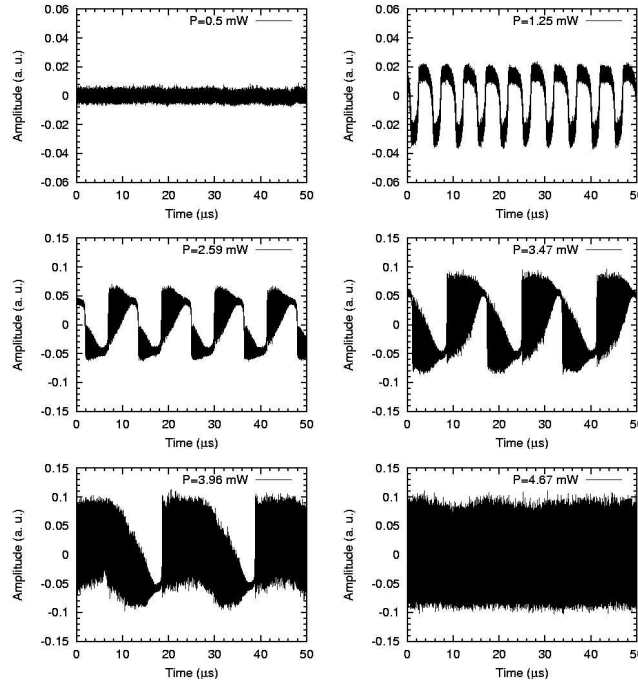


Figure 2.11. Experimental evolution of the breathers as the feedback gain is increased (through the input power P of the semiconductor laser). These figures can be compared with those of Fig. 2.7.

strength is increased is shown. As predicted by the theory and observed numerically, the system remains in the fixed point when the feedback is weak. Then, a first threshold is crossed when appears the Hopf-induced limit cycle. The breathers then emerge and as they continuously grow, they start to merge to form bigger structures through a kind of **gluing bifurcation**. For strong feedback, the system enters in the regime of full hyperchaos and the periodic structure introduced by the breathers is lost.

2.7 Influence of random noise: stochastic effects

The dynamics of this system is naturally affected by a random noise induced by the various fluctuations occurring into the circuitry. It is therefore of interest to understand how does noise interact with the system, and to find a method which would enable to measure the statistical properties of this noise without ambiguity.

For the identification of the sources of noise, we should operate in a regime where the delayed system does not by itself develop a proper dynamics, that is,

around the stable trivial fixed point $x_{st} = 0$. It has been demonstrated earlier that this trivial fixed point is stable independently of the value of ϕ when $\beta < 1$. In that case, random noise can be studied without interference with an eventual intrinsic dynamics of the system.

A second step is to define the statistical and spectral characteristics of the noise involved in the system. Experimental data indicate in first approximation that this noise can be considered as Gaussian and white. In Fig. 2.12a, where the probability density function is displayed, the observable bell-shape can be approximated by a Gaussian. The experimental Fourier spectrum of this noise is also displayed in Fig. 2.12b, and it indicates that the white noise hypothesis can also be considered as acceptable.

The third step is to define how the noise has to be introduced in the model. There are *a priori* two sources of noise. The first one is an **additive** noise corresponding to environmental fluctuations; the second one is a **multiplicative** noise around the fixed value of the overall gain β . This supposition is made on the physical basis that the parameter β is proportional to all the gain and losses of the electro-optical loop, so that any noisy fluctuation around each of these parameters would yield after multiplication and linearization a noisy β . However, in that case, when $\beta = 0$, the intensity of the noise should either be equal to 0 if the noise is proportional to β , or either be of constant amplitude in case of a noise independent of β .

The stochastic model would therefore be

$$x + \tau \frac{dx}{dt} + \frac{1}{\theta} \int_{t_0}^t x(s) ds = \beta [1 + \sigma_m \xi_m(t)] \cos^2[x(t-T) + \phi] + \sigma_a \xi_a(t), \quad (2.26)$$

where $\xi_a(t)$ and $\xi_m(t)$ are two independent δ -correlated Gaussian white noises fulfilling $\langle \xi_{a,m}(t) \xi_{a,m}(t') \rangle = 2\delta_{a,m} \delta(t-t')$, and their variances σ_a and σ_m indicate in sub-indices their additive and multiplicative physical nature. Assuming a small-noise amplitude, we can linearize $x(t)$ around the trivial fixed point and we can simultaneously discard in first approximation the constant and the integral term to obtain the following approximated noise-driven first-order differential equation

$$\begin{aligned} \tau \frac{dx}{dt} = & -x - \beta \sin 2\phi x_T \\ & -\beta \sin 2\phi \sigma_m \xi_m(t) x_T + \beta \cos^2 \phi \sigma_m \xi_m(t) + \sigma_a \xi_a(t). \end{aligned} \quad (2.27)$$

In the above **stochastic differential equation** (SDE), the first two terms on the right hand-side are noise-free and correspond to the deterministic model. The third term includes a multiplicative noise, while the fourth and fifth terms act as additive noise. One should notice that in this additive noise, there is now a contribution

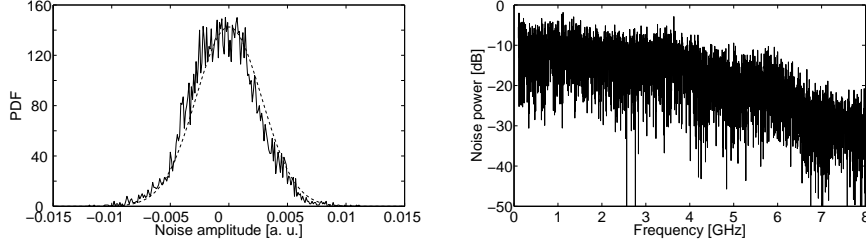


Figure 2.12. Experimental data about the statistical properties of the random noise involved in the system, when $P = 0$ mW (*i. e.*, when $\beta = 0$). *a*) Experimental probability density function, of the noise-driven fluctuations in the system (solid line) and Gaussian fitting (dashed line). Here, the gaussianity hypothesis can be validated in first approximation. *b*) Experimental Fourier transform of the noise. The cutting frequency around 3 GHz on the figure is in fact due to the limited bandwidth of the oscilloscope. In fact this noise can be considered as white noise at up to several tens of GHz.

proportional to σ_m , and which depends on ϕ . According to this model, When $\beta = 0$, x simply obeys to

$$\tau \frac{dx}{dt} = -x + \sigma_a \xi_a(t), \quad (2.28)$$

so that the amplitude of x becomes independent of ϕ .

This is exactly what was observed experimentally in Fig. 2.13a. On the other hand, when $\beta \neq 0$, Eq. (2.27) clearly indicates a periodic dependence of the amplitude of x with the off-set phase ϕ . However, as soon as $\phi = \pm\pi/2$, Eq. (2.27) reduces to Eq. (2.28), so that the recorded amplitudes should fit with the one we have when $\beta = 0$. This is also confirmed by the experiments in Fig. 2.13b. Hence, in this regime where $\beta < 1$, $\phi = \pm\pi/2$ are the optimal values which minimize the the amplitude of noise.

These experimental data enable an accurate calibration of the noise. Effectively, the absolute minima in Fig. 2.13b is proportional to the additive noise variance σ_a^2 , while the amplitude of the modulation (difference between absolute extrema) is proportional to the variance σ_m^2 of the multiplicative noise. It is therefore possible to determine experimentally these noise parameters, which can then be introduced in the stochastic model for theoretical estimations or numerical simulations.

2.8 Conclusion

In this chapter, we have investigated the dynamics of a semiconductor laser system subjected to an electro-optical feedback loop. We have presented the experimental set-up under study, as well as the model which enables the understanding of

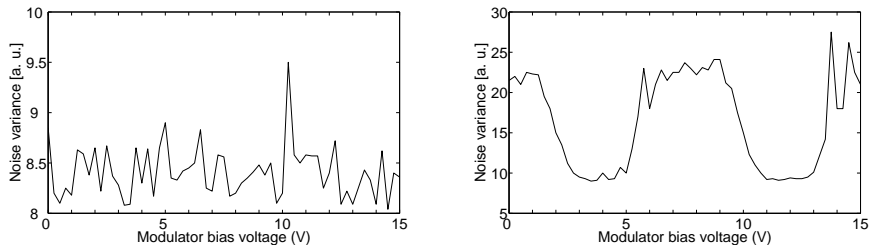


Figure 2.13. Experimental variation of the noise amplitude (variance σ^2) as the bias voltage V_B (i.e., ϕ) is varied. *a*) $P = 0$ mW. Note that the amplitude is roughly constant at $\sigma^2 \simeq 8.5$ (in arbitrary units), and independent of ϕ . *b*) $P = 1$ mW. Here, a clear dependence on ϕ is observed. The values of the minima correspond to the constant amplitude measured at $P = 0$ mW ($\sigma^2 \simeq 8.5$), while the maxima are around $\sigma^2 \simeq 24$.

its dynamical behavior. Various dynamical regimes have been investigated, both theoretically and experimentally. In particular, the study has evidenced the existence of chaotic breathers, which are characterized by a slow-scale periodicity and a fast-scale chaotic dynamics. We have also constructed a correct stochastic model to account for the noise in the system.

The next chapter will focus on the synchronized dynamics of two such systems when they are unidirectionally coupled in the fully hyperchaotic regime. We will particularly focus on the issue of parameter mismatch, that is, the influence of non-identity on the quality of synchronization.

Chapter 3

Chaos Synchronization of Semiconductor Laser Systems with Electro-Optical Feedback: Influence of Parameter Mismatch

“When a fool shakes the little bell, always should dance another fool...”

Ahmadou Kourouma, The suns of independence.

3.1 Introduction

WE investigate in this second chapter the synchronization phenomenon occurring between semiconductor laser systems subjected to electro-optical feedback, with a particular emphasis on the problem of parameter mismatch. After the presentation of the experimental set-up under study, we first consider the effects of the various mismatches taken separately, *i.e.*, when one of them is considered, all the others are set to zero. This study will enable us to understand and quantify the sensitivity attached to the matching of each parameter. Then, we will focus on the general and important case where all the mismatches are simultaneously taken into account. This will enable us to study the synchronization quality in situations that are closer to the experimental ones, and also to understand the interplay between the various mismatches. We will at last focus on how different parameter mismatches can be compensated to improve the quality of the synchronization.

3.2 Synchronization of electro-optical laser hyperchaos

The problem of parameter mismatch

As emphasized in the general introduction, the issue of parameter mismatch is important from both the fundamental and applied points of view. As far as chaos cryptosystems are concerned, accurate synchronization between the emitter and the receiver is essential.

It is therefore important to gain insight into the time-domain manifestation of mismatch, the so-called **mismatch noise**, in order to evaluate its statistical properties in function of the nature and the amplitude of the various mismatches.

3.2.1 Coupled system under study

The coupled system under study is represented in Fig. 3.1. The chaotic emitter consists of a closed-loop electro-optical feedback, whose characteristics are in all points similar to those of the system described in section 2.3.1 of Chapter 2. The receiver is built symmetrically to the emitter, with the difference that only the light coming from the emitter enters into the delay loop: it is therefore an open-loop coupling scheme, since the receiver is unidirectionally forced by the coupling signal from the emitter. The emitter-receiver coupling is ensured by an asymmetric “2 × 2” fiber-coupler which inserts part of the emitter chaotic output into the transmission channel with a coupling factor ρ .

If we consider the variables

$$\begin{aligned} x(t) &= \frac{\pi V_{em}(t)}{2V_{\pi RF}} \\ y(t) &= \frac{\pi V_{rec}(t)}{2V'_{\pi RF}} \end{aligned} \quad (3.1)$$

as the dimensionless voltages across the electric path in the emitter and receiver feedback loops respectively, their dynamics can be modelled by the following system of coupled integro-differential delay equations [49]

$$x + \tau \dot{x} + \frac{1}{\theta} \int_{t_0}^t x(s) ds = \beta \cos^2[x(t - T) + \phi], \quad (3.2)$$

$$y + \tau' \dot{y} + \frac{1}{\theta'} \int_{t_0}^t y(s) ds = \beta' \cos^2[x(t - T') + \phi'] \quad (3.3)$$

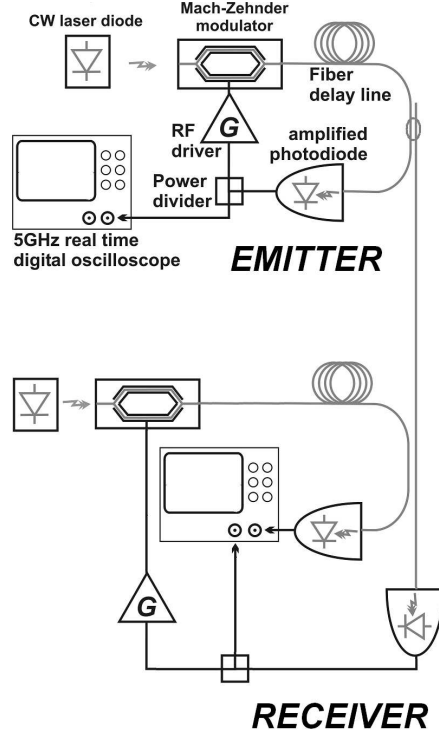


Figure 3.1: The experimental set-up.

where

$$\begin{aligned}
 \beta &= \pi \rho \kappa G S P / 2 V_{\pi R F}; & \phi &= \pi V_B / 2 V_{\pi D C}; \\
 \theta &= 1 / 2 \pi f_L; & \tau &= 1 / 2 \pi f_H; \\
 \beta' &= \pi \rho' \kappa' G' S' P' / 2 V'_{\pi R F}; & \phi' &= \pi V'_B / 2 V'_{\pi D C}; \\
 \theta' &= 1 / 2 \pi f'_L; & \tau' &= 1 / 2 \pi f'_H.
 \end{aligned} \tag{3.4}$$

The overdot denotes derivation relatively to the time t , and the receiver parameters are labeled with a prime because they generally differ from the transmitter ones. All additional attenuations in the receiver feedback-loop are contained in the coefficient ρ' . For simplicity we have not considered the transmission delay time between emitter and receiver, as it only induces a time-shift of the timetraces. We therefore have 5 control parameters in the model: the delay time T , the nonlinear feedback strength β , the off-set phase ϕ , the low cut-off response time θ , and the high cut-off response time τ . Throughout the whole chapter, we take the numerical values $T=20$ ns, $\beta=5$, $\phi=0.1$, $\theta=2$ μ s, and $\tau=50$ ps for the emitter system.

3.2.2 Synchronization error and cross-correlation function

To investigate the precision and robustness of the synchronization of the mismatched laser systems, it is convenient to find an approximate stationary integral form for the coupled evolution equations. This has two advantages: first it skips away the transient dynamics which is not suitable for the statistical analysis, and secondly, it gives a useful pseudo-explicit mathematical expression for the chaotic dynamic variables [31, 32]. The first step of this mathematical transformation is to introduce the variable $u(t)$ as

$$u(t) = \int_{t_0}^t x(s) ds, \quad (3.5)$$

so that Eq. (3.2) for the emitter dynamics can be formally written as a linear second order ordinary differential equation for u with a chaotic external forcing

$$\dot{u} + \tau \ddot{u} + \frac{1}{\theta} u = \beta \cos^2[x(t - T) + \phi]. \quad (3.6)$$

The roots of the characteristic polynomial corresponding to the homogeneous solution are

$$r_{\pm} = \frac{1}{2\tau} \left[-1 \pm \sqrt{1 - 4\frac{\tau}{\theta}} \right]. \quad (3.7)$$

Owing to the very large bandwidth of the filter, typically $\tau/\theta \sim 10^{-5} \ll 1$, the roots can be approximated as

$$r_+ \simeq -\frac{1}{\theta}, \quad r_- \simeq -\frac{1}{\tau}. \quad (3.8)$$

They can respectively stand for the low and high cut-off angular frequencies of the band-pass filter. Using Eq. (3.8) the stationary solution for u can be formally expressed as

$$u(t) = \beta \int_{t_0}^t \left[e^{\frac{s-t}{\theta}} - e^{\frac{s-t}{\tau}} \right] \cos^2[x(s - T) + \phi] ds, \quad (3.9)$$

and therefore, the stationary solution for x is given by

$$x(t) = \beta \int_{t_0}^t U(s, t) \cos^2[x(s - T) + \phi] ds, \quad (3.10)$$

where

$$U(s, t) = \left(\frac{1}{\tau} e^{\frac{s-t}{\tau}} - \frac{1}{\theta} e^{\frac{s-t}{\theta}} \right) \quad (3.11)$$

is an evolution operator which only depends on the filter parameters θ and τ . Similarly, one can obtain the following integral expression for the receiver

$$y(t) = \beta' \int_{t_0}^t U'(s, t) \cos^2[x(s - T') + \phi'] ds, \quad (3.12)$$

with $U'(s, t)$ being defined as $U(s, t)$ for the receiver parameters θ' and τ' .

We will use two indicators to characterize physically the effect of the parameter mismatch.

The first one is normalized average root-mean squared **synchronization error** which is a quantitative indicator measuring the time-averaged proximity of the emitter and receiver timetraces. We can define for each parameter p the instantaneous synchronization error as

$$\epsilon_{\Delta p}(t) = y_{p'}(t) - x_p(t), \quad (3.13)$$

where $\Delta p = p' - p$ is the parameter mismatch and $x_p(t)$ and $y_{p'}(t)$ are the transmitter and receiver timetraces obtained with the values of the parameter p and p' respectively. Therefore, the normalized average synchronization error would be

$$\sigma_{\Delta p} = \sqrt{\frac{\langle \epsilon_{\Delta p}^2 \rangle}{\langle x_p^2 \rangle}}, \quad (3.14)$$

where $\langle \bullet \rangle$ stands for the time average. The evaluation of this average should be performed integrating over a time much longer than any characteristic timescale of the model, in particular longer than θ which is the slowest timescale. Furthermore the integration time should be long enough so that the average reaches a stationary value, which typically takes place when the trajectory samples all the regions of the chaotic attractor. The synchronization error σ can be used as an indicator of the sensitivity as well as an indicator of threshold under which any encoded message can not be recovered, namely, the minimum modulation index in chaos cryptography.

The second indicator is the normalized **cross-correlation function**, defined as

$$\Gamma_{\Delta p}(s) = \frac{\langle (x_p(t) - \langle x_p(t) \rangle)(y_{p'}(t+s) - \langle y_{p'}(t) \rangle) \rangle}{\sqrt{\langle (x_p(t) - \langle x_p(t) \rangle)^2 \rangle \langle (y_{p'}(t) - \langle y_{p'}(t) \rangle)^2 \rangle}}, \quad (3.15)$$

which is a qualitative indicator showing how the receiver trajectory is topologically distorted by the mismatch. It may also be considered as a robustness indicator. We should note that the presence of the low cut-off integral term in equations (3.2) and (3.3) implies that the mean value of $x(t)$ and $y(t)$ is zero (otherwise the solutions

would linearly diverge to infinity). Therefore, in our case, Eq. (3.15) is equivalent to

$$\Gamma_{\Delta p}(s) = \frac{\langle x_p(t)y_{p'}(t+s) \rangle}{\sqrt{\langle x_p^2(t) \rangle \langle y_{p'}^2(t) \rangle}}, \quad (3.16)$$

and it is this latter expression of the cross-correlation that will be used in this chapter.

3.3 Single parameter-mismatches

In the following sub-sections we investigate the effect of a mismatch in each of the system parameters individually.

3.3.1 Delay-time mismatch (T)

The delay mismatch is met experimentally for a different delay length of fiber between the emitter and receiver set-up. The global delay includes the group delay of the RF components, and also the eventual electric cables that might be required in the set-up.

Assuming $\beta = \beta'$, $\phi = \phi'$, $\theta = \theta'$, $\tau = \tau'$ and defining $\Delta T = T' - T$, Eq. (3.12) can be written as

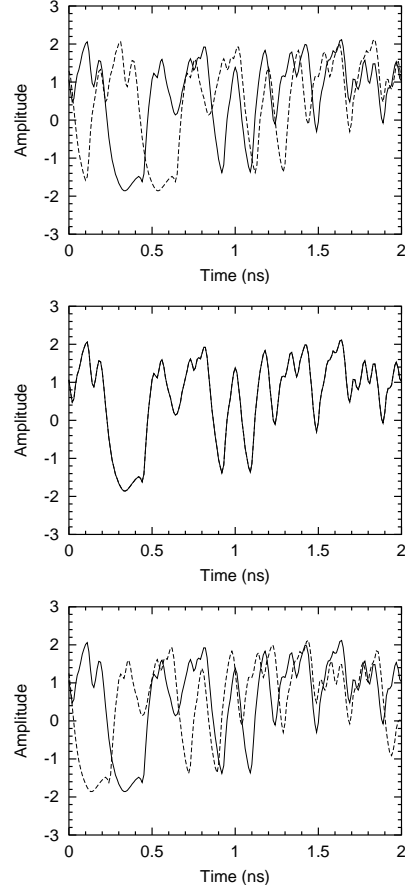
$$\begin{aligned} y(t) &= \beta \int_{t_0}^t U(s, t) \cos^2[x(s - T - \Delta T) + \phi] ds \\ &= x(t - \Delta T) + \beta \int_{t_0 - \Delta T}^{t_0} U(s', t - \Delta T) \cos^2[x(s' - T) + \phi] ds', \end{aligned} \quad (3.17)$$

where $s' = s - \Delta T$. Since the second integral term of the right hand-side exponentially decays to zero, one may simply expect in the stationary regime

$$y(t) = x(t - \Delta T). \quad (3.18)$$

The effect of the T mismatch is therefore to shift the receiver timetrace back or forth depending on the sign and amplitude of ΔT . This comes from the fact that the receiver equation is a linear differential equation externally forced by a nonlinear function of the chaotic variable $x(t - T)$. Hence, the T mismatch is a change of the time origin, which therefore does not qualitatively affect the dynamics of the receiver system.

Figure 3.2. Emitter (solid line) and receiver (dashed line) chaotic time traces. *a)* $\Delta T = 0.2$ ns, the receiver is lagging behind the emitter; *b)* $\Delta T = 0$, the receiver is isochronous to the emitter ; *c)* $\Delta T = -0.2$ ns, the receiver anticipates the emitter.



This is clearly illustrated in Fig. 3.2 which shows the emitter and receiver time traces for different values of ΔT .

The timetraces have been obtained integrating numerically Eqs. (3.2) and (3.3) using a fourth-order predictor-corrector algorithm and a time step of 10 ps. The timetrace is shown after integrating for a time $t_0 = 10\theta$, large enough to ensure the decay of the transient dynamics. In Fig. 3.2a, $\Delta T = 0.2$ ns, and the receiver is delayed relatively to the emitter; in Fig. 3.2b, $\Delta T = 0$ ns and the receiver is isochronous to the emitter; at last in Fig. 3.2c, $\Delta T = -0.2$ ns and the receiver anticipates the dynamics of the emitter. It may be important to note that the same initial conditions have been considered for the three cases.

An analytic approximation for $\sigma_{\Delta T}$ and $\Gamma_{\Delta T}$ can be obtained as follows. First

we consider the Fourier transform $X(\omega)$ of $x(t)$

$$X(\omega) = \frac{1}{\sqrt{2\pi}} \int_{-\infty}^{+\infty} x(t) e^{-i\omega t} dt, \quad (3.19)$$

which satisfies $X(\omega) = X^*(-\omega)$ since it is the Fourier transform of a real variable. From Eq. (3.18) we have $Y(\omega) = e^{-i\omega\Delta T} X(\omega)$, where $Y(\omega)$ is the Fourier transform of $y(t)$. Therefore in the Fourier space, the synchronization error is

$$E(\omega) = [e^{-i\omega\Delta T} - 1] X(\omega) = H_T(\omega) X(\omega), \quad (3.20)$$

where $H_T(\omega)$ is the **transfer function** from $E(\omega)$ to $X(\omega)$ for a ΔT mismatch. Hence, the synchronization error can theoretically be derived through the Parseval theorem as

$$\sigma_{\Delta T}^2 = \frac{\int_{-\infty}^{+\infty} |H_T(\omega)|^2 |X(\omega)|^2 d\omega}{\int_{-\infty}^{+\infty} |X(\omega)|^2 d\omega}. \quad (3.21)$$

As the integrals depend on the chaotic time trace they cannot be explicitly determined analytically. However, owing to hyperchaoticity, we can consider in first approximation that $X(\omega)$ is a perfectly flat band-limited white-noise spectrum, the limits being those of the band-pass filter, so that

$$X(\omega) = \begin{cases} S^* & \text{if } \omega \in \left[-\frac{1}{\tau}, -\frac{1}{\theta}\right] \\ S & \text{if } \omega \in \left[\frac{1}{\theta}, \frac{1}{\tau}\right] \\ 0 & \text{otherwise} \end{cases}, \quad (3.22)$$

where $S \in \mathbb{C}$ is an arbitrary complex constant. In fact the value of $|S|$ is not relevant here because the synchronization error is normalized with the average intensity of the chaotic carrier. We are therefore led to the following expression for the synchronization error

$$\begin{aligned} \sigma_{\Delta T}^2 &\approx \frac{1}{\tau^{-1} - \theta^{-1}} \int_{1/\theta}^{1/\tau} |H_T(\omega)|^2 d\omega \\ &\approx 2 \left[1 - \text{sinc} \left(\frac{\Delta T}{\tau} \right) \right], \end{aligned} \quad (3.23)$$

where *sinc* is the sine-cardinal function. The accuracy of this result relies on the validity of the approximation when considering that the chaotic spectrum looks like a white noise within a bandwidth defined by the cut-off times θ and τ .

Figure 3.3a displays the comparison between numerical and analytical results for the synchronization error. Despite the simplicity of the approximation, Eq.

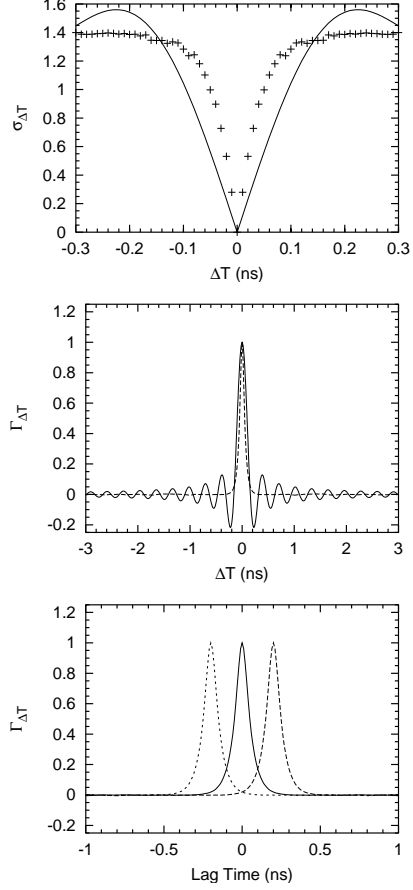


Figure 3.3. *a)* Synchronization error for a ΔT mismatch. The analytical results are solid lines, and the numerical results are in symbols. *b)* Cross-correlation function at equal times for a ΔT mismatch. The analytical results is the solid line, while the numerical results is the dotted line. *c)* Cross-correlation function $\Gamma_{\Delta T}(s)$ for $\Delta T = 0.2$ ns (long-dashed line), $\Delta T = 0$ (continuous line) and $\Delta T = -0.2$ ns (short-dashed line).

(3.23) gives a good prediction although the numerical results show for small mismatch values a larger synchronization error than theoretically predicted. Both analytical prediction and numerical results indicate a very high sensitivity to time delay mismatch: a 1% synchronization error is induced when $\Delta T = 1$ ps, that is, for a relative error of $\Delta T/T \simeq 5 \times 10^{-5}$. As indicated by Eq. (3.23), this high sensitivity comes from the large bandwidth $\Delta f \simeq 1/2\pi\tau \gg 1/T$. Consequently, for a satisfying synchronization quality, the length of the fiber delay-lines should practically be adjusted with a relative precision of the order of 10^{-6} . In the case of a larger bandwidth filter (as it would ideally be the case), this sensitivity would be increased proportionally to the high cut-off frequency.

To determine analytically the cross-correlation function, we can use a corollary of the Wiener-Khinchin theorem which states that the cross-correlation function is the inverse Fourier transform of the cross-power spectral density function [98, 99].

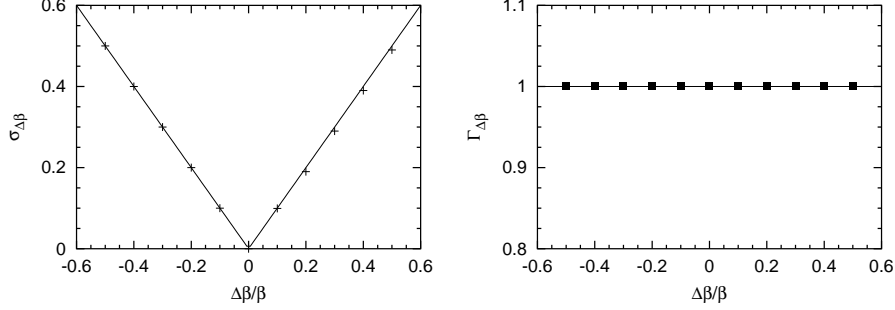


Figure 3.4. a) Average synchronization error and b) Cross-correlation at equal times for β mismatch. The analytical results are in solid lines, and the numerical ones are in symbols.

Hence, the expression of $\Gamma_{\Delta T}$ as a function of its lag-time argument s reads

$$\begin{aligned} \Gamma_{\Delta T}(s) &= \frac{\int_{-\infty}^{+\infty} X(\omega)Y^*(\omega) e^{i\omega s} d\omega}{\sqrt{\left[\int_{-\infty}^{+\infty} |X(\omega)|^2 d\omega\right] \left[\int_{-\infty}^{+\infty} |Y(\omega)|^2 d\omega\right]}} \\ &\simeq \text{sinc}\left(\frac{s + \Delta T}{\tau}\right). \end{aligned} \quad (3.24)$$

Figure 3.3b displays the comparison between Eq. (3.24) and the numerical results for the cross-correlation at zero lag time ($s = 0$) obtained integrating Eqs. (3.2) and (3.3). Again, despite its simplicity, Eq. (3.24) is a quite good approximation of the correlation function. The numerical calculations show that by increasing the delay time mismatch, the correlation decays, in fact, slightly faster than the analytical prediction (3.24). The oscillations that appear in the theoretical curve come from the vertical cut-off we have considered for the hyperchaotic spectrum ($X(\omega)$ was approximated as a rectangular function). They could be eliminated by approximating $X(\omega)$ as a function with a smooth decay to zero, which would be a more realistic approximation for the spectra of the chaotic time trace. However, this would be made at the cost of a higher complexity for the calculations.

Equation (3.24) also indicates that, as we may expect from Eq. (3.18), the effect of ΔT is to shift the autocorrelation function to the left ($\Delta T < 0$) or to the right ($\Delta T > 0$) by an amount ΔT . This analytical prediction is numerically confirmed in Fig. 3.3c. The influence of time-delay mismatch is in absolute rather than relative value since the timetraces and correlation functions are shifted proportionally to ΔT .

3.3.2 Nonlinear feedback-strength mismatch (β)

The β mismatch corresponds to a normalized gain in the experimental setup, which includes various physical parameters: the electronic feedback gain, the electro-optic sensitivity of the modulator, the detector sensitivity, the optical losses, and the continuous-wave laser optical power P . The precise dependence on these parameters is given in Eq. (3.4). Only the mismatch in the resulting β is relevant and not in the individual physical parameters, since, for example, an RF gain mismatch can be compensated by an optical power mismatch.

Assuming $\phi = \phi'$, $\theta = \theta'$, $\tau = \tau'$, $T = T'$ and defining $\Delta\beta = \beta' - \beta$ one obtains from Eqs. (3.10) and (3.12) that $x(t) = \beta y(t)/\beta'$. The receiver time trace is exactly the same as the transmitter but with different amplitude. This can also be obtained directly from Eqs. (3.2) and (3.3) by rescaling y with β/β' . Therefore, this result is mathematically exact, independently of the approximations we have done to obtain the stationary integral form. Then $\epsilon(t) = (\Delta\beta/\beta)x(t)$, so that the average synchronization error is

$$\sigma_{\Delta\beta} = \left| \frac{\Delta\beta}{\beta} \right|. \quad (3.25)$$

Therefore the synchronization error depends on the relative β mismatch. Thus, for example, a 1% $\Delta\beta$ mismatch induces a 1% synchronization error. Since x and y are strictly proportional, the cross-correlation function at equal times is always perfect, namely $\Gamma_{\Delta\beta}(0) = 1$.

Figure 3.4 displays the synchronization error and the cross-correlation at equal times. The analytical results coincide exactly with the numerical ones, as expected from the fact that no approximation were needed to obtain the analytical results.

3.3.3 Off-set phase mismatch (ϕ)

The ϕ mismatch stems from a residual optical path difference in the emitter and receiver Mach-Zehnder modulators, but it can be experimentally compensated while changing the DC bias of the electro-optic voltage.

To obtain an analytical approximation for the effects of this mismatch, we rewrite Eq. (3.10) as

$$x(t) = \frac{\beta}{2} \int_{t_0}^t U(s, t) ds + \frac{\beta}{2} \int_{t_0}^t U(s, t) \cos[2x(s - T) + 2\phi] ds. \quad (3.26)$$

The first integral term exponentially decays to zero, which physically comes from the DC filtering property of the band-pass filter. Therefore the stationary solution

of $x(t)$ and $y(t)$ can be written as

$$\begin{aligned} x(t) &= \frac{\beta}{2} \int_{t_0}^t U(s, t) \cos[2x(s - T) + 2\phi] ds, \\ y(t) &= \frac{\beta}{2} \int_{t_0}^t U'(s, t) \cos[2x(s - T') + 2\phi'] ds. \end{aligned} \quad (3.27)$$

For the sake of compactness, let us introduce

$$Q(s, t, \phi) = U(s, t) \cos[2x(s - T) + 2\phi]. \quad (3.28)$$

Assuming $\beta = \beta'$, $\theta = \theta'$, $\tau = \tau'$, $T = T'$ and defining $\Delta\phi = \phi' - \phi$, the instantaneous synchronization error may be expressed as

$$\epsilon(t) = -\beta \sin(\Delta\phi) \int_{t_0}^t Q \left[s, t, \phi + \frac{\Delta\phi}{2} - \frac{\pi}{4} \right] ds. \quad (3.29)$$

Starting from here, we assume that for long enough delay times, the average properties of the chaotic attractor are independent of the off-set phase. This statistical phase invariance hypothesis is supported by the results from the numerical computation of the Lyapunov exponents of the system [100], and also by previous investigations led in ref. [101] which show that when β and T are large enough, the number and values of the positive Lyapunov exponents are practically independent of the off-set phase. Therefore, we have

$$\begin{aligned} \langle \epsilon_{\Delta\phi}^2 \rangle &\approx \beta^2 \sin^2(\Delta\phi) \left\langle \left[\int_{t_0}^t Q(s, t, \phi) ds \right]^2 \right\rangle \\ &= 4 \sin^2(\Delta\phi) \langle x^2 \rangle, \end{aligned} \quad (3.30)$$

so that finally, the average synchronization error is given by

$$\sigma_{\Delta\phi} = 2 |\sin(\Delta\phi)|. \quad (3.31)$$

The synchronization error $\sigma_{\Delta\phi}$ does not depend on the value of the off-set phase ϕ itself, and this is a consequence of our assumption; therefore there is no optimal value of ϕ . Equation (3.31) also indicates the extreme sensitivity of this parameter: for example, if we consider a small $\Delta\phi$ mismatch of 0.01 (ϕ is a ratio between two voltages), the induced synchronization error is 2%, which is quite important.

According to Eq. (3.27) the numerator of the cross-correlation at equal times is given by

$$\begin{aligned} \langle xy \rangle &= \frac{\beta^2}{4} \cos(2\Delta\phi) \left\langle \left[\int_{t_0}^t Q(s, t, \phi) ds \right]^2 \right\rangle \\ &\quad - \frac{\beta^2}{4} \sin(2\Delta\phi) \left\langle \left[\int_{t_0}^t Q(s, t, \phi) ds \right] \left[\int_{t_0}^t Q(s, t, \phi - \frac{\pi}{4}) ds \right] \right\rangle. \end{aligned} \quad (3.32)$$

We here assume that the hyperchaotic behavior induced by the electro-optical system is **ergodic**, so that we can equate the average over time to an average over the attractor in phase-space. Although we can not prove this hypothesis, it is consistent with the fact that time averages are performed over long times so that they reach a stationary value as discussed after Eq. (3.14). Furthermore, the results we obtain are in quite good agreement with numerical simulations as we will show below. The ergodic assumption implies that the last average of Eq. (3.32) vanishes since it involves the product of a symmetric with an antisymmetric function. We can therefore write

$$\langle xy \rangle \approx \cos(2\Delta\phi) \langle x^2 \rangle, \quad (3.33)$$

and we also have

$$\begin{aligned} \langle y^2 \rangle &= \frac{\beta^2}{4} \left\langle \left[\int_{t_0}^t Q(s, t, \phi + \Delta\phi) ds \right]^2 \right\rangle \\ &\simeq \frac{\beta^2}{4} \left\langle \left[\int_{t_0}^t Q(s, t, \phi) ds \right]^2 \right\rangle \\ &= \langle x^2 \rangle, \end{aligned} \quad (3.34)$$

where we have again assumed that the time-average properties of the chaotic attractor are independent of the off-set phase delay. Therefore the cross-correlation is given by

$$\Gamma_{\Delta\phi}(0) = \cos(2\Delta\phi). \quad (3.35)$$

Logically it turns out that the cross-correlation and the synchronization error are π -periodic as the nonlinear feedback function. Also from Eq. (3.35) for $\Delta\phi = \pm\pi/2$, $\Gamma_{\Delta\phi}(0) = -1$ so that the receiver timetrace is in exact phase opposition with respect to the emitter one; that is why the corresponding synchronization error value is exactly 2 in that case which can be referred to as **perfect anti-synchronization**.

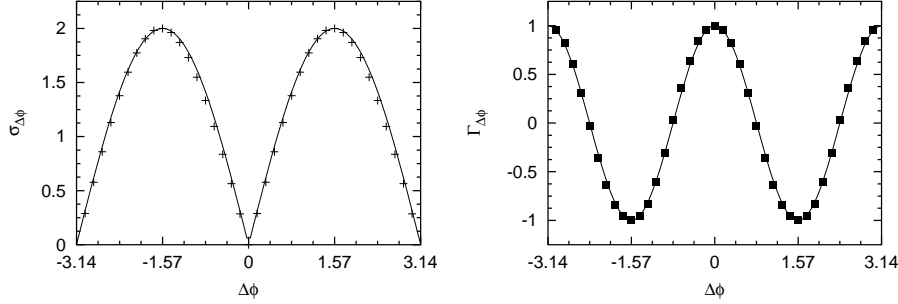


Figure 3.5. *a)* Average synchronization error and *b)* Cross-correlation at equal times for off-set phase mismatch. Analytical approximations are shown in solid lines and numerical results in symbols.

Figure 3.5 displays the average synchronization error and the cross-correlation at equal times. Equation (3.35) shows an excellent agreement with the numerical results, which indicates the validity of the assumptions we have made. However, one may not expect such a good concordance in the case of small values of β or T , where for example the statistical off-set phase invariance can not be guaranteed.

The above results can also be obtained in the Fourier space as follows. From Eq. (3.27) we have

$$Y(\omega) = e^{2i\Delta\phi}V(\omega) + e^{-2i\Delta\phi}V^*(-\omega), \quad (3.36)$$

where $V(\omega)$ is defined as

$$V(\omega) = \frac{\beta}{4\sqrt{2\pi}} \int_{-\infty}^{+\infty} \int_{t_0}^t U(s, t) e^{2i(x(s-T)+\phi)} e^{-i\omega t} ds dt. \quad (3.37)$$

We can write $V(\omega) = \frac{1}{2}[X(\omega) + iA(\omega)]$ where

$$A(\omega) = \frac{\beta}{2\sqrt{2\pi}} \int_{-\infty}^{+\infty} \int_{t_0}^t U(s, t) \sin[2x(s-T) + 2\phi] e^{-i\omega t} ds dt, \quad (3.38)$$

and then, using $X(\omega) = X^*(-\omega)$ and $A(\omega) = A^*(-\omega)$ which come from the fact that they are Fourier transforms of real functions, we are led to

$$Y(\omega) = \cos(2\Delta\phi)X(\omega) + \sin(2\Delta\phi)A(\omega). \quad (3.39)$$

The Fourier transform of the synchronization error therefore reads

$$E(\omega) = [\cos(2\Delta\phi) - 1]X(\omega) + \sin(2\Delta\phi)A(\omega), \quad (3.40)$$

so that the average synchronization error can be obtained through the Parseval theorem following

$$\sigma_{\Delta\phi}^2 = \frac{\int_{-\infty}^{+\infty} |E(\omega)|^2 d\omega}{\int_{-\infty}^{+\infty} |X(\omega)|^2 d\omega}. \quad (3.41)$$

The numerator can be written as

$$\begin{aligned} \int_{-\infty}^{+\infty} |E(\omega)|^2 d\omega &= (\cos(2\Delta\phi) - 1)^2 \int_{-\infty}^{+\infty} |X(\omega)|^2 d\omega \\ &+ \sin^2(2\Delta\phi) \int_{-\infty}^{+\infty} |A(\omega)|^2 d\omega + [\cos(2\Delta\phi) - 1] \times \\ &\sin(2\Delta\phi) \int_{-\infty}^{+\infty} [X(\omega)A^*(\omega) + X^*(\omega)A(\omega)] d\omega. \end{aligned} \quad (3.42)$$

while the integral $\mathcal{I} = \int_{-\infty}^{+\infty} X(\omega)A^*(\omega) d\omega$ can be written under the form

$$\begin{aligned} \mathcal{I} &= \frac{\beta}{4} \int_{-\infty}^{+\infty} \int_{-\infty}^{+\infty} \int_{-\infty}^{+\infty} \left[\int_{t_0}^t U(s, t) \cos[2x(s - T) + 2\phi] ds \right] \\ &\times \left[\int_{t_0}^{t'} U(s, t') \sin[2x(s - T) + 2\phi] ds \right] e^{i\omega(t' - t)} dt dt' d\omega \end{aligned} \quad (3.43)$$

which corresponds to the average appearing in the last term of Eq. (3.32): hence, the last term of Eq. (3.42) vanishes. On the other hand, the function $A(\omega)$ obtained from Eq. (3.38) for an off-set phase ϕ is precisely $X(\omega)$ for an off-set phase $\phi - \pi/4$. Therefore under the assumption that the average properties of the chaotic attractor are independent of the off-set phase, we are going to consider that

$$\int_{-\infty}^{+\infty} f(\omega) |A(\omega)|^2 d\omega = \int_{-\infty}^{+\infty} f(\omega) |X(\omega)|^2 d\omega, \quad (3.44)$$

for any function $f(\omega)$. Then the average synchronization error is given by

$$\sigma_{\Delta\phi}^2 = [\cos(2\Delta\phi) - 1]^2 + \sin^2(2\Delta\phi) = 4 \sin^2(\Delta\phi), \quad (3.45)$$

exactly as obtained before in Eq. (3.30).

The cross-correlation can be determined as in subsection 3.3.1 following

$$\int_{-\infty}^{+\infty} X(\omega)Y^*(\omega)e^{i\omega s} d\omega = \cos(2\Delta\phi) \int_{-\infty}^{+\infty} |X(\omega)|^2 e^{i\omega s} d\omega + \sin(2\Delta\phi) \int_{-\infty}^{+\infty} X(\omega)A^*(\omega)e^{i\omega s} d\omega. \quad (3.46)$$

Here, and later on in section 3.4, we have to evaluate integrals of the form

$$\mathcal{J} = \int_{-\infty}^{+\infty} f(\omega)X(\omega)A^*(\omega) d\omega \quad (3.47)$$

where $f(\omega) = f_R(\omega) + if_I(\omega)$ is a complex function such that the real part $f_R(\omega)$ is symmetric in ω and the imaginary part $f_I(\omega)$ is antisymmetric. As discussed above $X(\omega)A^*(\omega)$ is an antisymmetric function, therefore the symmetric $f_R(\omega)$ does not contribute to the integral. To evaluate the contribution from $f_I(\omega)$ we assume the band-pass filter approximation of the chaotic spectrum given in Eq. (3.22), so that

$$\int_{-\infty}^{+\infty} f(\omega)X(\omega)A^*(\omega) d\omega = 2|S|^2 \int_{1/\theta}^{1/\tau} f_I(\omega) d\omega. \quad (3.48)$$

Therefore, we finally obtain

$$\Gamma_{\Delta\phi}(s) = \frac{\sin(2\Delta\phi + s\tau^{-1}) - \sin(2\Delta\phi + s\theta^{-1})}{s(\tau^{-1} - \theta^{-1})}, \quad (3.49)$$

which in the limit $s \rightarrow 0$ reduces to Eq. (3.35). The Fourier approach just discussed will be used later on when discussing the effect of simultaneous mismatch on different parameters.

3.3.4 Low cut-off response time mismatch (θ)

The low- and high cut-off response times are practically determined by the RF-amplifier and by the photodiode bandwidth. In practice it is very difficult to tune them, and the components involved in the setup are ordered to be matched by the suppliers.

Assuming all the other parameters are equal, we have from Eqs. (3.2) and (3.3)

$$\epsilon + \tau\dot{\epsilon} + \frac{1}{\theta + \Delta\theta} \int_{t_0}^t \epsilon(s) ds = \frac{\Delta\theta}{\theta(\theta + \Delta\theta)} \int_{t_0}^t x(s) ds, \quad (3.50)$$

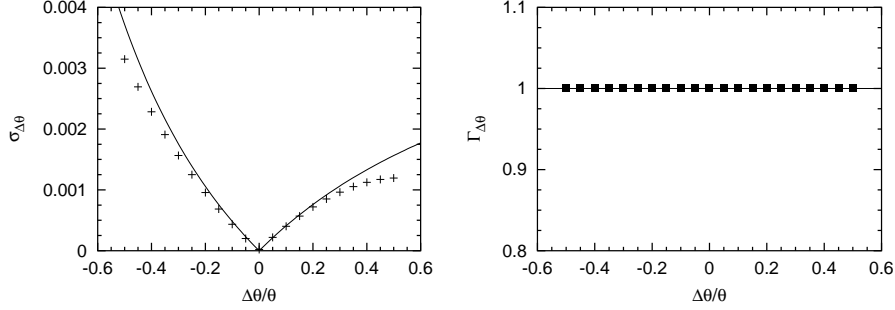


Figure 3.6. a) Average synchronization error and b) Cross-correlation at equal times for θ mismatch. Analytical approximations are shown in solid lines and numerical results in symbols.

which in Fourier domain gives

$$E(\omega) = \frac{\frac{\Delta\theta}{\theta}}{1 + i\omega(\theta + \Delta\theta)(1 + i\omega\tau)} X(\omega). \quad (3.51)$$

As in subsection 3.3.1, we approximate $X(\omega)$ by a rectangular function, thus leading to

$$\sigma_{\Delta\theta}^2 = \frac{\left(\frac{\Delta\theta}{\theta}\right)^2}{\frac{1}{\tau} - \frac{1}{\theta}} \int_{1/\theta}^{1/\tau} \frac{d\omega}{(1 - \omega^2\tau(\theta + \Delta\theta))^2 + \omega^2(\theta + \Delta\theta)^2}, \quad (3.52)$$

so that at first order in τ/θ , we finally have

$$\sigma_{\Delta\theta} = \sqrt{\frac{\tau}{\theta}} \left| \frac{\Delta\theta}{\theta} \right| \sqrt{\frac{\pi - 2 \arctan(1 + \Delta\theta/\theta)}{2(1 + \Delta\theta/\theta)}}. \quad (3.53)$$

For typical parameter values, this synchronization error is very small (of the order 10^{-3}) hence, we can conclude that even a large mismatch for θ does not significantly affect the quality of the synchronization. Physically this comes from the fact that the low cut-off frequency is of the order of tens of kHz, while the chaotic oscillations are typically within the GHz range. Therefore, any mismatch at such a low frequency range can not really destabilize the synchronization manifold.

Figure 3.6 displays the average synchronization error. The analytical approximation (3.53) shows a very good agreement with the numerical results obtained integrating Eqs. (3.2) and (3.3) specially for small mismatch. The small synchronization error indicates that the emitter and receiver time traces are very similar, therefore we can assume that the equal time cross-correlation is practically perfect, yielding $\Gamma_{\Delta\theta}(0) = 1$.

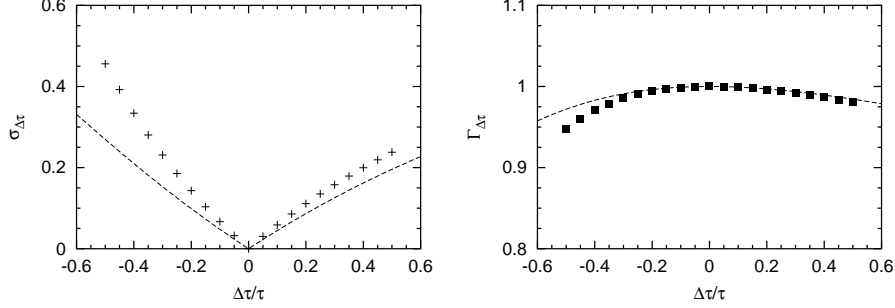


Figure 3.7. a) Average synchronization error and b) Cross-correlation at equal times for τ mismatch. Analytical approximations are shown in solid lines and numerical results in symbols.

3.3.5 High cut-off frequency mismatch (τ)

Assuming all the other parameters are equal, from Eqs. (3.2) and (3.3) we have the following evolution for $\epsilon(t)$

$$\epsilon + (\tau + \Delta\tau)\dot{\epsilon} + \frac{1}{\theta} \int_{t_0}^t \epsilon(s) ds = -\Delta\tau\dot{x} \quad (3.54)$$

which in the Fourier domain gives

$$E(\omega) = \frac{\omega^2 \theta \Delta\tau}{1 - \omega^2 \theta (\tau + \Delta\tau) + i\omega\theta} X(\omega). \quad (3.55)$$

Approximating $X(\omega)$ by a rectangular function we obtain

$$\sigma_{\Delta\tau}^2 = \frac{(\Delta\tau)^2}{\frac{1}{\tau} - \frac{1}{\theta}} \int_{1/\theta}^{1/\tau} \frac{\omega^4 \theta^2}{(1 - \omega^2 \theta (\tau + \Delta\tau))^2 + \omega^2 \theta^2} d\omega, \quad (3.56)$$

so that, at first order in τ/θ ,

$$\sigma_{\Delta\tau} = \left| \frac{\Delta\tau}{\tau + \Delta\tau} \right| \sqrt{1 - \frac{\arctan(1 + \Delta\tau/\tau)}{1 + \Delta\tau/\tau}}. \quad (3.57)$$

The cross-correlation can be calculated in a similar way as in section 3.3.1. Approximating $X(\omega)$ by a rectangular function, at first order in τ/θ , we have

$$\Gamma_{\Delta\tau}(0) = \frac{1 + \frac{\Delta\tau}{\tau} + \frac{\Delta\tau}{\tau} \arctan(1 + \frac{\Delta\tau}{\tau})}{(1 + \frac{\Delta\tau}{\tau}) \sqrt{1 + \frac{\Delta\tau}{\tau} \arctan(1 + \frac{\Delta\tau}{\tau})}}. \quad (3.58)$$

Equation (3.57) implies that for typical parameter values there is a relatively high sensitivity of the synchronization manifold to the high cut-off frequency, since a 1% error in τ induces approximately a 0.5% synchronization error. Figure 3.7 displays the synchronization error and the cross-correlation at equal times. The analytical approximations show a quite satisfactory agreement with the numerical results, mainly for small parameter mismatches.

3.4 Multiple parameter-mismatch

3.4.1 Global synchronization error and cross-correlation

In this section, we address the important configuration where all the mismatches are considered simultaneously, as it is the case in the experimental system.

The first step is to rewrite Eqs. (3.2) and (3.3) as

$$x + \tau \dot{x} + \frac{1}{\theta} \int_{t_1}^t x(s) ds = \beta \cos[2x(t - T) + 2\phi] \quad (3.59)$$

$$y + \tau' \dot{y} + \frac{1}{\theta'} \int_{t_1}^t y(s) ds = \beta' \cos[2x(t - T') + 2\phi'], \quad (3.60)$$

where t_1 is such that $\int_{t_0}^{t_1} x(s) ds = \beta\theta$. We can introduce two complex variables v, w obeying

$$v + \tau \dot{v} + \frac{1}{\theta} \int_{t_1}^t v(s) ds = \beta e^{2i(x(t-T)+\phi)}, \quad (3.61)$$

$$w + \tau' \dot{w} + \frac{1}{\theta'} \int_{t_1}^t w(s) ds = \beta' e^{2i(x(t-T')+\phi')}, \quad (3.62)$$

so that $\Re[v] = x$ and $\Re[w] = y$: hence, the following equalities hold in the Fourier space

$$\begin{aligned} X(\omega) &= V(\omega) + V^*(-\omega) \\ Y(\omega) &= W(\omega) + W^*(-\omega). \end{aligned} \quad (3.63)$$

We have demonstrated that the effect of the delay time mismatch in the stationary state is to shift in time the chaotic trajectory. Therefore we introduce

$w_1(t) = w(t + \Delta t)$, and assuming that in the stationary state $\int_{t_1-\Delta T}^{t-\Delta T} w_1(s) ds = \int_{t_1}^t w_1(s) ds$, we have

$$w_1 + \tau' \dot{w}_1 + \frac{1}{\theta'} \int_{t_1}^t w_1(s) ds = \beta' e^{2i(x(t-T)+\phi')}. \quad (3.64)$$

From Eqs. (3.61) and (3.64), we can also write

$$v + \tau \dot{v} + \frac{1}{\theta} \int_{t_1}^t v(s) ds = \frac{\beta}{\beta'} \left[w_1 + \tau' \dot{w}_1 + \frac{1}{\theta'} \int_{t_1}^t w_1(s) ds \right] e^{2i\Delta\phi}, \quad (3.65)$$

so that, in the Fourier space, we have $W_1(\omega) = \frac{\beta'}{\beta} e^{2i\Delta\phi} F(\omega) V(\omega)$, where

$$F(\omega) = \frac{\frac{\theta'}{\theta} - \omega^2 \tau \theta' + i\omega \theta'}{1 - \omega^2 \tau' \theta' + i\omega \theta'}. \quad (3.66)$$

From the definition of w_1 we have $W(\omega) = e^{-i\omega\Delta T} W_1(\omega)$, inducing

$$W(\omega) = \frac{\beta'}{\beta} e^{-i\omega\Delta T} e^{2i\Delta\phi} F(\omega) V(\omega) \quad (3.67)$$

and subsequently

$$Y(\omega) = \frac{\beta'}{\beta} e^{-i\omega\Delta T} F(\omega) [\cos(2\Delta\phi) X(\omega) - \sin(2\Delta\phi) A(\omega)], \quad (3.68)$$

where $A(\omega)$ is the Fourier transform of the imaginary part of v , and where $X(\omega) = X^*(-\omega)$, $A(\omega) = A^*(-\omega)$ and $F(\omega) = F^*(-\omega)$ have been assumed. The synchronization error is then given by

$$E(\omega) = \frac{\beta'}{\beta} e^{-i\omega\Delta T} F(\omega) [\cos(2\Delta\phi) X(\omega) - \sin(2\Delta\phi) A(\omega)] - X(\omega), \quad (3.69)$$

and the average synchronization error can be obtained through the Parseval theorem of Eq. Eq. (3.41). Calculating the integrals as discussed in subsection 3.3.3, we finally obtain

$$\begin{aligned} \sigma^2 = & \frac{1}{\tau^{-1} - \theta^{-1}} \left[\left(1 + \frac{\Delta\beta}{\beta} \right)^2 \int_{1/\theta}^{1/\tau} |F(\omega)|^2 d\omega \right. \\ & - 2 \left(1 + \frac{\Delta\beta}{\beta} \right) \left\{ \cos(2\Delta\phi) \int_{1/\theta}^{1/\tau} \Re[e^{-i\omega\Delta T} F(\omega)] d\omega \right. \\ & \left. \left. + \sin(2\Delta\phi) \int_{1/\theta}^{1/\tau} \Im[e^{-i\omega\Delta T} F(\omega)] d\omega \right\} \right]. \quad (3.70) \end{aligned}$$

Therefore, the squared synchronization error is a quadratic function of $\Delta\beta$, and a sinusoidal function of $\Delta\phi$. Evaluating the integrals up to the second order in parameter mismatch, we obtain the following expression for the synchronization error

$$\begin{aligned} \sigma^2 = & \frac{1}{3} \left(\frac{\Delta T}{\tau} \right)^2 + \left(\frac{\Delta\beta}{\beta} \right)^2 + 4(\Delta\phi)^2 \\ & + \left(1 - \frac{\pi}{4} \right) \left(\frac{\Delta\tau}{\tau} \right)^2 + 2[1 - \ln(2)] \Delta\phi \frac{\Delta T}{\tau} \\ & - 2 \left(1 - \frac{\pi}{4} \right) \frac{\Delta\beta}{\beta} \frac{\Delta\tau}{\tau} - 2 \left(1 - \frac{\pi}{4} \right) \frac{\Delta T}{\tau} \frac{\Delta\tau}{\tau} \\ & + \frac{\tau}{\theta} \left[\frac{\pi}{4} \left(\frac{\Delta\beta}{\beta} + \frac{\Delta\theta}{\theta} \right)^2 - 4 \ln \left(\frac{\theta}{2\tau} \right) \Delta\phi \frac{\Delta\theta}{\theta} \right]. \end{aligned} \quad (3.71)$$

At the order τ/θ (last block), only the terms containing the $\Delta\theta$ mismatch have been kept since this mismatch does not appear at zero order in τ/θ . For the other mismatches there are also contributions at first order in τ/θ but they can be neglected as compared to the zeroth order contributions.

The synchronization error can be rewritten as the square-root of a positive-definite quadratic form

$$\sigma = \sqrt{\sum_{i,j=1}^5 M_{ij} z_i z_j} = \sqrt{\mathbf{z}^T \mathbf{M} \mathbf{z}} \quad (3.72)$$

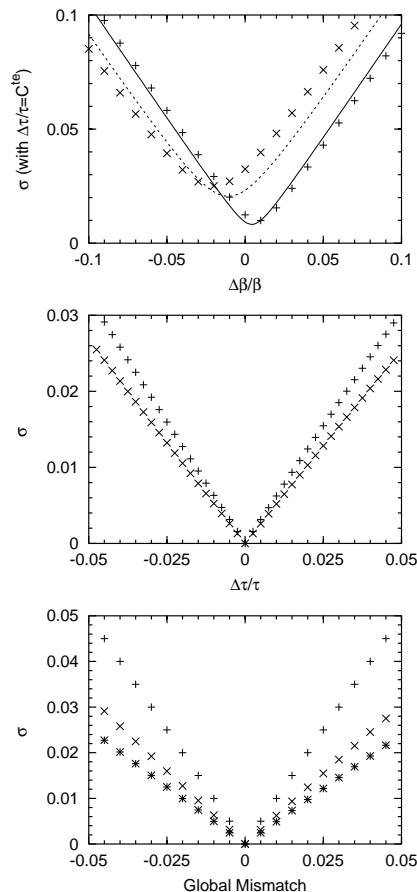
where \mathbf{z} is the 5-dimensional vector $\left(\frac{\Delta T}{\tau}, \frac{\Delta\beta}{\beta}, \Delta\phi, \frac{\Delta\theta}{\theta}, \frac{\Delta\tau}{\tau} \right)$, while \mathbf{M} is the symmetric characteristic matrix of the quadratic form. Its components M_{ij} can directly be determined from Eq. (3.71). The diagonal terms of \mathbf{M} correspond to the results we have obtained while considering the mismatches separately, and the non-diagonal terms indicate the various interactions between the different mismatches.

On the other hand, the Wiener-Khintchin formula yields with a satisfying precision the following expression for the cross-correlation function

$$\Gamma(s) = \frac{\sin(2\Delta\phi + \frac{s+\Delta T}{\tau}) - \sin(2\Delta\phi + \frac{s+\Delta T}{\theta})}{(s + \Delta T)(\tau^{-1} - \theta^{-1})}. \quad (3.73)$$

As one could have *a priori* expected, the parameters which individually most influence the cross-correlation are still influent.

Figure 3.8. *a)* Synchronization error as a function of $\Delta\beta/\beta$ when the mismatch $\Delta\tau/\tau$ is fixed to 2% (the solid line shows the analytical approximations and the symbols (+) the numerical results) and -5% (dashed line for analytical approximations, (\times) for numerical results). *b)* Results obtained from numerical simulation for the synchronization error as a function of $\Delta\tau/\tau$ when the mismatch $\Delta\beta/\beta = 0$ (+), and when $\Delta\beta/\beta$ is optimally tuned accordingly to Eq. (52) (\times). *c)* Evaluation of σ from numerical simulation for β -only-mismatch (+), τ -only-mismatch (\times), and for a multiple mismatch within the eigendirection defined analytically in Eq. (3.81) (*).



With these results, one can investigate what the effect of multiple parameter mismatch is relatively to the case of single parameter mismatches. For this purpose, we make the distinction between two cases: in the first one, only one mismatch can be adjusted while all the others are fixed, while in the second case, all the mismatches can simultaneously be tuned.

3.4.2 One-parameter optimization

This particular case of a single tunable parameter is of great experimental importance. For example, in the experimental setup, β (which is proportional to the laser output power) and ϕ (which is the ratio of two voltages) are much more easily tunable than the length of the delay line or the bandwidth of the filter. Therefore, the point is to find for which value of the tunable mismatch minimizes the synchronization error is reduced.

Let us consider that z_k is the tunable mismatch while all the others z_i are fixed. In that case, the synchronization error becomes a one-variable function which is

minimized when

$$\frac{\partial \sigma}{\partial z_k} = 0 \quad (3.74)$$

that is, for

$$z_k = - \sum_{\substack{i=1 \\ i \neq k}}^5 \frac{M_{ik}}{M_{kk}} z_i. \quad (3.75)$$

When some M_{ik} are different from zero, the optimal mismatch is also different from zero: Hence, this equation can be considered as a kind of **compensation formula**.

Let us take for example the case where the emitter and receiver band-pass filters are mismatched. We have shown that the low cut-off mismatch is not influent. Hence, we will focus on the high cut-off mismatch $\Delta\tau$, which induces according to equation (3.71) a synchronization error of $\sqrt{1 - \pi/4} |\Delta\tau/\tau|$ when all the other mismatches are uniformly set to 0. If we tune the $\Delta\beta$ mismatch, we find that synchronization error is minimized when $\Delta\beta$ is given by

$$\frac{\Delta\beta}{\beta} = \left(1 - \frac{\pi}{4}\right) \frac{\Delta\tau}{\tau}. \quad (3.76)$$

According to Eq. (3.71), for this optimal value of $\Delta\beta$ the synchronization error is

$$\sigma_{\Delta\beta, \Delta\tau}^{\min} = \sqrt{\frac{\pi}{4} \left(1 - \frac{\pi}{4}\right)} \cdot \left| \frac{\Delta\tau}{\tau} \right| = \sqrt{\frac{\pi}{4}} \sigma_{\Delta\tau}, \quad (3.77)$$

which is a 12% reduction in the synchronization error. We therefore reach the quite counter-intuitive conclusion that under certain conditions, **multiple parameter mismatch can improve the quality of the synchronization**, since it can lead to a smaller value of σ .

This analysis is confirmed by the numerical simulations. In Fig. 3.8a, it clearly appears that the minimum error does not occur when $\Delta\beta = 0$, but rather when $\Delta\beta$ is shifted by an amount in good concordance with equation (3.76). In Fig. 3.8b, the numerical simulation also shows that when the $\Delta\beta$ mismatch is optimally tuned the synchronization error is smaller, by an amount close to the 12% we have predicted.

It is important to note even though a off-set phase mismatch $\Delta\phi$ is also easily tuneable, it cannot significantly help to compensate for a filter mismatch because $M_{34} \simeq M_{35} \simeq 0$ (however, it can for example compensate for a ΔT mismatch since $M_{31} \neq 0$).

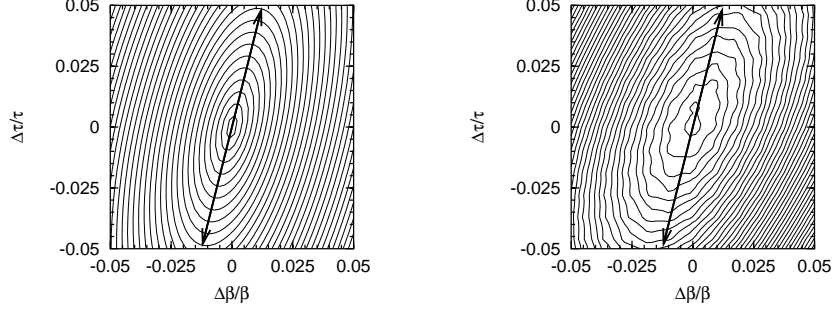


Figure 3.9. *a)* Analytical level-curve pattern in the parameter mismatch subspace of $\Delta\beta/\beta$ and $\Delta\tau/\tau$. The optimal eigendirection which induces the slowest synchronization error growth rate is indicated by the solid double-arrow. *b)* Corresponding numerical level-curve pattern. One can notice that the eigendirection obtained analytically approximately indicates the optimal direction of slowest error growth rate.

3.4.3 Multiple-parameter optimization

Here, we treat the case where all the mismatches can be tuned simultaneously. We are now looking for the optimal manifold in the 5-dimensional parameter-mismatch space which leads to the smallest synchronization error growth rate. The first step is to diagonalize \mathbf{M} as

$$\mathbf{M} = \sum_{k=1}^5 \Lambda_k \mathbf{q}_k \mathbf{q}_k^T, \quad (3.78)$$

where the Λ_k are the real and positive eigenvalues of \mathbf{M} , and the \mathbf{q}_k are the related orthonormal eigenvectors. Hence, the optimal manifold is the eigendirection corresponding to the smallest eigenvalue $\Lambda^{(-)}$, which is in fact the square of the smallest growth rate. On the other hand, the highest eigenvalue $\Lambda^{(+)}$ is related to the eigendirection leading to the strongest error growth rate.

To illustrate this approach, let us take the case of a double and *simultaneously* tunable $\Delta\beta$ and $\Delta\tau$ mismatch. The corresponding characteristic matrix is

$$\mathbf{M} = \begin{pmatrix} 1 & -K \\ -K & K \end{pmatrix}, \quad (3.79)$$

with $K = 1 - \frac{\pi}{4}$, and the corresponding eigenvalues are

$$\Lambda^{(\pm)} = \frac{1}{2} \left[1 + K \pm \sqrt{(1 + K)^2 - 4K(1 - K)} \right], \quad (3.80)$$

that is, $\Lambda^{(-)} = 0.160$ and $\Lambda^{(+)} = 1.054$. Consequently, the optimal mismatch combination geometrically corresponds to the eigendirection of $\Lambda^{(-)}$, which is

defined by

$$\frac{\Delta\tau}{\tau} = \frac{1 - \Lambda^{(-)}}{K} \frac{\Delta\beta}{\beta}. \quad (3.81)$$

This mismatch combination leads within that eigendirection to a growth rate of $\sqrt{\Lambda^{(-)}} = 0.40$, while this growth rate is 1 for pure $\Delta\beta$ mismatch (60% reduction of σ), and $\sqrt{1 - \pi/4} = 0.46$ for pure $\Delta\tau$ mismatch (14% reduction). In Fig. 3.8c we show the numerical results for the synchronization error in these three cases. Once again, a combination of mismatches improves the quality of the synchronization. In Fig. 3.9, the analytical and numerical contour lines are depicted, and illustrate the eigendirection analysis. This kind of contour-line patterns have yet been used in reference [35] in the case of the wavelength hyperchaos model. It was found numerically that the $\Delta\beta$ and $\Delta\phi$ mismatches were almost ‘‘orthogonal’’, as it is also the case for the electro-optical model considered here since $M_{23} = 0$. However, since $\Delta\beta$ and $\Delta\tau$ do precisely interact here at a quadratic approximation ($M_{25} \neq 0$), the optimal manifold is an oblique line as shown in figure 3.9

3.5 Experimental Results

For¹ the experimental verification of our theory, the electro-optical modulators were pigtailed LiNbO₃ integrated Mach-Zehnder modulators with a DC value of $V_{\pi_{DC}} = 4.0$ V, and a RF value (at 1 GHz) of $V_{\pi_{RF}} = 4.2$ V for $\lambda_0 = 1550$ nm. The Mach-Zehnder modulators had a electrical bandwidth of 10 GHz. The coherent optical feeders of these modulators were InGaAsP Distributed FeedBack (DFB) semiconductor lasers with a polarization maintaining pigtail, designed for 10 Gbits/s digital system equipments. The delay-lines were 6 meter long single-mode optical-fibers yielding an overall time delay of 30 ns. We also used a matched pair of photodetectors with a sensitivity of 2 V/mW. The amplification within the nonlinear feedback loops was performed by a pair of RF-amplifiers with a power gain of 18 dB and a bandwidth ranging from 30 kHz to 26.5 GHz.

The experimental time-traces and Fourier spectrum of the hyperchaotic carrier are depicted in Figs. 3.10a and 3.10b respectively. The bandwidth of the carrier is found to be approximately equal to 7 GHz, thereby allowing for chaos-encrypted communications at bit-rates of several gigabits per second. We have also represented in Fig. 3.10c the transfer-functions of the Mach-Zehnder modulators, and one can observe that, experimentally, they are shifted one with respect to the other by an amount of 0.7 V. This shift corresponds to the difference between the bias voltages of the 2 modulators while matching experimentally the ϕ parameter for

¹These experimental results have been obtained in collaboration with N. Gastaud and L. Larger at the Optoelectronics Laboratory of GeorgiaTech-Lorraine, Metz, France.

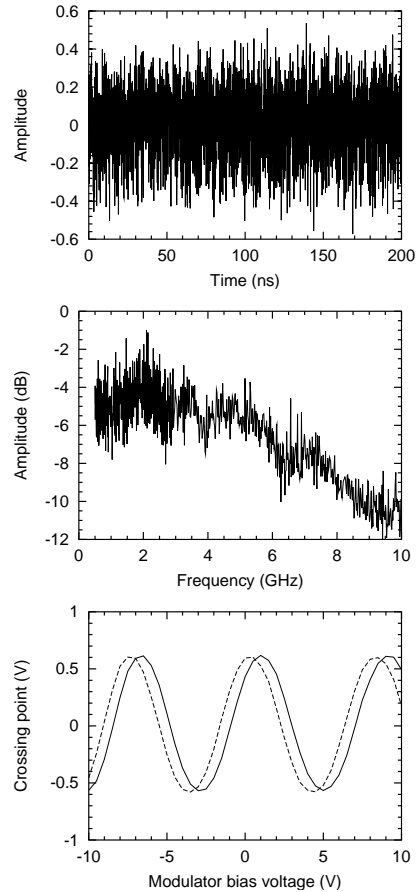


Figure 3.10. *a)* Experimental hyperchaotic carrier at large scale, with $P = 7.60$ mW and $V_B = 1.05$ V. *b)* Experimental Fourier spectrum of the hyperchaotic carrier. *c)* Experimental transfer-function curves for the Mach-Zehnder modulators. Solid line for the emitter, and dashed line for the receiver.

synchronization.

We have first studied the effect of a time-delay mismatch. For that purpose, we have varied the value of T' around T using a variable delay-line, and the results are presented in figure 3.11. It can be seen that as theoretically predicted, the receiver time-trace is shifted back and forth according to the value of ΔT . This is of great experimental importance, since in reality, the receiver should synchronize to the emitter regardless of the coupling delay (or “flying” time) T_c . Therefore, for this hyperchaotic communication scheme, all the time-delays (flying time, time delays due to the electrical connections, response times of the optoelectronic devices) play exactly the same role as the receiver time-delay.

We now focus on the parameters whose mismatch can be easily tuned in the system, namely the nonlinear feedback strength and the off-set phase. Experimentally, β' and ϕ' can be tuned through the receiver laser output power P' and the receiver modulator bias voltage V'_B respectively. To achieve our theoretical study, we

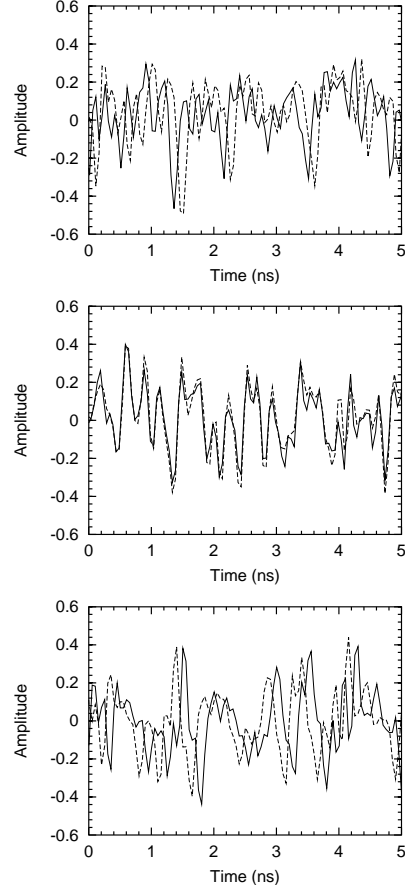


Figure 3.11. Experimental hyperchaotic timetraces, with x in continuous lines, and y in dashed lines. The parameters are $P = 7.60$ mW, $V_B = 1.05$ V (emitter), and $P' = 3.91$ mW, $V'_B = 0.34$ V (receiver) *a)* $\Delta T = 0.15$ ns, the receiver is delayed relatively to the emitter; *b)* $\Delta T = 0$, the receiver is isochronous to the emitter; *c)* $\Delta T = -0.15$ ns, the receiver anticipates the emitter.

initially set all the mismatches to 0, and then we studied their influence one by one. Experimentally, this is obviously impossible. Therefore, the experimental study is intrinsically related to the situation we analyzed in the multiple-mismatches subsection. The available electronic equipment allowed a matching accuracy down to a few percent, except for the delay which could be tuned within a $2 \cdot 10^{-3} \tau$ accuracy. Hence, we principally explored the validity of our theoretical results in the large mismatch case.

Figure 3.12a displays the variations of σ as the receiver output power P' is increased. Starting from $P' = 0$ mW (where $\sigma = 1$), the synchronization error decreases to a minimum (around $P' = 2$ mW) and then increases again. In concordance with the theory, this experimental curve follows a the square root of a quadratic form (solid line). On the other hand, Fig. 3.12b displays the variations of σ as the receiver bias voltage V'_B is varied. The measured values for σ follow the square root of a sinusoidal function in agreement with the theoretical prediction (3.70). The periodicity is given by the receiver modulator bias voltage and the

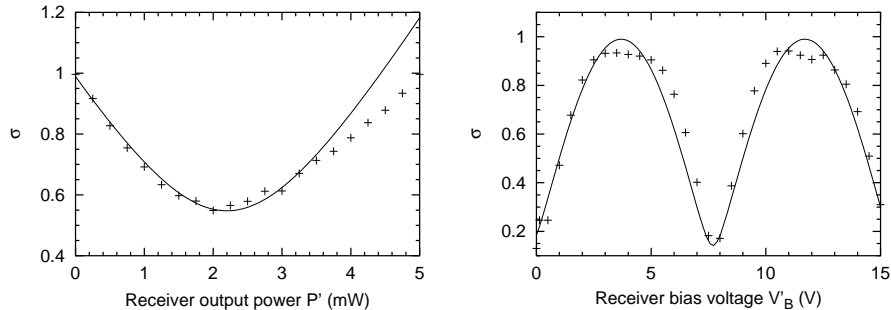


Figure 3.12. The symbols show the experimental results of the synchronization error when one parameter is changed while keeping all the others constant. *a)* Synchronization error as function of P' obtained with $P = 2.88$ mW, $V_B = 1.25$ V, $V_B' = 0.55$ V. The solid line corresponds to a function of the form $\sigma = \sqrt{a_2 P'^2 + a_1 P' + a_0}$. The parameters a_i have been fitted to adjust the results. *b)* Synchronization error as function of V_B' obtained with $P = 5.0$ mW, $P' = 2.94$ mW, $V_B = 3.49$ V. The solid line corresponds to a function of the form $\sigma = \sqrt{b_0 + b_1 \cos(\pi V_B'/V_\pi) + b_2 \sin(\pi V_B'/V_\pi)}$ predicted theoretically. The parameters b_i have been fitted to adjust the results.

minima are clearly sharper than the maxima, as theoretically predicted.

As far as the filter mismatches are concerned, it is very difficult to perform any experimental verification. The reason is that the bandwidth of the experimental system results from the combination of the various bandwidths attached to different elements of the electro-optical feedback-loop (RF-amplifiers, photodetectors, Mach-Zehnder modulator, etc...). Therefore, the bandwidth of the experimental set-up is neither tuneable nor characterized by only two time-scales. Hence, even though the fundamental features of the system are captured by the linear first-order band-pass filter, the model can to be theoretically improved at that level.

3.6 Conclusion

We have determined in this chapter the synchronization error and cross-correlation amplitudes individually associated to each parameter mismatch. In a real experiment, parameter mismatches do never appear in that isolated way, in the sense that there is always a mismatch in all the parameters at the same time. We have therefore also analyzed the situation of multiple-parameter mismatch, and we have derived for both the synchronization error and cross-correlation function a general formula taking into account the interplay between the various mismatches. It has been demonstrated that a noticeable reduction of the synchronization error can be achieved in such a multiple parameter mismatch configuration. Some numerical simulations and experimental measurements have confirmed the main statements of our analysis.

The next chapter will focus on the issue of *optical chaos cryptography*, performed with these synchronized semiconductor laser systems in the hyperchaotic regime. We will lay a particular emphasis on the bit-error rate induced by the mismatch noise which has been studied in this chapter.

Chapter 4

Optical Chaos Cryptography Using Semiconductor Laser Systems with Electro-Optical Feedback

*“We are the ninth symbol of the dwarf-
land, our secret belongs to Kaïdara, the
far away and close by Kaïdara.”*

Amadou Hampâté Bâ, Kaïdara.

4.1 Introduction

WE will address the issue of optical chaos cryptography in this chapter. We first briefly review the fundamentals of software and quantum cryptography, as well as the most archetypal encryption schemes in each case. Then, will present the optical chaos cryptosystem under study, as well as the evolution equations governing its dynamics. The mismatch noise will be analytically calculated, and its influence on the signal-to-noise ratio when a binary message is decrypted will be determined. At last, the quality of the communication scheme will be evaluated in terms of bit error-rate, and related to the signal-to-noise ratio, *i. e.*, to the mismatch noise.

4.2 Software cryptography

Most of modern telecommunication systems are only compatible with digital information, that is, strings of binary data. It is therefore understood that any analogic signal (voice, video, text, etc...) should be first digitalized before being processed

and transmitted. The purpose of software cryptography is therefore to take a digital message which has to be secretly transmitted, convolute it with a given binary pattern supposed to be known by the sender and the addressee of the message, and thereby obtain new binary string which can be safely sent in a public communication channel. If the software cryptosystem is properly designed, only the addressee - the one knowing how to deconvolute the message - can have access to the originally encrypted message.

In conformity with the conventional nomenclature of cryptography, the message to be sent is called **plaintext**, the **key** is the (secret or public) binary pattern convoluted with the message to perform the encryption, while the **ciphertext** is the binary string resulting from the encryption of the plaintext with the key. Also according to that nomenclature, the person transmitting the message is called **Alice**, the addressee of the message is called **Bob**, and any eventual eavesdropper trying to intercept the transmitted message is called **Eve**. This practical and widespread terminology will be used throughout all this chapter.

4.2.1 A secret-key cryptosystem: the Vernam cipher

The so-called **Vernam cipher** has been proposed in 1918 by the american scientist **Gilbert Vernam**¹. To illustrate its operating principle, let us consider a plaintext of length N which has to be secretly transmitted, and let us also consider another binary pattern of same length N as the binary key, which is naturally supposed to be shared only by Alice and Bob.

The Vernam encryption scheme is simply a bit-by-bit (or “bitwise”) XOR operation between the plaintext and the secret key, that is, the first bit of the plaintext is XORed with the first bit of the secret key to obtain the first bit of the ciphertext, and so on for the N bits of the plain text [36]. For example, if the plain text is $P = 1001011$ and the secret key is $K = 0101111$, then the ciphertext will be $C = P \otimes K = 1100100$, where \otimes stands for the bitwise XOR operation. The eavesdropper Eve can have access to the ciphertext C , but if she does not have the secret key K , she can by no means know what was the original message P , although as everybody, she can construct the $2^N = 2^7$ possible binary messages of length $N = 7$. On the other hand, The addressee Bob can decrypt the ciphertext and recover the originally encrypted message by simply XORing the key and the ciphertext following $D = K \otimes C$, yielding $D = 1001011$ which is exactly the original plaintext.

Despite its desarming simplicity, the Vernam cipher is up to date the unique cryptosystem proven to be absolutely unbreakable. This is why it has intensively been used in the past century, and is still indispensable nowadays when extremely

¹**Gilbert S. Vernam**, U.S. Patent 1310719: “*Secret signaling system*”, issued on July 22, 1919.

sensitive informations have to be transmitted. However, the absolute security of the Vernam cipher can be guaranteed if and only if the following conditions are strictly observed:

- **The key should be absolutely secret:** this is not an easy condition to fulfill. When for example one has to rely on somebody or on some hardware system to convey or invigilate the key, the fulfilment of this condition is seriously threatened. Therefore, guarding keys for long time in view of an future encryption threatens the safety of message transmission since they have to be kept absolutely secret during all the time. This also explains why the Vernam cipher is known as a *secret key cryptosystem*, because the unique key needed for encryption and decryption remains secret.

- **The key should be truly random:** it means that this key should not be generated by the mean of a deterministic process and that the chosen physical random generator should fulfill very hard statistical constraints.

- **The key should be as long as the message:** this is not particularly a problem, but for very long messages, generating the secret keys becomes also more lengthy and keeping them secret becomes more difficult because they do occupy a larger physical space.

- **The key should be used only once:** this means that all the efforts deployed to keep the key secret are inverted for the transmission of a single message. Since as we earlier explained it is not safe to keep unused keys for long time, this condition imposes that a new key to be generated preferentially a short time before a message encrypted with that key is sent.

These very constraining conditions are usually incompatible with the flexibility required in modern telecommunication systems. The Vernam cipher is for example not suitable for secure communications between to persons who do not know each other: for that reason, it is not suitable for e-business and digital signature. To circumvent the drawbacks of the Vernam cipher, other software cryptosystems have been developped, and the most popular of them is beyond any doubt the RSA algorithm.

4.2.2 A public-key cryptosystem: the RSA algorithm

The **RSA algorithm** was published in 1978 by **Ron Rivest, Adi Shamir** and **Len Adelman** [37]. Its safety relies the on number theory, more precisely on the difficulty to factorize large integers. The principal advantage of this algorithm is that it generates two keys, one public and one private, so that two persons who did not knew each other before can communicate securely.

The first task of the RSA algorithm is the generation of the keys. This is made in five steps

- Random generation of two large prime numbers p and q of approximately

equal size, such that their product $n = pq$ is of the required bit length, for example 512 or 1024 bits.

- Computation of $n = pq$ and $r = (p - 1)(q - 1)$.
- Random selection of a **public exponent**, which is an integer e such that $1 < e < r$ and $\text{gcd}(e, r) = 1$, where “gcd” stands for *greatest common denominator*.
- Computation of the **secret exponent**, which is an integer d such that $1 < d < r$ and $ed \equiv 1 \pmod{r}$
- The **public key** is (n, e) and the **secret key** is (n, d) , p and q should be kept secret.

To perform the encryption, Alice should first receive from Bob the public key (n, e) , which can be freely intercepted by whoever, and represent the plaintext she wants to encrypt under the form of a positive integer $m < n$. Then, she computes the ciphertext following $c = m^e \pmod{n}$ and sends it back to Bob.

To decrypt the ciphertext, Bob uses its private key (n, d) to compute $m = c^d \pmod{n}$, and thereby extracts the plaintext from its integer representative m .

At the opposite of the Vernam cipher, RSA algorithm is not unbreakable. Assuming that Eve only knows the public key, the algorithmic complexity associated to the known cracking algorithms is exponential. It is currently assumed that RSA encryption with a 512 bits key can hardly be cracked by particulars, and that even specialized cryptanalysts with up-to-date ultra-fast supercomputers can not crack a 4096 bits RSA-encrypted message. In fact, most of commercial operations in e-business are led with a key of 128 bits, which provides a more than satisfying security for that purpose.

In 1994, the american scientist **Peter Shor** published an article where he demonstrated that quantum computers could run factorization algorithms in polynomial time [38]. The Shor algorithm has even been implemented experimentally with a rudimentary prototype of quantum computer based on nuclear magnetic resonance (see ref. [102]). Since the Shor algorithm may potentially crack *any* ciphertext encrypted with a public key algorithm, there is a strong hint that the era of public key cryptosystems will one day come to an end.

4.3 Quantum cryptography

The principal problem associated with software cryptography lies in the **key distribution problem**. The Vernam cipher for example is unbreakable as long as the secret key remains secure. Since each key has to be used only one time, a quite dense traffic of key distribution between senders and receivers may be necessary, and this is obviously prejudicial to the secrecy of the keys shared thereby. Public key cryptosystems such as the RSA intend to circumvent the difficulty of secret key distribution by generating two keys (one public and one secret), relying on the

fact that recovering the secret key from the public one remains a *quasi*-untractable mathematical problem. However, here again, nothing prevents clever algorithms from crossing over this barrier.

The aim of quantum cryptography is therefore to ensure with the fundamental laws of quantum mechanics an extremely high (if not absolute) privacy for the secret key during its transmission in a public channel, being understood that this securely transmitted secret key will be later used to encrypt a message with the Vernam cipher.

4.3.1 Fundamental principles of quantum cryptography

The theoretical backbone of quantum cryptography is the **Heisenberg** uncertainty principle, which states that there exist *conjugated* pairs of physical variables related in such a way that measuring one variable prevents from simultaneously accessing the value of its conjugated counterpart. Moreover, it can be demonstrated from the same uncertainty principle that single measurement can not determine with certainty the value of a quantum variable, except when the same basis is used for both the preparation and the measurement of the quantum state. A pair of conjugated variables is also called a *conjugate basis*, and two pairs of conjugate bases are said to be *orthogonal* when the measurement of the quantum object in one base completely randomizes a subsequent measurement of the same object in the other base. In consequence, if a quantum state is prepared (produced) in a given base

- On the one hand, it can further be accurately be measured in a second base *identical* to the first one.
- On the other, its information content is completely lost if it is further measured in a second base *orthogonal* to the first one.

The principle of quantum cryptography is therefore the following.

Alice and Bob will randomly communicate with two orthogonal conjugate bases $B_1 = (p_1, q_1)$ and $B_2 = (p_2, q_2)$. In each base, the bits 1 and 0 can be represented by the two conjugated variables p and q constituting the base. For example, it can be conventionally agreed that the state p corresponds to the bit 0 and q to the bit 1. Hence, Alice encodes a random binary string, using randomly either the basis B_1 or B_2 . Bob also detects the quantum binary string, randomly using either the basis B_1 or B_2 . At the end of the transmission, they publicly discuss the sequence of basis they have used during the key transfer process: Alice indicates the basis she used to encode the bits, and Bob keeps the bits for which he had used the correct base for detection (for example, Alice sent a bit with B_2 and he also detected it with B_2), while he discards the bits for which he had used the wrong base (for example, Alice used B_2 while he used B_1). Since they openly only discuss the basis they have used *and not* the quantum states (bits) that have been transferred, there is no risk of information leaking. They can also use some error correcting

codes (sequential parity checking, etc...) to skip out eventual errors induced by noise and uncontrollable perturbations.

Let us now consider that the eavesdropper Eve is tapping the line.

If she tries to sample and read the quantum information flowing into the communication channel, she will unavoidably – according to the Heisenberg uncertainty principle – modify its properties, and such a modification will be easily detected by Bob.

If she rather tries to intercept (and then, destroy) the flowing quantum information, read its content and retransmit a reconstructed clone, her presence will be discovered at the public discussion stage between Alice and Bob, because Eve would retransmit the quantum information without knowing the basis initially used by Alice. Hence, a disagreement in the basis choices between Alice and Eve will help to point out the presence of an intruder.

Several modifications may be brought to this schematical description, but more or less, the fundamental principle remains the same. In actual implementations of quantum cryptography prototypes, the quantum information vectors are photons circulating in optical fibers or travelling in free-space, and the conjugates basis B_1 and B_2 are generally orthogonal pairs of polarization states. We hereafter present one of the most important quantum cryptography protocol, the BB84 protocol.

4.3.2 The BB84 protocol

Charles Bennett and **Gilles Brassard** published in 1984 the first article where a quantum key distribution protocol was described [39]. The **BB84** (named after its authors) which enables to send securely bits encoded with the polarization quantum states of photons operates as follows.

As explained earlier, Alice and Bob are equipped with two bases B_1 and B_2 each. Here, the base B_1 is the rectilinear “ $0^\circ/90^\circ$ ” (or “+”) base that can emit \uparrow or \rightarrow polarized photons. The base B_2 is the diagonal “ $45^\circ/135^\circ$ ” (or “ \times ”) base that can emit \nearrow or \nwarrow polarized photons. Emitting photons polarized in a given direction may be easily realized by forcing them to pass through a suitably oriented polarizer. The bases B_1 and B_2 are orthogonal because a photon prepared in the + base may be polarized following \uparrow or \rightarrow , and if it is further measured with a \times polarizer, it will randomly choose *with equal probability* either the \nearrow or the \nwarrow polarization direction.

Hence, using the bases + and \times , Alice begins to send randomly \nearrow , \nwarrow , \uparrow and \rightarrow polarized photons, whereas Bob measures them also choosing randomly one of bases + and \times . Since both Alice and Bob communicate randomly, the bases they sequentially choose may match or not. When they match Bob accurately determines the polarization state of the photon, and when they do not match, Bob

does not know if its measure is correct or not. For example, if Alice sends a \uparrow photon and Bob measures it with its $+$ polarizer, he will correctly deduce that Alice had sent a \uparrow photon, but if he uses its \times polarizer, he will on one hand wrongly deduce that Alice had sent either a \nearrow or a \nwarrow photon, and on the other hand his measurement would have irreversibly destroyed the original \uparrow polarization state of the photon sent by Alice.

As explained earlier, the security provided by this protocol lies in the fundamental laws of quantum mechanics. The first important point is that a single photon can not be divided, and using one photon per bit prevents against the possibility that Eve might use a partially reflective mirror to sample the optical signal and extract her own copy of the bits. The second important point is that the non-destructive measure of these “single bit” photons is impossible. At last, the random change of bases also impedes to Eve to intercept the photons, read them and send new ones to Bob.

Quantum cryptography has yet reached the stage of reliable field applications and there are even some commercially available quantum cryptosystem [103].

4.4 Principles of optical chaos cryptography

4.4.1 Chaos cryptography

The purpose of chaos cryptography is quite simple: to use the apparently random oscillations of a chaotic system to hide a message [40, 104]. Encryption therefore relies on the **unpredictability** of chaotic systems, in the sense that it is achieved through the mixing of a small information-bearing signal with the noise-like output of a chaotic emitter. On the other hand, decryption relies on the **determinism** of chaos materialized by the possibility of chaos synchronization: effectively, a chaotic receiver initially synchronized with the emitter can recognize the chaotic component of the incoming carrier and extract it to reveal the originally encrypted message. Such an operation - recognition and separation of a chaotic (and deterministic) component in a composite signal - is called **chaos-pass filtering**.

The security attached to chaos cryptography therefore relies on two important points:

- **In case of software attack:** the size of information-bearing signal is very small relatively to one of the masking chaotic carrier, whose complex and random waveform is expected to provide a satisfying “protecting screen”. Since the time needed to run attractor-reconstruction algorithms increases exponentially with the size of the chaotic attractor, software attacks based on time-series analysis may become inefficient in optimal conditions (very small amplitude message, very complex chaotic attractor).

• **In case of hardware attack:** the decryption of the message is possible only when the emitter and receiver systems are almost perfectly identical: if it is not the case, synchronization does not occur and chaos-pass filtering becomes inoperant. It is expected that an eventual eavesdropper trying to build a chaotic receiver identical to the emitter would have to face this **parameter mismatch problem**, which impedes a proper extraction of the encrypted message.

These two aspects therefore have to be kept in mind when a security evaluation is to be performed.

As earlier noticed, the first experimental chaos cryptosystem was built-up in 1993 by Cuomo and Oppenheim, as they succeeded to show with a Lorenz-like chaotic electrical circuit that information (audio-signals) could be encrypted and decrypted through synchronization and chaos-pass filtering. However, the bandwidth of this cryptosystem was inherently limited by its electronic nature (few kHz), but this successful experience was a breakthrough suggesting that with optical systems, the bandwidth available for information transmission could be increased to few gigahertz, and therefore interesting for fiber-optic communications.

4.4.2 Cryptography in optical fiber networks

An ever increasing proportion of information in modern telecommunication systems is vehicled by optical fibers networks. Emitters in these networks are semiconductor lasers emitting in the infrared range of the electromagnetic spectrum. In general, information is encoded in the laser light through a modulation process, which can be internal (modulation of the pumping current) or external (modulating the output laser light).

Therefore, as earlier emphasized, performing chaos encryption in such networks requires synchronized semiconductor lasers emitting in a chaotic regime. Naturally, this encryption technique in consequence performed at the physical layer of the network architecture [40]. It also requires a modulation scheme which can allow a small-amplitude signal to imperceptibly modify a physical property of the hyperchaotic carrier. A wide variety of such cryptosystems has yet been proposed, and here we will lay an emphasis upon an encryption scheme which relies on semiconductor laser systems with electro-optical feedback.

4.4.3 The problem of mismatch noise in chaos cryptosystems

A key issue in optical chaos communication schemes [40] is to quantify the detrimental influence of parameter mismatch on the quality of the decrypted message, since the little discrepancies between the emitter and receiver systems parameters unavoidably give rise to sustained deviations from the perfect synchronization manifold. In the temporal domain, the related parasite oscillations correspond to

the instantaneous synchronization error, and they are sometimes referred to as **mismatch noise**.

An important characteristic of the mismatch noise is that *it is not* a random noise: it is rather a **chaotic noise**, that is, deterministic, even though unpredictable. Generally, this chaotic noise may be divided into three main contributions. The first one is the **deviation chaotic noise**, which is equal to zero when the emitter and the receiver are identical, and whose amplitude generally grows proportionally to the mismatch [31, 105]. The second contribution is the **bursting chaotic noise**, whose origin relies on the local unstable invariant sets eventually embedded within the globally stable synchronization manifold [106]. Although this bursting noise vanishes for perfect matching, it increases drastically with the amplitude of the mismatches, and it can be quite significant even in case of quasi-perfect matching. These two contributions are independent of any message insertion: the first one is associated to system matching accuracy while the second one is associated to synchronization robustness. The third and last contribution, to which few attention has been paid in the literature, is the **nonlinear mixing chaotic noise** and it is directly related to the encryption/decryption process. It arises when the chaotic carrier nonlinearly mixes the former two mismatch noise contributions with the message. Consequently, studying the influence of parameter mismatch in a chaos communication scheme requires to take into account five key features: the system itself, the amplitude of the various mismatches, the type of coupling between emitter and receiver, the characteristics of the message, and at last, the encryption/decryption process.

4.4.4 The optical chaos cryptosystem under study

The electro-optical laser chaos communication scheme under study has been represented in Fig. 4.1. This system has been for the first time proposed in ref. [107], and it corresponds to a significant improvement of the set-up reported in ref. [49].

The chaotic emitter consists in a closed electro-optical feedback loop whose main components are:

- A LiNbO₃ 12.5 Gb/s integrated electro-optic Mach-Zehnder (MZ) modulator, RF-modulated by a large amplitude voltage $V(t)$ to ensure a strong nonlinear dynamical operation of the electro-optic interferometer.
- A continuous-wave (CW) semiconductor laser operating at 1550 nm and serving as the light source feeding the Mach-Zehnder, whose constant optical power P is modulated as $P \cos^2[\pi V(t)/(2V_{\pi_{RF}}) + \pi V_B/(2V_{\pi_{DC}})]$.
- A second semiconductor laser with a close wavelength, which is directly modulated by the digital message to be hidden in the chaotic carrier. The bits 0 are assumed to correspond to a null optical power, and the bits 1 have an optical power αP . The parameter α can be considered as a measure of the masking efficiency of the message within the chaotic carrier. The binary message

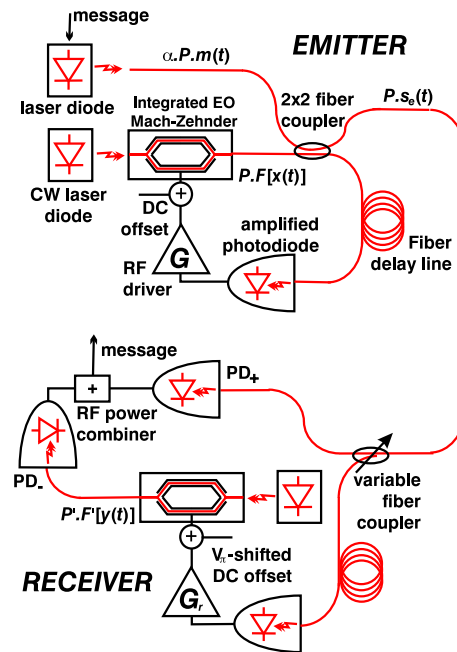


Figure 4.1: The experimental set-up of the cryptosystem.

light beam can thus be written $\alpha Pm(t)$, where $m(t) = 0$ or 1 .

- A “ 2×2 ” 50/50 fiber coupler serving as an all-optical mean for mixing the message within the chaos. The chaos and the message optical beams are assumed to be added in intensity, *i.e.*, without interfering one with each other. This can be ensured for example by properly adjusting orthogonal relative polarizations of the two beams in the fiber coupler; note that a fast polarization scrambler should be used before transmission of the chaos + message light beam, to prevent from eavesdropping through polarization separation. One output of the fiber coupler is used to transmit the chaos encoded light beam to the receiver, while the other output serves as a feedback signal in the emitter for the generation of the chaotic oscillations.

- An amplified photodiode detects the feedback chaos + message light beam, and converts it into an electrical signal with a sensitivity S .

- A RF-amplifier with a gain G is finally used to close the chaotic oscillation loop, applying the previous electrical signal to the RF-electrode of the Mach-Zehnder.

Practical values of the bifurcation parameter β varies between 5 and 10, thus allowing the hyperchaotic regimes required for encryption. These gain values are required for a high amplitude of the electro-optic modulation voltage, thus allow-

ing a highly nonlinear dynamical operation of the Mach-Zehnder interferometer; typically 2 to 3 constructive and destructive interference conditions are scanned dynamically, since $V(t) \gg V_{\pi_{RF}}$.

The integro-differential delay equation ruling the emitter dynamics is thus written as

$$x + \tau \dot{x} + \frac{1}{\theta} \int_{t_0}^t x(s) ds = \beta \{ \cos^2[x(t - T) + \phi] + \alpha m(t - T) \}, \quad (4.1)$$

where parameters are the same meaning as in Eq. (3.2). The inloop addition of the message might change significantly the chaotic oscillations with respect to the free message chaotic oscillations, depending on the actual masking efficiency α used to tune the relative weight of the message compared to the chaos.

The receiver is constructed similarly to the emitter, except it is organized in an open-loop architecture. The received optical signal is splitted first into two branches using a variable fiber-coupler. One output of the coupler is directly detected by a fast photodiode, thus giving an electrical signal $K[\cos^2(x(t - T) + \phi) + \alpha m(t)]$, where K is a detection factor depending on the receiver optical splitting ratio, and on the fast photodiode sensitivity. The other coupler output is processed in a similar way than that at the emitter after the feedback output of the 50/50 fiber coupler, in order to provide at the receiver a replicated optical chaos $K' \cos^2[y(t - T') + \phi']$, with:

$$y + \tau' \dot{y} + \frac{1}{\theta'} \int_{t_0}^t y(s) ds = \beta' \{ \cos^2[x(t - T') + \phi'] + \alpha m(t - T') \}, \quad (4.2)$$

where the parameters are the same as in Eq. (3.3). Here, K' is determined by the continuous-wave laser power feeding the receiver Mach-Zehnder, and by the photodiode sensitivity involved for the detection of the receiver Mach-Zehnder output signal. The electrical outputs of the two receiver branches are added using a wide-band power combiner.

The message is practically retrieved if a chaos cancellation can be performed in the RF power combiner, which is achieved when a proper bias is applied to the receiver MZ; the parameter ϕ' has to be adjusted such that $\cos^2 \phi = 1 - \cos^2 \phi'$, *i.e.*, $\phi' = \phi \pm \pi/2$. Hence, the condition $x(t) = -y(t)$ is obtained in case of perfect matching, so that decryption relies on the phenomenon of **anti-synchronization** which has yet been evidenced in the system in Chapter 3.

As before, we therefore have 5 control parameters: the time delay T , the nonlinear feedback strength β , the off-set phase ϕ , the low cut-off response time θ ,

and the high cut-off response time τ . As usual, the primes indicate the receiver parameters, which are in practice always slightly different from the emitter ones.

4.5 Performances of the electro-optical laser chaos cryptosystem

4.5.1 Determination of the Signal-to-Noise Ratio

The message to be encrypted in this optical chaos communication scheme is a non-return-to-zero (NRZ) polar sequence of bits at a fixed bit-rate B . The two possible discrete values of this binary signal are 0 for a bit 0, and $K\alpha = \mu C$ for a bit 1, where $C^2 = \langle x^2(t) \rangle$ is the quadratic average amplitude of the carrier, and the proportionality coefficient μ is the *Signal-to-Carrier Ratio* (SCR).

The instantaneous decrypted signal at the receiver can be obtained from Eqs. (4.1) and (4.2) following

$$\begin{aligned} s(t) &= K[\cos^2(x_T + \phi) + \alpha m(t)] + K' \cos^2(y_{T'} + \phi') \\ &= \frac{K + K'}{2} + \mu C m(t) + n(t) \end{aligned} \quad (4.3)$$

where

$$n(t) = \frac{1}{2}K \cos(2x_T + 2\phi) + \frac{1}{2}K' \cos(2y_{T'} + 2\phi') \quad (4.4)$$

is the mismatch noise. It is important to notice that in the set-up, the mismatch noise $n(t)$ is *different* from the synchronization error $\epsilon(t) = x(t) - y(t)$, even though $n(t)$ does [like $\epsilon(t)$] uniformly vanish to zero in case of perfect matching.

In the small mismatch approximation, the mismatch noise $n(t)$ can be approximated as

$$n(t) = \frac{1}{2}K[\epsilon(t) + \Delta\phi] \sin(2x_T + 2\phi) - \frac{1}{2}\Delta K \cos(2y_{T'} + 2\phi') \quad (4.5)$$

where $\Delta p = p' - p$ stands for the mismatch related to a given parameter p . From the above equation, the root-mean-square (*rms*) amplitude of $n(t)$ can also be approximated as

$$\begin{aligned} \langle n^2 \rangle &= \frac{1}{4}K[\langle \epsilon^2 \rangle + (\Delta\phi)^2] + \frac{1}{4}(\Delta K)^2 \\ &= \eta^2 C^2 \end{aligned} \quad (4.6)$$

where η is the amplitude of the mismatch noise relatively to the *rms* amplitude C of the hyperchaotic carrier. We have shown in the precedent chapter that for small

mismatch, $\langle \epsilon^2 \rangle = \sigma^2 C^2$ with

$$\begin{aligned} \sigma^2 = & \frac{1}{3} \left(\frac{\Delta T}{\tau} \right)^2 + \left(\frac{\Delta \beta}{\beta} \right)^2 + 4(\Delta \phi)^2 \\ & + \left(1 - \frac{\pi}{4} \right) \left(\frac{\Delta \tau}{\tau} \right)^2 + 2(1 - \ln(2)) \Delta \phi \frac{\Delta T}{\tau} \\ & - 2 \left(1 - \frac{\pi}{4} \right) \frac{\Delta \beta}{\beta} \frac{\Delta \tau}{\tau} - 2 \left(1 - \frac{\pi}{4} \right) \frac{\Delta T}{\tau} \frac{\Delta \tau}{\tau}, \end{aligned} \quad (4.7)$$

so that the *rms* amplitude η of the mismatch noise can completely be determined analytically with Eqs. (4.6) and (4.7). It appears that for the physical understanding of the various features of the system, all amplitudes (namely μ , η , and σ) should be expressed relatively to the *rms* amplitude C of the hyperchaotic carrier. Therefore, we will state that the mismatch noise η (or the signal-to-chaos ratio μ) has an amplitude of 1% if its amplitude is one hundred times smaller than the C , namely if $\eta = 0.01$.

From Eq. (4.3), we can consider that the convenient SNR is the *peak-to-peak signal to rms mismatch noise ratio* following

$$\text{SNR} = \frac{K\alpha}{\sqrt{\langle n^2 \rangle}} = \frac{\mu}{\eta} \quad (4.8)$$

Some important remarks can be made at this point. The first one is that there is no bursting mismatch noise contribution in this electro-optical communication scheme. The reason of this absence is that the receiver is a linear oscillator externally excited by a chaotic carrier. Therefore, the synchronization manifold is *unconditionally* and *uniformly* stable. Consequently, neither the signal nor the mismatch noise can destabilize the receiver. The second remark is that encryption/decryption process we are using does not introduce any nonlinear mixing of the message with the mismatch noise: it only adds them *linearly*, even though the message is still nonlinearly mixed with the hyperchaotic carrier. This is a key-property that allows for an analytical definition of the SNR. Note that Eq. (4.3) implicitly assumes that the mismatch noise σ with or without message remains the same. An interesting advantage of this configuration is that the SNR is *independent* of the bit-rate of the encrypted message, so that the full bandwidth of the hyperchaotic carrier can be exploited. In the general case where a significant amount of mismatch noise is induced by the nonlinear mixing, the SNR can not be determined as straightforwardly as we did, because of the strong correlation between the noise and the message, and moreover, severe limitation of bit rate is generally observed in these cases. Therefore, this encryption scheme can be considered as optimal in the sense that only one type of mismatch noise (on the three possible) is present in the communication channel.

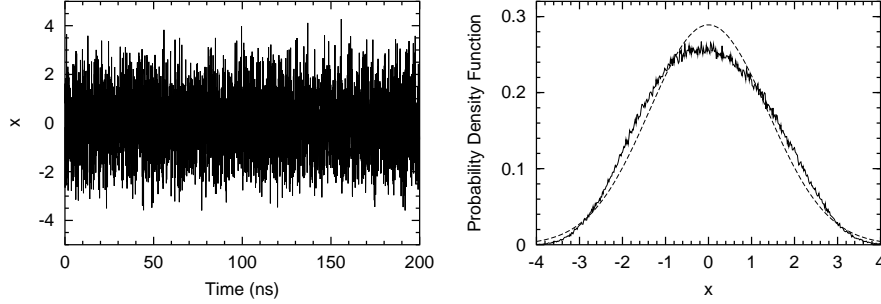


Figure 4.2. Numerical simulations of hyperchaotic carrier and its PDF (solid line). The Gaussian counterpart of the PDF has also represented (dashed line) for comparison. The parameters used for the simulation are $\beta = 10$, $\phi = 0.1$, $T = 40$ ns, $\theta = 5$ μ s, and $\tau = 25$ ps. This set of parameters is compatible with the experimental ones, and it will be used throughout all the chapter.

4.5.2 Determination of the Bit Error-Rate

We now use the previous results to calculate analytically the BER [98]. Generally, each bit is evaluated at a sampling time t_s chosen at half of the bit period. Since the binary message is a NRZ polar sequence of bits relatively to its mean value $\mu C/2$ (which is cancelled together with $(K + K')/2$ in the process of decryption), the digital level-decision system considers that an incoming bit is a 1 if $s(t_s) > 0$ and is a 0 otherwise. A bit 1 is mistaken as a 0 when $n(t_s) < -\frac{1}{2}\mu C$, so that $s(t_s) < 0$. Similarly, a bit 0 is mistaken as a 1 when $n(t_s) > \frac{1}{2}\mu C$. Since a 0 precludes a 1 appearing (and vice-versa), and since both of them have an $\frac{1}{2}$ probability of appearance, the BER may be evaluated as the relative sum of the mistaken bits 1 and 0 following

$$\text{BER} = \frac{1}{2}\text{Prob} \left[n(t_s) < -\frac{\mu C}{2} \right] + \frac{1}{2}\text{Prob} \left[n(t_s) > \frac{\mu C}{2} \right]. \quad (4.9)$$

These probabilities can be evaluated from the probability density function (PDF) of the channel noise $f_n(x)$. It is convenient to scale this PDF with its variance η as

$$\tilde{f}_n(x) = \frac{1}{\eta} f_n \left(\frac{x - \nu}{\eta} \right) \quad (4.10)$$

where ν is the center value of f_n . The scaled PDF has exactly the same shape as the original PDF but with zero mean value and variance 1. Throughout all the chapter, the tilde over a PDF will denote such scaling. From Eqs. (4.8), (4.9), and

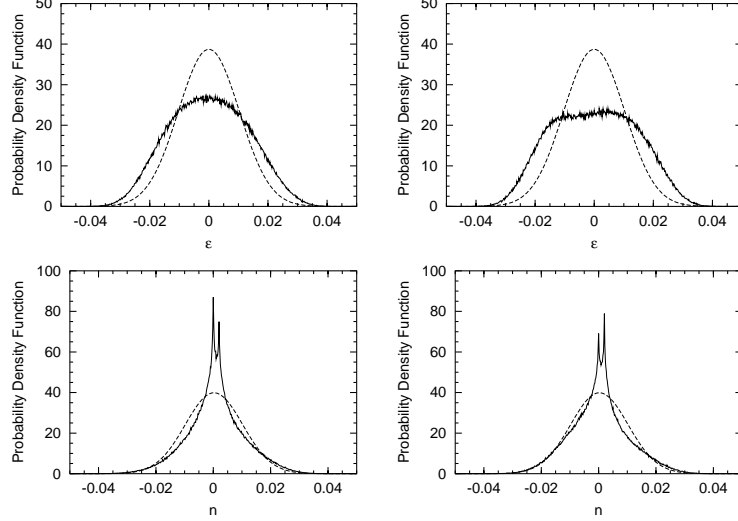


Figure 4.3. PDFs for the synchronization error and for the mismatch noise. The upper row corresponds to the PDF of the synchronization error $\epsilon(t)$, while the lower row corresponds to the PDF of the mismatch noise $n(t)$. The left column corresponds to the PDFs for simultaneous $\Delta\beta/\beta = 0.005$ and $\Delta\phi = 0.004$ mismatches (tuneable mismatches), while the right column corresponds to the PDFs for simultaneous $\Delta\theta/\theta = 0.02$ and $\Delta\tau/\tau = 0.015$ mismatches (filter mismatches). In all cases, a photodetector mismatch of $\Delta K/K = -0.002$ has been considered (with $K = 1.0$). The Gaussian counterparts have also been represented in dashed lines.

(4.10), it can therefore be deduced that

$$\begin{aligned}
 \text{BER} &= \frac{1}{2} \int_{-\infty}^{-\frac{1}{2} \frac{\mu}{\eta}} \tilde{f}_n(u) du + \frac{1}{2} \int_{+\frac{1}{2} \frac{\mu}{\eta}}^{+\infty} \tilde{f}_n(u) du \\
 &= \frac{1}{2} \left[1 - \int_{-\frac{\text{SNR}}{2}}^{+\frac{\text{SNR}}{2}} \tilde{f}_n(u) du \right]. \tag{4.11}
 \end{aligned}$$

The key-issue is therefore the determination of the PDF \tilde{f}_n of the mismatch noise.

It can be seen in Fig. 4.2a, the variable $x(t)$ displays an hyperchaotic behavior when the nonlinear feedback gain parameter β is high enough, as it is usual for that kind of delayed systems [100, 101]. The corresponding PDF is almost Gaussian (see Fig. 4.2b), and the main qualitative difference between both is that unlike the Gaussian PDF, the PDF of $x(t)$ does naturally not have infinite tails. Therefore, it can be considered with a good approximation that the scaled PDF of the carrier is

very close to its Gaussian counterpart

$$\tilde{f}_{\text{gau}}(u) = \frac{1}{\sqrt{2\pi}} e^{-\frac{1}{2}u^2}. \quad (4.12)$$

In Fig. 4.3, the PDFs of the synchronization error $\epsilon(t)$ and of the mismatch noise $n(t)$ have been depicted for various kind of mismatches. We have divided the mismatched parameters into two groups: the so-called “**tuneable mismatches**” corresponding to β and ϕ on one hand, and the “**filter mismatches**” corresponding to the response-times θ and τ on the other. We have set ΔT to 0 because the delay-time parameter T can be matched with a relatively high precision at the experimental level. For the synchronization error, the PDF still present a smooth bell-shaped form, even though the maximum is significantly lower than the one of their Gaussian counterpart. On the other hand, for the mismatch noise, one can notice that a better quantitative similitude is observed with the Gaussian, but qualitatively important differences are observed. For example, the PDFs of the mismatch noise are peaky (the two peaks correspond to the two contributions in Eq. (4.5)), and the convexity of the two curves is not always the same.

A measure of non-Gaussianity: the Gram-Charlier expansion

The above analysis indicates that an analytical tool is needed for the comparison of these PDFs relatively to the “reference” Gaussian PDF. The best tool to investigate the effect of the non-Gaussianity of a PDF is the **Gram-Charlier** (GC) expansion [99]. Any scaled PDF can be expressed as a function of a Gaussian and its derivatives following the infinite series

$$\tilde{f}(u) = \tilde{g}(u) + \sum_{k=3}^{+\infty} a_k \tilde{g}^{(k)}(u), \quad (4.13)$$

with $\tilde{g} \equiv \tilde{f}_{\text{gau}}$. Knowing that

$$\tilde{g}^{(k)}(u) = (-1)^k \text{He}_k(u) \tilde{g}(u), \quad (4.14)$$

the Gram-Charlier coefficients a_k can be recovered through

$$a_k = \frac{(-1)^k}{k!} \int_{-\infty}^{+\infty} \text{He}_k(u) \tilde{f}(u) du, \quad (4.15)$$

where He_k are Hermite polynomials. From a purely mathematical point of view, Eq. (4.15) enables to recover the a_k coefficients owing to the orthogonality of Hermite polynomials, as well as Fourier coefficients are recovered owing to the

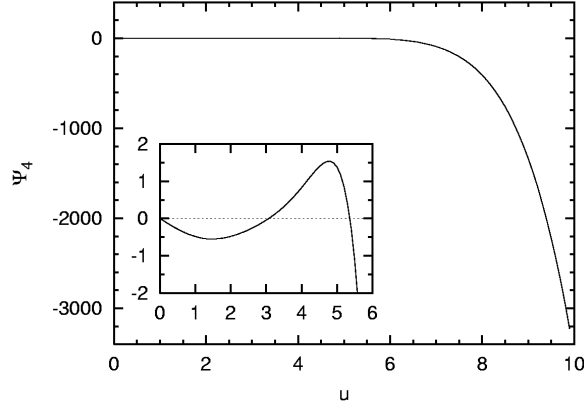


Figure 4.4. Representation of the function Ψ_4 . The inset shows a zoom-in for an argument between 0 and 6.

orthogonality of trigonometric functions. In the Gram-Charlier formalism, any PDF is fully characterized by its a_k coefficients which are uniformly equal to zero in case of a Gaussian PDF.

Using both Eqs. (4.11) and (4.13), the BER for a non-gaussian mismatch noise can therefore be evaluated as a function of its GC coefficients following

$$\text{BER} = \text{BER}_{\text{gau}}(\text{SNR}) + \sum_{k=3}^{+\infty} a_k \Psi_k(\text{SNR}), \quad (4.16)$$

where

$$\text{BER}_{\text{gau}}(u) = \frac{1}{2} \text{erfc} \left(\frac{u}{2\sqrt{2}} \right) \quad (4.17)$$

is the BER corresponding to a purely gaussian noise, and

$$\Psi_k(u) = (-1)^{k+1} 2^{\frac{k-3}{2}} u \frac{\Phi \left[\frac{k+1}{2}, \frac{3}{2}; -\left(\frac{u}{2\sqrt{2}} \right)^2 \right]}{\Gamma \left[\frac{1-k}{2} \right]} \quad (4.18)$$

is the k -th correction of the Gaussian BER, which has to be weighted with the GC coefficient a_k . It may be interesting to note that the three special functions involved in these equations. It may be interesting to note that the *complementary error function* erfc , the *confluent hypergeometric function* Φ and the *complete Gamma function* Γ (see ref. [108] for contextual definitions) appear quite frequently when the BER has to be evaluated analytically in optical or microwave communication systems [109–111].

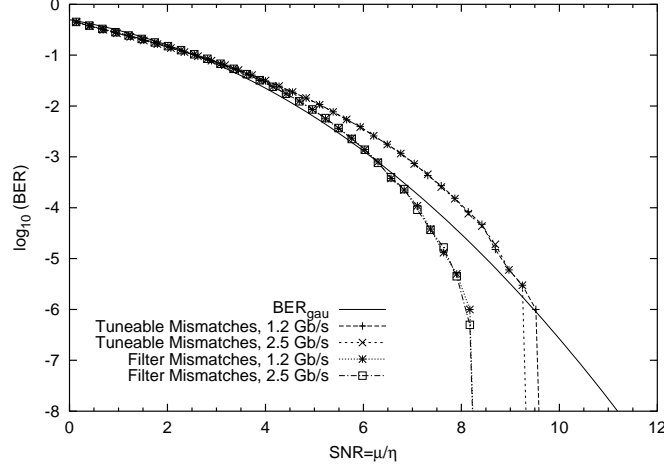


Figure 4.5. Numerical simulation for the dependence of the BER with the SNR. Symbols correspond to numerical integration of Eqs. (4.1) and (4.2) with a binary message of $2^{20} \sim 10^6$ bits. Tuneable and Filter mismatches are considered as in Fig. 4.3.

4.5.3 Influence of the non-Gaussianity of the chaotic mismatch noise

According to Eq. (4.15), the GC coefficients rapidly decrease to zero as k is increased, so that high-order coefficients have less relevance. Hence, only the first coefficients should be considered in first approximation for the analytical BER evaluation. Let us consider the first odd (a_3) and the first even (a_4) GC coefficients. Typically, a_3 describes the asymmetry relatively to the central-value, and it is considered that noticeable asymmetry is observed when $|a_3| > 0.1$, while $|a_3| > 0.3$ corresponds to an extreme asymmetry. On the other hand, a_4 describes the decay to zero of the PDF's tails at infinity, in the sense that $a_4 < 0$ denotes a fast decay to 0 while $a_4 > 0$ indicate a slow decay to 0.

It can be demonstrated that $\Psi_k(u)$ is uniformly equal to zero when k is odd, so that only the even GC coefficients are involved in the BER evaluation at this precision: in particular, the first corrective term relatively to the Gaussian BER-law will be $a_4\Psi_4(\text{SNR})$. For the mismatch noise $n(t)$, numerical simulations indicate that $a_4 \sim 10^{-3} > 0$, in conformity with Figs. 4.3c and 4.3d where it can be seen that the PDFs decay slower than the Gaussian to zero. To evaluate the BER correction, we have also computed the function $\Psi_4(u)$ in Fig. 4.4. One can notice that in terms of order of magnitude, no significant deviation relatively to the Gaussian BER-law should be expected for $\text{SNR} < 6$. More precisely, let us consider the correction term $a_4\Psi_4(\text{SNR})$. According to the inset of Fig. 4.4, the BER in the system should be slightly smaller than BER_{gau} for $\text{SNR} < 3$, slightly greater than BER_{gau} for $3 < \text{SNR} < 5.5$, while drastic changes are to be expected for

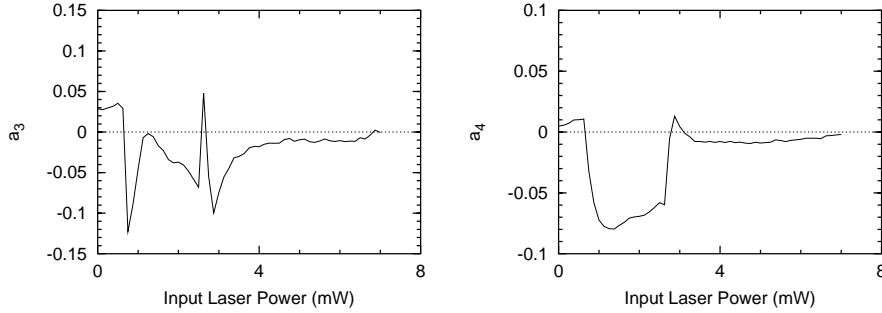


Figure 4.6. Experimental evolution of the first odd (a_3) and first even (a_4) Gram-Charlier coefficients when the power P of the emitter feeder semiconductor laser is continuously increased from 0 to 7 mW. Note the convergence to 0 as P is increased.

$\text{SNR} > 6$. In fact, this drastic change is a “**threshold effect**”: since the PDF of the noise has finite tails (unlike the Gaussian PDF), there is a limit of the SNR above which the *mismatch-induced* BER drops to 0 according to Eq. (4.11).

4.5.4 Numerical simulations

Numerical simulations completely support the above analysis. In Fig. 4.5, we have numerically evaluated the BER as a function of the SNR for different configurations, varying the bit-rate and the origin of the mismatch. Two bit-rates we have considered, the OC-24 standard bit-rate of 1.2 Gb/s, and the OC-48 standard of 2.5 Gb/s (more precisely, and as used in both numerical simulations and experiments, they respectively correspond to bit-rates of 1.24416 and 2.48832 Gb/s). As earlier mentioned, we have divided the mismatched parameters into two groups, the tuneable mismatches corresponding to β and ϕ on one hand, and the filter mismatches corresponding to the response-times θ and τ on the other. For comparison purposes, we have also plotted the theoretical BER_{gau} corresponding to a Gaussian PDF.

In conformity with our theoretical analysis, the BER is practically independent of the bit-rate, and it does only weakly depend on the origin of the mismatch. As the SNR is increased, the qualitative behavior predicted from the $a_4\Psi_4(\text{SNR})$ corrective term is effectively observed: from a quantitative point of view, there is no significant difference between the BER computed numerically and the theoretical BER_{gau} . Qualitatively, the features predicted analytically are numerically recovered: one can effectively notice that the simulated BER is slightly lower than BER_{gau} when $\text{SNR} < 3$, and then turns to be slightly higher than BER_{gau} until the occurrence of the threshold effect. However, in a realistic situation, even though the mismatch-induced BER may drastically decrease, other sources of BER like

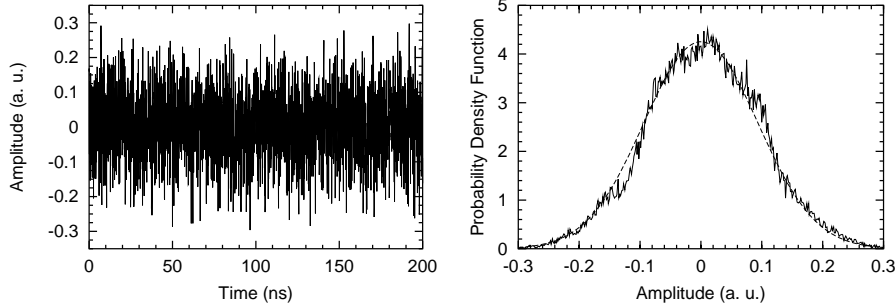


Figure 4.7. Experimental timetrace of the hyperchaotic carrier, and its related PDF (without scaling), for a feeder laser power of $P = 7$ mW. The Gaussian PDF has also been represented in dashed line to facilitate the comparison.

random noise or fiber distortions (induced by chromatic dispersion and nonlinearities) may become increasingly important for such high SNR values.

4.6 Experimental Results

In² the experimental set-up, the electro-optical modulators were pigtailed LiNbO₃ integrated Mach-Zehnder modulators with a DC value of $V_{\pi_{DC}} = 4.0$ V, and a RF value (at 1 GHz) of $V_{\pi_{RF}} = 4.2$ V for $\lambda = 1550$ nm. The coherent optical feeders of these modulators were InGaAsP Distributed FeedBack (DFB) semiconductor lasers with a polarization maintaining pigtail, designed for 10 Gb/s digital system equipments. The delay-lines were 7 meter long single-mode optical-fibers yielding an overall time delay of 40 ns (taking into account the signal speed reduction in electrical connections). We also used a matched pair of photodetectors with a gain of 2 V/mW. The amplification within the nonlinear feedback loops was performed by a pair of RF-amplifiers with a power gain of 18 dB and a bandwidth ranging from 30 kHz to 12 GHz.

Figure 4.6 shows the experimental evolution of the Gram-Charlier coefficients when the power of the emitter feeder laser P is continuously increased (note that it corresponds to an increase of β). We have only plotted the first odd (a_3) and first even (a_4) GC coefficients. It can be observed that for low input power, $|a_3|$ may reach at specific points a noticeable asymmetry, while a_4 clearly indicates a PDF structure which is quite far from a Gaussian. The system undergoes a bifurcation around $P = 3$ mW after which the PDF converges to a Gaussian (a_3 and a_4 both converge to 0). It is also confirmed that the quality of the decryption does practically not depend on the bit rate.

²These experimental results have been obtained in collaboration with N. Gastaud and L. Larger at the Optoelectronics Laboratory of GeorgiaTech-Lorraine, Metz, France.

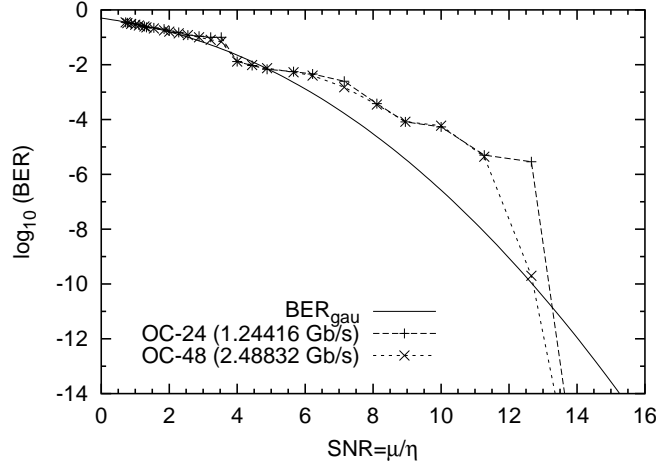


Figure 4.8. Experimental variations of the of the BER at the standard bit-rates of OC-24 (1.24416 Gb/s) and OC-48 (2.48832 Gb/s). The experimental parameters for the OC-24 curve are $P = 5$ mW, $V_B = 0.34$ V, $P' = 2.88$ mW and $V'_B = 3.42$ V. Those of the OC-48 curve are $P = 5$ mW, $V_B = 3.38$ V, $P' = 2.97$ mW and $V'_B = 7.20$ V.

Figure 4.7 displays the hyperchaotic carrier used for encryption, as well as its related PDF. It can be noticed in the timetrace as well as on the PDF that for high values of the laser power (7 mW), the hyperchaotic oscillations are practically Gaussian, so that according to the theoretical analysis performed in the previous section, the mismatch noise is also expected to present the same features as in Fig. 4.3.

Figure 4.8 shows the BER experimentally recorded for the bit-rates 1.2 and 2.5 Gb/s. The concordance with analytic and numerical results is good, and the qualitative features analytically predicted are recovered. However, some quantitative discrepancies are noticed above $\text{SNR} = 7$, probably due to the random noise present in the system. Additive random noise would play exactly the same role as the mismatch noise, so that it may not be the source of this deviation. Experimental measures have evidenced the presence of a multiplicative noise associated to a noisy overall gain (that is, a randomly fluctuating value for β), and which should be responsible of that deviation. It thereby results an experimental BER slightly higher than the theoretical one.

It should also be emphasized that up to SNR values as high as 10, the experimental curves at 1.2 Gb/s and 2.5 Gb/s are quasi-perfectly superposed, in complete concordance with our theory which states that in first approximation, the bit-rate has no influence on the BER variation-law.

Finally, a threshold effect is still experimentally observed: around the value of $\text{SNR} = 14$, the BER sharply drops to zero, or at least, to values which are

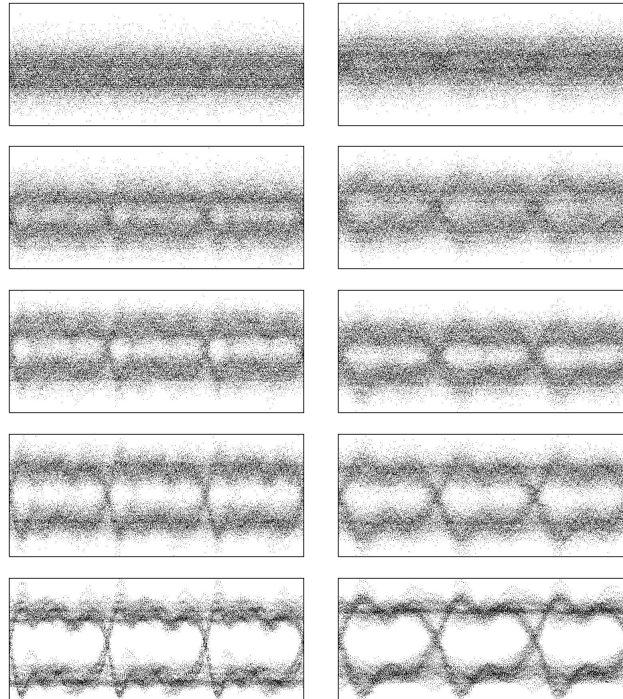


Figure 4.9. Experimental eye-diagrams at the standard bit-rates of OC-24 (1.24416 Gb/s) and OC-48 (2.48832 Gb/s). The experimental parameters are those of Fig. 4.8. The left row corresponds to the OC-24 standard, while the right row is corresponds to the OC-48. From top to bottom the SNR is equal to 2, 5, 8, 11 and 14.

by far below 10^{-15} . From a more global perspective, one can notice that above $\text{SNR} = 12$, a small increase of the SNR leads to a very strong improvement of the BER. This limit therefore seems to be objective to be reached for the fulfilment of the BER requirements in standard optical communication systems.

This threshold effect can also be detected with the experimental eye-diagrams of Fig. 4.9. The aperture of the eyes undergoes a sharp amelioration between $\text{SNR} = 11$ and $\text{SNR} = 14$. Such eye-diagrams have also been yet determined numerically in other optical chaos cryptosystems [112].

4.7 Conclusion

In this study, we have investigated the influence of the mismatch noise on the BER of an electro-optical chaos communication scheme. We have shown that the probability density function of the hyperchaotic carrier and the peak-to-peak-signal-to-rms-noise ratio are the only relevant parameters for the BER evaluation.

This important result is of high experimental and practical interest. Effectively, owing to the absence of nonlinear mixing between the message and the mismatch noise, the value of the *rms* mismatch noise σ measured experimentally without message can be considered as the same as when there is an encrypted message, so that knowing the amplitude of the message μ , the mismatch SNR can be completely evaluated experimentally.

On the other hand, the PDF of the hyperchaotic carrier can be easily measured and we have shown that typically, this PDF has the same shape than the one of the mismatch noise. This allows for a practical control of the mismatch-induced BER. The existence of a threshold value of the SNR is also very interesting in practice, because it means that efforts in order to improve the SNR may lead to a decisive improvement of the BER.

Part II

Nonlinear and Stochastic Dynamics of Ultra-Pure Microwave Generators

Chapter 5

Single-Mode Microwave Dynamics of Opto-Electronic Oscillators

“It’s of no use whatsoever. This is just an experiment that proves Maestro Maxwell was right.”

Heinrich Hertz, to his students.

5.1 Introduction

OUR focus in this chapter is the deterministic dynamics of a single-mode microwave generator referred to as the **opto-electronic oscillator** (OEO). The particularity of the OEO is its exceptional performance in terms of phase noise, that is, in terms of frequency purity. We first briefly present some fundamental notions on microwaves, emphasizing on radar technology and applications. Then, we investigate the particular case of the OEO, and a deterministic model consisting in a delay-differential complex envelope equation is constructed. The corresponding stationary solutions are derived, and their stability is determined as a function of the feedback gain. It is found that bifurcation phenomena do occur beyond a critical value, thereby implying either a drastic restriction or a performance improvement as far as applications are concerned.

5.2 Fundamental principles of radars

5.2.1 Microwaves and radar frequencies

A *microwave* is an electromagnetic wave whose frequency in vacuum is between 300 MHz and 300 GHz, thus corresponding to a wavelength between 1 mm and 1

m. Therefore, they span over three standard frequency ranges of the electromagnetic spectrum: *ultra-high frequencies* (or UHF, from 0.3 to 3 GHz), *super-high frequencies* (or SHF, from 3 to 30 GHz), and *extremely-high frequencies* (or EHF, from 30 to 300 GHz).

The existence of electromagnetic waves was first theoretically predicted by **James Clerk Maxwell** in 1864, and experimentally evidenced in 1888 by **Heinrich Hertz**. Few years later, **Nikola Tesla**¹ and **Guglielmo Marconi**² independently applied for the first patents ever to rely on electromagnetic waves: this was the birth of radio-communications, the precursor of **microwave technology**.

If microwaves do naturally propagate in free space, they also do in confined media like in wave-guides or in co-axial cables. This multiplicity of possible propagation media empowered the emergence of microwave technology, which can therefore be defined as the science of producing, conveying, receiving and analyzing microwave signals. Nowadays, microwaves are the backbone of a wide variety of technological applications, ranging from radio/television broadcasting to radars, passing through microwave ovens and mobile telecommunications networks.

However, the purity of the microwave frequencies needed for these applications is not the same in all cases. For example, in microwave ovens, there is no need for an exceptionally pure microwave, as long as the peak frequency coincides with the transitional frequency $f = 2.45$ GHz which thermally excites the water molecules. In mobile telecommunications, fairly pure microwaves are required, because they are used as carriers to be modulated by information-bearing signals. But in some applications like in radar or in lightwave technologies, *exceptionally pure* microwaves are required, because purity is in these cases directly attached to performance, and the physical indicator of purity for these microwave frequencies is *phase noise*.

Typically, all microwaves can serve as radar frequencies: more precisely, radar-frequencies may vary from 1 to 300 GHz, as it can be seen in Table 5.1. However, to any specific task or application is attached a precise radar-frequency band.

There are five fundamental radar bands which are labelled L, S, C, X and K (splitted in Ku, K and Ka). Beyond the K band, there is the so-called “mm band” (millimetric waves) which is also sometimes divided in sub-bands. The following sub-section will focus on some basic types of radars.

¹**Nikola Tesla**, U.S. Patent 645576: ‘System of transmission of electrical energy’, issued on March 20, 1900.

²**Guglielmo Marconi**, U.S. Patent 676332: ‘Apparatus for wireless telegraphy’, issued on June 11, 1901.

Designation	Frequency range (GHz)
L band	1 – 2
S band	2 – 4
C band	4 – 8
X band	8 – 12
Ku band	12 – 18
K band	18 – 27
Ka band	27 – 40
mm band	40 – 300

Table 5.1: Radar frequency bands.

5.2.2 Types of radars

There are two fundamental types of radars: the *pulsed radar* and the *continuous-wave radar*: there are also some hybrid radars which are combinations of both. We hereafter briefly present these radars as well as their mode of operation.

The pulsed radar

The pulsed radar -or *pulse-modulated radar*- emits short microwave pulses, which are reflected back by the target. These pulses generally have a duration between 0.1 and 10 μs , and they are spaced by silence intervals which are of the order of milliseconds. If the echo is received after a time-lag T , then the distance d between the target and the antenna can simply be evaluated as $d = cT/2$, where c is the velocity of light. However, the velocity of the target can not be evaluated with a single pulse: hence, unless comparing distances evaluated from various pulses emitted at equidistant intervals (which is quite inefficient), these radars are not basically suited for velocity evaluation.

The continuous-wave radar

At the opposite of pulsed radars, continuous-wave radars are emitting uninterruptedly. They rely on the Doppler effect, so that they are also commonly known as *Doppler radars*. Effectively, if the target has radial a velocity $v(t)$ relatively to the radar, the reflected back microwave suffers a frequency shift $\Delta f(t) = -f_0[v(t)/c]$, the so-called *Doppler shift*: the velocity can therefore be monitored in real time with an excellent precision. Unfortunately, Doppler radars can not detect stationary targets, nor targets whose radial velocity is null; moreover, and this is an important drawback, Doppler radars do not enable the evaluation of distances.

Some hybrid radars: the frequency-modulated continuous-wave radar and the pulse-Doppler radar

These radars combine the advantages of pulsed and continuous wave radars, and they can detect both distance and velocity of targets.

In the *frequency-modulated continuous wave radar*, the frequency of the microwave is ramp-modulated: this frequency modulation is a kind of signature which can be recognized in the echo, thereby enabling the distance evaluation as in pulsed radar. The velocity is still evaluated in this case with the Doppler effect. On the other hand, in *pulse-Doppler radars*, the amplitude of the microwave is on/off-modulated. This radar combines time and frequency domain analysis to evaluate the distance and the velocity of the target.

As well as Doppler radars, these kinds of hybrid radars are particularly sensitive to the microwave purity because the echo peak for a slowly moving target would be very near the reference peak, where phase noise is predominant; hence, phase noise is here a key factor that determines the performance and detection range of the radar.

5.2.3 Applications of radars***Detection and ranging***

The historic application of radars is the detection and ranging of moving targets. In civilian applications, radars are generally used to detect planes, cars, and ships. They are also used for high-precision altimetry in aircrafts. In military applications, radars are of course used to detect planes, but they also serve for the guiding of missiles and unmanned planes.

Meteorology

Radars are widely used in meteorology. The emitted microwave is scattered back by snow, rain, or hail. In meteorology, the unit of reflectivity is the dBZ, and this logarithmic unit is used for the determination scattering object's nature: this is due to the fact that the size and the dielectric constant of rain drops, snow flakes and hailstones are different. For example, snow corresponds to a reflectivity of around 10 dBZ, while rain corresponds to around 40 dBZ; hail corresponds to values which can be as high as 70 dBZ. After proper calibration, it is therefore possible to evaluate the characteristics of meteorological formations from backscattered radar microwaves.

Satellite imaging

Satellite imaging is a domain where radars have found an impressive plethora of applications, principally because some microwaves frequencies are not significantly affected by clouds. In wind scatterometry for example, the reflectivity of sea waves is used to indicate the intensity and direction of wind. Radar altimetry can provide a topographic picture of land, that is, a 3D-chart of the landscape. Radar satellite imaging is also used for ecological purposes (detection of oil spills, forestry, agriculture, etc...), climatology (monitoring of icebergs, ozone, etc...), geology (monitoring of earthquakes, landslides, volcanoes, etc...), and of course meteorology (large scale trajectory of hurriquanes, etc...).

5.2.4 Other applications of ultra-pure microwave generators

Time-frequency metrology

Time-frequency metrology is the science of measuring time and frequencies with precision. Between the extreme precision provided by atomic clocks and the less precise one provided by solid-state resonators, there is a gap which can be filled by ultra-low phase noise oscillators. They can for example be used for the calibration of systems (high resolution spectrometers, etc...), or as reference oscillators in clock-driven systems.

Microwave photonics

The aim of microwave photonics is the of study of phenomena involving interactions between microwave and optical signals.

Generally, ultra-low phase noise microwave generators are used in lightwave technology to produce multi gigabits/s optical pulses with extremely low time-jitter. They also have a strong potential for ultra-fast analog-to-digital conversion. [113]. For example, in optical telecommunication networks, ultra-low phase noise microwave photonics can enable to produce multiple-wavelength synchronized pulses with a fs-jitter [68]. Another application where ultra-pure microwaves and photonics are simultaneously used is the so-called **Radio over fiber technology**, which will be widely used in 3G networks with the UMTS³ standard.

5.3 The opto-electronic oscillator

In opto-electronic oscillators, a few kilometers-long fiber delay line is combined to a narrow-band microwave filter, to build a frequency-selective feedback loop

³Universal Mobile Telecommunications System.

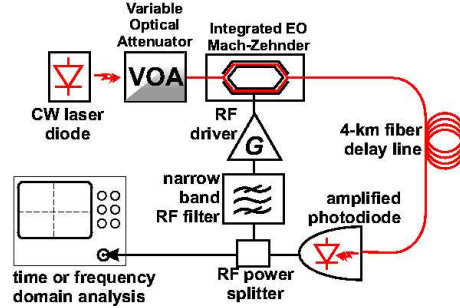


Figure 5.1: Experimental set-up.

[59, 60]. It has been shown that single-mode OEOs are able to produce radio-frequency oscillations with extremely high spectral purity in the microwave range at up to tens of GHz, with extremely low sideband phase noise levels.

5.3.1 The system

A schematic representation of the OEO under study is displayed in Fig. 5.1. Its generic architecture is globally identical to the one of the electro-optical laser hyperchaos generator. Unexpectedly, however, the epithet “**opto-electronic**” has been preferred to “**electro-optical**” to characterize this oscillator. We therefore adopt this nomenclature in order to be consistent with related works in the scientific literature.

The oscillation loop consists of the following elements:

- A wideband integrated optics LiNbO₃ Mach-Zehnder modulator; it is seeded by a continuous-wave semiconductor laser of optical power P , which serves as a bifurcation parameter for scanning the OEO feedback gain; the modulator is characterized by a half-wave voltage $V_{\pi DC} \simeq V_{\pi RF} = 4.2$ V, which defines the amplitude scale required at the microwave Mach-Zehnder driving voltage $V(t)$ for operation in the nonlinear regime.
- A thermalized 4 km fiber performs a time delay of $T = 20$ μ s on the microwave signal carried by the optical beam; the long delay is intended to support thousands of the microwave ring-cavity modes, whose free spectral range is equal to $\Omega_T/2\pi = 1/T = 50$ kHz.
- A fast amplified photodiode with a conversion factor $S = 2.2$ V/mW.
- A narrow-band microwave filter, intended to select the frequency range for the amplified modes; its central frequency is $\Omega_0/2\pi = 3$ GHz, and the -3 dB bandwidth is $\Delta\Omega/2\pi = 20$ MHz; the system is therefore intended to produce a radar frequency in the S-band according to Table 5.1.
- A microwave amplifier with gain G is required to close the loop. All optical

and electrical losses are gathered in a single attenuation factor κ .

It therefore appears to some extent that the electro-optical hyperchaos generator and the OEO have almost perfectly opposite qualitative features: on the one the hand, we have a wide bandwidth and a relatively short delay-line, intended to generate a radio-frequency spectrum as flat and as broad as possible; on the other hand, we have a narrow bandwidth and a very long fiber cavity in order to select a single cavity mode, that is, a single frequency.

5.3.2 A deterministic model for the OEO

Generally, the frequency-domain approach is privileged in the theoretical studies of microwave generators. This is due to the fact that resonator-based oscillators have an extremely high quality factor Q ($> 10^9$), inducing extremely slow energy decay-time compared to the fast oscillation period. These huge timescale differences are generally incompatible with affordable numerical integration and tractable analytical developments in the time domain. However, in the case of the OEO, we should be able to keep the time-domain description because the very large energy storage time is ensured by the delay, and not by the microwave resonant filter whose quality factor is rather low ($Q = \Omega_0/\Delta\Omega = 150$).

Since the architecture of the system is the same as the one of the electro-optical generator, the steps to derive the governing equations are almost exactly the same, except that the filter may not be consider as two cascaded first-order filters, but as a single and resonant bandpass filter . Hence, if we consider in first approximation this filter to be linear with central frequency Ω_0 and bandwidth $\Delta\Omega$, the RF voltage $V(t)$ should obey to

$$\begin{aligned} V(t) + \frac{1}{\Delta\Omega} \frac{d}{dt} V(t) + \frac{\Omega_0^2}{\Delta\Omega} \int_{t_0}^t V(s) ds \\ = \kappa GSP \cos^2 \left[\frac{\pi V(t-T)}{2V_{\pi_{RF}}} + \frac{\pi V_B}{2V_{\pi_{DC}}} \right]. \end{aligned} \quad (5.1)$$

Hence, the dynamics of the microwave oscillation can therefore be described in terms of the usual dimensionless variable $x(t) = \pi V(t)/2V_{\pi_{RF}}$ following

$$x + \tau \frac{dx}{dt} + \frac{1}{\theta} \int_{t_0}^t x(s) ds = \beta \cos^2[x(t-T) + \phi], \quad (5.2)$$

where $\beta = \pi\kappa GSP/2V_{\pi_{RF}}$ is the normalized feedback gain, $\phi = \pi V_B/2V_{\pi_{DC}}$ is the Mach-Zehnder off-set phase, while $\tau = 1/\Delta\Omega$ and $\theta = \Delta\Omega/\Omega_0^2$ are the characteristic timescale parameters of the bandpass filter.

The dynamics of the OEO can unfortunately not be studied under the form of Eq. (5.2), because the ratio between the fastest and slowest dynamical timescales $\Omega_0^2/(\Omega_T \cdot \Delta\Omega) \sim 10^7$ is too high. However, owing to the narrow-bandwidth band-pass filter, only the oscillations whose frequency is within the bandwidth can arise. Therefore, an option to circumvent this problem is to represent the solution under the form of a carrier of frequency Ω_0 , slowly modulated by a complex amplitude $\mathcal{A}(t)$, yielding

$$x(t) = \frac{1}{2}\mathcal{A}(t)e^{i\Omega_0 t} + \frac{1}{2}\mathcal{A}^*(t)e^{-i\Omega_0 t} \quad (5.3)$$

with $\mathcal{A} = |\mathcal{A}|e^{i\psi}$. The challenge is now to find an equation for the complex envelope amplitude $\mathcal{A}(t)$, which is assumed to vary slowly relatively to the central carrier frequency Ω_0 , that is $|\dot{\mathcal{A}}(t)| \ll \Omega_0|\mathcal{A}(t)|$.

Equation (5.2) can furthermore be significantly simplified. Effectively, using the Jacobi-Anger expansion

$$e^{iz \cos \alpha} = \sum_{n=-\infty}^{+\infty} i^n J_n(z) e^{in\alpha}, \quad (5.4)$$

where J_n is the n -th order Bessel function of the first kind. It can be shown that the cosine of a sinusoidal function of frequency Ω_0 can be Fourier-expanded in harmonics of Ω_0 . In other words, knowing that $\cos^2(z) = [1 + \cos(2z)]/2$, if $x(t)$ is nearly sinusoidal around Ω_0 , then the Fourier spectrum of $\cos^2[x(t-T) + \phi]$ will be sharply distributed around the harmonics of Ω_0 . Since the filter of the feedback loop is narrowly resonant around Ω_0 , it is an excellent approximation to discard all the spectral components of the signal except the fundamental. Therefore, using Eqs. (5.3) and (5.4), the original Eq. (5.2) can be rewritten as

$$\begin{aligned} x + \tau \frac{dx}{dt} + \frac{1}{\theta} \int_{t_0}^t x(s) ds &= -\beta \sin 2\phi \\ &\times J_1[2|\mathcal{A}(t-T)|] \cos[\Omega_0(t-T) + \phi(t-T)]. \end{aligned} \quad (5.5)$$

To avoid the integral term which is complicated to manage analytically and numerically, it is mathematically more convenient use the intermediate variable

$$u(t) = \int_{t_0}^t x(s) ds, \quad (5.6)$$

which is also nearly sinusoidal around 0. Therefore can also write

$$u(t) = \frac{1}{2}\mathcal{B}(t)e^{i\Omega_0 t} + \frac{1}{2}\mathcal{B}^*(t)e^{-i\Omega_0 t}, \quad (5.7)$$

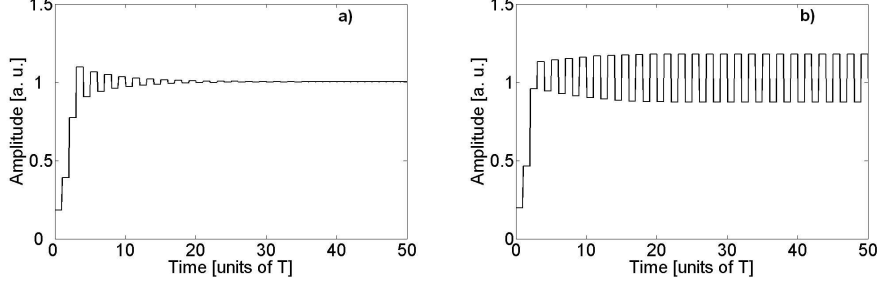


Figure 5.2. Numerical simulations of Eq. (5.10), for various values of the effective feedback gain γ , with $\sigma = 0$ and $\phi = -\pi/4$ (i. e., $\gamma < 0$). The initial condition is constant in the interval $[-T, 0]$ ($=10^{-2}$). a) $|\gamma| = 2.2 < \gamma_{cr}$: the system converges to a stable fixed point after some oscillatory transients. b) $|\gamma| = 2.4 > \gamma_{cr}$: the system is beyond the supercritical Hopf bifurcation value, and its amplitude is modulated with a period equal to $2T = 40 \mu s$.

from which we can later deduce $\mathcal{A}(t)$ using the relation $x(t) = \dot{i}(t)$.

To derive an evolution equation for $\mathcal{B}(t)$, we can just inject Eq. (5.7) into Eq. (5.5), and we obtain

$$\begin{aligned} \ddot{\mathcal{B}} + 2(\mu + i\Omega_0)\dot{\mathcal{B}} + 2i\mu\Omega_0\mathcal{B} \\ = -2\mu\gamma J_1[2|\dot{\mathcal{B}}_T + i\Omega_0\mathcal{B}_T|] e^{-i\Omega_0 T} e^{i\psi_T}, \end{aligned} \quad (5.8)$$

where $\mu = \Delta\Omega/2$ is the half-bandwidth, and $\gamma = \beta \sin 2\phi$ is the effective feedback gain. We can also define the cumulated loop phase as $\sigma = \Omega_0 T$, and the importance of a careful thermal stabilization of the 4-km long fiber delay-line appears here: effectively, a relative thermic dilatation of only 10^{-5} is yet able to induce noticeable changes of the loop phase, that is, to the dynamics of the system.

Assuming the slowly-varying conditions $|\dot{\mathcal{B}}| \ll \Omega_0|\mathcal{B}| \ll \Omega_0^2|\mathcal{B}|$ and taking into account $\mu \ll \Omega_0$, Eq. (5.8) can be reduced to

$$i\Omega_0\dot{\mathcal{B}} + i\mu\Omega_0\mathcal{B} = -\mu\gamma J_1[2\Omega_0|\mathcal{B}_T|] e^{-i\sigma} e^{i\psi_T}. \quad (5.9)$$

The phase factor of the variable $x(t-T)$ can also be rewritten as $e^{i\psi_T} = \mathcal{A}_T/|\mathcal{A}_T|$. Therefore, if we assume $\mathcal{A} \simeq i\Omega_0\mathcal{B}$, we are led to the following evolution equation for the complex envelope \mathcal{A} of the microwave variable $x(t)$

$$\dot{\mathcal{A}} = -\mu\mathcal{A} - 2\mu\gamma e^{-i\sigma} J_{c1}[2|\mathcal{A}_T|]\mathcal{A}_T, \quad (5.10)$$

where J_{c1} is the **Bessel-cardinal** function defined as $J_{c1}(x) = J_1(x)/x$. It may be interesting to note that the Bessel cardinal function is qualitatively very similar to the sinus-cardinal function, but its absolute maximum is $1/2$ instead of 1.

We have therefore derived a first-order nonlinear delay-differential equation with a complex variable to investigate the dynamics of the microwave generator. In the following subsections, we will use this equation to study the stationary states, which are of interest for our purpose, as well as their local stability.

5.4 Stationary solutions of the OEO and their stability

5.4.1 Stationary solutions

The theoretical advantage of dealing with an envelope equation is that pure monochromatic microwave solutions are *fixed points* of the amplitude equation. Hence, stability analysis of these solutions are mathematically more tractable. The fixed points of our system obey the algebraic nonlinear equation

$$\mathcal{A} \{1 + 2\gamma e^{-i\sigma} \text{Jc}_1[2|\mathcal{A}|\}] = 0. \quad (5.11)$$

The trivial fixed point $\mathcal{A}(t) \equiv 0$ corresponds to the non-oscillating solution. To check for its stability of this solution, we can perturbate it with $\delta\mathcal{A}$, and track the evolution of the perturbation with

$$\delta\dot{\mathcal{A}} = -\mu\delta\mathcal{A} - \mu\gamma e^{-i\sigma} \delta\mathcal{A}_T \quad (5.12)$$

The sufficient stability conditions for this kind of delayed variational equations can be obtained analytically [114,115]. The phase matching condition $e^{i\sigma} = \pm 1$ has to be fulfilled for an oscillation to be sustained. It means that if $\Omega_0 T$ is not an integer multiple of π , then the mode would oscillate with a frequency shift ϖ such that $(\Omega_0 + \varpi)T \equiv 0$ modulo π . The trivial solution is therefore stable when $|\gamma| < 1$, or if $\gamma e^{-i\sigma} \geq 1$ and $T < T_{cr} = \arccos[-e^{i\sigma}/\gamma]/[\mu\sqrt{\gamma^2 - 1}]$. Since in our system $T \gg 1/\mu$, the second case can generally not be fulfilled. In the branch $\gamma e^{-i\sigma} < 0$, there is a bifurcation at $|\gamma| = 1$. On the other hand, in the branch $\gamma e^{-i\sigma} > 0$, there is a bifurcation right above $|\gamma| = 1$. However, this solution does not emerge experimentally, as the whole RF spectrum shifts by an amount of $\Omega_T/2$: thereby, $e^{-i\sigma}$ is of opposite sign and the oscillator flips back to the first bifurcation branch. Hence, we can globally consider that the trivial fixed point is stable only when the loop gain is such that $|\gamma| < 1$.

When $|\gamma| = 1$, we therefore have to consider the supercritical pitchfork bifurcation occurring between the solution $\mathcal{A}(t) = 0$ the non-trivial fixed point $\mathcal{A}(t) = \mathcal{A}_0 \neq 0$ which corresponds to the dynamical behavior we are looking for, that is, a purely sinusoidal solution of the kind $x(t) = |\mathcal{A}_0| \cos[\Omega_0 t + \psi_0]$. From Eq. (5.10), it can be deduced that the amplitude of this oscillating solutions obeys to the following transcendental equation:

$$\text{Jc}_1[2|\mathcal{A}_0|] = -\frac{1}{2\gamma} e^{i\sigma}. \quad (5.13)$$

In the following we will set $e^{i\sigma}$ to 1, without loss of generality.

The amplitude \mathcal{A}_0 is defined by the intersection between the Bessel cardinal function and the horizontal line of height $-1/2\gamma$. Since the loop gain $\gamma = \beta \sin 2\phi$ can be either positive or negative depending on the value of the bias offset ϕ , we have four distinct cases: no solutions when $\gamma < -15.52$ or $\gamma > 7.56$, one solution for $-15.52 < \gamma < -1$, and multiple solutions for $-1 < \gamma < 7.56$. It clearly appears that the range of interest for our purpose is the one for which γ is *negative*, with $1 < |\gamma| < 15.52$.

5.4.2 Stability analysis: emergence and stability of the monochromatic solution

Beyond the existence of the monochromatic solution described above, we still have to check for its stability. Using the conventional stability analysis method, we are led to the perturbation equation

$$\delta\dot{\mathcal{A}} = -\mu \delta\mathcal{A} - 2\mu\gamma \{J_{c_1}[2|\mathcal{A}_0|] + 2|\mathcal{A}_0|J'_{c_1}[2|\mathcal{A}_0|]\} \delta\mathcal{A}_T, \quad (5.14)$$

whose stability is ensured for amplitudes $|\mathcal{A}_0|$ fulfilling the condition

$$\left| \frac{1}{2} + \frac{|\mathcal{A}_0|J'_{c_1}[2|\mathcal{A}_0|]}{J_{c_1}[2|\mathcal{A}_0|]} \right| < \frac{1}{2}, \quad (5.15)$$

corresponding to values of γ belonging to the intervals $[-2.31, -1]$, $[-8.11, -7.56]$ and $[-15.94, -15.08]$ (there are an infinity of such windows in the multiple-solutions range, when $\gamma < -15.52$).

In fact, we are restricted to the first stability interval because conventional radio-frequency opto-electronic devices do not enable to obtain gain values higher than 5. Therefore, the theory predicts that a pure monochromatic solution emerges at $|\gamma| = 1$, and remains stable up to $\gamma_{cr} = 2.31$. Beyond γ_{cr} , the system undergoes a supercritical Hopf bifurcation, as the fixed point \mathcal{A}_0 loses its stability while a limit cycle $\mathcal{A}_0 + a_0 \exp(i\Omega_H t)$ emerges. This Hopf bifurcation therefore leads to an *amplitude modulation* of the microwave signal $x(t)$, that is, to the emergence of deterministic modulation side-peaks in the radio-frequency Fourier spectrum. On the one hand, it can be demonstrated from the classical theory of Hopf bifurcations that the modulation amplitude $|a_0|$ initially grows as $|\gamma - \gamma_{cr}|^{1/2}$, that is, as the square-root of the gain increase from the bifurcation. On the other hand, it is also possible to determine analytically the frequency Ω_H of the Hopf-induced amplitude modulation. Effectively, the time-varying component $a_0 \exp(i\Omega_H t)$ is initially very small and can be treated as a perturbation, which should obey to Eq. (5.14) according to

$$i\Omega_H = -\mu - 2\mu\gamma \{J_{c_1}[2|\mathcal{A}_0|] + 2|\mathcal{A}_0|J'_{c_1}[2|\mathcal{A}_0|]\} e^{-i\Omega_H T}. \quad (5.16)$$

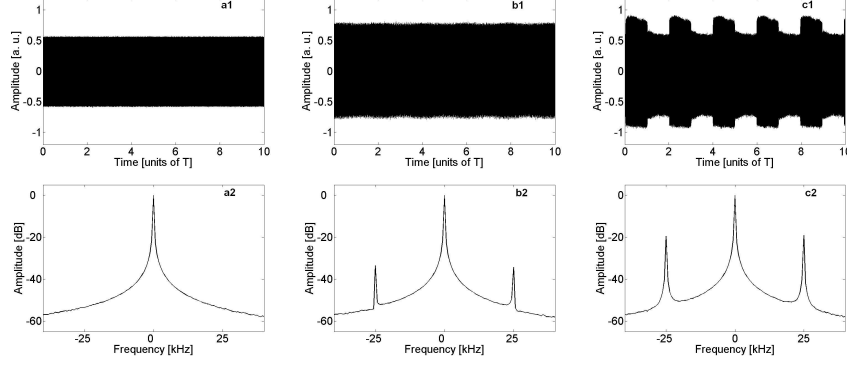


Figure 5.3. Experimental evidence of the Hopf-induced amplitude modulation, as the gain is increased; *a1*, *b1* and *c1* are timetraces, and *a2*, *b2* and *c2* are the Fourier spectra of the corresponding reconstructed envelopes (relatively to the carrier at $\Omega_0/2\pi = 3$ GHz). *a*) Before the bifurcation. *b*) At the onset of the bifurcation. *c*) After the bifurcation.

After splitting this equation into its real and imaginary parts, it appears that the Hopf frequency Ω_H obeys the transcendental equation

$$\Omega_H = -\mu \tan[\Omega_H T], \quad (5.17)$$

whose physical solution $\Omega_H \simeq \frac{1}{2}\Omega_T$ corresponds to a modulation period $T_H = 2T = 40 \mu\text{s}$.

Numerical simulations fully confirm the theoretical analysis. In Fig. 5.2, various timetraces obtained through the simulation of Eq. (5.10) are displayed. When $|\gamma| = 2.2$, the system converges towards its stable fixed point, but only after some oscillatory transients. When the gain is further increased to $|\gamma| = 2.4$, the system has yet undergone the supercritical Hopf bifurcation at $\gamma_{cr} = 2.31$. As a consequence, the amplitude is modulated, and the modulation period is effectively twice the delay-time as predicted. Therefore, the numerical simulations are in perfect concordance with the theory, both quantitatively and qualitatively.

5.5 Experimental results

The⁴ experimental evidence of this Hopf-induced amplitude modulation is presented in Fig. 5.3. Before the bifurcation, the amplitude is constant and there is a single peak in the Fourier spectrum. Exactly at the onset of the bifurcation, the amplitude starts to be modulated with the Hopf frequency $\Omega_H/2\pi = \Omega_T/4\pi = 25$ kHz: therefore, two modulation peaks appear beside the carrier at the frequencies $\pm\Omega_H/2\pi$. Careful measurement of the corresponding critical value of the

⁴These experimental results have been obtained in collaboration with L. Larger, H. Tavernier and R. Bendoula at the Optoelectronics Laboratory of the FEMTO-ST Institute, Besançon, France.

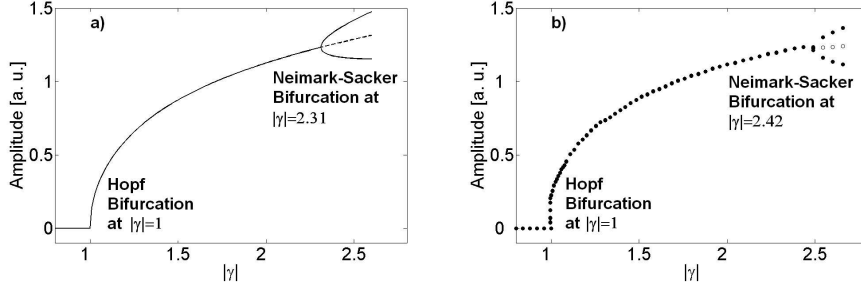


Figure 5.4. Bifurcation diagrams for the microwave variable $x(t)$ revealing unexpected non-linear effects. *a)* Theoretical diagram. *b)* Experimental diagram.

loop gain has given the experimental value of $\tilde{\gamma}_{cr} = 2.42$, which is very near the analytical value $\gamma_{cr} = 2.31$ given by the theory with the stability condition of Eq. (5.15). Note that the lowest Hopf critical value was obtained after adjusting the Mach-Zehnder bias, most probably due to thermal drifts induced by the increasing RF power. After the bifurcation, the amplitude is strongly square-wave modulated with the same frequency Ω_H , and the modulation side-peaks become stronger. This experimental phenomenology is therefore in perfect concordance with the analytically predicted scenario.

The bifurcation diagrams for the microwave variable $x(t)$ are displayed in Fig. 5.4. In fact, removing the periodic fast-scale oscillation at Ω_0 is geometrically equivalent to represent the dynamics of a Poincaré section: therefore, at $|\gamma| = 1$, the amplitude variable $\mathcal{A}(t)$ undergoes a pitchfork bifurcation (from the trivial fixed point to another fixed point) while the corresponding microwave variable $x(t)$ undergoes a Hopf bifurcation (from a fixed point to a limit-cycle); and at $|\gamma| = \gamma_{cr}$, $\mathcal{A}(t)$ undergoes a Hopf bifurcation while $x(t)$ rather undergoes a **Neimark-Sacker** bifurcation, that is, a bifurcation from a limit-cycle to a torus. In ref. [60], a similar bifurcation diagram was plotted but only at up to 2.1, so that the Neimark-Sacker bifurcation was not observed.

5.6 Conclusion

We have proposed a deterministic time-domain model for the study of single-mode optoelectronic oscillators. This model whose variable is the complex envelope amplitude of the microwave takes into account the intrinsic features of OEOs, that is a strong nonlinearity on the one hand and a very large delay on the other. The model predicts a supercritical Hopf bifurcation for the amplitude variable as the loop gain is increased, that is, to an amplitude modulation which thereby induces the emergence of robust parasite side-peaks in the radio-frequency Fourier spectrum. This

behavior has been also recovered experimentally.

In the next chapter, we will focus on the stochastic and multimode dynamics of this microwave generator.

Chapter 6

Stochastic and Multimode Microwave Dynamics of Opto-Electronic Oscillators

“If the reference moves, where are men going?”

Cheikh Hamidou Kane, *The ambiguous adventure*.

6.1 Introduction

THERE are two fundamental factors that can affect the purity of a microwave generated by an opto-electronic oscillator: **noise fluctuations** (mainly related to phase noise) on the one hand, and **multimode dynamics** on the other. The aim of this chapter is to investigate these two aspects. We will first consider the problem of phase noise in the oscillator. Using the deterministic model constructed in the precedent chapter, we will build a stochastic model in order to understand how noisy intrinsic and environmental influences are transferred into phase fluctuations. Then we will study the multimode behavior of the system. Evidence will be given that the mode competition is so strong that it may persist even at macroscopic timescales. The multiple-time scale methodology will be used to gain a theoretical understanding on the mechanisms of this modal competition.

6.2 Stochastic microwave dynamics of OEOs

6.2.1 Phase noise

In the time domain, a perfectly pure monochromatic microwave can be mathematically expressed as $A(t) = A_0 \cos(\Omega t + \varphi)$, where its amplitude A_0 and its phase φ are rigorously constant. In the Fourier domain, the spectrum of this signal is a Dirac peak of amplitude A_0 , centered on the frequency Ω . However, perfectly pure microwave do not exist in practice, since theoretically, they are at least affected by an unavoidable quantum noise; but in fact, real-world microwaves are not perfectly pure because they are polluted by the thermal noise originating from the electrical circuitry needed to produce them, as well as by unavoidable environmental perturbations. Hence, amplitude and phase are no more rigorously constant: they become fluctuating - or better said, *stochastic*- variables.

Except in some exceptional cases, (small) amplitude noise is generally not a critical problem, at the opposite of phase noise. The effect of this phase noise in the Fourier domain is to transform the zero-autocorrelation Dirac peak into a peak of non-zero auto-correlation, that is, a frequency peak with a given “waist”.

Phase noise is generally designated with the Fourier transform variable $S_\varphi(f)$ whose unit is the rad^2/Hz , or the dBrad^2/Hz . Alternatively, the technical variable $\mathcal{L}(f) = \frac{1}{2}S_\varphi(f)$ is used, and its unity is the dBc/Hz which stands for *decibels below the carrier in a 1-Hz bandwidth*.

It is sometimes convenient to consider that phase noise can be characterized through the following power-law expansion of the frequency around the central peak

$$S_\varphi(f) = \sum_{i=0}^4 b_{-i} f^{-i}, \quad (6.1)$$

where the b_{-i} are empiric coefficients, weighting respectively (from 0 to 4) the **white phase noise**, **flicker phase noise**, **white frequency noise**, **flicker frequency noise** and **random-walk frequency noise** [116]. The influence of these various contributions is generally highlighted in conventional log-log spectra plots. It is common to synthetically express the phase noise performance of a microwave generator in terms of dBc/Hz at a given frequency shift from the carrier, for example “ $-150 \text{ dBc}/\text{Hz} @ 10 \text{ kHz}$ ”.

6.2.2 The stochastic model

In the sub-section 2.7 of Chapter 2, we did focus on the influence of noise on the electro-optical hyperchaos generator. For that purpose, we had demonstrated that a convenient stochastic model for that system had to have two contributions,

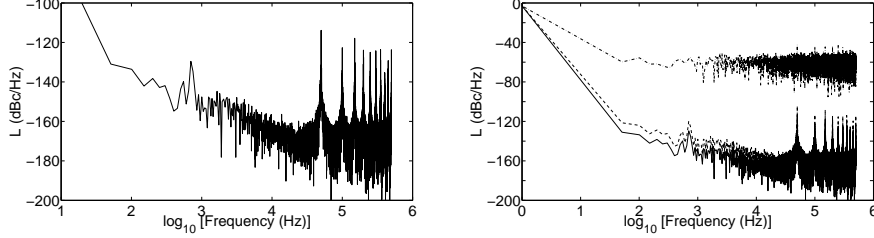


Figure 6.1. Phase noise spectra. *a)* The amplitude of additive noise is $\sigma_a = 5.0 \times 10^{-3}$, and the amplitude of multiplicative noise is fixed to $\sigma_m = 1.0 \times 10^{-5}$. *b)* Effect of the various noise contributions when their amplitudes is multiplied by three, the continuous curve being the same as in *a)* (reference curve). The dashed curve is obtained by setting $\sigma_a = 15.0 \times 10^{-3}$ (σ_m remaining the same), and the dashed-dotted curve by setting $\sigma_m = 3.0 \times 10^{-5}$ (σ_a remaining the same).

namely a **multiplicative noise** contribution due to a noisy loop gain, and an **additive noise** contribution induced by environmental fluctuations. We had also shown that experimental measurements allowed us to consider these noises as white and Gaussian.

Since the opto-electronic generator has exactly the same architecture, it is logical to suppose that this stochastic model is still valid, with different parameters, though. However, the variable of the stochastic delay-differential equation (2.26) is the microwave variable $x(t)$: hence, we have to use the slowly-varying approximation of Eq. (5.3) to derive a stochastic equation for the complex amplitude variable $\mathcal{A}(t) = |\mathcal{A}(t)|e^{i\psi(t)}$.

In this configuration, the additive noise $\xi_a(t)$ of interest should be centered around the carrier frequency Ω_0 , while the multiplicative noise $\xi_m(t)$ fluctuates around the feedback gain value. Therefore, decomposing these noises into complex conjugates yields

$$\begin{aligned}\xi_a(t) &= \frac{1}{2}\zeta_a(t)e^{i\Omega_0 t} + \frac{1}{2}\zeta_a^*(t)e^{-i\Omega_0 t} \\ \xi_m(t) &= \frac{1}{2}\zeta_m(t) + \frac{1}{2}\zeta_m^*(t),\end{aligned}\quad (6.2)$$

where $\zeta_a(t)$ and $\zeta_m(t)$ are complex Gaussian white noises, which are correlated as $\langle \zeta_{a,m}(t)\zeta_{a,m}^*(t') \rangle = 4\delta_{a,m}\delta(t-t')$. The slowly-varying amplitude $\mathcal{B}(t)$ of the

integral variable $u(t) = \int_{t_0}^t x(s) ds$ therefore obeys

$$\begin{aligned} & \{\ddot{\mathcal{B}} + 2(\mu + i\Omega_0)\dot{\mathcal{B}} + 2i\mu\Omega_0\mathcal{B}\}e^{i\Omega_0 t} + \text{c.c.} \\ &= -4\mu\gamma \left[\left(\frac{1}{2} + \frac{1}{2}\sigma_m\zeta_m(t) \right) + \text{c.c.} \right] \left[\frac{1}{2}e^{i\Omega_0(t-T)}e^{i\psi_T} + \text{c.c.} \right] \\ & \times J_1[2|\dot{\mathcal{B}}_T + i\Omega_0\mathcal{B}_T|] + 4\mu \left[\frac{1}{2}\sigma_a\zeta_a(t)e^{i\Omega_0 t} + \text{c.c.} \right], \end{aligned} \quad (6.3)$$

where c.c. stands for the complex conjugate of the preceding term. With the usual approximations, Eq. (6.3) can be reduced to the following stochastic delay-differential equation for the variable $\mathcal{A}(t)$

$$\dot{\mathcal{A}} = -\mu\mathcal{A} - 2\mu\gamma [1 + \sigma_m\xi_m(t)] e^{-i\sigma} J_{c_1}[2|\mathcal{A}_T|]\mathcal{A}_T + 2\mu\sigma_a\zeta_a(t). \quad (6.4)$$

It therefore appears that in the complex amplitude equation, the initial multiplicative noise remains a *real* variable, while the additive noise becomes *complex*.

From this theoretical analysis, the amplitude of the phase noise fluctuations should increase with the amplitude of the additive and multiplicative noises σ_a and σ_m . This equation also predicts that the amplitude of phase noise should decrease as the amplitude $|\mathcal{A}_0|$ of the microwave increases. At last, this equation indicates that phase noise fluctuations are closely related to the delay time and to bandwidth of the RF filter. Deeper analysis is however necessary in order to understand exactly what is the effect of these parameters on the spectral properties of phase noise.

6.2.3 Numerical simulations

We have simulated the complete Eq. (6.4) in order to plot the Fourier spectrum of phase noise $\psi(t)$. In Fig. 6.1a, the numerical results are displayed in the conventional log-log coordinates. This spectra is both qualitatively and quantitatively very similar to those who are obtained experimentally. Here, the peaks indicate the noise-driven amplitude of the cavity-modes which are spaced by $\Omega_T/2\pi = 50$ kHz: however, these peaks are not particularly detrimental as far as applications are concerned, because they are relatively far from the central peak. In this numerical spectra, the phase noise performance of the OEO is around -160 dBc/Hz @ 10 kHz.

To understand the influence of additive and multiplicative noises, we have multiplied each of them by three while the other was remaining constant. The results are shown in Fig. 6.1b, and it can be seen that as expected, the phase noise globally increases with the noise amplitude. It is striking that comparatively to additive noise, multiplicative noise is exceptionally critical, since multiplying the initial value by three yields a spectrum whose level of noise is exceptionally high.

However, it should also be emphasized that the intensities of the additive and multiplicative noises are still to be calibrated experimentally in order to have more

realistic values. For example, the amplitude of the multiplicative noise can have been overestimated in numerical simulations. Therefore, no definitive conclusion can be drawn *a priori* about the criticality of this multiplicative noise from the numerical analysis.

6.3 Temporal evolution of the radio-frequency spectrum

Until now, we have only investigated the case where a single-mode was oscillating. However, if the cavity-modes are spaced by $\Omega_T = 50$ kHz as in our case, there are some 400 modes that can be amplified when the RF filter has a bandwidth of $\Delta\Omega = 20$ MHz. We may guess *a priori* what should occur when the system is switched on abruptly. Normally, all these modes should be excited; then, they would compete for the available gain, and at last, after the transient time corresponding to modal competition, the highest-gain mode should oscillate while all the others are definitively damped out. This is the usual scenario in resonator-based oscillators, like lasers for example, where this transient time is generally very short - of the order of few nanoseconds. In our system, though, nothing guarantees the validity of this scenario, mostly because the system is very high-dimensional owing to the hundredths of modes which can potentially oscillate. We may therefore expect that different initial conditions do lead to different final states.

It is an excellent approximation to expand the slowly varying amplitude $\mathcal{A}(t)$ as a sum of cavity-mode amplitudes, following

$$\mathcal{A}(t) = \sum_{n=0}^{N_{max}} \mathcal{A}_n(t) e^{in\Omega_T t}, \quad (6.5)$$

where $N_{max} \sim \mu/\Omega_T$ is half the number of modes that are within the bandwidth. The modal amplitudes \mathcal{A}_n have a detuning frequency $\Omega_n = n\Omega_T$ relatively to the central frequency Ω_0 , and we can safely suppose that a cavity mode outside the bandwidth can definitely not oscillate; hence, summing the modes up to N_{max} is more than sufficient.

In the precedent chapter, the initial condition was taken constant over the interval $[-T, 0]$. Spectrally, it means that *all* the energy was initially present in the fundamental mode \mathcal{A}_0 , while no energy was provided to the side-modes. It is known in oscillators theory that oscillation is subsequent to amplification: hence, the fundamental mode was the unique mode which could potentially oscillate. That is why we obtained a single-mode operation (see Fig. 5.2) - and it was exactly what we were looking for.

Experimentally, however, it is impossible to concentrate the initial energy in only one mode to favour its single-mode operation. In fact, the initial condition is noisy. This can easily be derived from Eq. (6.4) by setting the gain γ to 0; the

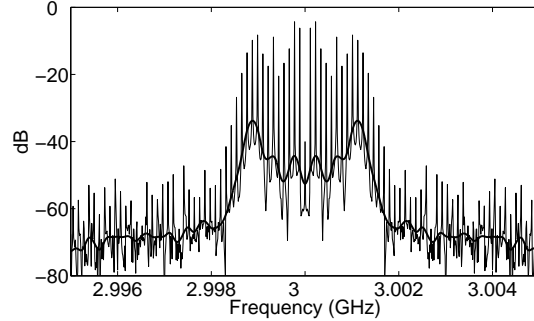


Figure 6.2. Numerical simulation of the radio-frequency spectrum of the OEO after 1 s, in a 10 MHz window. The thin line represents the result of the simulation, while the thick line represents an averaging of the spectrum with a 125 kHz resolution, in order to facilitate comparison with the oscilloscope display of Fig. 6.3.

amplitude becomes noise-driven according to

$$\dot{\mathcal{A}} = -\mu\mathcal{A} + 2\mu\sigma_a\zeta_a(t). \quad (6.6)$$

The solution of this stochastic differential equation is a **Ornstein-Uhlenbeck** Gaussian noise whose amplitude is proportional to σ_a . A noisy initial condition over the interval $[-T, 0]$ means that all the modes do initially possess energy: hence, they can all potentially oscillate. Therefore, the initial dynamics of the OEO is always multimode.

However, a single-mode operation can be obtained experimentally by a slow increase of the feedback gain, that is, with a switching on procedure starting from under to above threshold. In this case, the modal competition at threshold is relatively fast because there is only a very small quantity of available energy for all the modes.

To have a better insight on this multimode dynamics, we have simulated the deterministic Eq. (5.10), but the initial condition in the interval $[-T, 0]$ has been taken to be Gaussian random numbers, which for our purpose can perfectly replace the more realistic Ornstein-Uhlenbeck noise. We have thereby provided equal opportunity to all the modes (within and outside) the bandwidth to be amplified and at last oscillate. The result of this simulation is displayed in Fig. 6.2. It can be seen that after 1 second, the dynamics of the OEO is highly multimode, with several modes oscillating within a 3 MHz bandwidth. It should be emphasized that 1 second is a macroscopic timescale for this system, for which the largest time-scale is $T = 20 \mu\text{s}$. Hence, this simulations confirms that when realistic initial conditions are chosen, a persistent multimode behavior is observed, which may or not lead to a single-mode behavior after a transient process which is macroscopical.

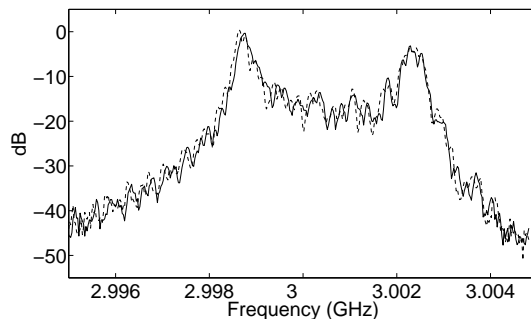


Figure 6.3. Experimental radio-frequency spectrum of the OEO after 30 seconds (dashed line) and after 2 hours (continuous line), in a 10 MHz window. The modal competition can be considered in this case as permanent.

6.4 Experimental results

The¹ persistent multimode dynamics that was obtained numerically has also been observed experimentally. When the system is switched on continuously from below to above threshold, the system oscillates in a single mode. But when the switching is abrupt, all the modes within the bandwidth are initially amplified, and at macroscopical timescales the modal dynamics is still going on within 4 MHz around the central frequency.

One may note the agreement between the numerical simulation and the experimental result. Beyond the striking qualitative similarity between both spectra, it is worth noting that the bandwidth within which the modal competition occurs is quite correctly recovered by the simulations. The level between the oscillating modes and the damped modes within the filter bandwidth is also more or less the same numerically and experimentally, that is, approximately equal to 40 dB.

6.5 A modal expansion approach to OEO's dynamics

Numerical and experimental evidence has been given about the complexity and the persistence of the multimode dynamics in OEOs. We are in front of a situation where hundredths of modes (or oscillators) are coupled in a very complex fashion. The aim of this section is to provide an analytical insight into the modal dynamics of the OEO, and to gain understanding into the mechanisms which are behind the observed dynamical behavior.

¹These experimental results have been obtained in collaboration with L. Larger, H. Tavernier and R. Bendoula at the Optoelectronics Laboratory of the FEMTO-ST Institute, Besançon, France.

6.5.1 The multiple timescales method

The timescales involved in the dynamics of the opto-electronic oscillator are widely separated. Principally, we have the carrier frequency $\Omega_0/2\pi$ in the GHz range, the filter half-bandwidth $\mu/2\pi$ in the MHz range, and at last the free spectral range $\Omega_T/2\pi$ in the kHz range. The separation of timescales by the same 3 orders of magnitudes makes the OEO an ideal case for the multiple time scales method [117, 118]. This method relies on the expansion of the variables in function of the various timescales involved in the system. Then, a different dynamics is assumed at each time scale and therefore, an evolution equation is derived at each timescale.

Let us then consider the smallness parameter ϵ which separates the various parameters. In our case, a straightforward value is $\epsilon = 10^{-3}$. Then, we can define the various timescales as $T_k = \epsilon^k t$, where k is a positive integer. According to this definition, $T_0 = t$ is the fastest timescale, while as k increases, the times T_k are attached to slower variations. However, only a limited number k_{max} of timescales is needed to take into account all the dynamical features of the system. Here, $k_{max} = 3$ covers the totality of the dynamics of interest. Since the timescales are supposed to be independent, the time derivative can be expanded as

$$\frac{d}{dt} = \sum_{k=0}^{k_{max}} \epsilon^k \frac{\partial}{\partial T_k} \equiv \sum_{k=0}^3 \epsilon^k D_k, \quad (6.7)$$

where D_k has just been introduced as a practical notation for the partial derivative $\partial/\partial T_k$. The temporal parameters may be rescaled as

$$\begin{aligned} \mu &= \epsilon \hat{\mu} \\ \Omega_T &= \epsilon^2 \hat{\Omega}_T, \end{aligned} \quad (6.8)$$

and the integral variable $u(t)$ of Eq. (5.6) can therefore be expanded as

$$u(t) = \sum_{k=0}^3 \epsilon^k u_k(T_0, T_1, T_2, T_3) + \mathcal{O}(\epsilon^4), \quad (6.9)$$

where the variables u_k are associated to the timescales T_k .

Using the relationship $x = \dot{u}$, the microwave variable $x(t)$ can also be expanded at the various orders of ϵ according to

$$\begin{aligned} x(t) &= \left\{ \sum_{k=0}^3 \epsilon^k D_k \right\} \times \left\{ \sum_{k=0}^3 \epsilon^k u_k(T_0, T_1, T_2, T_3) \right\} \\ &= \sum_{k=0}^3 \epsilon^k x_k(T_0, T_1, T_2, T_3) + \mathcal{O}(\epsilon^4), \end{aligned} \quad (6.10)$$

Since the nonlinearity in the microwave evolution equation is quadratic, the *amplitude* of the quasi-sinusoidal variable $x(t)$ should also be expanded in orders of ϵ . If we write this amplitude under the form $|\mathcal{A}(t)|$, then we have the expansion

$$|\mathcal{A}(t)| = \sum_{k=0}^3 \epsilon^k |\mathcal{A}_k(T_0, T_1, T_2, T_3)| + \mathcal{O}(\epsilon^4). \quad (6.11)$$

It is important to note that this amplitude should not be confused with the instantaneous value of the variable $x(t)$.

6.5.2 Modal equations

The purpose of the method is to derive equations at each timescale, and for each mode.

Using Eqs. (6.7), (6.9) and (6.11), the microwave evolution equation (5.5) can be rewritten as

$$\begin{aligned} & \left\{ \sum_{k=0}^3 \epsilon^k D_k \right\}^2 \times \left\{ \sum_{k=0}^3 \epsilon^k u_k \right\} + 2\epsilon\hat{\mu} \left\{ \sum_{k=0}^3 \epsilon^k D_k \right\} \times \left\{ \sum_{k=0}^3 \epsilon^k u_k \right\} \\ & + \Omega_0^2 \left\{ \sum_{k=0}^3 \epsilon^k u_k \right\} = -2\epsilon\hat{\mu}\gamma J_1 \left[2 \sum_{k=0}^3 \epsilon^k |\mathcal{A}_{kT}| \right] \cos[\Omega_0 T_0 - \sigma + \psi_T]. \end{aligned} \quad (6.12)$$

In order to maintain uniformly the polynomial expansion in powers of ϵ , the Bessel nonlinearity can be Taylor-expanded as

$$\begin{aligned} J_1 \left[2 \sum_{k=0}^3 \epsilon^k |\mathcal{A}_{kT}| \right] &= J_1 [2|\mathcal{A}_{0T}|] \\ &+ \epsilon \left\{ 2|\mathcal{A}_{1T}| \cdot J_1' [2|\mathcal{A}_{0T}|] \right\} \\ &+ \epsilon^2 \left\{ 2|\mathcal{A}_{2T}| \cdot J_1' [2|\mathcal{A}_{0T}|] + 2|\mathcal{A}_{1T}|^2 \cdot J_1'' [2|\mathcal{A}_{0T}|] \right\} \\ &+ \mathcal{O}(\epsilon^3) \end{aligned} \quad (6.13)$$

Here an expansion to order 2 is sufficient because the nonlinearity is multiplied by the filter parameter which is of order ϵ .

Therefore, we can equate the various contributions of same order in Eq. (6.12) in order to derive evolution equations at each order ϵ^k . This procedure leads us to the following equations:

- Order ϵ^0

$$D_0^2 u_0 + \Omega_0^2 u_0 = 0 \quad (6.14)$$

- Order ϵ^1

$$\begin{aligned} D_0^2 u_1 + \Omega_0^2 u_1 &= -2D_0 D_1 u_0 - 2\hat{\mu} D_0 u_0 \\ &\quad - 2\hat{\mu}\gamma J_1 [2|\mathcal{A}_{0T}|] \\ &\quad \times \cos[\Omega_0 T_0 - \sigma + \psi_T] \end{aligned} \quad (6.15)$$

- Order ϵ^2

$$\begin{aligned} D_0^2 u_2 + \Omega_0^2 u_2 &= -2D_0 D_1 u_1 - (D_1^2 + 2D_0 D_2) u_0 - 2\hat{\mu}(D_0 u_1 + D_1 u_0) \\ &\quad - 2\hat{\mu}\gamma \left\{ 2|\mathcal{A}_{1T}| \cdot J_1' [2|\mathcal{A}_{0T}|] \right\} \\ &\quad \times \cos[\Omega_0 T_0 - \sigma + \psi_T] \end{aligned} \quad (6.16)$$

- Order ϵ^3

$$\begin{aligned} D_0^2 u_3 + \Omega_0^2 u_3 &= -2D_0 D_1 u_2 - (D_1^2 + 2D_0 D_2) u_1 \\ &\quad - 2(D_0 D_3 + D_1 D_2) u_0 - 2\hat{\mu}(D_0 u_2 + D_1 u_1 + D_2 u_0) \\ &\quad - 2\hat{\mu}\gamma \left\{ 2|\mathcal{A}_{2T}| \cdot J_1' [2|\mathcal{A}_{0T}|] + 2|\mathcal{A}_{1T}|^2 \cdot J_1'' [2|\mathcal{A}_{0T}|] \right\} \\ &\quad \times \cos[\Omega_0 T_0 - \sigma + \psi_T] \end{aligned} \quad (6.17)$$

These equations correspond to the various dynamical equations at each timescale.

From the Eq. (6.14) corresponding to order ϵ^0 , we can deduce that

$$u_0 = \frac{1}{2} \mathcal{B}(T_1, T_2, T_3) e^{i\Omega_0 T_0} + \frac{1}{2} \mathcal{B}^*(T_1, T_2, T_3) e^{-i\Omega_0 T_0}, \quad (6.18)$$

which corresponds to our initial hypothesis of quasi-sinusoidal oscillations for x and its indefinite integral u . We can therefore only keep this term, and consider

that $u_k \equiv 0$ for $k > 0$.

However, in order to obtain meaningful modal equations, we still have split $\mathcal{B}(T_1, T_2, T_3)$ into the various timescales T_1 , T_2 , and T_3 . In the spirit of the modal expansion of Eq. (6.5), we propose the following decomposition

$$\mathcal{B}(T_1, T_2, T_3) = B(T_1) \cdot \sum_{n=0}^{N_{max}} b_n(T_3) e^{in\hat{\Omega}_T T_2}. \quad (6.19)$$

Here, the dependence in T_1 is justified by the fact that dynamics of the microwave's slowly-varying amplitude is ruled by the filter bandwidth which is of order ϵ ; hence, there should be a multiplicative term at this order. The exponential dependence in T_2 is straightforward, since Ω_T was assumed to be of order ϵ^2 . At last, the dynamics of the modal amplitudes b_n should be slower than their detuning frequency $n\Omega_T$, so that it is logical to consider that they depend on the slowest timescale T_3 . The dynamics of the system is therefore ruled by the "fast" complex amplitude $B(T_1)$ associated to the carrier Ω_0 , and the "slow" complex modal amplitudes $b_n(T_3)$ associated to the detuning frequencies $n\Omega_T$.

The modal decomposition of Eq. (6.19) enables the expansion of the amplitude $|\mathcal{A}(t)|$, that is, the determination of the higher order terms $|\mathcal{A}_n|$ which are involved in the global Eq. (6.12). Since only $|\mathcal{A}_0|$, $|\mathcal{A}_1|$ and $|\mathcal{A}_2|$ are involved in our dynamical Eqs. (6.14) to (6.17), this expansion has to be led only up to order ϵ^2 ; hence, according to Eq. (6.10), we obtain the expansion

$$\begin{aligned} x &= D_0 u_0 + \epsilon(D_1 u_0 + D_0 u_1) + \epsilon^2(D_2 u_0 + D_1 u_1 + D_0 u_2) + \mathcal{O}(\epsilon^3) \\ &= \frac{1}{2} i\Omega_0 B \sum_{n=0}^{N_{max}} b_n e^{in\hat{\Omega}_T T_2} e^{i\Omega_0 T_0} + \text{c.c.} \\ &\quad + \epsilon \left\{ \frac{1}{2} \frac{\partial B}{\partial T_1} \sum_{n=0}^{N_{max}} b_n e^{in\hat{\Omega}_T T_2} e^{i\Omega_0 T_0} + \text{c.c.} \right\} \\ &\quad + \epsilon^2 \left\{ \frac{1}{2} \hat{\Omega}_T B \sum_{n=0}^{N_{max}} i n b_n e^{in\hat{\Omega}_T T_2} e^{i\Omega_0 T_0} + \text{c.c.} \right\} \\ &\quad + \mathcal{O}(\epsilon^3), \end{aligned} \quad (6.20)$$

where as usual c.c. stands for the complex conjugate of the preceding term. The

square of the amplitude of x can therefore be determined as

$$\begin{aligned}
|\mathcal{A}|^2 &= \Omega_0^2 |B|^2 \left| \sum_{n=0}^{N_{max}} b_n e^{in\hat{\Omega}_T T_2} \right|^2 \\
&+ \epsilon \left\{ i\Omega_0 \left(\frac{\partial B^*}{\partial T_1} \cdot B - B^* \cdot \frac{\partial B}{\partial T_1} \right) \left| \sum_{n=0}^{N_{max}} b_n e^{in\hat{\Omega}_T T_2} \right|^2 \right\} \\
&+ \epsilon^2 \left\{ \left| \frac{\partial B}{\partial T_1} \right|^2 \left| \sum_{n=0}^{N_{max}} b_n e^{in\hat{\Omega}_T T_2} \right|^2 + \hat{\Omega}_T \Omega_0 |B|^2 \right. \\
&\quad \left. \times \left[\sum_{n=0}^{N_{max}} b_n e^{in\hat{\Omega}_T T_2} \sum_{n=0}^{N_{max}} n b_n^* e^{-in\hat{\Omega}_T T_2} + \text{c.c.} \right] \right\} \\
&+ \mathcal{O}(\epsilon^3). \tag{6.21}
\end{aligned}$$

This expansion is of the kind $|\mathcal{A}|^2 = \alpha_0^2 + \epsilon \alpha_1^2 + \epsilon^2 \alpha_2^2$ from which we can deduce that the amplitude expands as $|\mathcal{A}| = \alpha_0 + \epsilon(\alpha_1^2/2\alpha_0) + \epsilon^2(\alpha_2^2/2\alpha_0)$, thereby leading to

$$\begin{aligned}
|\mathcal{A}_0| &= \Omega_0 |B| \left| \sum_{n=0}^{N_{max}} b_n e^{in\hat{\Omega}_T T_2} \right| \\
|\mathcal{A}_1| &= \frac{1}{2|B|} i \left(\frac{\partial B^*}{\partial T_1} \cdot B - B^* \cdot \frac{\partial B}{\partial T_1} \right) \left| \sum_{n=0}^{N_{max}} b_n e^{in\hat{\Omega}_T T_2} \right| \\
|\mathcal{A}_2| &= \frac{1}{2\Omega_0 |B|} \left| \frac{\partial B}{\partial T_1} \right|^2 \left| \sum_{n=0}^{N_{max}} b_n e^{in\hat{\Omega}_T T_2} \right| \\
&+ \frac{1}{2} \hat{\Omega}_T |B| \frac{\left[\sum_{n=0}^{N_{max}} b_n e^{in\hat{\Omega}_T T_2} \sum_{n=0}^{N_{max}} n b_n^* e^{-in\hat{\Omega}_T T_2} + \text{c.c.} \right]}{\left| \sum_{n=0}^{N_{max}} b_n e^{in\hat{\Omega}_T T_2} \right|}. \tag{6.22}
\end{aligned}$$

These explicit relationships will enable us to understand exactly how the Bessel nonlinearity does affect the dynamics of the OEO at the various timescales.

The equations of higher order can not be solved analytically as the Eq. (6.14) corresponding to order ϵ^0 . But we can notice the equation of order ϵ^k may be considered as an undamped harmonic oscillator of variable u_k and eigenfrequency Ω_0 , with external forcing. The so-called secularity conditions are obtained by equating to zero the resonant terms of this external forcing, thereby impeding a divergence

to infinity of the higher order variables u_k .

At order ϵ^1 , cancelling the resonant term yields

$$\begin{aligned} -i\Omega_0 \frac{\partial B}{\partial T_1} \sum_{n=0}^{N_{max}} b_n e^{in\hat{\Omega}_T T_2} - i\hat{\mu}\Omega_0 B \sum_{n=0}^{N_{max}} b_n e^{in\hat{\Omega}_T T_2} \\ - \hat{\mu}\gamma J_1 [2|\mathcal{A}_{0T}|] e^{-i\sigma} e^{i\psi_T} = 0. \end{aligned} \quad (6.23)$$

According to Eq. (6.20), the slowly-varying amplitude of the microwave at order ϵ^0 reads

$$x_0 = \frac{1}{2} \mathcal{A}(T_1, T_2, T_3) e^{i\Omega_0 T_0} + \frac{1}{2} \mathcal{A}^*(T_1, T_2, T_3) e^{-i\Omega_0 T_0} \quad (6.24)$$

with $\mathcal{A}(T_1, T_2, T_3) = i\Omega_0 \mathcal{B}(T_1, T_2, T_3)$; therefore, we may assume

$$\begin{aligned} a_n(T_3) &\equiv b_n(T_3) \\ A(T_1) &= i\Omega_0 B(T_1) \\ e^{i\psi_T} &= \frac{\mathcal{A}_T}{|\mathcal{A}_T|} = i \frac{B_T}{|B_T|} \frac{\sum_{n=0}^{N_{max}} b_n e^{in\hat{\Omega}_T T_2}}{\sum_{n=0}^{N_{max}} b_n e^{in\hat{\Omega}_T T_2}}. \end{aligned} \quad (6.25)$$

We can furthermore assume the approximation $a_n(T_3 - T) \simeq a_n(T_3)$ because the timescale T_3 is much slower than Ω_T which is of order ϵ^2 . Using the secular Eq. (6.23), the equation ruling the dynamics at the scale T_1 can therefore be written as

$$\frac{\partial A}{\partial T_1} = -\hat{\mu}A - 2\hat{\mu}\gamma e^{-i\sigma} \frac{J_1 \left[2|A_T| \cdot \left| \sum_{n=0}^{N_{max}} a_n e^{in\hat{\Omega}_T T_2} \right| \right]}{\left[2|A_T| \cdot \left| \sum_{n=0}^{N_{max}} a_n e^{in\hat{\Omega}_T T_2} \right| \right]} A_T. \quad (6.26)$$

It may be interesting to note that in the single-mode approximation (*i. e.* setting $a_n \equiv 0$ except a_0), this equation degenerates to Eq. (5.10), that is, to the equation we had obtained in our initial single-mode analysis.

We now need an equation to rule the dynamics of the modal amplitudes $a_n(T_3)$. For that purpose, we have to consider the resonant term of Eq. (6.17) of the order ϵ^3 because it is the only equation to have a D_3 derivative factor. Cancellation of

the resonant term at that order yields

$$\begin{aligned}
& -\hat{\mu}\hat{\Omega}_T B \sum_{n=0}^{N_{max}} b_n e^{in\hat{\Omega}_T T_2} - i\Omega_0 B \sum_{n=0}^{N_{max}} \frac{\partial b_n}{\partial T_3} e^{in\hat{\Omega}_T T_2} \\
& -\hat{\Omega}_T \frac{\partial B}{\partial T_1} \sum_{n=0}^{N_{max}} n b_n e^{in\hat{\Omega}_T T_2} - \hat{\mu}\gamma \left\{ 2|\mathcal{A}_{2T}| \cdot J_1' [2|\mathcal{A}_{0T}|] \right. \\
& \left. + 2|\mathcal{A}_{1T}|^2 \cdot J_1'' [2|\mathcal{A}_{0T}|] \right\} e^{-i\sigma} e^{i\psi_T} = 0.
\end{aligned} \tag{6.27}$$

This equation englobes the collective dynamics of the modes, but does not enable to track the dynamics of an individual mode. In order to extract modal equations, let us write the left-hand side of Eq. (6.27) under the form

$$\mathcal{H}(T_1, T_2, T_3) = \sum_{n=0}^{N_{max}} \mathcal{H}_n(T_1, T_2, T_3) e^{in\hat{\Omega}_T T_2} = 0. \tag{6.28}$$

If $\partial\mathcal{H}_n/\partial T_2 \simeq 0$, then we can project this collective dynamics onto the various cavity modes $m\Omega_T$ following

$$\begin{aligned}
\mathcal{H}(T_1, T_2, T_3) = 0 & \Rightarrow \int_0^T \mathcal{H}(T_1, T_2, T_3) e^{-im\hat{\Omega}_T T_2} dT_2 = 0 \\
& \Rightarrow \sum_{n=0}^{N_{max}} \mathcal{H}_n(T_1, T_2, T_3) \int_0^T e^{in\hat{\Omega}_T T_2} e^{-im\hat{\Omega}_T T_2} dT_2 = 0 \\
& \Rightarrow \mathcal{H}_n(T_1, T_2, T_3) = 0 \quad \forall n,
\end{aligned} \tag{6.29}$$

that is, we can equate each modal term \mathcal{H}_n to zero. If we assume that the collective dynamics has a slower dynamics than the individual modes, the condition $\partial\mathcal{H}_n/\partial T_2 \simeq 0$ can be considered as valid in our case because the T_2 dependence only appears in a norm on the denominator of the phase factor $e^{i\psi_T}$. Therefore, combining Eqs. (6.25), (6.27) and (6.29) give the following equation for the modal dynamics

$$\begin{aligned}
\frac{\partial a_n}{\partial T_3} = -in \frac{\hat{\Omega}_T}{\Omega_0} \left\{ \hat{\mu} + \frac{1}{A} \frac{\partial A}{\partial T_1} \right\} a_n \\
- 2\hat{\mu}\gamma e^{-i\sigma} \frac{\left\{ 2|\mathcal{A}_{2T}| \cdot J_1' [2|\mathcal{A}_{0T}|] + 2|\mathcal{A}_{1T}|^2 \cdot J_1'' [2|\mathcal{A}_{0T}|] \right\}}{\left[2|\mathcal{A}_T| \cdot \left| \sum_{n=0}^{N_{max}} a_n e^{in\hat{\Omega}_T T_2} \right| \right]} \frac{A_T}{A} a_n,
\end{aligned} \tag{6.30}$$

where the $|\mathcal{A}_n|$ are defined as in Eq. (6.22). The coupled system of Eqs. (6.26) and (6.30) constitute the final result of the modal analysis. They may enable to understand the intrinsic mechanisms of the mode competition in OEOs.

6.6 Multimode dynamics of OEOs: a paradigm for globally coupled oscillators

From the multiple time scale analysis, it appears that in the multimode regime, the system is constituted by hundreds of microwave ring-cavity modes which are strongly and nonlinearly coupled through the Mach-Zehnder interferometer. To the best of our knowledge, earlier studies on OEOs have never reported such multimode behavior. Here, experimental and analytical evidences of such a multimodal dynamics have been given.

It can be seen in Eq. (6.30) that the modal variables a_n are subjected to a nonlinear global coupling, along with winding frequency terms which are stronger as the modal frequency detunings $n\Omega_T$ increase. It is worth noting that the modes have not been coupled phenomenologically as it is sometimes done in the literature: here, the coupling emerges naturally from the intrinsic nonlinearity of the system. This global nonlinear coupling is indeed very complex, if one remembers that terms as complicated as those of Eq. (6.22) are involved in the modal dynamics.

As emphasized earlier, the key advantage of a modal expansion approaches is that they enable to track the dynamics of individual modes, and to have an insight into the nature of their coupling. This complexity can not even be suspected if one only considers Eq. (5.10) which rules the total amplitude $\mathcal{A}(t)$.

From a fundamental point of view, it is still to be investigated if the complexity of this modal dynamics may not be the source of other types of behaviors, different from single-mode and “trivial” collective multimode behavior; this possibility can be considered as probable if one keeps in mind the high dimensionality of the system, and the unexpected emergence of breather-like behaviors at the other extreme of this same architecture (cf. Chapter 2).

From a technological point of view, it should be in principle possible to evaluate the feasibility of mode-locking schemes, either with resonant frequency modulation or with tailored saturable absorbers. Here again, the possibility to follow the dynamics of individual modes, and potentially to investigate their stability, would be a convenient tool which could open the way to interesting results.

6.7 Conclusion

We have given a insight on the stochastic and multimode dynamics of OEOs. It has first been shown that the phase noise properties of the oscillator can be recovered

by taking into consideration an additive and a multiplicative noise in the complex amplitude equation.

We have also studied the multimode dynamics of the system, and shown that under certain conditions, the mode competition could persist even at macroscopic timescales. The multiple time scale method has permitted to determine approximate modal equations where it clearly appears that the cavity-modes are subjected to a nonlinear global coupling. This mechanism where the center-most modes are weakly damped but strongly coupled is therefore responsible for the observed behavior, that is, persisting multimode competition within few MHz around the central frequency of the RF filter.

Part III

Transverse-Mode Control in Vertical-Cavity Surface-Emitting Lasers

Chapter 7

Modelization of Multimode VCSELs with Polarization- and Frequency-Selective Feedback

“A splendid light has dawned on me about the absorption and emission of radiation.”

Albert Einstein, in a letter to Michele Besso.

7.1 Introduction

WE will focus in this chapter on the modelization of Vertical-Cavity Surface-Emitting Semiconductor Lasers (VCSELs) with polarization- and frequency selective feedback. It is known that for moderate to strong pumping, VCSELs exhibit a strong multi-transverse mode behavior, as well as a complex polarization dynamics. An efficient way to control the dynamical and spectral emission properties of VCSELs is to subject them to polarization- and frequency-selective optical feedback. The aim of this chapter is to give an introduction to VCSELs and to derive a model to study the frequency-selective feedback stabilization scheme. This analysis is intended to provide an analytic insight into the optimal conditions under which this feedback control strategy could be satisfactory.

7.2 Principles of VCSELs

This section is devoted to some generalities on the fundamental operation principles of VCSELs. After a brief review on semiconductor lasers, the specific case of VCSELs will be addressed, with a particular emphasis on the gain medium, the optical resonator, and the carrier injection/confinement.

Semiconductor lasers

In semiconductor lasers, the concept of energy levels is replaced by the one of energy bands, namely the **conduction** band lying around an energy level E_c and filled with electrons; and the **valence** band lying around E_v and filled with holes. These two bands are separated by a **band-gap energy** E_g , and instead of stimulated decay between atomic energy levels, the coherent photons of frequency $\nu \simeq h/E_g$ originate from the stimulated recombination between the electrons and holes of the two bands.

In the semiconductor bulk material, the probability for an electron to occupy a given state of energy E is given by the Fermi-Dirac distribution

$$f(E) = \frac{1}{\exp[(E - E_f)/kT] + 1}, \quad (7.1)$$

where k is the **Boltzmann constant**, T the absolute temperature and E_f is the **Fermi level**. On the other hand, the optical joint density of states with which a photon of energy $h\nu$ interacts with the semiconductor bulk medium can be explicitly expressed as

$$\varrho(\nu) = 4\pi \frac{(2m_r)^{3/2}}{h^2} (h\nu - E_g)^{1/2}, \quad (7.2)$$

where h is the **Planck constant**, and $m_r = m_c m_v / (m_c + m_v)$ is the reduced electron-hole mass, m_c and m_v being respectively the effective masses of the electrons and the holes in their bands.

The gain of the semiconductor material can be in first approximation defined as the exponential amplification rate of the stimulated radiations in the medium. It can be demonstrated that the optical gain in the semiconductor medium is given by

$$G(\nu) \simeq \frac{\varrho(\nu)}{\tau_r} \frac{c^3}{8\pi\nu^2} [f(E_c) - f(E_v)], \quad (7.3)$$

where τ_r is the *electron-hole recombination lifetime*. This gain is negative at thermal equilibrium because $E_c > E_v$, implying $f(E_c) < f(E_v)$ according to Eq. (7.1). Therefore, as all materials, semiconductor media absorb light under usual thermodynamic conditions.

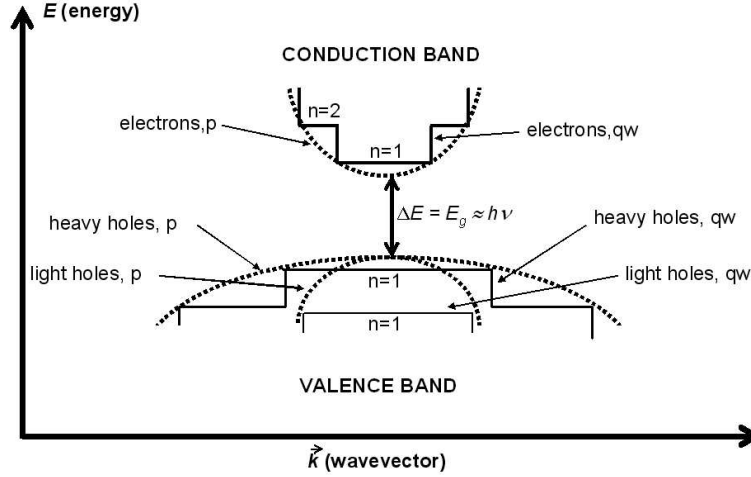


Figure 7.1. The E - \vec{k} diagram of a quantum-well VCSEL. The parabolic profile of a conventional p - n junction laser (p) and the quantized (step-like) variations induced by the longitudinal confinement (qw) have been represented. The valence band is divided into two sub-bands, namely the heavy-hole and the light-hole bands.

When the semiconductor medium is doped, the Fermi level moves in opposite directions depending on the nature of the doping: upwards for a n -doping, and downwards for a p -doping. Therefore, when a p - n junction is forward-biased, the Fermi level splits into two *quasi-Fermi levels* E_{fc} and E_{fv} respectively associated to the electrons in the conduction band and to the holes in the valence band. In consequence, if we attach the Fermi distributions f_c and f_v to these quasi-Fermi levels, the gain in the semiconductor medium reads

$$G(\nu) \simeq \frac{g(\nu)}{\tau_r} \frac{c^3}{8\pi\nu^2} [f_c(E_c) - f_v(E_v)], \quad (7.4)$$

and for strong enough doping/pumping, the double condition $E_{fc} > E_c$ and $E_{fv} < E_v$ becomes fulfilled, yielding $G(\nu) > 0$: **the semiconductor medium becomes active**. Here, the inversion of population is realized between electrons and holes around their respective quasi-Fermi levels, and coherent radiation is generated by their stimulated recombination.

By analogy to the Fabry-Pérot resonator, the resonator associated to this gain medium may simply be the semiconductor/air interface. Despite its low reflectivity (~ 0.3), this reflector is nevertheless sufficient to overcome the cavity and facet losses, thereby enabling laser emission.

The above lasers are commonly referred to as **edge-emitter** semiconductor lasers. Some sophistications (like hetero-structures) can be brought to increase

their performances, and nowadays, they are used in several areas of science and technology, ranging from lightwave telecommunications to multimedia systems; they can even be used, as we have seen in the precedent chapters, for ultra-pure microwave generation.

However, the most fabricated semiconductor lasers rely on a different architecture, and bear a specific name: **VCSELs**. Typically, the VCSEL cavity is a cylinder of a one-wavelength height and few micrometers of diameter. The active medium is a very thin layer at the mid-height of the cavity which is passive elsewhere, and the resonator is made of **Bragg mirrors** of exceptionally high reflectivity. Hereafter we briefly review the inner structure of these lasers with a particular emphasis on the active medium, the Bragg reflectors, and the confinement mechanisms for the carriers.

7.2.1 The active medium: quantum wells

In VCSELs, the active medium typically consists in several **quantum wells**, which geometrically define thin layers of the cylindrical waveguide. When an electron is localized within a thin semiconductor layer sandwiched with layers of higher bandgap energy, the electron is energetically trapped into a potential energy well. From the quantum mechanics point of view, the energy of this electron is therefore *quantized*. In the infinite well approximation, the energy levels are distributed as

$$E_n = \frac{h^2}{8m_e W^2} n^2, \quad (7.5)$$

where $W \sim 10$ nm is the width of the quantum well, and m_e is the mass of the electron.

Hence, a straightforward advantage of quantum wells is that it enables to achieve very high concentrations of electrons (and holes) by trapping them into these localized energy levels, instead of having electrons and holes which are energetically spread as in conventional *p-n* junction (see Fig. 7.1). Such high densities in discrete energy levels enable to obtain significantly lower threshold currents through a higher recombination efficiency. Moreover, another advantage of quantum wells is that they allow a great flexibility in terms of lasing wavelengths, just by changing the width of the wells (and thereby the energy levels): this is much more complicated in usual *p-n* junctions lasers, where doing so would require the modification of the doping concentrations. Unfortunately, here also resides the disadvantage of quantum well lasers: they are very sensitive to temperature, because thermic dilatation may drastically modify the energy level values through W [119].

The schematic representation of a VCSEL is shown in Fig. 7.2. Usually, there are several quantum wells in the active region, so that the term **multi-quantum**

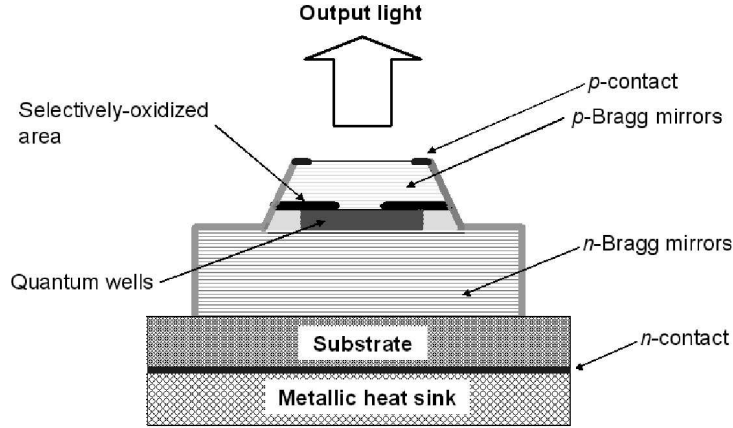


Figure 7.2. A top-emitting selectively-oxidized VCSEL. Here, the carriers and the photons are counter-propagating.

well (MQW) is sometimes used to characterize the gain medium. To simplify the modelling, we will scale all these wells to a single one.

7.2.2 The resonator: Bragg reflectors

A particular feature of VCSELs is that their cavity length is very short. In fact, this cavity is typically only one wavelength long ($\sim 1 \mu\text{m}$). Therefore, and this is an important advantage relatively to the edge-emitter lasers, VCSELs emit a single longitudinal mode.

However, the active region constituted with the quantum wells is extremely thin, generally thinner than $0.05 \mu\text{m}$, so that the one-trip amplification is very small, of the order of 1%. Hence, comparatively to edge-emitting lasers whose active region can be as long as $300 \mu\text{m}$, VCSELs need a resonator of exceptionally high reflectivity in order to compensate for the low amplification rate. Such reflectivities are achieved with the so-called **Distributed Bragg Reflectors (DBR)**, which are constituted with alternatively stacked low- and high-index layers. The thickness of each of these layers is equal to one fourth of the laser's wavelength in the corresponding medium, and it can be demonstrated that for a number N of layer pairs, the overall reflectivity amounts to

$$R_B = \left[\frac{1 - \frac{n_{tr}}{n_{in}} \left(\frac{n_L}{n_H} \right)^{2N}}{1 + \frac{n_{tr}}{n_{in}} \left(\frac{n_L}{n_H} \right)^{2N}} \right]^2, \quad (7.6)$$

where n_L and n_H are respectively the low and high reflective indices of the stack, while n_{in} and n_{tr} are respectively the refraction indices of the media correspond-

ing to the incident and transmitted wave. It is straightforward from Eq. (7.6) that the reflectivity rapidly converges to 1 as the number of layer pairs N goes to infinity. In general, the number of pairs which are needed for a sufficiently high reflectivity ranges from 20 to 40.

These Bragg reflectors, which are respectively also p -doped or n -doped for the top and bottom mirror stacks, enable to obtain a reflectivity higher than 99%, thereby permitting to overcome the cavity losses despite the very low amplification rate. This high reflectivity also ensures that the quantum wells which are localized at the center of the cavity coincide with an anti-node of the longitudinal mode amplitude, thereby ensuring a maximal interaction between the light and the active medium.

7.2.3 Injection and confinement of carriers

Carrier injection

The principal difference between VCSELs and edge-emitter lasers is the fact that the carriers are injected along the propagation direction of the output light. Hence, considering the cylindrical structure of the VCSEL, the carriers and the photons are either co- or counter-propagating, perpendicularly to the thin disk of the active region. Conventionally, a VCSEL is said to be **top-emitting** if it emits through the p -DBR mirror, and is said to be **bottom-emitting** if the emission is made through the n -DBR mirror.

Figure 7.2 for example represents a top-emitting VCSEL.

Transverse confinement of carriers

As emphasized earlier, the active region is a very thin disk at the middle of the VCSEL cavity. Therefore, a mechanism should somehow be implemented in order to steer these carriers towards the smallest area (or spot) possible around the center of the active region cross-section, in order to compensate for the transverse diffusion of the injected carriers: this is the concept of **transverse confinement**. Effectively, without confinement, the carriers would spread across the whole surface of the disk, thereby inducing a lower surface density, and a lower overall efficiency. In fact, carrier confinement is tightly related to optical confinement because the photons originate from stimulated recombination, that is, the optical field more or less overlaps the cross-section of the carrier flow across the surface of the active region. Therefore, from a technological point of view, the principal interest of carrier confinement is that it favours the fundamental mode emission, which is the most important for most of technological applications.

There are two principal carrier confinement methods.

The first one is **index-guiding**, where the carriers are confined by the conductivity, in the sense that the cylindrical waveguide filled with semiconductor material is surrounded by a medium of very low conductivity. Hence, the injected electrons are forced to stay within the waveguide and to cross the active region section. An archetypal example of the so-called **index-guided air-post** VCSEL, where the cylindrical waveguide is surrounded by air. In fact, this index-guided structure also serves to guide the optical transverse modes, but its drawbacks are an inefficient heat dissipation from the laser cavity and a carrier loss induced by outer surface recombination.

The second confinement method is **gain-guiding**, where the carriers are actively confined towards the axis of the cylinder waveguide. In *ion-implanted VCSELs*, for example, some ions (most of the time H^+ , but also sometimes F^+ , N^+ , or O^+) are introduced with a tubular symmetry in order to trap the electrons inside the “tube”. However, ion-implantation generally damages the crystalline structure of the semiconductor, and the ions also diffuse in the bulk material, thereby limiting the lifetime of the laser.

An hybrid solution combines index-guiding and gain-guiding: these are **selectively oxide-confined VCSELs**. In these lasers, the active region is surrounded by a thin annular oxidized area of significantly lower conductivity. Here, gain-guiding is achieved because the carriers predominantly pass through the non-oxidized cross-section, and index-guiding originates from the difference in refraction indices between the active region and its lateral surroundings.

Fig. 7.2 shows how, by being placed just above the multi-quantum wells layer, the selectively-oxidized area can enable carrier confinement.

7.2.4 Emission properties of VCSELs

Multi-transverse mode behavior

As earlier emphasized, VCSELs are intrinsically single-longitudinal mode lasers. However, the cylindric waveguide supports a certain number of transverse modes depending on its diameter and on the optical properties (refraction indices) of its different sub-structures. Typically, this number of transverse modes may easily be higher than 20 for a diameter of only $10\ \mu\text{m}$. These modes have different stability properties, which are strongly related to their transverse confinement factor, that is, the the overlap between the spatial profile of the mode and the circular section of the VCSEL’s active medium. In general, the higher the order of the mode, the smaller its transverse confinement factor: hence, the fundamental mode results as the most stable of all. Therefore, when the VCSEL is pumped just above threshold, the first mode to lase is generally the fundamental mode, whose spatial profile is simply a bright spot.

When the diameter of the VCSEL is small ($< 5\ \mu\text{m}$), the fundamental mode

may lase alone even when the laser is pumped quite far above threshold. This is due to the fact that the waveguide supports only very few modes, whose transverse confinement factors are very different. But when the diameter of the VCSEL is increased, the waveguide supports much more transverse modes whose confinement factors are nearly degenerated when they are of the same order. Hence, as the pumping is increased, the quasi-degenerated higher order modes start to lase for almost the same threshold value.

In all cases, higher transverse modes are always excited when the pumping is strong enough. Several of these modes may compete and the resulting optical field would display a very complex spatiotemporal dynamics which has been thoroughly studied in recent years (see refs. [81, 82, 120, 121] and references therein).

Multi-polarization behavior

The circular aperture VCSELs supports two orthogonal polarizations. Ideally these two polarization directions are degenerated, but in reality, the bulk semiconductor material, the active medium and the Bragg mirrors are anisotropic, namely **dichroic** and **birefringent**. Dichroism induces different attenuation factors to the two polarizations, while the effect of birefringence is to induce different optical phase-shifts for these polarizations. The first consequence of these anisotropies is that dichroism favours one polarization at the threshold (lifting of the losses degeneracy), while when both polarizations are lasing, they are spectrally splitted because of birefringence (lifting of optical phase degeneracy).

Therefore, when the VCSEL is pumped far above threshold, a rich multi-polarization behavior can be observed (see refs. [83, 85, 91] and references therein).

7.3 Equations for the field and carrier dynamics

The aim of this section is the derivation of deterministic evolution equations which can describe the dynamics of a VCSEL submitted to polarization- and frequency-selective feedback (PFSF). Such equations are intended to provide a theoretical understanding of the effect of PFSF on the spectral and dynamical emission properties of the VCSEL.

Full spatiotemporal models have yet been proposed for the modelization of solitary VCSELs [122]. However, despite their relatively high accuracy, they may not be computationally cost effective in our case since we would simultaneously have to take into account carrier diffusion, the field diffraction and the external feedback time delay.

An interesting alternative is to implement a **modal-expansion model** for the laser electric field. The advantage of a modal model is that on the one hand, the simulations can be performed in a reasonable time, and on the other, the frequency-shift of each transverse mode can be determined *a priori*, so that we can easily

match the central frequency of the grating to the frequency of the transverse mode we want to feed back into the laser.

The mesoscopic evolution equations we are going to derive are inspired from the modal expansion model for VCSELs proposed in [121], which corresponds to a modal decomposition of the spatiotemporal model presented in [120]. The main difference between these contributions and our study is the presence of polarization- and frequency-filtered feedback in our case.

7.3.1 Field dynamics

Maxwell equations

The field equations will be derived on a semi-classical basis; we therefore start from the Maxwell equations

$$\vec{\nabla} \cdot \vec{\mathcal{D}} = 0 \quad (7.7)$$

$$\vec{\nabla} \cdot \vec{\mathcal{B}} = 0 \quad (7.8)$$

$$\vec{\nabla} \times \vec{\mathcal{E}} = -\frac{\partial \vec{\mathcal{B}}}{\partial t} \quad (7.9)$$

$$\vec{\nabla} \times \vec{\mathcal{H}} = \vec{\mathcal{J}} + \frac{\partial \vec{\mathcal{D}}}{\partial t}, \quad (7.10)$$

where we have assumed that there are no free charges.

It is convenient to rewrite these equations in the Fourier domain, using the transformation

$$\tilde{\mathcal{E}}_k(\omega) = \frac{1}{\sqrt{2\pi}} \int_{-\infty}^{+\infty} \mathcal{E}_k(t) e^{-i\omega t} dt, \quad (7.11)$$

where $\mathcal{E}_k(t)$ is a scalar projection of the electric field vector onto a cartesian direction $k = x, y, z$. We can assume the ohmic relation $\vec{\mathcal{J}} = \sigma \vec{\mathcal{E}}$ where σ is the electric conductivity; and we can also assume a linear relation $\vec{\mathcal{P}} = \varepsilon_0 [\chi^{tot}] \cdot \vec{\mathcal{E}}$ between the material polarization and the electric field, $[\chi^{tot}]$ being the total susceptibility tensor. Note that the conductivity and the susceptibility will be assumed to be frequency-independent during the whole thesis.

It can therefore be shown from the Maxwell equations that if the total susceptibility tensor is diagonal, the cartesian components k of the electric field $\vec{\mathcal{E}}$ obey

$$\vec{\nabla}^2 \tilde{\mathcal{E}}_k(\omega, \vec{r}) + \left(\frac{\omega}{c}\right)^2 \varepsilon_k(\omega, \vec{r}, N) \tilde{\mathcal{E}}_k(\omega, \vec{r}) = 0 \quad (7.12)$$

with

$$\varepsilon_k(\omega, \vec{r}, N) = 1 + \chi_k^{tot}(\omega, \vec{r}, N) - \frac{i\sigma}{\varepsilon_0\omega} \quad (7.13)$$

$$= 1 + \chi_k^b + \Delta\chi^{exc}(\vec{r}) + \chi_k^{nl}(\vec{r}, N) - \frac{i\sigma}{\varepsilon_0\omega}. \quad (7.14)$$

In the above equation, the susceptibility has been explicitly expressed as a sum of various components: the **background material susceptibility** χ_k^b , supposed to be constant; the **excess susceptibility** $\Delta\chi^{exc}(\vec{r})$, which is induced by the quantum wells, so that it is uniformly equal to zero except in the quantum wells; and finally the **nonlinear susceptibility** $\chi_k^{nl}(\vec{r}, N)$, which corresponds to the susceptibility variation induced by the laser pumping. This latter contribution accounts for the population inversion, and therefore strongly depends on the carrier population density N . As the excess susceptibility, the nonlinear susceptibility is strictly equal to zero outside the active region volume. All these susceptibilities have *a priori* complex values, and except for χ_k^b , their norm is small compared to 1. However, χ_k^{tot} is assumed to have different values along the various axes k : therefore, we consider the bulk and active media to be *anisotropic*.

Using the relationship $n_k^2 = 1 + \chi_k^{tot}$ where n is the complex refractive index, we can explicitly write the refractive index along each direction as

$$n_k(\vec{r}, N) = [n_{b,k} + n_{s,k}(\vec{r}, N)] + i[n_{g,k}(\vec{r}, N) - n_{a,k}(\vec{r})], \quad (7.15)$$

with

$$n_{b,k} = \sqrt{1 + \Re[\chi_k^b]} \quad (7.16)$$

$$n_{s,k}(\vec{r}, N) = \frac{\Re[\Delta\chi^{exc}(\vec{r})]}{2n_{b,k}} + \frac{\Re[\chi_k^{nl}(N)]}{2n_{b,k}} \quad (7.17)$$

$$n_{a,k}(\vec{r}) = -\frac{\Im[\chi_k^b]}{2n_{b,k}} - \frac{\Im[\Delta\chi^{exc}(\vec{r})]}{2n_{b,k}} \quad (7.18)$$

$$n_{g,k}(\vec{r}, N) = -\frac{\Im[\chi_k^{nl}(\vec{r}, N)]}{2n_{b,k}}, \quad (7.19)$$

where $n_{b,k}$ is the background refractive index, $n_{s,k}$ is the carrier-induced refraction index shift, $n_{a,k}$ is the internal attenuation index factor, and $n_{g,k}$ is the internal gain factor which is induced by the pumping. We therefore see that the pumping has two principal effects: a modification of the refraction index, and a modification of global attenuation factor. In particular, the pumping may change the sign of this attenuation factor in the quantum wells medium, thereby transforming it from passive to active.

Modal expansion

We now assume a modal expansion of the kind

$$\tilde{\mathcal{E}}_k(\omega, \vec{r}) = \sum_{\nu} \tilde{\mathcal{E}}_{k,\nu}(\omega, z) \Phi_{\nu}(\vec{r}_{\perp}), \quad (7.20)$$

where $\vec{r}_{\perp} = (x, y)$, ν stands for the cavity modes of the optical waveguide, and $\Phi_{\nu}(\vec{r}_{\perp})$ stands for their normalized planar profiles. This “planar” expansion where the electric field is assumed to vary in z while the transverse spatial dependence is contained in the modal profiles is valid for weakly index-guided structures, where the waveguide-induced polarization effects can be neglected.

Therefore, Eq. (7.12) may be explicitly rewritten as

$$\sum_{\nu} \left\{ [\nabla_{\perp}^2 + \partial_z^2] \tilde{\mathcal{E}}_{k,\nu}(\omega, z) \Phi_{\nu}(\vec{r}_{\perp}) + \left(\frac{\omega}{c}\right)^2 \varepsilon_k(\omega, \vec{r}, N) \tilde{\mathcal{E}}_{k,\nu}(\omega, z) \Phi_{\nu}(\vec{r}_{\perp}) \right\} = 0. \quad (7.21)$$

We can use the so-called **effective index approximation** to separate this equation into a **transverse equation** of variable $\Phi_{\nu}(\vec{r}_{\perp})$ which would exclusively gather the waveguiding aspects, and a **longitudinal equation** of variable $\tilde{\mathcal{E}}_{k,\nu}(\omega, z)$ which would describe the modal dynamics of the system. We will need for that purpose a *separation variable* labelled as $\beta_{eff}(\omega) = [\omega/c]n_{eff}(\omega)$, which enables to split Eq. (7.21) into a transverse and a longitudinal equation following

$$\begin{aligned} & \sum_{\nu} \tilde{\mathcal{E}}_{k,\nu}(\omega, z) \left\{ \nabla_{\perp}^2 \Phi_{\nu}(\vec{r}_{\perp}) \right. \\ & \left. + \left(\frac{\omega}{c}\right)^2 \left[1 + \Re(\chi^b) + \Re(\Delta\chi^{exc}(\vec{r})) - n_{eff}^2(\omega) \right] \Phi_{\nu}(\vec{r}_{\perp}) \right\} = 0 \quad (7.22) \\ & \sum_{\nu} \Phi_{\nu}(\vec{r}_{\perp}) \left\{ \partial_z^2 \tilde{\mathcal{E}}_{k,\nu}(\omega, z) + \left(\frac{\omega}{c}\right)^2 \left[\Re(\Delta\chi_k^b) + i\Im(\chi_k^b) \right. \right. \\ & \left. \left. + i\Im(\Delta\chi^{exc}(\vec{r})) + \chi_k^{nl}(\vec{r}, N) - \frac{i\sigma}{\varepsilon_0\omega} + n_{eff}^2(\omega) \right] \tilde{\mathcal{E}}_{k,\nu}(\omega, z) \right\} = 0, \end{aligned} \quad (7.23)$$

where

$$\begin{aligned} \chi^b &= \frac{1}{2}[\chi_x^b + \chi_y^b] \\ \Delta\chi_x^b &= \frac{1}{2}[\chi_x^b - \chi_y^b] = -\Delta\chi_y^b. \end{aligned} \quad (7.24)$$

This separation will enable to uncouple the transverse and the longitudinal dynamical properties of the system.

From Eq. (7.22), we can deduce that the orthonormal modal profiles are solutions of the eigenfunction equation

$$\nabla_{\perp}^2 \Phi_{\nu}(\vec{r}_{\perp}) + \left(\frac{\omega}{c}\right)^2 \left[1 + \Re(\chi^b) + \Re(\Delta\chi^{exc}(\vec{r})) - n_{eff}^2(\omega)\right] \Phi_{\nu}(\vec{r}_{\perp}) = 0, \quad (7.25)$$

while on the other hand, we can track the dynamics of individual modes by projecting Eq. (7.23) onto a transverse mode $\Phi_{\mu}^*(\vec{r}_{\perp})$, thereby yielding

$$\begin{aligned} \partial_z^2 \tilde{\mathcal{E}}_{k,\mu}(\omega, z) + \left(\frac{\omega}{c}\right)^2 \left[\Re(\Delta\chi_k^b) + i\Im(\chi_k^b) + i\Gamma_{\mu}^{(t)}\Im(\Delta\chi^{exc}(z)) \right. \\ \left. + \bar{\chi}_{k,\mu}^{nl}(z, N) - \frac{i\sigma}{\varepsilon_0\omega} + n_{eff}^2(\omega) \right] \tilde{\mathcal{E}}_{k,\mu}(\omega, z) = 0, \end{aligned} \quad (7.26)$$

where the transverse mode confinement factor $\Gamma_{\mu}^{(t)}$ and the transverse modal susceptibility $\bar{\chi}_{k,\mu}^{nl}$ are defined as

$$\Gamma_{\mu}^{(t)} = \iint_{S_w} |\Phi_{\mu}(\vec{r}_{\perp})|^2 d^2\vec{r}_{\perp} \quad (7.27)$$

$$\bar{\chi}_{k,\mu}^{nl}(z, N) = \iint_{S_w} \chi_k^{nl}(\vec{r}, N) |\Phi_{\mu}(\vec{r}_{\perp})|^2 d^2\vec{r}_{\perp}, \quad (7.28)$$

S_w being the surface of the waveguide cross-section.

It appears that Eq. (7.26) can be solved if and only if the modal profiles $\Phi_{\mu}(\vec{r}_{\perp})$ are explicitly known, in particular for the determination of the transverse confinement factors and modal susceptibilities: we therefore need first to find the solutions of the cavity-modes Eq. (7.25).

The waveguide eigenfunctions

An eigenfrequency Ω_{μ} can univocally be associated to the cold-cavity eigenmodes $\Phi_{\mu}(\vec{r}_{\perp})$. Therefore, Eq. (7.25) can be rewritten under the form

$$\left[\nabla_{\perp}^2 + \left(\frac{\Omega_{\mu}}{c}\right)^2 \cdot 2n_b \Delta n(\vec{r}_{\perp}) \right] \Phi_{\mu}(\vec{r}_{\perp}) = \left(\frac{W_{\mu}}{r_w}\right)^2 \Phi_{\mu}(\vec{r}_{\perp}), \quad (7.29)$$

where the background refractive index, the excess refractive index and the cavity-mode eigenvalue are respectively defined as

$$\begin{aligned} n_b &= \sqrt{1 + \Re[\chi^b]} \\ \Delta n(\vec{r}_\perp) &= \frac{\Re[\Delta\chi^{exc}(\vec{r}_\perp)]}{2n_b} \\ \left(\frac{W_\mu}{r_w}\right)^2 &= \left(\frac{\Omega_\mu}{c}\right)^2 [n_{eff}^2(\Omega_\mu) - n_b^2], \end{aligned} \quad (7.30)$$

while r_w is the waveguide radius. The parameters W_μ which univocally define the cavity's eigenvalues are also sometimes labelled as *cladding propagation constants*, and the effective propagation constants for the various modes μ can therefore be written as

$$\begin{aligned} \beta_{eff}(\Omega_\mu) &= \left(\frac{\Omega_\mu}{c}\right)^2 n_{eff}^2(\Omega_\mu) \\ &= \left(\frac{\Omega_\mu}{c}\right)^2 n_b^2 + \left(\frac{W_\mu}{r_w}\right)^2. \end{aligned} \quad (7.31)$$

The excess refractive index is constant within the waveguide, and equal to zero outside: it takes into account the differences between the refractive indices of the core and the cladding. Hence, knowing that $\vec{r}_\perp = (r, \varphi)$, this excess refractive index can be rewritten as a function of the reduced radius $R = r/r_w$ following $\Delta n(\vec{r}_\perp) = \Delta n h(R)$. For the sake of simplicity, we here consider a step-variation, where the profile function h is equal to 1 for $R < 1$, and to 0 otherwise.

Owing to the cylindrical symmetry of the boundary conditions of Eq. (7.29), we may look for a solution of the form

$$\Phi_{mn}(\vec{r}_\perp) = \Psi_{mn}(R) e^{im\varphi}, \quad (7.32)$$

where the integer m is the azimuthal order of the eigenfunction, and n is the radial order; we therefore assume the equivalence $\mu \equiv \{m, n\}$. Hence, Eq. (7.29) can be rewritten as a function of the reduced radius R following

$$\left\{ R^2 \frac{d^2}{dR^2} + R \frac{d}{dR} - m^2 + R^2 [V^2 h(R) - W_{mn}^2] \right\} \Psi(R) = 0, \quad (7.33)$$

where

$$V_{mn} = \frac{\Omega_{mn}}{c} r_w \sqrt{2n_b \Delta n} \simeq V \quad (7.34)$$

is the **waveguide parameter**, which is considered as modally uniform in first approximation.

Equation (7.33) is a **Bessel equation** and if the continuity constraint at $R = 1$ between the core and the cladding is applied, its solution reads

$$\Psi_{mn}(R) = \begin{cases} \frac{J_m[R\sqrt{V^2 - W_{mn}^2}]}{J_m[\sqrt{V^2 - W_{mn}^2}]} & \text{if } R \leq 1 \\ \frac{K_m[RW_{mn}]}{K_m[W_{mn}]} & \text{if } R > 1 \end{cases} \quad (7.35)$$

The determination of the propagation constants W_{mn} can be achieved by considering the constraint of continuity for the eigensolution's derivative at $R = 1$, thereby yielding

$$\sqrt{V^2 - W_{mn}^2} \frac{J_{m+1}[\sqrt{V^2 - W_{mn}^2}]}{J_m[\sqrt{V^2 - W_{mn}^2}]} = W_{mn} \frac{K_{m+1}[W_{mn}]}{K_m[W_{mn}]} . \quad (7.36)$$

In order to fulfill the orthonormality condition

$$\iint_{\infty} \Phi_{mn}(\vec{r}_{\perp}) \Phi_{kl}^*(\vec{r}_{\perp}) d^2\vec{r}_{\perp} = \delta_{mk} \delta_{nl} , \quad (7.37)$$

a normalization constant A_{mn} can be introduced as

$$A_{mn} = \left[\iint_{\infty} |\Psi_{mn}(\vec{r}_{\perp})|^2 d^2\vec{r}_{\perp} \right]^{-1/2} , \quad (7.38)$$

so that at last the cavity-modes can explicitly expressed under the form

$$\Phi_{mn}(\vec{r}_{\perp}) = A_{mn} \Psi_{mn}(r/r_w) e^{im\varphi} . \quad (7.39)$$

Typically, a mode Φ_{mn} more or less fits within the circular cross-section of the waveguide; it has $2m$ zeros in the azimuthal direction, and $n - 1$ zeros in the radial one. Hence, according to that terminology, the fundamental mode is Φ_{01} . These modes are also sometimes referred to as **linearly polarized** or LP_{mn} transverse modes.

Amongst all the solutions W_{mn} that may be obtained from the algebraic Eq. (7.36), the constraint of a real and positive argument for the radial profiles $\Psi_{mn}(R)$ in Eq. (7.35) imposes $0 < W_{mn} < V$: therefore, only the modes fulfilling this double condition are physically acceptable for our purpose, and they are usually referred to as **guided modes**.

Boundary conditions and propagation wavenumbers

We now need to derive the boundary conditions for the partial differential equation (7.26) in order to proceed with its resolution.

A schematical representation of the system under study is shown in Fig. 7.3. We have here neglected the reflectivity induced by the active layer's interfaces, and its transmittivity has been considered as very close to 1. Therefore, we will only need two field variables, namely $\tilde{\mathcal{A}}_{k,\mu}^{\pm}(\omega)$ in the VCSEL's cavity, and $\tilde{\mathcal{B}}_{k,\mu}^{\pm}(\omega)$ in the external cavity. The parameters r stand for the various reflectivities, while the parameters t stand for the transmittivities. The subscripts b and t respectively stand for the bottom and top facets; on the other hand, the primes indicate internal parameters while the absence of such primes indicate external parameters. The relation between internal and external parameters is given by the **Stokes** relationships $r' = -r$ and $tt' = 1 - r^2$. We have also considered the reflectivities to be polarization-dependent so that they all bear the subscript $k = x, y$. At last, polarization and the frequency selection is supposed to be ensured by a mirror whose internal reflectivity $r'_{ext,k}(\omega)\delta_{kl}$ is frequency-dependent in one polarization, and equal to zero for the other ($l = x$ or $l = y$).

The field $\tilde{\mathcal{E}}_{k,\mu}(\omega, z)$ can therefore be expressed as

$$\tilde{\mathcal{E}}_{k,\mu}(\omega, z) = \begin{cases} \tilde{\mathcal{A}}_{k,\mu}^+(\omega)e^{-iq_{k,\mu}(\omega)z} + \tilde{\mathcal{A}}_{k,\mu}^-(\omega)e^{iq_{k,\mu}(\omega)z} \\ \text{for } -L \leq z \leq 0 \\ \tilde{\mathcal{B}}_{k,\mu}^+(\omega)e^{-ip_{k,\mu}(\omega)z} + \tilde{\mathcal{B}}_{k,\mu}^-(\omega)e^{ip_{k,\mu}(\omega)z} \\ \text{for } 0 < z \leq L_e \end{cases} \quad (7.40)$$

so that in the laser cavity, Eq. (7.26) can be rewritten as

$$\begin{aligned} & [\beta_{eff}^2(\omega) - q_{k,\mu}^2(\omega)]\tilde{\mathcal{E}}_{k,\mu}(\omega, z) + \left(\frac{\omega}{c}\right)^2 \left[\Re(\Delta\chi_k^b) + i\Im(\chi_k^b) \right. \\ & \left. + i\Gamma_{\mu}^{(t)}\Im(\Delta\chi^{exc}(z)) + \bar{\chi}_{k,\mu}^{nl}(z, N) - \frac{i\sigma}{\varepsilon_0\omega} \right] \tilde{\mathcal{E}}_{k,\mu}(\omega, z) = 0. \end{aligned} \quad (7.41)$$

The propagation wavenumber $q_{k,\mu}(\omega)$ can be explicitly determined through the boundary conditions at the facets of the VCSEL and at the external reflector:

$$z = -L : \tilde{\mathcal{A}}_{k,\mu}^+(\omega)e^{iq_{k,\mu}(\omega)L} = r'_{b,k}\tilde{\mathcal{A}}_{k,\mu}^-(\omega)e^{-iq_{k,\mu}(\omega)L} \quad (7.42)$$

$$z = 0 : \tilde{\mathcal{B}}_{k,\mu}^+(\omega) = t'_{t,k}\tilde{\mathcal{A}}_{k,\mu}^+(\omega) + r_{t,k}\tilde{\mathcal{B}}_{k,\mu}^-(\omega) \quad (7.43)$$

$$\tilde{\mathcal{A}}_{k,\mu}^-(\omega) = r'_{t,k}\tilde{\mathcal{A}}_{k,\mu}^+(\omega) + t_{t,k}\tilde{\mathcal{B}}_{k,\mu}^-(\omega) \quad (7.44)$$

$$z = -L_e : \tilde{\mathcal{B}}_{k,\mu}^-(\omega)e^{ip_{k,\mu}(\omega)L_e} = r'_{ext,k}(\omega)\delta_{kl}\tilde{\mathcal{B}}_{k,\mu}^+(\omega)e^{-ip_{k,\mu}(\omega)L_e}. \quad (7.45)$$

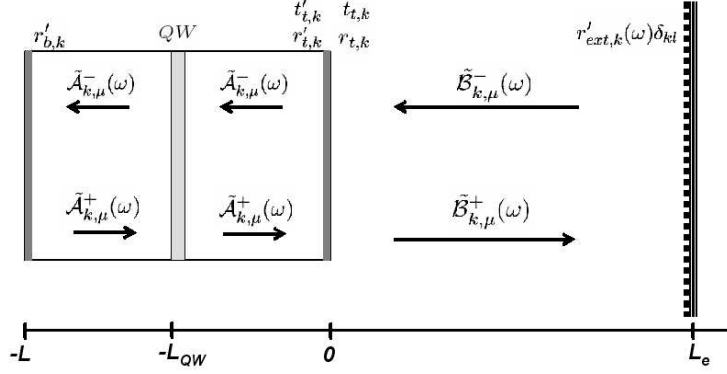


Figure 7.3. A schematical representation of a VCSEL with PFSF. Here, the horizontal axis is the z -axis, and the transverse plane is perpendicular to the plane of the figure.

The external propagation constant can be expressed as

$$p_{k,\mu}(\omega) = \frac{\omega}{c} - i \frac{a_{ext,\mu}}{2}, \quad (7.46)$$

where $a_{ext,\mu}$ stands for the losses in the external cavity due to diffraction and other eventual optical devices. This term depends on μ because for example, the various transverse modes have different diffraction angles and are not mode-matched with the same efficiency. Alternatively, considering the external travelling path of length $2L_e$, Eq. (7.46) can be rewritten under the form

$$e^{-2p_{k,\mu}(\omega)L_e} = \rho_{ext,\mu} e^{-i\omega T}, \quad (7.47)$$

where $T = 2L_e/c$ is the external cavity round-trip time, and $\rho_{ext,\mu}^2 = e^{-L_e a_{ext,\mu}}$ is the total power attenuation induced by the external cavity.

From Eqs. (7.43), (7.44) and (7.45), it can be shown that the counter-propagating waves in the laser cavity are related as

$$\tilde{A}_{k,\mu}^-(\omega) = -r_{t,k} [1 + R_{k,\mu}(\omega)\delta_{kl}] \tilde{A}_{k,\mu}^+(\omega), \quad (7.48)$$

where

$$R_{k,\mu}(\omega) = \frac{1 - r_{t,k}^2}{r_{t,k}} \frac{r_{ext,k}(\omega)\rho_{ext,\mu} e^{-i\omega T}}{1 + r_{t,k}r_{ext,k}(\omega)\rho_{ext,\mu} e^{-i\omega T}} \quad (7.49)$$

is a frequency-dependent term which accounts for the effect of the frequency-selective external feedback.

Equations (7.42) and (7.48) constitute an homogeneous set of linear algebraic equations which may have solutions if and only if the associated determinant is null, that is

$$r_{b,k}r_{t,k} [1 + R_{k,\mu}(\omega)\delta_{kl}] e^{-iq_{k,\mu}(\omega)L} = 1, \quad (7.50)$$

from which we can at last deduce an explicit expression for the propagation wavenumber within the laser cavity as

$$q_{k,\mu}(\omega) = \frac{M\pi}{L} - \frac{i}{2L} \ln [r_{b,k}r_{t,k}] - \frac{i}{2L} \ln [1 + R_{k,\mu}(\omega)\delta_{kl}], \quad (7.51)$$

where the integer M is the order of the lasing longitudinal mode such that

$$\frac{M\pi}{L} = \beta_{eff}(\Omega) \simeq \frac{\Omega}{c} n_b, \quad (7.52)$$

where Ω is the longitudinal resonance frequency defined by the Bragg reflectors. This frequency defines the operating wavelength of the laser.

It can therefore be deduced from Eqs. (7.42) and (7.40) that the electric field may also explicitly be rewritten as

$$\tilde{\mathcal{E}}_{k,\mu}(\omega, z) = \tilde{\mathcal{A}}_{k,\mu}(\omega) f_k(z) + \text{c.c.} \quad (7.53)$$

with

$$\begin{aligned} \tilde{\mathcal{A}}_{k,\mu}(\omega) &\equiv \tilde{\mathcal{A}}_{k,\mu}^+(\omega) \\ f_k(z) &= e^{-iq_{k,\mu}(\omega)z} - \frac{e^{2iq_{k,\mu}(\omega)L}}{r_{b,k}} e^{iq_{k,\mu}(\omega)z}. \end{aligned} \quad (7.54)$$

The function $f_k(z)$ describes the longitudinal mode profile of the electric field in the laser cavity. Typically, this profile can be considered as isotropic, so that $f_x(z) \simeq f_y(z) \equiv f(z)$.

We can obtain an equation for the amplitude $\tilde{\mathcal{A}}_{k,\mu}(\omega)$ by projecting Eq. (7.41) onto $f^*(z)$ following

$$\begin{aligned} &[\beta_{eff}^2(\omega) - q_{k,\mu}^2(\omega)] \tilde{\mathcal{A}}_{k,\mu}(\omega) + \left(\frac{\omega}{c}\right)^2 [\Lambda_k - i\Upsilon_{k,\mu}(\omega)] \tilde{\mathcal{A}}_{k,\mu}(\omega) \\ &+ \left(\frac{\omega}{c}\right)^2 \Gamma^{(l)} \bar{\chi}_{k,\mu}^{nl}(\bar{N}) \tilde{\mathcal{A}}_{k,\mu}(\omega) = 0 \end{aligned} \quad (7.55)$$

where \bar{N} is the averaged carrier density across the active region width W , $\Gamma^{(l)}$ is the longitudinal confinement factor defined as

$$\Gamma^{(l)} = \frac{\int_{-L_{QW}-W/2}^{-L_{QW}+W/2} |f(z)|^2 dz}{\int_{-L}^0 |f(z)|^2 dz}, \quad (7.56)$$

and the material parameters are synthetically gathered within the new parameters

$$\Lambda_k = \Re(\Delta\chi_k^b) \quad (7.57)$$

$$\Upsilon_{k,\mu}(\omega) = -\Im(\chi_k^b) - \Gamma^{(l)}\Gamma_\mu^{(t)}\Im(\Delta\chi^{exc}) + \frac{\sigma}{\varepsilon_0\omega} > 0, \quad (7.58)$$

respectively gathering the passive influence of the semiconductor medium on the amplitude and phase of the electric field.

The slowly varying envelope approximation

To derive dynamical equations in the temporal domain, we need to develop explicitly the first term of Eq. (7.55). The effective wavenumber can be Taylor-expanded around the carrier frequency Ω , and if we restrict ourselves to first order terms, we are led to

$$\beta_{eff}^2(\omega) - q_{k,\mu}^2(\omega) \simeq \left\{ \beta_{eff}^2(\Omega) + (\omega - \Omega) \left. \frac{d\beta_{eff}^2}{d\omega} \right|_{\omega=\Omega} \right\} - \left\{ \frac{M\pi}{L} - \frac{i}{2L} \ln[r_{b,k}r_{t,k}] - \frac{i}{2L} \ln[1 + R_{k,\mu}(\omega)\delta_{kl}] \right\}^2. \quad (7.59)$$

We can use Eq. (7.31) and the relation $[\beta_\Omega^2]' = 2\beta_\Omega\beta_\Omega'$ to obtain

$$\beta_{eff}^2(\omega) \simeq \left(\frac{\Omega}{c}\right)^2 n_b^2 + \left(\frac{W_\mu}{r_w}\right)^2 + 2(\omega - \Omega) \frac{\Omega}{c} n_b \frac{n_g}{c}, \quad (7.60)$$

where n_g is the **group-velocity refraction index**. On the other hand, the terms that can be gathered within $[\Im(q_{k,\mu})]^2$ in Eq. (7.59) are second-order term which can be neglected. Therefore, using Eqs. (7.52) and (7.60), Eq. (7.55) can be reduced to

$$i(\omega - \Omega)\tilde{\mathcal{A}}_{k,\mu}(\omega) = \frac{1}{2} \left[-\kappa_{k,\mu} + 2i\omega_\mu + 2i\vartheta_k + i\frac{\Omega}{n_b n_g} \Gamma^{(l)} \bar{\chi}_{k,\mu}^{nl}(\bar{N}) \right] \tilde{\mathcal{A}}_{k,\mu}(\omega) + \frac{1}{\tau_{in}} \ln[1 + R_{k,\mu}(\omega)\delta_{kl}] \tilde{\mathcal{A}}_{k,\mu}(\omega) \quad (7.61)$$

with

$$\tau_{in} = \frac{2Ln_g}{c} \quad (7.62)$$

$$\kappa_{k,\mu} = \frac{\Omega}{n_b n_g} \Upsilon_{k,\mu}(\Omega) + \frac{2}{\tau_{in}} \ln \left[\frac{1}{r_{b,k}r_{t,k}} \right] > 0 \quad (7.63)$$

$$\vartheta_k = -\frac{\Omega}{n_b n_g} \Lambda_k \quad (7.64)$$

$$\omega_\mu = -\frac{c^2}{2n_e n_g \Omega} \left(\frac{W_\mu}{r_w} \right)^2. \quad (7.65)$$

The parameter τ_{in} is the **internal cavity round-trip time** of the VCSEL, that is, the time needed for a photon to go back and forth in the longitudinal dimension of the optical cavity; the parameter $\kappa_{k,\mu}$ stands for the **polarization-dependent modal cavity losses**, and their inverses $\tau_{k,\mu}^p = 1/\kappa_{k,\mu}$ are sometimes referred to as the **modal photon lifetimes**; the parameter ϑ_k accounts for the **polarization-induced frequency-shift** induced by the optical phase anisotropies of the laser cavity. At last, a particularly important set of parameters is ω_μ , which stands for the various **modal eigenfrequencies** of the guided cavity-modes. Since $\omega_\mu < 0$, it appears that the cavity-modes are *red-shifted* relatively to the nominal Bragg resonance frequency. It can also be shown that if the **order** of a transverse mode is defined as $\mathcal{O} = m + 2n - 1$, then the transverse modes of the same order are nearly frequency-degenerated.

Since we are dealing with coherent light, we can assume that the dynamics of the electric field is very slow comparatively to the optical carrier frequency. Therefore, we may rather derive an equation for the so-called **slowly varying envelope** of the electric field whose representation in the temporal and frequency spaces is defined through

$$\mathcal{A}_{k,\mu}(t) = \frac{1}{2}E_{k,\mu}(t)e^{i\Omega t} \Rightarrow \tilde{\mathcal{A}}_{k,\mu}(\omega) = \frac{1}{2}\tilde{E}_{k,\mu}(v). \quad (7.66)$$

where $v = \omega - \Omega$ is the relative frequency of the electric field. Therefore, using the derivative property $iv \rightarrow \partial_t$, the inverse Fourier transform of Eq. (7.61) yields the following integro-differential equation for the slowly varying envelope of the electric field

$$\begin{aligned} \partial_t E_{k,\mu}(t) &= \frac{1}{2} \left[-\kappa_{k,\mu} + 2i\omega_\mu + 2i\vartheta_k + i\frac{\Omega}{n_b n_g} \Gamma^{(l)} \bar{\chi}_{k,\mu}^{nl}(\bar{N}) \right] E_{k,\mu}(t) \\ &+ \frac{1}{\tau_{in}} \frac{1}{\sqrt{2\pi}} \int_{-\infty}^{+\infty} \ln [1 + R_{k,\mu}(v + \Omega)\delta_{kl}] \tilde{E}_{k,\mu}(v) e^{ivt} dv. \end{aligned} \quad (7.67)$$

The last term of this equation gathers all the information about the polarization- and frequency-selective feedback. However, this equation can be theoretically studied if and only if $R_{k,\mu}(\omega)$ is explicitly known, that is, if the filtering properties of the external cavity are explicitly defined through the function $r_{ext,k}(\omega)$.

The frequency-selective feedback

A convenient way to take into account the frequency selection of the feedback is to consider the grating as a frequency-selective mirror with a **Lorentzian** characteristic. The Lorentzian filter may have the disadvantage to have quite large tails (that

is, not to be selective enough), but it has the great advantage to be very simple to implement numerically, as it just corresponds to an additional first-order filtering equation for the amplitude of each lasing mode. The filtering properties of the grating can be modeled with a Lorentzian [123], and in general, if the transverse modes separation is significantly larger than the bandwidth of the filter (something that is likely to happen when only few modes are considered), the particular features of the filter may not be relevant, as resonance should only match with a single transverse mode at the time.

The transfer function of a Lorentzian filter can be written as

$$r_{ext,k}(\omega) = \frac{\Delta\omega_G}{\Delta\omega_G + i[\omega - \Omega_G]}, \quad (7.68)$$

where on the one hand Ω_G is the central frequency of the grating, to be matched with the overall frequency of the lasing mode to be fed back, and on the other $\Delta\omega_G$ is the half-width at half-maximum, quantifying the bandwidth of the filter. We will consider the case of narrow filters for which $\Delta\omega_G/2\pi < 10$ GHz, that is, smaller than the spacing between the lasing transverse modes. The reflectivity for a perfectly matched mode of polarization k is supposed to be equal to 1.

In VCSELs, the facets reflectivity are extremely high (always superior to 99%); hence, we have $r_{t,k} \simeq 1$ so that $|R_{k,\mu}(\omega)| \ll 1$ according to Eq. (7.49), and in consequence

$$\ln[1 + R_{k,\mu}(\omega)\delta_{kl}] \simeq R_{k,\mu}(\omega)\delta_{kl}. \quad (7.69)$$

Finally, if we restrict ourselves to case $|r_{ext,k}(\omega)| \ll 1$ corresponding to weak or moderate feedback strengths, $R_{k,\mu}(\omega)$ can simply expressed as

$$R_{k,\mu}(\omega) = \frac{1 - r_{t,k}^2}{r_{t,k}} r_{ext,k}(\omega) \rho_{ext,\mu} e^{-i\omega T}. \quad (7.70)$$

It may be interesting to note that in the conventional optical feedback case, it is possible to consider the case of strong feedback and still analytically derive a differential equation for the temporal dynamics [85].

Hence, the integral term in the right-hand side of Eq. (7.67) can simply be rewritten as $K_{k,\mu} F_{k,\mu}(t) \delta_{kl}$, where

$$K_{k,\mu} = \frac{1 - r_{t,k}^2}{r_{t,k}} \frac{1}{\tau_{in}} \rho_{ext,\mu} \quad (7.71)$$

is the **modal feedback strength** in each polarization, and

$$F_{k,\mu}(t) = \frac{e^{-i\theta}}{\sqrt{2\pi}} \int_{-\infty}^{+\infty} \frac{\Delta\omega_G}{\Delta\omega_G + i[v + \Omega - \Omega_G]} \tilde{E}_{k,\mu}(v) e^{iv(t-T)} dv \quad (7.72)$$

is the **modal amplitude** that is fed back into the laser cavity, with

$$\theta = \Omega T \quad (7.73)$$

standing for the reference **optical feedback phase**.

The particular form of the Lorentzian integral of Eq. (7.72) enables the derivation of a differential equation for the filtered modal field $F_{k,\mu}(t)$ [123]. Effectively, the integral can be rewritten as

$$F_{k,\mu}(t) = \frac{e^{-i\theta}}{2\pi} \int_{-\infty}^{+\infty} dv \left\{ \frac{\Delta\omega_G}{\Delta\omega_G + i[v + \Omega - \Omega_G]} e^{iv(t-T)} \times \int_{-\infty}^{+\infty} dt' E_{k,\mu}(t') e^{-ivt'} \right\}. \quad (7.74)$$

The order of integration relatively to the variables t' and v can be exchanged, and using the Cauchy residue theorem, we have

$$\int_{-\infty}^{+\infty} \frac{\Delta\omega_G}{\Delta\omega_G + i[v + \Omega - \Omega_G]} e^{iv(t-T-t')} dv = 2\pi i \times \begin{cases} -i\Delta\omega_G e^{-(\Delta\omega_G + i\Omega - i\Omega_G)(t-T-t')} & \text{for } t - T - t' \leq 0 \\ 0 & \text{for } t - T - t' > 0 \end{cases} \quad (7.75)$$

so that Eq. (7.74) can be rewritten as

$$F_{k,\mu}(t) = e^{-i\theta} \Delta\omega_G \int_{-\infty}^{t-T} E_{k,\mu}(t') e^{-(\Delta\omega_G + i\Omega - i\Omega_G)(t-T-t')} dt' \quad (7.76)$$

which finally yields after time differentiation

$$\begin{aligned} \partial_t F_{k,\mu}(t) &= -[\Delta\omega_G + i(\Omega - \Omega_G)] F_{k,\mu}(t) \\ &\quad + \Delta\omega_G E_{k,\mu}(t-T) e^{-i\theta}. \end{aligned} \quad (7.77)$$

This differential equation rules the dynamics of the modal fed back field, and it clearly appears that we simply have $F_{k,\mu}(t) = E_{k,\mu}(t-T) e^{-i\theta}$ in the adiabatic limit for a perfectly frequency-matched mode.

Field equations in the circular polarization base

We are now going to express the field equations in a circular basis. In fact, the polarization of the photons is defined by the spin difference between the valence and conduction sub-bands before electrons-hole recombination. This interaction is diagonal in the so-called circular basis where the field is expressed as

$$E_{\pm\mu}(t) = \frac{E_{x,\mu}(t) \pm iE_{y,\mu}(t)}{\sqrt{2}}. \quad (7.78)$$

A discrimination should therefore be made between the carriers according to their spin. In particular, the electrons will be divided into two groups of density \bar{N}_+ and \bar{N}_- such that $\bar{N} = \bar{N}_+ + \bar{N}_-$. The associated spin dynamics will be studied in detail in the next sub-section, devoted to the carrier dynamics.

The total electric field in each circular polarization can therefore be rewritten under the form

$$\mathcal{E}_{\pm,mn}(\vec{r}, t) = \frac{1}{2} \sum_{m,n} f(z) \Phi_{mn}(\vec{r}_\perp) E_{\pm,mn}(t) e^{i\Omega t} + \text{c.c.} \quad (7.79)$$

and the Eq. (7.67) ruling the field amplitude can be rewritten as

$$\begin{aligned} \partial_t E_{\pm\mu}(t) &= \frac{1}{2} \left[-\kappa_\mu + 2i\omega_\mu + 2i\vartheta + i \frac{\Omega}{n_b n_g} \Gamma^{(l)} \bar{\chi}_{\pm\mu}^{nl}(\bar{N}_\pm) \right] E_{\pm\mu}(t) \\ &\quad - [\gamma_{a,\mu} + i\gamma_{p,\mu}] E_{\mp\mu}(t) \\ &\quad + \frac{1}{\sqrt{2}} [K_{x,\mu} F_{x,\mu}(t) \delta_{lx} \pm iK_{y,\mu} F_{y,\mu}(t) \delta_{ly}], \end{aligned} \quad (7.80)$$

where $l = x$ or $l = y$ fixes the polarization of the feedback. The new parameters thereby emerging are

$$\begin{aligned} \kappa_\mu &= \frac{1}{2} [\kappa_{x,\mu} + \kappa_{y,\mu}] \\ \vartheta &= \frac{1}{2} [\vartheta_x + \vartheta_y] \simeq 0 \end{aligned} \quad (7.81)$$

where κ_μ stand for the **modal losses**, while

$$\begin{aligned} \gamma_{a,\mu} &= -\frac{1}{2} [\kappa_{x,\mu} - \kappa_{y,\mu}] \\ \gamma_p &= -\frac{1}{2} [\vartheta_x - \vartheta_y] \end{aligned} \quad (7.82)$$

are respectively the **modal dichroism** and the **birefringence**. Here, these anisotropies only have two contributions namely bulk and facet contributions, but in the general case, other contributions such as the elasto-optic one, or the strain-induced

anisotropies, may play a very important role.

A x - or y -polarized transverse mode is optimally fed back when its overall optical frequency is matched with the central frequency of the grating. These effective modal lasing frequencies are non-uniformly shifted, thereby leading to a spectral splitting. They are first red-shifted relatively to the Bragg frequency Ω by an amount ω_μ which is imposed by the laser cavity. It also appears in Eq. (7.67) that the output radiation of the laser is globally blue-shifted by an amount

$$\Delta\Omega_{k,\mu} = \vartheta_k + \frac{1}{2} \frac{\Omega}{n_b n_g} \Gamma^{(l)} \Re \left[\bar{\chi}_{k,\mu}^{nl}(\bar{N}) \right]. \quad (7.83)$$

whose two contributions are respectively the phase anisotropy and the amplitude-phase coupling.

It is important to note that the grating can only be matched to one transverse mode at the time; to avoid any confusion, we will refer to the matched mode as the mode μ_0 and therefore, the **frequency matching condition** for the k -polarized transverse mode μ_0 is

$$\Omega_G = \Omega + \omega_{\mu_0} + \Delta\Omega_{k,\mu_0}, \quad (7.84)$$

Hence, for each mode μ , the equation to be coupled to Eq. (7.80) should either be rewritten under the form

$$\begin{aligned} \partial_t F_{x,\mu}(t) &= -[\Delta\omega_G - i(\omega_{\mu_0} + \Delta\Omega_{x,\mu_0})] F_{x,\mu}(t) \\ &\quad + \frac{\Delta\omega_G}{\sqrt{2}} [E_{+\mu}(t-T) + E_{-\mu}(t-T)] e^{-i\theta} \end{aligned} \quad (7.85)$$

in case of x -polarized feedback, and under the form

$$\begin{aligned} \partial_t F_{y,\mu}(t) &= -[\Delta\omega_G - i(\omega_{\mu_0} + \Delta\Omega_{y,\mu_0})] F_{y,\mu}(t) \\ &\quad + \frac{\Delta\omega_G}{i\sqrt{2}} [E_{+\mu}(t-T) - E_{-\mu}(t-T)] e^{-i\theta}. \end{aligned} \quad (7.86)$$

in case of y -polarized feedback.

7.3.2 Carrier dynamics

Spin dynamics

The weakly index-guided cavity of VCSELs supports “**linearly polarized**” transverse modes which are almost parallel to cavity’s cross-section. Because of the circular symmetry of the VCSEL aperture, the polarization direction of the output field is not fixed. However, the material and facet anisotropies we have highlighted

in the preceding sections do preferentially pin the polarization direction in two orthogonal directions within the cross-section plane.

In the active medium, the photons of the electromagnetic field interact with the electrons and the holes, and it is known from quantum mechanics that this interaction should conserve the total angular momentum. If projected onto the cavity's axis of symmetry z , the spin of the electrons is equal to $J_{e,z} = \pm\frac{1}{2}$ in units of \hbar (the so-called *spin-up* and *spin-down* angular momenta). In the valence band, two sub-bands corresponding to significantly different effective masses for the holes have to be considered: the **light-hole** sub-band of spin $J_{lh,z} = \pm\frac{1}{2}$, and the **heavy-hole** sub-band of spin $J_{hh,z} = \pm\frac{3}{2}$. In first approximation, the effect of light-holes can be neglected because of their lower energy. We therefore only have to consider the interactions between the electrons and the heavy holes, and in that case, two kinds of interactions can be considered: the radiative electron-holes recombinations for with $\Delta J_z = \pm 1$, and the non-radiative interactions with $\Delta J_z = \pm 2$, which are of no interest for our purpose.

As far as radiative recombinations are concerned, an angular momentum variation of $\Delta J_z = 1$ (from $\frac{1}{2}$ to $\frac{3}{2}$) would correspond to the stimulated emission of a *left* circularly polarized photon, while a variation $\Delta J_z = -1$ (from $-\frac{1}{2}$ to $-\frac{3}{2}$) would correspond to the emission of a *right* circularly polarized photon. The carrier reservoir N therefore has to be divided into two "sub-reservoirs" N_+ and N_- , each of them respectively leading to the generation of either left- or right-polarized photons whose modal density are respectively equal to $|\mathcal{E}_-(t)|^2$ and $|\mathcal{E}_+(t)|^2$.

However, these two sub-reservoirs are coupled by the so-called *spin-flip* mechanism, which accounts for the fact that the spin of some electrons can flip from one sign to the other. The global effect of spin flip is to equilibrate the spin densities of the sub-reservoirs: therefore, its intensity is proportional to the difference of spin-up and spin-down carrier densities, and the related proportionality coefficient γ_s is sometimes referred to as **spin-flip rate**. In general, only the spin-flip of electrons is considered, as the spin-flip of holes is significantly less intense because of their higher effective mass. This phenomenological frame for the study of spin dynamics is known as **Spin-Flip Model** (SFM), or **San Miguel-Feng-Moloney** model [83], and it therefore relies on a pair of two-level systems which are coupled through electron spin-flip.

Evolution equation

If $N_{\pm}(\vec{r}, t)$ is the volumic carrier density of electrons with spin up (N_+) and down (N_-) in the quantum wells area, its variation rate depends on five different factors.

The first one is the pumping current I , which provides a continuous flow of carriers with normalized a surface density $C(\vec{r})$; the induced density variation is inversely proportional to the active region's thickness W . Typically, the pumping

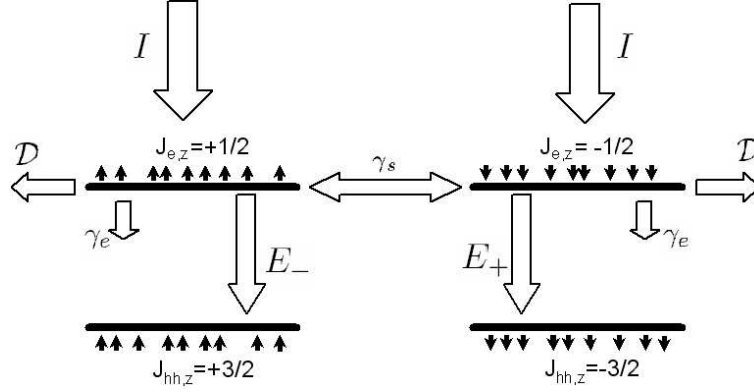


Figure 7.4. Representation of the various contributions of the carrier dynamics, namely the pumping (I), the diffusion (\mathcal{D}), the non-radiative decay (γ_e), the radiative recombinations (E_{\pm}), and the spin-flip coupling (γ_s) between the two sub-reservoirs of carriers.

provides an equal number of “up” and “down” electrons of electric charge e , and an internal quantum efficiency η_i precising fraction of carriers which effectively arrive to the active region can be attached to I .

The second contribution arises from non-radiative recombination, and it can simply be view as a linear decay process of rate γ_e . Here, we can in first approximation neglect the bimolecular recombination contribution which is quadratic in N_{\pm} .

The third contribution is transverse diffusion, as the carriers transversely spread within the active region volume. This diffusion can be accounted for with a diffusion constant \mathcal{D} associated to the transverse Laplacian operator.

The fourth factor contributing to the density variation is the spin-flip rate, which accounts for the exchanges of carriers between the reservoirs of carriers N_+ and N_- as described in the precedent subsection.

At last, the carrier density obviously varies in function of the radiative recombination rate, which is proportional to the energy density of the stimulated radiation’s field. More precisely, this light-matter interaction is proportional to the field $\mathcal{E}(\vec{r}, t)$ and to the nonlinear polarization

$$\mathcal{P}_{\pm}(\vec{r}, N_{\pm}, t) = \varepsilon_0 \chi_{\pm}^{nl}(\vec{r}, N_{\pm}) \mathcal{E}_{\pm}(\vec{r}, t) \quad (7.87)$$

which is here assumed to follow adiabatically the field dynamics (class-B lasers approximation).

Taking into account these five contributions therefore yields

$$\begin{aligned}
\partial_t N_{\pm}(\vec{r}, t) &= \frac{\eta_i I}{2eW} C(\vec{r}_{\perp}) - \gamma_e N_{\pm}(\vec{r}, t) \mp \gamma_s [N_+(\vec{r}, t) - N_-(\vec{r}, t)] \\
&\quad + \mathcal{D} \nabla_{\perp}^2 N_{\pm}(\vec{r}, t) \\
&\quad - \frac{i}{\hbar} [\mathcal{P}_{\pm}(\vec{r}, N_{\pm}, t) \mathcal{E}_{\pm}^*(\vec{r}, t) - \mathcal{P}_{\pm}^*(\vec{r}, N_{\pm}, t) \mathcal{E}_{\pm}(\vec{r}, t)] .
\end{aligned} \tag{7.88}$$

Using Eqs. (8.10) and (7.87), the last term of the right-hand side of Eq. (7.88) which stands for the stimulated recombination variation rate can be explicitly rewritten as

$$\begin{aligned}
\mathcal{S}_{\pm}(\vec{r}, N_{\pm}, t) &= \frac{2\varepsilon_0}{\hbar} \Im[\chi_{\pm}^{nl}(\vec{r}, N_{\pm})] |\mathcal{E}_{\pm}(\vec{r}, t)|^2 \\
&= \frac{2\varepsilon_0}{\hbar} \Im[\chi_{\pm}^{nl}(\vec{r}, N_{\pm})] |f(z)|^2 \left\{ \sum_{\mu} |\Phi_{\mu}(\vec{r}_{\perp})|^2 |\mathcal{E}_{\pm, \mu}(t)|^2 \right. \\
&\quad \left. + \sum_{\mu, \nu \neq \mu} \Phi_{\mu}(\vec{r}_{\perp}) \Phi_{\nu}^*(\vec{r}_{\perp}) \mathcal{E}_{\pm, \mu}(t) \mathcal{E}_{\pm, \nu}^*(t) e^{i(\omega_{\mu} - \omega_{\nu})t} \right\}
\end{aligned} \tag{7.89}$$

The stimulated recombination can therefore be split into two contributions.

The first one accounts for the interaction of individual modes with the reservoir of carriers, through stimulated recombination. The second contribution includes the cross-saturation terms, and it appears that this reservoir-induced coupling between the transverse modes explicitly generates *beating notes*. When large frequency splitting between the modal frequencies, this term can in first approximation be neglected, so that we will only keep the first contribution of this stimulated recombination term [121].

Since the active region is very thin ($W \ll L$), the longitudinal variations of the the volumic density $N_{\pm}(\vec{r}, t)$ are of no major interest; moreover, only the transverse variations of N_{\pm} are needed in the field equations. Hence, the problem can be simplified by averaging this density across the quantum wells width following

$$\bar{N}_{\pm}(\vec{r}_{\perp}, t) = \frac{1}{W} \int_{-L_{QW}-W/2}^{-L_{QW}+W/2} N_{\pm}(\vec{r}, t) dz . \tag{7.90}$$

Therefore, applying to Eq. (7.88) this longitudinal average operator finally yields

$$\begin{aligned}
\partial_t \bar{N}_{\pm}(\vec{r}_{\perp}, t) &= \frac{\eta_i I}{2eW} C(\vec{r}_{\perp}) - \gamma_e \bar{N}_{\pm}(\vec{r}_{\perp}, t) \mp \gamma_s [\bar{N}_{+}(\vec{r}_{\perp}, t) - \bar{N}_{-}(\vec{r}_{\perp}, t)] \\
&\quad + \mathcal{D} \nabla_{\perp}^2 \bar{N}_{\pm}(\vec{r}_{\perp}, t) \\
&\quad + \frac{2\varepsilon_0}{\hbar} \Im[\chi_{\pm}^{nl}(\vec{r}_{\perp}, \bar{N}_{\pm})] \Gamma^{(l)} \left\{ \frac{1}{W} \int_{-L}^0 |f(z)|^2 dz \right\} \\
&\quad \times \sum_{\mu} |\Phi_{\mu}(\vec{r}_{\perp})|^2 |\mathcal{E}_{\pm, \mu}(t)|^2, \tag{7.91}
\end{aligned}$$

where $\Gamma^{(l)}$ is the longitudinal confinement factor as defined in Eq. (7.56).

7.4 Conclusion

In this chapter, we have modeled the system consisting in a multimode VCSEL subjected to polarization- and frequency-selective feedback. We have taken into account the material anisotropies of the laser cavity, as well as the mesoscopic features of spin dynamics. The final model is therefore the set of equations constituted by Eq. (7.80) for the electric field $E_{\pm\mu}(t)$, Eq. (7.85) or (7.86) for the filtered optical feedback field $F_{\mu}(t)$, and Eq. (7.91) for the carrier dynamics.

The next chapter will be devoted to the exploitation of the model we have derived to investigate the modal dynamics of the system, as well as its optimization in view of transverse-mode control.

Chapter 8

Transverse-Mode Control in VCSELs: Modal Gain and Stationary Modal Amplitudes

“Controlling big and small number of elements is a single and same thing, it is only a matter of formation and transmission of signals.”

Sun Tzu, The art of war.

8.1 Introduction

WE aim in this chapter to study the dynamical properties of VCSELs with polarization- and frequency-selective feedback (PFSF) using the model derived in the precedent chapter. We first analyze the role of geometrical anisotropies of the VCSEL's cross-section, as they can play an important role as far as the spectral and intensity properties of certain transverse modes are concerned. Hence, we will determine the external-cavity modes (ECMs), laying an emphasis on the specific effect of the filtering upon the ECMs which are commonly obtained in the case of conventional optical feedback. At last, we will focus on the determination of the modal gain and of the stationary modal amplitudes of the system. It will be shown that PFSF succeeds in stabilizing the VCSEL, and that the lasing condition for the various modes depends on a selection rule which is strongly attached to the transverse confinement factor and to the modal gain.

8.2 The system

8.2.1 The experimental set-up

The experimental set-up for the polarization- and frequency-selective feedback of VCSELs is presented in Fig. 8.1.

The VCSEL under study emits at 850 nm, and its threshold current is approximately equal to 1.3 mA. Its cross-section is slightly elliptical, with axes of diameter 9.8 and 8.8 μm respectively.

The frequency selection is performed by a grating which plays the role of a frequency-selective mirror. The fed back radiation is the first-order diffraction beam, so that this set-up corresponds to the so-called **Littman** configuration. The width $\Delta\omega_G$ of the filter is fixed and it depends on the resolution of the grating (number of lines per mm), while the central frequency Ω_G is tuned by tilting the angle of the external mirror. Since the transverse modes are spectrally splitted, a given transverse mode can thereby be selected unambiguously. On the other hand, polarization selection is here ensured by a linear polarizer which selects the polarization we are willing to feed back.

This experimental set-up is intended to enable an excellent mode-matching, that is, the applied feedback beam profiled overlaps almost perfectly the spatial aperture of the VCSEL. This is an important feature because the determination of the modal gain, as well as the interferometrically-induced quenching of enhancing of modes strongly depends on this spatial overlap condition.

Using beam splitters, two detection arms can be implemented and connected to the external cavity: the first one serves to the observation of the VCSEL's dynamics, while the second one monitors the feedback radiation and helps for a precise selection of the chosen fed back mode. Globally, the intensity of fed back radiation amounts to few percents of the VCSEL's output, and the external cavity is approximately 57 cm long, corresponding to a delay-time of 3.8 ns.

The observables of this experimental set-up are therefore the output and filtered electromagnetic intensities, which can be resolved in space (modal profiles), time, frequency and polarization.

8.2.2 Effect of geometrical anisotropies

The first anisotropy to consider is here **ellipticity**. The circular symmetry supports degenerated polarization modes with arbitrary spatial orientation. Ellipticity lifts this degeneracy by introducing *two privileged orientations* for the modes, corresponding to the principal axes of the ellipse [124, 125].

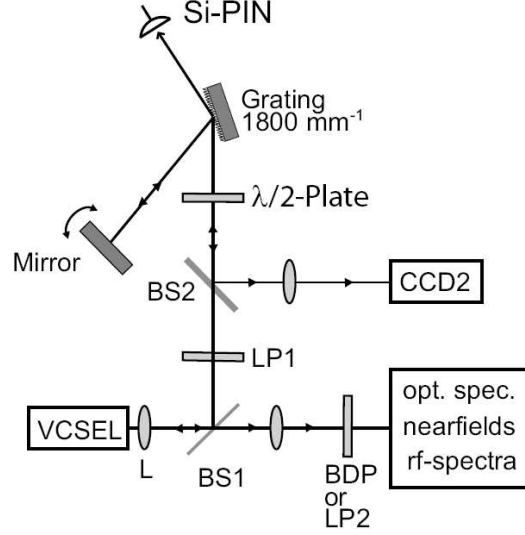


Figure 8.1. Polarization- and frequency-selective feedback set-up to control the emission properties of a VCSEL. L: Lens; LP: Linear Polarizer; BS: Beam Splitter; BDP: Beam Displacement Prism.

Hence, the degenerated mode $\Phi_{mn}(\vec{r}_\perp) = |\Phi_{mn}(r/r_w)|e^{im\varphi}$ with arbitrary spatial orientation will therefore be split into two *spatially complementary modes*, with fixed spatial orientation, respectively called *cosinus mode* and the *sinus mode*, where the cos and sin functions will rule the azimuthal variations of the mode profiles [126, 127]. These modes can also be referred to as *orientation modes*.

Beyond pinning the modal orientation in the transverse plane, ellipticity also modifies the *spatial shape* of the modal profiles. For slightly elliptical cross-sections, we can deduce the new modal profiles from those obtained for the circular cross-section resonator. Effectively, if we consider an elliptical aperture with half-axes $r_a > r_b$, we can in first approximation replace the reduced radius $r/r_w = \sqrt{(x/r_w)^2 + (y/r_w)^2}$ in Eq. (7.39) by the "elliptical" reduced radius $\varrho = \sqrt{(x/r_a)^2 + (y/r_b)^2}$, so that the cosinus and sinus eigenmodes of the elliptical resonator can be expressed as the following real functions

$$\begin{aligned}\Phi_{mn}^c(\vec{r}_\perp) &= [\delta_{m0} + \sqrt{2}(1 - \delta_{m0})] |\Phi_{mn}(\varrho)| \cos(m\varphi) \\ \Phi_{mn}^s(\vec{r}_\perp) &= [\delta_{m0} + \sqrt{2}(1 - \delta_{m0})] |\Phi_{mn}(\varrho)| \sin(m\varphi),\end{aligned}\quad (8.1)$$

where $[\delta_{m0} + \sqrt{2}(1 - \delta_{m0})]$ is a normalization factor equal to 1 when $m = 0$, and to $\sqrt{2}$ when $m \neq 0$ [126].

The last effect of this geometrical anisotropy is the lifting of the *frequency degeneracy* of the orientation modes. Therefore, a given mode may have two distinct eigenfrequencies for the two spatial orientations. The frequency splitting between orientation modes generally amounts to few tens of GHz [124, 128], and we will here consider that these geometrically induced frequency shifts are equal to $\omega_{mn}^c = \omega_{mn} - \delta\omega$ and $\omega_{mn}^s = \omega_{mn} + \delta\omega$ respectively, with $\delta\omega/2\pi = 10$ GHz.

8.2.3 Effect of material anisotropies

The second type of anisotropies to consider is material anisotropy, namely amplitude anisotropy (dichroism) and phase anisotropy (birefringence), as explained in the precedent chapter. Both have an **electro-optical** contribution induced by the voltage across the active medium, a **facet** contribution induced by the Bragg mirrors, but also an **elasto-optical** contribution induced by stress and strain exerted upon the crystalline structure of the semiconductor [128]. We can consider that ellipticity does not affect the electro-optical and facet contributions of dichroism and birefringence.

However, it may drastically affects the values of elasto-optic anisotropies. Effectively, an elliptical structure can simply be considered as a circular domain with a positive stress in the direction of the short half-axis, and a symmetrical negative stress in the direction of the long half-axis. These mechanical constrains of opposite signs may therefore induce opposite sign shifts for the elasto-optical contributions, *i. e.* different values for dichroism and birefringence according to the orientation of the lasing mode. Therefore, if we introduce these shifts in a symmetrical way, the cosine modes may have anisotropies of the kind $\gamma_{a,p}^c = \gamma_{a,p} + \Delta\gamma_{a,p}$ and the sine modes will be subjected to anisotropies of the kind $\gamma_{a,p}^s = \gamma_{a,p} - \Delta\gamma_{a,p}$. Even though this hypothesis is the one we will consider in our case, there may be other effects induced by ellipticity which could play a significant role in the VCSELs dynamics and emission properties.

8.2.4 The model

Starting from now, we will skip the overbar on the carriers density variables N_{\pm} , being understood that the densities are averaged along the active region's thickness. Along the same line, the superscript "nl" of the nonlinear susceptibility will also be omitted, since no confusion is to be expected at this stage.

The variables of the mesoscopic model are therefore the guided modes $E_{\pm mn}^{c,s}(t)$, the carrier density $N_{\pm}(\vec{r}_{\perp}, t)$, and the filtered feedback variable $F_{mn}^{c,s}(t)$.

For a x -polarized feedback mode $\mu_0 = \{m_0, n_0\}$, the full model can therefore

be written as

$$\begin{aligned} \partial_t E_{\pm mn}^{c,s} &= \frac{1}{2} \left[-\kappa_{mn} + 2i\omega_{mn}^{c,s} + i\frac{\Omega}{n_g n_b} \Gamma^{(l)} \bar{\chi}_{\pm mn}^{c,s} \right] E_{\pm mn}^{c,s} \\ &\quad - (\gamma_{a,mn}^{c,s} + i\gamma_{p,mn}^{c,s}) E_{\mp mn}^{c,s} + \frac{1}{\sqrt{2}} K_{mn} F_{mn}^{c,s} \end{aligned} \quad (8.2)$$

$$\begin{aligned} \partial_t F_{mn}^{c,s} &= - [\Delta\omega_G - i\omega_{\mu_0}^{c,s} - i\Delta\Omega_{x,\mu_0}] F_{mn}^{c,s} \\ &\quad + \frac{1}{\sqrt{2}} \Delta\omega_G [E_{+mn}^{c,s}(t-T) + E_{-mn}^{c,s}(t-T)] e^{-i\theta} \end{aligned} \quad (8.3)$$

$$\begin{aligned} \partial_t N_{\pm} &= \frac{\eta_i I}{2eW} C(\vec{r}_{\perp}) - \gamma_e N_{\pm} \mp \gamma_s [N_{+} - N_{-}] + \mathcal{D} \nabla_{\perp}^2 N_{\pm} \\ &\quad + \frac{2\varepsilon_0}{\hbar} \Im\{\chi_{\pm}[\vec{r}_{\perp}, N_{\pm}]\} \left[\frac{1}{W} \int_{-L}^0 |f(z)|^2 dz \right] \Gamma^{(l)} \\ &\quad \times \sum_{m,n} \sum_{c,s} |\Phi_{mn}^{c,s}(\vec{r}_{\perp})|^2 |E_{\pm mn}^{c,s}|^2 \end{aligned} \quad (8.4)$$

and it enables a temporal, spectral, and polarization resolved insight of the VCSEL's output beam.

The internal cavity parameters

The various parameters of Eqs. (8.3), (8.4) and (8.4) are the modal losses κ_{mn} (uniformly set to 600 ns^{-1}), the longitudinal confinement factor $\Gamma^{(l)}$ (0.04), the spin-flip rate γ_s (100 ns^{-1}), the non-radiative recombination rate γ_e (1.0 ns^{-1}), the bimolecular diffusion coefficient \mathcal{D} ($0.5 \mu\text{m}^2 \text{ ns}^{-1}$), the background refractive index n_b (3.3), the group-velocity refractive index n_g (3.5), the step-index variation between the core and the cladding Δn (0.01), and the optical carrier frequency Ω (deduced from $\lambda = 850 \text{ nm}$). The electro-optic contributions of dichroism and birefringence are $\gamma_{a,mn}$ (uniformly set to 0.1 ns^{-1}) and γ_p (10 ns^{-1}), and the elasto-optic shifts are $\Delta\gamma_{a,mn}$ (uniformly set to 0.3 ns^{-1}) and $\Delta\gamma_p$ (15 ns^{-1}). In our study, the pumping current will have a constant intensity I (4.5 mA). The internal quantum efficiency is η_i ($= 0.7$), and W is the thickness of the active region ($= 0.032 \mu\text{m}$). We are also assume that the electrons are uniformly distributed in the aperture of the active region, so that the normalized surface current density profile reads

$$C(\vec{r}_{\perp}) = \frac{1}{\pi r_a r_b} \text{ if } \varrho = \sqrt{\frac{x^2}{r_a^2} + \frac{y^2}{r_b^2}} < 1, \text{ and } 0 \text{ otherwise} \quad (8.5)$$

We are also considering the linear and frequency independent susceptibility in the active region

$$\chi_{\pm}[\vec{r}_{\perp}, N_{\pm}] = -i\chi_0 (1 + i\alpha) \left[\frac{2N_{\pm}}{N_0} - 1 \right] \quad (8.6)$$

where χ_0 is the susceptibility amplitude ($= 0.05$), α is the linewidth enhancement factor ($= 3.0$), and N_0 is the carrier density at transparency ($= 1.5 \times 10^{24} \text{ m}^{-3}$). The modal susceptibility can therefore be calculated as

$$\bar{\chi}_{\pm mn}^{c,s} = \iint_{\mathcal{S}_{ab}} \chi_{\pm}[N_{\pm}] |\Phi_{mn}^{c,s}(\vec{r}_{\perp})|^2 d^2\vec{r}_{\perp}, \quad (8.7)$$

where \mathcal{S}_{ab} is the surface of the elliptic cross-section.

The external cavity parameters

The strength of the feedback is $K_{mn} = [(1 - R_{ext}^2)/R_{ext}] [\rho_{mn}/\tau_{in}]$, where τ_{in} is the round-trip time in the laser cavity (0.05 ps), ρ_{mn} is the external reflection amplitude for each mode (considered in first approximation to be uniform, equal to 3%), and R_{ext} is the external facet reflectivity of the VCSEL ($= 0.995$). The external-cavity round-trip time is T ($= 4$ ns). In accordance with the dimensions of the VCSEL used in the experiment, the half-axis of the elliptical aperture are taken as $r_a = 4.9 \text{ }\mu\text{m}$ and $r_b = 4.4 \text{ }\mu\text{m}$. With the above parameters, the eigen-spectrum ω_{mn} associated to the optical cavity can be determined, as well as the corresponding transverse confinement factors $\Gamma_{mn}^{(t)}$. The frequency redshifts ω_{mn} are evaluated with the mean radius $r_m = (r_a + r_b)/2$. This model therefore enables us to simulate the instantaneous complex amplitudes of the guided LP_{mn} modes, which are characterized by their polarization (x or y), and by their orientation (c or s). In the numerical simulations, all these modes are simultaneously taken into account.

Finally we can also find a simplified expression for the lasing blueshifts $\Delta\Omega_{x,y}$ defined in Eq. (7.83). In fact, the gain typically balances the losses, so that using Eqs. (7.81) and (7.82), the blueshift can be expressed as a function of dichroism, birefringence, and linewidth enhancement factor following

$$\begin{aligned} \Delta\Omega_x &= \frac{1}{2}\alpha\kappa - (\gamma_p - \alpha\gamma_a) \\ \Delta\Omega_y &= \frac{1}{2}\alpha\kappa + (\gamma_p - \alpha\gamma_a). \end{aligned} \quad (8.8)$$

Also note that in case of y -polarized feedback, the feedback coefficient is equal to $\pm iK_{mn}/\sqrt{2}$, instead of $K_{mn}/\sqrt{2}$ as for x -polarized feedback.

Dimensionless model

It is mathematically more convenient to deal with a dimensionless model, principally because synthetically reduces the number of pertinent parameters. It is also preferable to have the same reference frequency for all the transverse modes $\mu = \{m, n\}$. For this purpose, the electric fields $E_{\pm\mu}^{c,s}$ and $F_{\pm\mu}^{c,s}$ can be frequency shifted using the transformation

$$\begin{aligned} E_{\pm\mu}^{c,s} &\rightarrow E_{\pm\mu}^{c,s} e^{-i\omega_{\mu}^{c,s}t} \\ F_{\mu}^{c,s} &\rightarrow F_{\mu}^{c,s} e^{-i\omega_{\mu}^{c,s}t}, \end{aligned} \quad (8.9)$$

so that the global electric field in each circular polarization may now be expanded as

$$\mathcal{E}_{\pm,\mu}(\vec{r}, t) = \frac{1}{2} \sum_{\mu,c,s} f(z) \Phi_{\mu}^{c,s}(\vec{r}_{\perp}) E_{\pm,\mu}^{c,s}(t) e^{i[\Omega + \omega_{\mu}^{c,s}]t} + \text{c.c.} \quad (8.10)$$

We can introduce the differential gain g , the material gain G , and the modal gain G_{μ} , the frequency detuning ϖ_{μ} , the modal feedback phase $\theta_{\mu}^{c,s}$, and the electric field normalization factor Υ as

$$g = \frac{\Omega}{n_g n_b} \frac{\chi_0}{N_0} \Gamma^{(l)}, \quad (8.11)$$

$$G_{\pm}(N_{\pm}) = g [2N_{\pm} - N_0], \quad (8.12)$$

$$G_{\pm\mu}^{c,s} = \iint_{S_{ab}} G_{\pm}(N_{\pm}) |\Phi_{\mu}^{c,s}(\vec{r}_{\perp})|^2 d^2\vec{r}_{\perp}, \quad (8.13)$$

$$\varpi_{\mu}^{c,s} = \omega_{\mu_0}^{c,s} - \omega_{\mu}^{c,s}, \quad (8.14)$$

$$\theta_{\mu}^{c,s} = (\Omega + \omega_{\mu}^{c,s})T, \quad (8.15)$$

$$\Upsilon = \frac{2\varepsilon_0}{\hbar\Omega} n_g n_b \frac{1}{W} \int_{-L}^0 |f(z)|^2 dz. \quad (8.16)$$

The electric fields E and F can be rescaled to $\Upsilon^{\frac{1}{2}}$, so that the modal density of photons can be directly evaluated as $|\Phi_{\mu}|^2 |E_{\mu}|^2 \sim |E_{\mu}|^2 / (\pi r_a r_b)$. We can

therefore rewrite our original evolution equation under the form

$$\begin{aligned} \partial_t E_{\pm\mu}^{c,s} &= \frac{1}{2} [-\kappa + (1 + i\alpha)G_{\pm\mu}] E_{\pm\mu}^{c,s} \\ &\quad - (\gamma_a^{c,s} + i\gamma_p^{c,s}) E_{\mp\mu}^{c,s} + \frac{K}{\sqrt{2}} F_{\mu}^{c,s} \end{aligned} \quad (8.17)$$

$$\begin{aligned} \partial_t F_{\mu}^{c,s} &= - [\Delta\omega_G - i\varpi_{\mu}^{c,s} - i\Delta\Omega_x] F_{\mu}^{c,s} \\ &\quad + \frac{1}{\sqrt{2}} \Delta\omega_G [E_{+\mu}^{c,s}(t-T) + E_{-\mu}^{c,s}(t-T)] e^{-i\theta_{\mu}^{c,s}} \end{aligned} \quad (8.18)$$

$$\begin{aligned} \partial_t N_{\pm} &= \frac{\eta_i I}{2eW} C(\vec{r}_{\perp}) - \gamma_e N_{\pm} \mp \gamma_s [N_{+} - N_{-}] + \mathcal{D}\nabla_{\perp}^2 N_{\pm} \\ &\quad - G_{\pm}(N_{\pm}) \sum_{\mu} \sum_{c,s} |\Phi_{\mu}^{c,s}(\vec{r}_{\perp})|^2 |E_{\pm\mu}^{c,s}|^2, \end{aligned} \quad (8.19)$$

which is significantly simpler to manage theoretically.

Note that because of the frequency shifts of Eq. (8.9), there are three important changes in these dimensionless equations. Firstly, the eigenfrequencies ω_{μ} do not appear anymore in Eq. (8.17); secondly, the eigenfrequency of the fed back mode $\omega_{\mu_0}^{c,s}$ is replaced by the relative frequency $\varpi_{\mu}^{c,s}$; and thirdly, the feedback phase θ is replaced by the modal feedback phase $\theta_{\mu}^{c,s}$.

8.3 Effect of the PFSF on the dynamics of the VCSEL

8.3.1 Determination of the external cavity modes

Starting from this dimensionless model, we can determine the amplitudes of the various modes μ as a function of the various parameters of the system. To illustrate the effect of the PFSF, we here restrict ourselves to case of x -polarized dynamics, such that $E_{x,\mu} \equiv E_{\mu} = \sqrt{2}E_{\pm,\mu}$. We can in that case set in first approximation $N_{+} = N_{-} \equiv N/2$, and introduce an unique material gain function $G(N) = g(N - N_0)$. The corresponding stationary final states can therefore be expressed as

$$E_{\mu}(t) = \sqrt{P_{\mu}} e^{i\Delta\Omega_x t} e^{i\Delta\omega t} \quad (8.20)$$

$$F_{\mu}(t) = \sqrt{Q_{\mu}} e^{i\Delta\Omega_x t} e^{i\Delta\omega t} e^{i\sigma_{\mu}}, \quad (8.21)$$

and inserting Eqs. (8.20) and (8.21) in Eqs. (8.17) and (8.18) yields

$$i(\Delta\Omega_x + \Delta\omega)\sqrt{P_\mu} = \frac{1}{2}[-\kappa + (1 + i\alpha)G_\mu]\sqrt{P_\mu} + K\sqrt{Q_\mu}e^{i\sigma_\mu} - (\gamma_a + i\gamma_p)\sqrt{P_\mu} \quad (8.22)$$

$$i(\Delta\Omega_x + \Delta\omega)\sqrt{Q_\mu} = -[\Delta\omega_G - i\varpi_\mu - i\Delta\Omega_x]\sqrt{Q_\mu} + \Delta\omega_G\sqrt{P_\mu}e^{-i(\Delta\Omega_x + \Delta\omega)T}e^{-i\theta_\mu}e^{-i\sigma_\mu} \quad (8.23)$$

If we split the real and imaginary parts in Eq. (8.22), we can show that $\sqrt{P_\mu}$ and $\sqrt{Q_\mu}$ are related as

$$\Delta\omega\sqrt{P_\mu} = K\sqrt{1 + \alpha^2}\sqrt{Q_\mu}\sin[\sigma_\mu - \arctan \alpha] \quad (8.24)$$

while on the other hand, splitting Eq. (8.23) into its real and imaginary parts yields

$$\cos[\sigma_\mu + (\Delta\Omega_x + \Delta\omega)T + \theta_\mu] = \frac{\sqrt{Q_\mu}}{\sqrt{P_\mu}} \quad (8.25)$$

$$\sin[\sigma_\mu + (\Delta\Omega_x + \Delta\omega)T + \theta_\mu] = \frac{\varpi_\mu - \Delta\omega}{\Delta\omega_G} \frac{\sqrt{Q_\mu}}{\sqrt{P_\mu}}. \quad (8.26)$$

From Eqs. (8.24) and (8.25) we have

$$\Delta\omega = K\sqrt{1 + \alpha^2}\cos[\sigma_\mu + (\Delta\Omega_x + \Delta\omega)T + \theta_\mu]\sin[\sigma_\mu - \arctan \alpha], \quad (8.27)$$

while from Eqs. (8.25) and (8.26) we can extract

$$\sigma_\mu + (\Delta\Omega_x + \Delta\omega)T + \theta_\mu = \arctan\left[\frac{\varpi_\mu - \Delta\omega}{\Delta\omega_G}\right] + m\pi, \quad \text{with } m \in \mathbb{Z}. \quad (8.28)$$

Hence, inserting Eq. (8.28) into (8.27) and using the trigonometric relation $\cos[\arctan x] = 1/\sqrt{1 + x^2}$, we can finally derive the transcendental algebraic equation for the external cavity modes (ECMs)

$$\Delta\omega = \frac{-K\sqrt{1 + \alpha^2}}{\sqrt{1 + \left(\frac{\varpi_\mu - \Delta\omega}{\Delta\omega_G}\right)^2}} \times \sin\left[(\Delta\Omega_x + \Delta\omega)T + \theta_\mu - \arctan\left(\frac{\varpi_\mu - \Delta\omega}{\Delta\omega_G}\right) + \arctan \alpha\right]. \quad (8.29)$$

By resolving the above equation, it is possible to find the frequencies $\Delta\omega$ of the ECMs associated to each transverse mode μ .

From this equation it can be deduced that the effective feedback strength of the frequency-selective feedback (FSF) is

$$C_{eff} = \frac{C}{\sqrt{1 + \left(\frac{\varpi_\mu - \Delta\omega}{\Delta\omega_G}\right)^2}} \quad (8.30)$$

where $C = KT\sqrt{1 + \alpha^2}$ is the feedback strength for the conventional feedback. In particular, it may be interesting to notice that FSF converges towards conventional external feedback when the bandwidth of the filter is very large, that this feedback strength goes to zero if the filter is too narrow, as well as when the frequency of a transverse mode is too far from with the center frequency of the filter. These results are quite similar to those obtained in ref. [123] for single mode edge-emitter semiconductor lasers with FSF.

A given mode does lase if and only if $\sqrt{P_\mu}$ and $\sqrt{Q_\mu}$ are different from 0. If we consider the real parts (ruling the dynamics of the amplitude) in Eqs. (8.22) and (8.23), we are led to

$$\frac{1}{2}[-\kappa + G_\mu - \gamma_a]\sqrt{P_\mu} + K\sqrt{Q_\mu} \cos \sigma_\mu = 0 \quad (8.31)$$

$$\sqrt{P_\mu} \cos[\sigma_\mu + (\Delta\Omega_x + \Delta\omega)T + \theta_\mu] - \sqrt{Q_\mu} = 0, \quad (8.32)$$

and the lasing condition (non-zero $\sqrt{P_\mu}$ and $\sqrt{Q_\mu}$) imposes the nullity of the determinant following

$$\frac{1}{2}[-\kappa + G_\mu - \gamma_a] + K \cos \sigma_\mu \cos[\sigma_\mu + (\Delta\Omega_x + \Delta\omega)T + \theta_\mu] = 0, \quad (8.33)$$

that is

$$G_\mu = \kappa + \gamma_a - \frac{2K \cos \sigma_\mu}{\sqrt{1 + \left(\frac{\varpi_\mu - \Delta\omega}{\Delta\omega_G}\right)^2}}, \quad (8.34)$$

where the phase-shift σ_μ can be explicitly determined through Eq. (8.28). The above equation is a key result: it shows that because of the frequency-selective feedback, the modal gain is either increased or decreased for each transverse mode, by an amount which strongly depends on the mode. In fact, this effect of the feedback is noticeable only for the mode μ_0 selected by the grating (the one for which $\varpi = 0$); in that case, the gain can be increased/decreased by an amount of the order of 10 ns^{-1} . On the other hand, the modal gains of the other modes are not directly affected by the FSF, because their detuning ϖ relatively to frequency of fed back mode is too large relatively to $\Delta\omega_G$.

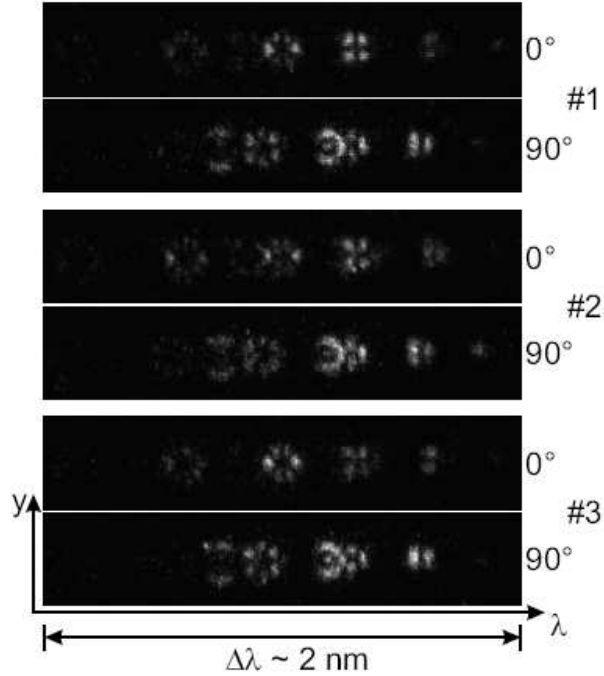


Figure 8.2. Experimental snapshots of spectrally resolved near-field intensity distributions. One transverse dimension is depicted in the vertical direction, while the horizontal direction exhibits the spectral dispersion maintaining the spatial resolution. The VCSEL was operated at a continuous-wave pump current of 4.5 mA. The snapshots number 1, 2 and 3 are taken at different successive instants, with an exposure time of 2 ns.

The issue is now to know if the effect of the FSF is precisely to increase or to decrease the modal gain of the fed back mode, that is, if the last term of Eq. (8.34) is positive or negative due to the term $\cos \sigma_\mu$. In that case, depending on the pumping current, the gain of the fed back mode can decrease below its threshold lasing value and stop lasing (feeding back this mode induces its suppression), or increase: hence, another (or more) mode(s), the least stable a priori, will indirectly be suppressed through a shortage of available carriers in the common reservoir. According to Eq. (8.33), a suitable parameter which can enable to increase or decrease the gain is the feedback phase $\theta_\mu = (\Omega + \omega_\mu)T$. In particular, tuning the laser central frequency Ω within the span of the external-cavity spacing frequency $\omega_{ext} = 2\pi/T$ should therefore lead to a wide variety of radically different dynamical regimes. Transverse mode selection can thereby be effective [87, 92].

8.3.2 Determination of the stationary modal amplitudes

In reference [82], **Valle** and **Pesquera** have shown that it is possible to find analytically the modal amplitudes of a VCSEL (without feedback) while operating under certain given conditions. We are going to apply and extend the method they have proposed to our case of VCSELs with FSF. We will first need to make one more approximation, assuming that owing to the strongly multimode dynamical state of the laser, the spatial fluctuations of the stationary carrier density $N(\vec{r}_\perp)$ are small compared to those of the spatial variations of the eigenmodes $\Phi(\vec{r}_\perp)$, so that

$$\begin{aligned} \sum_{\mu} G_{\mu} &= \sum_{\mu} \iint_{\mathcal{S}_w} G[N(\vec{r}_\perp)] |\Phi_{\mu}(\vec{r}_\perp)|^2 d^2 \vec{r}_\perp \\ &\simeq G(N) \sum_{\mu} \iint_{\mathcal{S}_w} |\Phi_{\mu}(\vec{r}_\perp)|^2 d^2 \vec{r}_\perp \\ &\simeq G(N) \sum_{\mu} \Gamma_{\mu}^{(t)}, \end{aligned} \quad (8.35)$$

where $\Gamma_{\mu}^{(t)}$ is the transversal confinement factor for the mode μ . In that case, if we restrict ourselves to cylindric-waveguide approximation, the partial differential equation for the stationary carrier density $N(r)$ can be deduced from Eq. (8.19) as

$$0 = \frac{\eta_i I}{eW} C(r) - \gamma_e N + \mathcal{D} \nabla_{\perp}^2 N - \sum_{\mu} \frac{1}{\Gamma_{\mu}^{(t)}} G_{\mu} |\Phi_{\mu}(r)|^2 |E_{\mu}|^2. \quad (8.36)$$

The above equation can be solved exactly using the Green method, and the solution reads [82]

$$N(r) = \sum_{\mu} \mathcal{A}_{\mu}(r) \cdot P_{\mu} + \mathcal{B}(r), \quad (8.37)$$

where $P_{\mu} = |E_{\mu}|^2$. The function $\mathcal{A}_{\mu}(r)$ is explicitly defined as

$$\begin{aligned} \mathcal{A}_{\mu}(r) &= -\frac{G_{\mu}}{\gamma_e \Gamma_{\mu}^{(t)}} \left[K_0 \left(\frac{r}{L_d} \right) \int_0^{\frac{r}{L_d}} \frac{|\Phi_{\mu}(vL_d)|^2 I_0(v)}{I_0(v)K_1(v) + I_1(v)K_0(v)} dv \right. \\ &\quad \left. + I_0 \left(\frac{r}{L_d} \right) \int_{\frac{r}{L_d}}^{+\infty} \frac{|\Phi_{\mu}(vL_d)|^2 K_0(v)}{I_0(v)K_1(v) + I_1(v)K_0(v)} dv \right], \end{aligned} \quad (8.38)$$

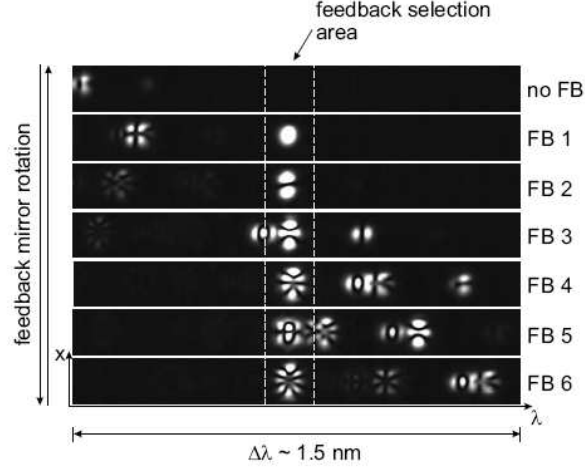


Figure 8.3. Experimental monitoring of the feedback mode with CCD2 (cf. Fig. 8.1). The mode within the area illustrated by the dashed rectangle is selected. By rotation of the external mirror, different transverse modes can be selected.

while $\mathcal{B}(r)$ reads

$$\mathcal{B}(r) = \frac{\eta_i I}{\gamma_e e W} \left[K_0 \left(\frac{r}{L_d} \right) \int_0^{\frac{r}{L_d}} \frac{C(vL_d) I_0(v)}{I_0(v) K_1(v) + I_1(v) K_0(v)} dv \right. \\ \left. + I_0 \left(\frac{r}{L_d} \right) \int_{\frac{r}{L_d}}^{+\infty} \frac{C(vL_d) K_0(v)}{I_0(v) K_1(v) + I_1(v) K_0(v)} dv \right], \quad (8.39)$$

where in both cases $L_d = \sqrt{D/\gamma_e}$ is the diffusion length of the carriers, while I_m and K_m are the m -th order modified Bessel functions of the first and second kind respectively. G_μ in $\mathcal{A}_\mu(r)$ is defined as in Eq. (8.34).

We can explicitly rewrite Eq. (8.34) as

$$\int_0^{r_m} g[N(r) - N_0] |\Phi_\mu(r)|^2 2\pi r dr = \kappa + \gamma_a - \frac{2K \cos \sigma_\mu}{\sqrt{1 + \left(\frac{\varpi_\mu - \Delta\omega}{\Delta\omega_G} \right)^2}} \quad (8.40)$$

and if we insert the solution of Eq. (8.37) in the above equation (8.40), we finally find that the optical output powers P_μ of the guided transverse modes obey the

following linear set of algebraic equations

$$\sum_{\nu} a_{\mu\nu} P_{\nu} = b_{\mu}, \quad (8.41)$$

with

$$a_{\mu\nu} = \int_0^{r_m} \mathcal{A}_{\nu}(r) |\Phi_{\mu}(r)|^2 r dr \quad (8.42)$$

$$b_{\mu} = - \int_0^{r_m} \mathcal{B}(r) |\Phi_{\mu}(r)|^2 r dr + \frac{\Gamma_{\mu}^{(t)}}{2\pi} N_0 + \frac{1}{2\pi g} \left[\kappa + \gamma_a - \frac{2K \cos \sigma_{\mu}}{\sqrt{1 + \left(\frac{\varpi_{\mu} - \Delta\omega}{\Delta\omega_G} \right)^2}} \right]. \quad (8.43)$$

The coefficients $a_{\mu\nu}$ and b_{μ} of the set (8.41) only have to be calculated once, they are constant: this is the principal advantage of the method, the fact that the modal amplitudes are obtained by solving a set of linear algebraic solutions.

However, the solutions P_{μ} of this set of equations *should absolutely be positive*. Therefore, if by solving Eq. (8.41) a negative value is found for a given mode P_{ν} , this mode must be discarded (following a precise procedure) and a new linear set of equations of lower dimensionality corresponding to the remaining modes must then be solved, and so on until only strictly positive solutions are obtained for all the lasing modes. The precise procedure to follow in order to carry out this process of discarding negative solutions is explained in detail in ref. [82].

From the theory presented above, we can understand why the FSF can affect several modes even though it directly affects only the fed back mode μ_0 for which $\varpi_{\mu_0} = 0$. In fact, in Eq. (8.41) the difference between a VCSEL without FSF and another with FSF is a perturbation (proportional to K) of the parameters $a_{\mu\mu_0}$ and b_{μ_0} . Before the perturbation is applied, we have exclusively positive solutions (lasing modes), but when this feedback perturbation is applied, some of these solutions turn to be negative, and in that case, they have to be discarded and a new set of equations of lower dimensionality whose solutions are strictly positive must be considered.

This is the mechanism that explains how a small perturbation only affecting one mode can lead to the suppression, excitation or amplitude variation of various others modes.

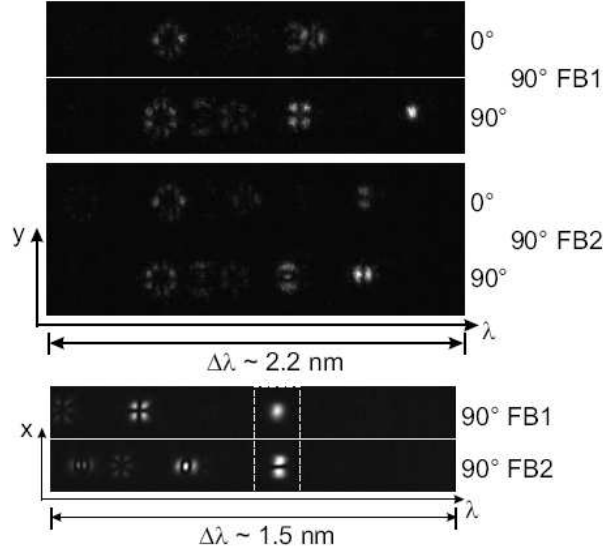


Figure 8.4. Experimental snapshots of polarization resolved spectrally dispersed near-field profiles at $I_{pump} = 4.5$ mA with FB of the fundamental mode LP_{01} (90° FB1) and with FB of the LP_{11}^c mode (90° FB2), all in the y -polarization direction. The mode-selection by CCD2 is depicted in the lower part of the figure.

8.4 Experimental results

The¹ first step in the experimental study has been the characterization of the VCSEL's dynamics when no feedback is applied.

In Fig. 8.2, successive single-shot measurements of the polarization- and spatially-resolved spectra are displayed. It can be seen that the lasing modes present a temporal dynamics, whose dominant frequencies have been shown to be rather low (< 0.5 GHz) [129]. However, the lasing modes remain the same despite their slow dynamics, that is, there is no dynamical exchange of stability between guided modes.

It can be observed that the intensity distributions of the two polarizations display a *spatial complementarity*, as local intensity maxima in one of the polarizations correspond to local intensity minima in the other polarization and vice versa. It also appears that the transverse modes are lasing in *complementary polarizations*, in the sense that when a cosine mode is lasing in one polarization, the corresponding sine mode preferentially lases in the other.

¹These experimental results have been obtained by Shyam Mandre, Ingo Fischer and Wolfgang Elsässer at the Technical University of Darmstadt, Germany. Figures 8.1, 8.2, 8.3 and 8.4 are reproduced after ref. [129], courtesy of the author.

It therefore results an *anti-correlation* amongst spatially overlapping modes, and a *correlation* between those who do not, or weakly overlap. The multimode competition dynamics of the system is globally ruled by these (anti-)correlations. For example, considering the case of the “six-lobes” LP_{31} modes, it can be seen that there is a mode competition between the spatially complementary modes LP_{31}^c and LP_{31}^s which are active in the two polarizations: a local intensity minimum in the 0° polarization corresponds to a local intensity maximum in the 90° polarization and vice versa.

The experimental selection procedure for the mode to be fed back is detailed in Fig. 8.3. The fed back mode is chosen by tilting the angle of the external mirror, so that only one transverse mode fits within the grating’s bandwidth, the others being washed out.

Figure 8.4 shows the results that are obtained when the fundamental mode $LP_{01,y}$ and a transverse mode $LP_{11,y}^c$ are fed back. It can be seen that typically, the fed back mode is enhanced, and even though the other modes may have a significantly lower intensity, some of them are not totally quenched. It should be emphasized that this enhancement is obtained through a suitable choice of the feedback phase: effectively, for another feedback phase value, the effect can be exactly opposite - the fed back mode being quenched and the others being enhanced.

In the first of single-shot measurements (90° FB1), the mode $LP_{01,y}$ is fed back and in consequence the selected fundamental mode is significantly enhanced. The optical spectra also reveal that modes which do not contribute to the VCSEL’s solitary emission (see Fig. 8.2) may be excited when feedback is applied, and they emit especially if their spatial profile is spatially complementary to the selected and enhanced mode’s profile. This occurs for example for the LP_{41} modes in both polarizations, and it can be considered that they take advantage from the fact that the fundamental mode depletes the carriers in the center of the VCSEL, while the peripheral carriers are still available for daisy-like modes.

The second pair of snapshot (90° FB2) presents similar qualitative features. Here, The fed back mode is $LP_{11,y}^c$ and it can be seen that the feedback enhances the mode intensity, almost switching off all the other modes. Still, according to what has been noted above, the mode $LP_{11,x}^s$ which is complementary in orientation and in polarization is also lasing, even though with a smaller intensity.

8.5 Numerical simulations

For the parameters we have chosen, there are 13 guided modes. In fact, this number has to be multiplied by 4 because each LP mode has two possible orientations (c,s) and two possible polarizations (x,y). We simulate all these modes simulta-

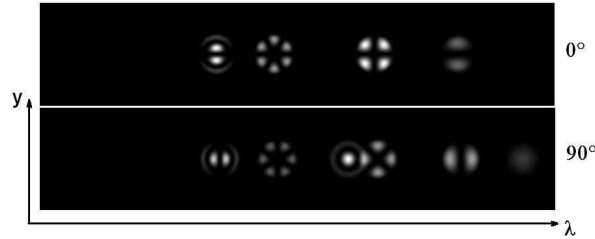


Figure 8.5. A numerical snapshot of the spectrally resolved near-field intensity distributions of the VCSEL without FSF, for $I = 4.5$ mA. This figure can be compared with Fig. 8.2.

neously, with a pumping current equal to $I = 4.5$ mA as in the experiment. The feedback reflectivity is fixed to $\rho = 3\%$, and the Lorentzian filter has a half-bandwidth $\Delta\omega_G/2\pi = 5$ GHz.

Globally, the features of the experimentally observed behavior is recovered.

In Fig. 8.5 for example, the numerical nearfield spectrum of the VCSEL is represented and it presents a strong similarity with the experimental spectrum of Fig. 8.2. It can be seen that free lasing modes (without feedback) are in general spatially complementary in order to deplete all the available carriers, and also complementary in polarizations. This double complementarity can be observed both experimentally and numerically. Ellipticity plays also an important role, as it favors the modes which are aligned along the longest half-axis, because these modes profit from a larger spatial overlap over the active medium. This can be clearly seen in the experimental spectra for the two-lobes modes LP_{11} without feedback. The modelling of ellipticity successfully enables to recover this modal discrimination, as the numerical simulations clearly replicate this experimental feature.

The effect of FSF can be observed in Fig. 8.6. Here again, the numerical spectrum is quite similar to the experimental spectrum of Fig. 8.4 in both polarizations. The only noticeable difference is that the LP_{41} is excited experimentally while it is the LP_{31} mode which is excited numerically. However, these two modes are both high-order transverse modes with approximately the same qualitative features, so the apparent difference is not very significative.

Typically, it can be observed that a feedback mode can always be amplified if fed back with the suitable feedback phase. Note for example that the fundamental mode is almost off without feedback, but lases strongly with feedback. Experiments, numerics and analytics coincide on that point. On the other hand, a mode lasing strongly without feedback can be practically switched off when polarization- and frequency selective feedback is applied, as it is the case for example for the mode LP_{21} . At last, it should also be noted that when a given mode is amplified, the spatially complementary mode is also amplified, with the *oppo-*

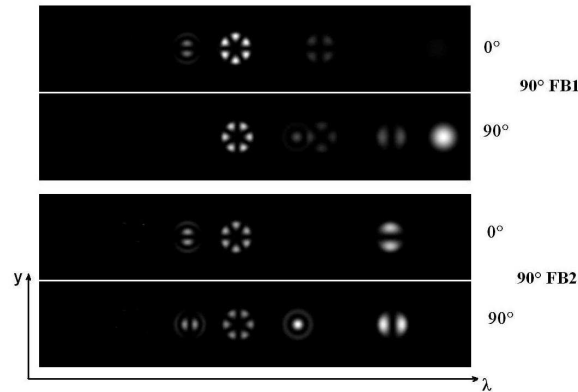


Figure 8.6. A numerical single-shot picture of polarization resolved spectrally dispersed near-field profiles at $I_{pump} = 4.5$ mA with FB of the fundamental mode LP_{01} (90° FB1) and with FB of the LP_{11}^c mode (90° FB2), all in the y -polarization direction. This figure can be compared with Fig. 8.4.

site polarization, and here again, there is a clear agreement between theory and experience.

Therefore, the model and the related numerical simulations are globally validated by the experimental measurements. However, it appears that enhancing a single mode while switching off all the others seems not to be possible for such strong pumpings ($> 3I_{th}$), low feedback strengths ($\sim 3\%$), and large-diameter VCSELs ($\sim 10 \mu\text{m}$). Obviously, for lower values of pumping ($< 1.5I_{th}$), exclusive stabilization of the fundamental mode is possible, but under extreme conditions as in our case, the PFSF has to be coupled with some other control mechanism in order to be fully effective.

8.6 Conclusion

We have investigated in this chapter the dynamics of a broad-area VCSEL under polarization- and frequency-selective feedback. The modal gains of the transverse modes have been calculated, and it has been shown that they are tightly related to the distribution of external-cavity modes, which are themselves dependent on the spectral properties of the external filter. It has therefore been possible to demonstrate that the optical phase attached to each transverse mode plays a decisive role as far as the enhancement or the quenching of that mode is concerned.

Numerical simulations have shown a good concordance with experimental measurements, in terms of spatial modal profiles and dynamics, and in terms of specific emission properties such as polarization and spatial complementarity.

General Conclusion

Chapter 9

General Conclusion

“The no-time imposes to time the tyranny of its spatiality.”

Aimé Césaire, *Me, kelp.*

THE focus of this thesis has been the study of the nonlinear dynamics related to some semiconductor laser systems with delayed feedback. In each case, analytical, numerical and experimental investigations have enabled a deep understanding of the related phenomenologies. An emphasis has also been laid on the innovative technological applications that can be derived from the observed behaviors.

The first part of the thesis was devoted to **Optical Chaos Cryptography**.

We have first evidenced that in delayed dynamical systems, fast-scale chaos can coexist with slow-scale periodicity, displaying a typical behavior which was referred to as **hyperchaotic breathers**. We have shown that this phenomenon can be observed in a relatively simple model, as the result of the interplay between a bandpass filter and a nonlinear feedback delay term. In systems where the filter is only low pass (and not bandpass) as in the Ikeda model [18], fast-scale chaos is observed when the feedback strength is high enough; however, slow-scale periodicity (breathers) can definitively not arise.

The disparity between the various time scales should also be emphasized, as in our case, for example, they span over 6 orders of magnitude. Neuronal systems also typically present a wide diversity of time scales in their dynamics, and they can display a large variety of spiking and bursting behaviors that are ruled by similar equations (see ref. [130] and references therein); if the propagation delay were taken into account in such models, we could expect chaotic breathers to appear.

In general, depending on the ratios between their related time scales, coexistence of chaos and periodicity could also be observed in other delayed dynamical systems, provided that the delayed feedback signal is subjected to a kind of bandpass filtering. It was also shown that when the nonlinear feedback strength was further increased, full hyperchaos could be observed.

Then, we have studied the synchronization of such hyperchaotic systems, and we have developed an analytical approximation to predict the effect of mismatch for the different parameters. The predictions give exact results in the case of mismatch in the nonlinear feedback amplitude term, excellent results for the off-set phase mismatch, and good results in the case of the time-delay mismatch and for the mismatch in the filter characteristic time scales. It was found that most of the parameters induce a synchronization error of the same order as the one of the mismatch.

In the case of multiple-parameter mismatch, we have given an analytic insight into a quite counterintuitive phenomenon: multiple-parameter mismatch can sometimes improve the quality of the synchronization. We have also obtained an approximation for the combined effects of all the mismatches taken simultaneously, showing how it is possible to improve the synchronization quality by compensating the mismatch in a given parameter with an added mismatch in another one. In practice, the interest of this multiple mismatch optimization would be at least to identify the conditions under which the synchronization error does not grow drastically in the case of multiple mismatches between the emitter and the receiver.

It may be interesting to extend our theory to other laser chaos synchronization schemes. For example, the Fourier spectrum of semiconductor lasers with a short external cavity can also in first approximation be assimilated to a band-limited white-noise spectrum (the relaxation oscillation frequency of the solitary laser is smaller than the external cavity- mode spacing frequency, so that the spectrum is not peaky). Therefore, it is a priori possible to apply our results to the study of parameter mismatch for that particular context. Another priority direction for future investigations is the improvement of the synchronization quality at the experimental level. This is by far the most complicated task: for example, even though some of the key components of the materials used for the experiments have been carefully matched *at the fabrication level* with a very high precision, much is still to be done to attain the final objective of a few percent synchronization error. In that spirit, the high sensibility of these devices functioning at multi-gigahertz frequencies requires to design the emitter and the receiver as integrated circuits. The influence of component and environmental fluctuations are issues that are still to be investigated, both theoretically and experimentally.

We have subsequently used the synchronized hyperchaotic systems to perform

optical chaos cryptography. In particular, we have investigated the influence of the mismatch noise on the BER, and we have shown that the probability density function of the hyperchaotic carrier and the peak-to-peak signal-to-rms-noise ratio are the only relevant parameters for the BER evaluation. The non-Gaussianity of the distributions associated to the mismatch noise can be analytically characterized by the Gram-Charlier coefficients, which enable to evaluate the BER of the cryptosystem as a correction of the well-known erfc-law corresponding to conventional Gaussian noise.

An interesting issue is to find the way to improve significantly the mismatch-induced BER, or equivalently, the SNR when it is below the threshold value. A first solution would be to decrease as much as possible the value of the *rms* mismatch noise. This issue has been thoroughly studied in the chapter on synchronization. A second option would be to increase the signal-to-carrier ratio, but this solution might threaten the security of the encrypted message, even though along that line, it has yet been shown that an eavesdropper directly tapping the communication channel achieves a BER of only 10^{-2} when the authorized chaos receiver achieves a 10^{-9} [107]. The two precedent options aim to improve directly the SNR. A third solution, sometimes used in numerical and experimental studies, may be to filter the decrypted signal at the receiver. The design of an optimal filter was not the purpose of this work, even though it seems at first glance that an integrator or an averager synchronized with the clock of the bit rate (to avoid the smoothening of the bit transitions) would be fairly convenient. This work has demonstrated that the probability density function of the carrier and the one of the mismatch noise also play a key role in the cryptosystem's performance and that the existence of a threshold value of the SNR above which the BER drops drastically is particularly interesting from a practical standpoint.

The second part of the thesis aimed to give a better understanding of the issue of **Radar-Frequency Generation** using opto-electronic oscillators.

We have first proposed a model for the study of the single-mode microwave dynamics of these oscillators. This model whose variable is the complex envelope amplitude of the microwave takes into account the intrinsic features of OEOs, that is a strong nonlinearity on the one hand and a very large delay on the other. The model had predicted a supercritical Hopf bifurcation of the amplitude as the loop gain is increased, that is, to an amplitude modulation which thereby induces the emergence of robust parasite side-peaks in the radio-frequency Fourier spectrum. This bifurcation has very important implication for the various applications of these oscillators: further studies will still have to define if this bifurcation is detrimental or not to the metrology performances of OEOs. This result is also important in the field of theoretical nonlinear dynamics, and particularly for the study of multiscale dynamics in delayed systems that can be encountered in various areas

of physics, engineering, chemistry and biology [3–5, 7, 18, 19, 51, 59].

Extensions of this work are numerous. A particular interest of this model is also that it can easily be adapted to a wide class of oscillators derived from the OEOs, like for example dual-loop [63], coupled [64], tuneable [65] or photonic filters OEOs. Along the same line, this modelling may improve the performance of these oscillators for other technological applications [66].

We have also focused on the stochastic and microwave dynamics of optoelectronic oscillators. The stochastic differential equation we have derived has reproduced the essential features of phase noise spectra as they are reported in the scientific literature. The relative influences of additive and multiplicative noises have been particularly highlighted.

We have given a insight into the multimode dynamics of OEOs. It has first been shown that under certain conditions, the mode competition could persist even at very large timescales. The multiple time scale method has permitted to determine approximate modal equations where it clearly appears that the cavity-modes are subjected to a nonlinear global coupling. This mechanism where the centermost modes are weakly damped but strongly coupled is therefore responsible for the observed behavior, that is, persisting multimode competition within few MHz around the central frequency of the RF filter. It is still to be investigated if with the aid of these modal equations, it may in principle be possible to evaluate the feasibility of active mode-locking schemes in view of technological applications.

At last, we have investigated a **Transverse-Mode Control** scheme in VCSELs based on polarization- and frequency-selective delayed feedback.

The multimode dynamics of the system has been modeled with a cold-cavity mode expansion obtained through the effective-index approximation, while the polarization dynamics was tracked using the spin-flip model. A Lorentzian filter has been considered to account for the filtering properties of the external cavity.

With this model, we have shown that the applied feedback configuration allows selection and feedback of single transverse modes, thereby affecting the modal composition of the laser optical spectrum. It has been demonstrated analytically that the modal gains are tightly related to the distribution of external-cavity modes, which are themselves dependent on the spectral properties of the external-cavity filter. It has therefore been possible to demonstrate that the optical phase attached to each transverse mode plays a decisive role as far as the enhancement or the quenching of a mode is concerned.

Numerical simulations have shown a good concordance with experimental measurements, in terms of spatial modal profiles and dynamics, and in terms of specific emission properties such as polarization and spatial complementarity. Our

work has at last shown that the emission dynamics of the VCSEL can be substantially stabilized when this twofold selective feedback is applied.

In conclusion, time delay in semiconductor lasers systems with feedback has presented in this thesis its ambivalent nature: sometimes a source of extreme disorder, and sometimes a source of extreme order; sometimes transforming the phase space into a boisterous river, and sometimes into a sea of tranquility.

In a system without dynamical spatial dimensions, time delay paradoxically appears as a signature of spatial extension: it therefore strangely resembles to that mysterious “no-time” of the poet. And fortunately for us, the ambivalency of the tyrant, associated to the wonderful properties of the “splendid light”, provides some opportunities of fascinating applications in lightwave and microwave technologies.

Bibliography

- [1] N. Krasovskii, “*Stability of Motion*”, (1959). Translation by Stanford University Press (1963).
- [2] J. K. Hale, *Proc. Natl. Acad. Sc.* **50**, 942 (1963).
- [3] W. H. Boykin Jr. and I. Flugge-Lotz, *J. of Spacecraft and Rockets* **6**, 685 (1969).
- [4] G. Stepan, T. Insperger, and R. Szalai, *Int. J. Bif. Chaos* **15**, 2783 (2005).
- [5] C. W. Eurich, A. Thiel and L. Fahse, *Phys. Rev. Lett.* **94**, 158104 (2005).
- [6] B. Doiron, M. J. Chacron, L. Maler, A. Longtin, and J. Bastian, *Nature* **421**, 539 (2003).
- [7] M. C. Mackey and L. Glass, *Science* **197**, 287 (1977).
- [8] A. Einstein, *Phys. Z.* **18**, 121 (1917).
- [9] R. D. Dupuis, *IEEE J. Quantum Electron.* **23**, 651 (1987).
- [10] <http://britneyspears.ac/physics/fplasers/fplasers.htm>
- [11] Hao Bai-Lin, “*Chaos*”, World Scientific, Singapore, Vol. I (1984) and Vol. II (1989).
- [12] J. Gleick, “*Chaos: Making a New Science*”, Heinemann (1987).
- [13] L. Glass and M. C. Mackey, “*From Clocks to Chaos, the Rhythmes of Life*”, Princeton University Press, Princeton (1988).
- [14] S. H. Strogatz, “*Nonlinear Dynamics and Chaos: with Applications in Physics, Biology, Chemistry and Engineering*”, Addison-Wesley, Reading (1994).
- [15] R. C. Hilborn, “*Chaos and Nonlinear dynamics*”, Oxford University Press, 2nd Edition, New-York (2000).
- [16] E. N. Lorenz, *J. Atmos. Sci.* **20**, 130 (1963).
- [17] H. Haken, *Phys. Lett. A* **53**, 77 (1975).
- [18] K. Ikeda, *Opt. Commun.* **30**, 257 (1979).
- [19] R. Lang and K. Kobayashi, *IEEE J. Quantum Electron.* **16**, 347 (1980).
- [20] K. Ikeda, H. Daido and O. Akimoto, *Phys. Rev. Lett.* **45**, 709 (1980).
- [21] D. Lenstra, B. H. Verbeek, and A. J. Den Boef, *IEEE J. Quantum Electron.* **21**, 674 (1985).
- [22] R. Vallee, P. Dubois, M. Cote and C. Delisle, *Phys. Rev. A* **36**, 1327 (1987).
- [23] R. Vallee and C. Mariott, *Phys. Rev. A* **39**, 197 (1989).
- [24] A. Pikovsky, M. Rosenblum and J. Kurths, “*Synchronization: A universal concept*”

in Nonlinear Sciences”; Cambridge University Press (2003).

- [25] H. Fujisaka and T. Yamada, *Prog. Theor. Phys.* **69**, 32 (1983).
- [26] L. M. Pecora and T. L. Carroll, *Phys. Rev. Lett.* **64**, 821 (1990).
- [27] L. M. Pecora and T. L. Carroll, *Phys. Rev. A* **44**, 2374 (1991).
- [28] H. G. Winful and L. Rahman, *Phys. Rev. Lett.* **65**, 1575 (1990).
- [29] R. Roy and K. S. Thornburg, *Phys. Rev. Lett.* **72**, 2009 (1994).
- [30] T. Sugawara, M. Tachikawa, T. Tsukamoto and T. Shimizu, *Phys. Rev. Lett.* **72**, 3502 (1994).
- [31] R. Brown, N. F. Rulkov and N. B. Tufillaro, *Phys. Rev. E* **50**, 4488 (1994).
- [32] G. A. Johnson, D. J. Mar, T. L. Carroll and L. M. Pecora, *Phys. Rev. Lett.* **80**, 3956 (1998).
- [33] A. Sanchez-Diaz, C.R. Mirasso, P. Colet, and P. Garcia-Fernandez, *IEEE J. Quantum Electron.*, **35**, 292 (1999).
- [34] J. Revuelta, C. R. Mirasso, P. Colet and L. Pesquera, *IEEE Photon. Tech. Lett.* **14**, 140 (2002).
- [35] L. Larger, J. P. Goedgebuer and F. Delorme, *Phys. Rev. E* **57**, 6618 (1998).
- [36] B. Schneier, “*Applied Cryptography*”; 2nd Edition, Wiley (1995).
- [37] R. Rivest, A. Shamir, L. Adelman, *Communications of the ACM* **21**, 120 (1978).
- [38] P. W. Shor, in *Proc. of the 35th Annual Symposium on Foundations of Computer Science*, (IEEE Press), 124 (1994).
- [39] C. H. Bennett and G. Brassard, in *Proceedings of IEEE International Conference on Computers, Systems and Signal Processing*, 175 (1984).
- [40] “Special issue on optical chaos and applications to cryptography”, ed. by S. Donati and C. R. Mirasso, *IEEE J. Quantum Electron.* **38** (2002).
- [41] K. M. Cuomo and A. V. Oppenheim, *Phys. Rev. Lett.* **71**, 65 (1993).
- [42] P. Colet and R. Roy, *Opt. Lett.* **19**, 2056 (1994).
- [43] G. D. Van Wiggeren and R. Roy, *Science* **279**, 1198 (1998).
- [44] G. Van Wiggeren and R. Roy, *Phys. Rev. Lett.* **81**, 3547 (1998).
- [45] J.-P. Goedgebuer, L. Larger, and H. Porte, *Phys. Rev. Lett.* **80**, 2249 (1998).
- [46] C. R. Mirasso, P. Colet and P. Garcia-Fernandez, *IEEE Phot. Tech. Lett.* **8**, 299 (1996).
- [47] V. Annovazzi-Lodi, S. Donati, and A. Scir`e, *IEEE J. Quantum Electron.* **32**, 953 (1996).
- [48] I. Fisher, Y. Liu and P. Davis, *Phys. Rev. A* **62**, 011801 (2000);
- [49] J.-P. Goedgebuer, P. Levy, L. Larger, C.-C. Chen and W. T. Rhodes, *IEEE J. Quantum Electron.* **38**, 1178 (2002).
- [50] L. Larger, V. S. Udaltsov, S. Poinot and E. Genin, *J. Opt. Technol.* **72**, 378 (2005).
- [51] Argyris, D. Syvridis, L. Larger, V. Annovazzi-Lodi, P. Colet, I. Fischer, J. Garcia-Ojalvo, C. R. Mirasso, L. Pesquera and K. A. Shore, *Nature* **438**, 343 (2005).
- [52] H. D. I. Abarbanel, M. B. Kennel, L. Illing, S. Tang, H. F. Chen, and J. M. Liu, *IEEE*

-
- J. Quantum Electron.* **37**, 1301 (2001).
- [53] Y. Liu, H. F. Chen, J. M. Liu, P. Davis, and T. Aida, *IEEE Trans. Circuits Syst. I* **48**, 1484 (2001).
- [54] N. F. Rulkov, M. A. Vorontsov, and L. Illing, *Phys. Rev. Lett.* **89**, 277905 (2002).
- [55] J. M. Liu, H. F. Chen and S. Tang, *IEEE Quantum Electron.* **38**, 1184 (2002).
- [56] V. Annovazzi-Lodi, S. Donati, and A. Scir`e, *IEEE J. Quantum Electron.* **33**, 1449 (1997).
- [57] C.R. Mirasso, J. Mulet and C. Masoller, *IEEE Phot. Tech. Lett.* **14**, 456 (2002).
- [58] J.-B. Cuenot, L. Larger, J.-P. Goedgebuer and W. T. Rhodes, *IEEE J. Quantum Electron.* **37**, 849 (2001).
- [59] X. S. Yao and L. Maleki, *Electron. Lett.* **30**, 1525 (1994).
- [60] X. S. Yao and L. Maleki, *J. Opt. Soc. Am. B.* **13**, 1725 (1996).
- [61] Y. Ji, X. S. Yao, and L. Maleki, *Proc. SPIE Gigahertz Devices and Systems* **3861**, 58 (1999).
- [62] D. Eliyahu, L. Maleki, *Proc. 2003 IEEE Int. Freq. Contr. Symposium*, 405 (2003).
- [63] X. S. Yao and L. Maleki, *IEEE J. Quantum Electron.* **36**, 79 (2000).
- [64] X. S. Yao, L. Davis, and L. Maleki, *J. Lightwave Technol.* **18**, 73 (2000).
- [65] S. Poinot, H. Porte, J.-P. Goedgebuer, W. T. Rhodes, and B. Bousset, *Opt. Lett.* **27**, 1300 (2002).
- [66] D. Strekalov, D. Aveline, N. Yu, R. Thompson, A. B. Matsko, and L. Maleki, *J. Lightwave Technol.* **21**, 3052 (2003).
- [67] J. Lasri P. Devgan, R. Tang, and P. Kumar, *Opt. Express* **11**, 1430 (2003);
- [68] P. Devgan, J. Lasri, R. Tang, and P. Kumar, *Electron. Lett.* **39**, 1337 (2003).
- [69] L. M. Narducci, J. R. Tredicce, L. A. Lugiato, N. B. Abraham and D. K. Bandy, *Phys. Rev. A*, **33**, 1842 (1986).
- [70] K. A. Winick, *IEEE J. Quantum Electron.* **35**, 10 (1999).
- [71] A. M. Yacomotti, L. Furfaro, X. Hachair, F. Pedaci, M. Giudici, J. Tredicce, J. Javaloyes, S. Balle, E. A. Viktorov and Paul Mandel *Phys. Rev. A* **69**, 053816 (2004).
- [72] J. L. Font, R. Vilaseca, F. Prati and E. Roldan, *Optics Commun.* **261**, 336 (2006).
- [73] H. Soda, K. Iga, C. Kitahara and Y. Suematsu, *Jpn. J. Appl. Phys.* **18**, 2329 (1979).
- [74] S. K. Mandre, I. Fischer, and W. Elsäßer, *Optics Commun.* **244**, 355 (2005).
- [75] H. Kuwahara, Y. Onoda, M. Goto, and T. Nakagami, *Appl. Opt.* **22**, 2732 (1983).
- [76] J. Sacher, W. Elsäßer and E. O. Göbel, *Phys. Rev. Lett.* **63**, 2224 (1989).
- [77] T. Sano, *Phys. Rev. A* **50**, 2719 (1994).
- [78] A. M. Levine, G. H. M. v. Tartwijk, D. Lenstra and T. Erneux, *Phys. Rev. A* **52**, R3436 (1995).
- [79] C. Masoller and N. B. Abraham, *Phys. Rev. A* **57**, 1313 (1998).
- [80] T. Heil, I. Fisher and W. Elsäßer, *Phys. Rev. A* **58**, R2672 (1998).
- [81] A. Valle, J. Sarma, and K. A. Shore, *IEEE J. Quantum Electron.* **31**, 1443 (1995).
- [82] A. Valle and L. Pesquera, *J. Opt. Soc. Am. B* **19**, 1549 (2002).

- [83] M. San Miguel, Q. Feng and J. V. Moloney, *Phys. Rev. A* **52**, 1728 (1995).
- [84] <http://io.intec.ugent.be//VCSELS.html>
- [85] M. Giudici, S. Balle, T. Ackemann, S. Barland, and J. R. Tredicce, *J. Opt. Soc. Am. B* **16**, 2114 (1999).
- [86] M. Sciamanna, T. Erneux, F. Rogister, O. Deparis, P. Mgret, and M. Blondel, *Phys. Rev. A* **65**, 041801 (2002).
- [87] J. Dellunde, A. Valle, and K. A. Shore, *J. Opt. Soc. Am. B* **13**, 2477 (1996).
- [88] J. Y. Law and G. P. Agrawal, *IEEE J. Sel. Top. in Quantum Electron.* **3**, 353 (1997).
- [89] M. S. Torre, C. Masoller, and Paul Mandel, *Phys. Rev. A* **66**, 053817 (2002).
- [90] N. A. Loiko, A. V. Naumenko, and N. B. Abraham, *J. Opt. B: Quantum Semiclass. Opt.* **3**, S100 (2001).
- [91] A. Barchanski, T. Gensty, C. Degen, I. Fischer, and W. Elsässer, *IEEE J. Quantum Electron.* **39**, 850 (2003).
- [92] F. Marino, S. Barland and S. Balle, *IEEE Photon. Technol. Lett.* **15**, 789 (2003).
- [93] B. E. A. Saleh and M. C. Teich, *Fundamentals of Photonics*, John Wiley & Sons, New-York (1991).
- [94] T. Erneux, L. Larger, M. W. Lee and J.-P. Goedgebuer, *Physica D* **194**, 49 (2004).
- [95] J. Rius, M. Figueras, R. Herrero, F. Pi, J. Farjas, and G. Orriols, *Phys. Rev. E* **62**, 333 (2000).
- [96] J. Rius, M. Figueras, R. Herrero, J. Farjas, F. Pi, and G. Orriols, *Chaos* **10**, 760 (2000).
- [97] Z. Qu, G. Hu, G. Yang and G. Qin, *Phys. Rev. Lett.* **74**, 1736 (1995).
- [98] M. Schwartz, *‘Information, Transmission, Modulation and Noise’*, 4th edition, McGraw Hill, 1990.
- [99] R. N. McDonough and A. D. Whalen, *‘Detection of Signals in Noise’*, 2nd edition, Academic Press, 1995.
- [100] R. Vicente, J. Dauden, P. Colet and R. Toral, in *‘Physics and Simulation of Optoelectronic Devices XI’*, ed. by M. Osinski, H. Amano and P. Blood, *Proc. SPIE* **4986**, 452 (2003).
- [101] B. Dorizzi, B. Grammaticos, M. Le Berre, Y. Pomeau, E. Ressayre and A. Tallet, *Phys. Rev. A* **35**, 328 (1987).
- [102] L. M. K. Vandersypen, M. Steffen, G. Breyta, C. S. Yannoni, M. H. Sherwood, and I. L. Chuang, *Nature* **414**, 883 (2001).
- [103] <http://www.smartquantum.com>
- [104] F. Daschelt and W. Schwartz, *IEEE trans. Circ. Syst. I* **48**, 1498 (2001).
- [105] Y. Chembo Kouomou and P. Wofo, *Phys. Lett. A*, **308**, 381 (2003).
- [106] J. F. Heagy, T. L. Carroll, and L. M. Pecora, *Phys. Rev. E*, **52**, R1253 (1995).
- [107] N. Gastaud, S. Poinot, L. Larger, J.-M. Merolla, M. Hanna, J.-P. Goedgebuer and F. Malassenet, *Electron. Lett.* **40**, 898 (2004).
- [108] I. G. Gradshteyn and I. M. Ryzhik, *‘Table of integrals, series and Products’*, 5th edition, Academic press (1994).

-
- [109] Q. T. Zhang, *IEEE Trans. on Communications*, **45**, 270 (1997).
- [110] M. K. Simon and M. S. Alouini, *IEEE Trans. on Communications*, **46**, 1625 (1998).
- [111] M. A. Najib and V. K. Prabhu, *IEEE Trans. on Vehicular Technol.*, **49**, 783 (2000).
- [112] C. R. Mirasso, R. Vicente, P. Colet, J. Mulet and T. Perez, *C. R. Physique* **5**, 613 (2004).
- [113] X. S. Yao and L. Maleki, *Opt. Lett.* **22**, 1867 (1997).
- [114] M. C. Mackey and I. G. Nechaeva, *Phys. Rev. E* **52**, 3366 (1995).
- [115] L. Illing and D. J. Gauthier, *Physica D* **210**, 180 (2005).
- [116] E. Rubiola, “*The Leeson effect - Phase noise in quasilinear oscillators*” (Rev 1.0), ArXiv:physics/0502143 v1, (2005).
- [117] A. H. Nayfeh, “*Problems in perturbation*”, John Wiley and Sons (1985).
- [118] Y. Chembo Kouomou and P. Wofo, *J. Sound and Vib.* **270**, 75 (2004).
- [119] C. Degen, “*Transverse mode formation in oxide-confined Vertical-Cavity Surface-Emitting Lasers: Analysis of the underlying mechanisms*”, PhD Thesis, Technical University of Darmstadt, Germany (2001).
- [120] J. Mulet and S. Balle, *IEEE J. Quantum Electron.* **38**, 291 (2002).
- [121] J. Mulet and S. Balle, *Phys. Rev. A* **66**, 053802 (2002).
- [122] J. Mulet, “*Semiconductor laser dynamics: Compound cavity, polarization and transverse modes*”, PhD Thesis, University of the Balearic Islands, Spain (2003).
- [123] M. Yousefi and D. Lenstra, “Dynamical behavior of a semiconductor laser with filtered external optical feedback”, *IEEE J. Quantum Electron.* **35**, 970 (1999).
- [124] K. D. Choquette and R. E. Leibenguth, *IEEE Photon. Technol. Lett.* **6**, 40 (1994).
- [125] G. P. Bava, P. Debernardi and L. Fratta, *Phys. Rev. A* **63**, 023816 (2001).
- [126] A. Valle, *IEEE J. Quantum Electron.* **34**, 1924 (1999).
- [127] A. Valle and L. Pesquera, *IEEE Photon. Technol. Lett.* **13**, 272 (2001).
- [128] P. Debernardi, G. P. Bava, C. Degen, I. Fischer and W. Elsässer, *IEEE J. Quantum Electron.* **38**, 73 (2002).
- [129] S. K. Mandre, “*Controlling the emission properties of high-power semiconductor lasers: stabilization by optical feedback and coherence-control*”, PhD thesis, Technical University of Darmstadt, Germany (2006).
- [130] E. M. Izhikevich, *Int. J. Bif. Chaos* **10**, 1171 (2000).

List of Figures

1.1	An edge-emitter semiconductor laser.	5
1.2	Ikeda optical turbulence	8
1.3	Huyghens clocks	8
1.4	Chaos synchronization in the Lorenz system	9
1.5	Optical fiber network of the Athens experiment.	12
1.6	Principle of OEOs.	15
1.7	Some phase noise spectra.	16
1.8	Electron microscope image of a VCSEL.	18
1.9	Multimode VCSEL emission	19
2.1	Electro-optic phase modulator	27
2.2	Electro-optic intensity modulator	28
2.3	Experimental set-up of the semiconductor laser system with electro-optical feedback.	30
2.4	Periodic solutions after $\gamma = 1$	34
2.5	Periodic solutions after $\gamma = -1$	34
2.6	Variation of the limit cycle-frequencies after the Hopf bifurcations.	35
2.7	Numerical simulation of the evolution of the breathers	36
2.8	Numerical zoom into the breathers' structure.	37
2.9	Large scale experimental timetraces of the breathers.	38
2.10	Small-scale experimental timetraces of the breathers.	38
2.11	Experimental evolution of the breathers.	39
2.12	Experimental data about the statistical properties of the random noise.	41
2.13	Dependence of the noise variance with the offset bias voltage.	42
3.1	Experimental set-up for the synchronization of the semiconductor laser systems	45
3.2	Shifting effect of the ΔT mismatch.	49
3.3	Synchronization error and cross-correlation for a ΔT mismatch.	51
3.4	Synchronization error and cross-correlation for a $\Delta\beta$ mismatch	52
3.5	Synchronization error and cross-correlation for a $\Delta\phi$ mismatch	56
3.6	Synchronization error and cross-correlation for a $\Delta\theta$ mismatch	59

3.7	Synchronization error and cross-correlation for a $\Delta\tau$ mismatch	60
3.8	Reduction of the synchronization error in case of multiple parameter mismatch	64
3.9	Level-curve patterns in a parameter mismatch subspace	66
3.10	Experimental hyperchaotic timetrace, Fourier spectrum and MZ transfer-function	68
3.11	Experimental verification of the shift effect	69
3.12	Experimental variations of the synchronization error	70
4.1	Experimental set-up of the cryptosystem.	82
4.2	Numerical simulations for the carrier used for cryptography, and related PDF	86
4.3	Numerical simulations of the mismatch noise	87
4.4	Deviation function for weighting the deviation from the erfc BER law	89
4.5	Numerical simulation of the BER variations	90
4.6	Experimental variation of the Gram-Charlier coefficients	91
4.7	Experimental hyperchaotic carrier, and related PDF	92
4.8	Experimental variations of the BER	93
4.9	Experimental eye-diagrams	94
5.1	Experimental set-up of an OEO	104
5.2	Numerical simulation of the complex amplitude equation	107
5.3	Experimental timetraces and Fourier spectra before, at and after the Neimark-Sacker bifurcation	110
5.4	Bifurcation diagrams showing the Neimark-Sacker bifurcation	111
6.1	Numerical phase noise spectra	115
6.2	Numerical simulation of the OEO spectrum after 1 second.	118
6.3	Experimental RF spectrum of an OEO in the multimode regime	119
7.1	The $E-\vec{k}$ diagram of a quantum-well VCSEL.	133
7.2	A selectively-oxidized VCSEL.	135
7.3	A schematical representation of a VCSEL with PFSF.	146
7.4	Representation of the various contributions of the carrier dynamics.	155
8.1	Experimental set-up for the PFSF of VCSELs.	161
8.2	Experimental snapshots of the VCSEL's dynamics.	169
8.3	Experimental monitoring of the PFSF.	171
8.4	Experimental single-shot images when the modes LP_{01} and LP_{11}^c are fed back.	173
8.5	Numerical snapshot of the VCSEL's dynamics without PFSF.	175
8.6	Numerical snapshot when some transverse modes are fed back.	176

CURRICULUM VITAE

Yanne CHEMBO KOUOMOU

Personal Data

First name : Yanne
Surnames : Chembo Kouomou
Date of birth : July 2nd, 1976
Place of birth : Blanc-Mesnil (France)
Nationality : Cameroonian
Civil Status : Single
e-mail : ckyanne@imedea.uib.es

Academic Degrees

Degree: M.Sc. in Physics
Center: University of Yaounde I (Cameroon)
Year: 2001

Degree: Ph.D. in Physics
Dissertation: *Contribution for the exploitation of coherent and incoherent nonlinear phenomena in telecommunication.*
Center: University of Yaounde I (Cameroon)
Years: November 2001- November 2005
Supervisor: Prof. Paul Wofo

Degree: Ph.D. in Physics
Dissertation: *Nonlinear dynamics of semiconductor laser systems with feedback: Applications to optical chaos cryptography, radar-frequency generation and transverse-mode control.*
Center: University of the Balearic Islands (Spain)
Years: November 2002- December 2006
Supervisor: Dr. Pere Colet

Current Affiliation

Fellowship holder from the *Govern de les Illes Balears*
since October 2003 at the University of the Balearic Islands.

Publications of the thesis

Articles

- Y. Chembo Kouomou, P. Colet, N. Gastaud and L. Larger, “Effect of parameter mismatch on the synchronization of semiconductor lasers with electro-optical feedback”, *Physical Review E* **69**, 056226 (2004).
- Y. Chembo Kouomou, P. Colet, L. Larger and N. Gastaud, “Mismatch-induced bit error-rate in optical communications using semiconductor lasers with electro-optical feedback”, *IEEE Journal of Quantum Electronics*, **41**, 156 (2005).
- Y. Chembo Kouomou, P. Colet, L. Larger and N. Gastaud, “Chaotic breathers in delayed electro-optical systems”, *Physical Review Letters* **95**, 203903 (2005).
- Y. Chembo Kouomou, L. Larger, H. Tavernier, R. Bendoula, P. Colet, and E. Rubiola, “Delayed frequency-selective optoelectronic oscillators in strongly nonlinear regimes”, *Submitted*.
- Y. Chembo Kouomou, S. K. Mandre, I. Fischer, W. Elsässer and P. Colet, “Frequency-selective feedback control of the multi-transverse mode dynamics in VCSELs”, *Submitted*.
- Y. Chembo Kouomou and P. Colet, “Performances of single-mode current-modulated VCSELs stabilized by frequency-selective feedback.”, *Submitted*.

In preparation:

- Y. Chembo Kouomou, L. Larger, P. Colet, H. Tavernier, R. Bendoula, and E. Rubiola, “Persistent multimode behavior in switched-on opto-electronic oscillators”.

Proceedings

- Y. Chembo Kouomou, P. Colet, L. Larger and N. Gastaud, “Effect of chaotic noise on the performance of optical chaos cryptosystems”, *Proceedings of SPIE, Noise in communication systems*, **5847**, 10 (2005).
- Y. Chembo Kouomou, P. Colet, L. Larger and N. Gastaud, “Fast scale hyperchaos on top of slow scale periodicity in delayed dynamical systems”, *First IFAC conference on analysis and control of chaotic systems* **1**, 375 (2006).

Other Publications

Articles

- Y. Chembo Kouomou and P. Wofo, “Triple resonant states and chaos control in an electrostatic transducer with two outputs”, *Journal of Sound and Vibrations* **270**, 75 (2004).
- Y. Chembo Kouomou and P. Wofo, “Cluster synchronization in coupled chaotic semiconductor lasers and application to switching in chaos-secured communication networks”, *Optics Communications*, **223**, 283 (2003).
- Y. Chembo Kouomou and P. Wofo, “Transitions from spatiotemporal chaos to cluster and complete synchronization states in a shift-invariant set of nonlinear coupled oscillators”, *Physical Review E* **67**, 046205 (2003).
- Y. Chembo Kouomou and P. Wofo, “Stability analysis for the synchronization of semiconductor lasers with ultra-high frequency current modulation”, *Physical Letters A* **308**, 381 (2003).
- Y. Chembo Kouomou and P. Wofo, “Optimization and stability boundaries for the synchronization of semiconductor lasers with external optical feedback”, *Physical Review E* **67**, 026214 (2003).
- Y. Chembo Kouomou and P. Wofo, “Generalized correlated states in a ring of coupled nonlinear oscillators with a local injection”, *Physical Review E* **66**, 066201 (2002).
- Y. Chembo Kouomou and P. Wofo, “Stability and optimal parameters for continuous feedback chaos control”, *Physical Review E* **66**, 036205 (2002).
- Y. Chembo Kouomou and P. Wofo, “Stability and optimization of chaos synchronization through feedback coupling with delay”, *Physics Letters A* **298**, 18 (2002).
- Y. Chembo Kouomou and P. Wofo, “Stability and chaos control in electrostatic transducers”, *Physica Scripta* **62**, 255 (2000).

Book Chapter

- Y. Chembo Kouomou and P. Wofo,
“Optimization of chaos synchronization and pattern formation in a lattice of nonlinear oscillators and semiconductor lasers”,
Recent Research Developments in Physics **3**, 577 (2002). Edited by S. G. Pandalai, Transworld Research Network, Kerala, INDIA

Specialization Courses

Ph.D. courses in the University of the Balearic Islands

- *Cooperation models based on agents*. M. San Miguel. UIB 2003 [3 credits]
- *Numerical simulation methods in physics*. R. Toral. UIB, 2003 [3 credits]
- *Dynamical systems*. O. Piro and E. Hernández. UIB, 2003 [3 credits]
- *Components for fiber communication systems*. C. R. Mirasso. UIB 2003 [3 credits]
- *Statistical mechanics: phase transitions and polymer systems*. R. Toral. UIB, 2004 [3 credits]
- *Polymers and biomolecules*. T. Sintès and R. Toral. UIB, 2004 [3 credits]
- *Dynamics of spatiotemporal structures*. E. Hernández, O. Piro, and M. San Miguel. UIB 2004 [5 credits]

Other specialization courses

- **School and Workshop on Dynamical Systems and Applications**,
3-8 May 2004, Porto, PORTUGAL.
Oral presentation:
“*Optical chaos cryptography using in semiconductor lasers with electro-optical feedback*”
Y. Chembo Kouomou, P. Colet, N. Gastaud and L. Larger.
- **Summer School on New Concepts in Photonics and Optical Communications**,
21-25 June 2004, Dijon, FRANCE.
- **Peyresq 2006 Summer School on Nonlinear Dynamics**,
18-25 September 2006, Peyresq, FRANCE.

Stays at foreign research centers

- **Georgia-Tech Lorraine,**
7-12 July 2003 and 22-23 April 2004, Metz, FRANCE
Collaboration with Prof. Laurent Larger.
- **Technical University of Darmstadt,**
2-5 August 2004, Darmstadt, GERMANY
Collaboration with Dr. Ingo Fischer.
- **Institute for Research in Electronics and Applied Physics, University of Maryland,**
From April 14th to July 14th, 2005, College Park, MD, USA
Collaboration with Prof. Rajarshi Roy
- **FEMTO-ST Institute, University of Franche-Comté,**
From February 3rd to August 2nd, 2006, Besançon, FRANCE
Collaboration with Prof. Laurent Larger.

Seminars

- **Instituto Mediterráneo de Estudios Avanzados (IMEDEA),**
18th December 2002, Esporles, SPAIN
“Analytical stability analysis for the synchronization of chaotic semiconductor lasers with external optical feedback or ultra-high frequency pumping-current modulation. ”
- **Instituto Mediterráneo de Estudios Avanzados (IMEDEA),**
21st July 2004, Palma de Mallorca, SPAIN
“Hyperchaotic breathers in delayed optical systems. ”
- **Technical University of Darmstadt,**
3rd August 2004, Darmstadt, GERMANY
“Simultaneous fast-scale hyperchaos and slow-scale periodicity in delayed optical systems. ”
- **Centre National d’Etudes Spatiales (CNES),**
27th June 2006, Toulouse, FRANCE
“A model for single-mode optoelectronic oscillators.”

Congress participations and presentations

- **OCCULT Meeting,**
14-15 February 2003, Pavia, ITALY.
Oral presentation:
“Effect of parameter mismatch on the synchronization of electro-optical intensity laser hyperchaos. ”
Y. Chembo Kouomou, P. Colet, and L. Larger.
- **European Quantum Electronics Conference EQEC 2003,**
22-27 June 2003, Munich, GERMANY.
Oral presentation:
“Performance comparison of different encoding schemes in chaotic optical communication systems. ”
R. Vicente, Y. Chembo Kouomou, T. Pérez, P. Colet and C. R. Mirasso.
- **Bristol Centre for Applied Nonlinear Mathematics (BCNAM) conference on “Delayed Equations and their Applications”,**
8-12 September 2003, Bristol, UNITED KINGDOM.
- **Weierstrass Institute for Applied Analysis and Stochastics (WIAS) workshop on “Dynamics of semiconductor lasers”,**
15-17 September 2003, Berlin, GERMANY.
Oral presentation:
“Influence of parameter mismatch on the performance of an electro-optical hyperchaotic communication scheme. ”
Y. Chembo Kouomou, P. Colet, N. Gastaud and L. Larger.
- **OCCULT Meeting,**
18-20 September 2003, Metz and Besançon, FRANCE.
Oral presentation:
“On the determination of the mismatch-induced bit error-rate in an hyperchaotic communication scheme. ”
Y. Chembo Kouomou, P. Colet, N. Gastaud and L. Larger.
- **Dynamics Days 2003,**
24-27 September 2003, Palma de Mallorca, SPAIN.
Oral presentation:
“On the mismatch-induced degradation of synchronization in hyperchaotic electro-optical systems. ”
Y. Chembo Kouomou, P. Colet, N. Gastaud and L. Larger.
- **Fises 2003,**
23-25 October 2003, Pamplona, SPAIN.
Poster:
“Parameter mismatch influence on the synchronization of chaotic lasers with

electro-optical feedback. ”

Y. Chembo Kouomou, P. Colet, N. Gastaud and L. Larger.

- **OCCULT Meeting,**
4-6 March 2004, Bangor, UNITED KINGDOM.
Oral presentation:
“*Noise and relaxation behavior in semiconductor lasers with electro-optical feedback.* ”
Y. Chembo Kouomou, P. Colet, N. Gastaud and L. Larger.
- **SPIE Photonics Europe 2004,**
26-30 April 2004, Strasbourg, FRANCE.
- **OCCULT Meeting,**
4-6 March 2004, Bangor, UNITED KINGDOM.
Oral presentation:
“*Noise and relaxation behavior in semiconductor lasers with electro-optical feedback.* ”
Y. Chembo Kouomou, P. Colet, N. Gastaud and L. Larger.
- **The 8th Experimental Chaos Conference,**
14-17 June 2004, Florence, ITALY.
Poster:
“*Coexistence of fast-scale hyperchaos and slow-scale periodicity in delayed optical systems.* ”
Y. Chembo Kouomou, N. Gastaud, L. Larger and P. Colet.
- **Dynamics Days 2004,**
13-17 September 2004, Palma de Mallorca, SPAIN.
Oral presentation:
“*Simultaneous fast-scale hyperchaos and slow-scale periodicity in delayed optical systems.* ”
Y. Chembo Kouomou, P. Colet, N. Gastaud and L. Larger.
- **The 3rd SPIE Conference on Noise and Fluctuations,**
23-26 May 2005, Austin-Texas, USA.
Oral presentation:
“*Effect of Chaotic Noise on the Performance of Optical Chaos Cryptosystems.* ”
Y. Chembo Kouomou, P. Colet, L. Larger and N. Gastaud.
- **CLEO Europe - EQEC 2005,**
12-17 June 2005, Munich, GERMANY.
Oral Presentations:
- “*Influence of Mismatch noise on the bit error-rate performance of an optical chaos cryptosystem.* ”

-“*Hyperchaotic breathers in semiconductor lasers with electro-optical feedback.*”

Y. Chembo Kouomou, P. Colet, L. Larger and N. Gastaud.

- **2005 Gordon Research Conferences on Nonlinear Science**,
June 26th-July 1st , 2005, Colby College, Waterville (ME), USA.
- **IXe Rencontres du Non-Linéaire**,
8-10 March 2006, Poincaré Institute, Paris, FRANCE.
- **1st IFAC Conference on analysis and Control of Chaotic Systems**,
28-30 June 2006, Reims, FRANCE.
Oral Presentation:
-“*Fast scale hyperchaos on top of slowscale periodicity in delayed dynamical systems.*”
Y. Chembo Kouomou, P. Colet, L. Larger and N. Gastaud.
- **Fises 2006**,
14-17 September 2006, Granada, SPAIN.
Poster:
“*A stochastic model for optoelectronic radar-frequency generators.*”
Y. Chembo Kouomou, L. Larger, H. Tavernier, R. Bendoula, P. Colet and E. Rubiola

Computer experience

- Programming: Fortran, Basic, Pascal, C++, Matlab, Gnuplot.
- Operating systems: UNIX, Windows, DOS.

Language skills

- French (excellent)
- English (good)
- Spanish (good)